Electrochemical modeling of lithium-ion cell behaviour for electric vehicles

Andrea Falconi

To cite this version:

Andrea Falconi. Electrochemical modeling of lithium-ion cell behaviour for electric vehicles. Catalysis. Université Grenoble Alpes, 2017. English. NNT : 2017GREAI043 . tel-01730759

HAL Id: tel-01730759
https://theses.hal.science/tel-01730759

Submitted on 13 Mar 2018

Communauté
UNIVERSITÉ Grenoble Alpes

THÈSE

Pour obtenir le grade de

DOCTEUR DE LA COMMUNAUTE UNIVERSITE GRENOBLE ALPES

Spécialité : **Matériaux, Mécanique, Génie civil, Electrochimie**

Arrêté ministériel : 25 mai 2016

Présentée par

Andrea FALCONI

Thèse dirigée par **Christine LEFROU,** Maitre de Conférence de l’Institut polytechnique de Grenoble, et codirigée par **Renaud CORNUT**, Ingénieur du Commissariat à l'Energie Atomique et aux Energies Alternatives préparée au sein du **Laboratoire d'Electrochimie et de Physico-Chimie des Matériaux et des Interfaces** dans **l'École Doctorale I-MEP2 : Ingénierie - Matériaux, Mécanique, Environnement, Energétique, Procédés, Production**

Modélisation électrochimique du comportement d'une cellule Li-ion pour application au véhicule électrique

Thèse soutenue publiquement le **5 Octobre 2017** devant le jury composé de :
Yann BULTEL
Professeur, Institut polytechnique de Grenoble, Président du jury
Christophe FORGEZ
Professeur, Université de technologie de Compiègne, Rapporteur
Vincent VIVIER
Directeur de Recherche, CNRS, Rapporteur
Valérie SAUVANT-MOYNOT
Chef de département, IFPEN, Examinatrice
David SICSIC
Ingénieur R&AE, Groupe Renault, Co-Encadrant
Monsieur Renaud CORNUT
Ingénieur, CEA Saclay, Co-Directeur de thèse
Christine LEFROU
Maître de Conférences, Grenoble INP, Directrice de thèse

Electrochemical Li-ion battery modeling for electric vehicles

Abstract

The future development of electric vehicles is mostly dependent of improvements in battery performances. In support of the actual research of new materials having higher performances in terms of energy, power, durability and cost, it is necessary to develop modeling tools. The models are helpful to simulate integration of the battery in the powertrain and crucial for the battery management system, to improve either direct (e.g. preventing overcharges and thermal runaway) and indirect (e.g. state of charge indicators) safety. However, the battery models could be used to understand its physical phenomena and chemical reactions to improve the battery design according with vehicles requirements and reduce the testing phases. One of the most common model describing the porous electrodes of lithium-ion batteries is revisited. Many variants available in the literature are inspired by the works of prof. J Newman and his research group from UC Berkeley. Yet, relatively few works, to the best of our knowledge, analyze in detail its predictive capability. In the present work, to investigate this model, all the physical quantities are set in a dimensionless form, as commonly used in fluid mechanics: the parameters that act in the same or the opposite ways are regrouped, and the total number of simulation parameter is greatly reduced. In a second phase, the influence of the parameter is discussed, and interpreted with the support of the limit cases. The analysis of the discharge voltage and concentration gradients is based on galvanostatic and pulse/relaxation current profiles and compared with tested commercial LGC cells. The simulations are performed with the software Comsol® and the post-processing with Matlab®. Moreover, in this research, the parameters from the literatures are discussed to understand how accurate are the techniques used to parametrize and feed the inputs of the model. Then, our work shows that the electrode isotherms shapes have a significant influence on the accuracy of the evaluation of the states of charges in a complete cell. Finally, the protocols to characterize the performance of commercial cells at different C-rates are improved to guarantee the reproducibility.

Keywords: Lithium-ion battery, electrochemical modeling, electric vehicles, porous electrodes, LIB COMSOL simulation, LIB test protocols, LIB state of charge identification.

Résumé

Le développement futur des véhicules électriques est lié à l'amélioration des performances des batteries qu'ils contiennent. Parallèlement aux recherches sur les nouveaux matériaux ayant des performances supérieures en termes d'énergie, de puissance, de durabilité et de coût, il est nécessaire développer des outils de modélisation pour : (i) simuler l'intégration de la batterie dans la chaine de traction et (ii) pour le système de gestion de la batterie, afin d'améliorer la sécurité et la durabilité. Soit de façon directe (par exemple, la prévention de surcharge ou de l'emballement thermique) soit de façon indirecte (par exemple, les indicateurs de l'état de charge). Les modèles de batterie pourraient aussi être utilisés pour comprendre les phénomènes physiques et les réactions chimiques afin d'améliorer la conception des batteries en fonction des besoins de l'utilisateur et de réduire la durée des phases de test. Dans ce manuscrit, un des modèles les plus communs décrivant les électrodes poreuses des batteries au lithium-ion est revisité. De nombreuses variantes dans la littérature s'inspirent directement du travail mené par le professeur J. Newman et son équipe de chercheurs à l'UC Berkeley. Pourtant relativement peu d'études analysent en détail les capacités prédictives de ce modèle. Dans ce travail, pour étudier ce modèle, toutes les grandeurs physiques sont définies sous une forme adimensionnelle, comme on l'utilise couramment dans la mécanique des fluides : les paramètres qui agissent de manière identique ou opposée sont regroupés et le nombre total de paramètres du modèle est considérablement réduit. Cette étude contient une description critique de la littérature incluant le référencement des paramètres du modèle développé par le groupe de Newman et les techniques utilisées pour les mesurer, ainsi que l'écriture du modèle dans un format adimensionnel pour réduire le nombre de paramètres. Une partie expérimentale décrit les modifications de protocoles mis en œuvre pour améliorer la reproductibilité des essais. Les études effectuées sur le modèle concernent d'une part l'identification des états de lithiation dans la cellule avec un attention particulière sur la précision obtenue, et enfin une prospection numérique pour examiner l'influence de chaque paramètre sur les réponses de la batterie en décharge galvanostatique puis en mode impulsion et relaxation.

Mot-clé : Batterie lithium-ion, modélisation électrochimique, véhicule électrique, électrode poreuse, simulation, COMSOL, protocole d'essais, identification état de charge.

Summary

List of symbols

SYMBOL [UNITS]	DESCRIPTION
$S[m^2]$	Electrodes Surface Area
$D_{S,+}\ , D_{S,-}\ [m^2 s^{-1}]$	Solid phase diffusivity
$D_{+,}, D_{-}, D_e[m^2 s^{-1}]$	Effective ions diffusivity in the electrolyte
$\sigma_+, \sigma_-[S\ m^{-1}]$	Electronic conductivity solid matrix
$d_+, d_-, d_e[m]$	Electrode and separator thickness
$R_+, R_-[m]$	Active material's Particles size
$t_+[adim]$	Transport number of lithium ions
$C^*[mol\ m^{-3}]$	Initial Li^+concentration
$C_{s+,max}, C_{s-,max}[mol\ m^{-3}]$	Maximum Li concentration in the active material
$\varepsilon_{+,s}, \varepsilon_{-,s}[m^3\ m^{-3}]$	Active material volume fraction
$\varepsilon_{+,l}, \varepsilon_{-,l}[m^3\ m^{-3}]$	Electrode Porosity (electrolyte volume fraction)
$k_+^*, k_-^*[mol\ m^{-2} s^{-1}]$	Reaction rate constant,
$\kappa_+, \kappa_-, \kappa_e[S\ m^{-1}]$	Electrolyte conductivity
$a_+, a_-[m^2\ m^{-3}]$	Active surface
$\theta_{+,c},\ \theta_{-,c}[adim]$	Positive/Negative Electrode Stoichiometry
$Q_+,\ Q_-[Ah]$	Electrode Capacity
$Q_{max}[Ah]$	Cell Capacity
$\alpha_+\alpha_-$	Kinetic transfer coefficients
$F\ [C\ mol^{-1}\ ]$	Faradays constant, 96487
$R[J\ mol^{-1}\ K^{-1}\ ]$	Gas Constant, 8.3143
$I\ [A]$	Current load
$T\ [K]$	Temperature
$\ddot{U}_+\ , \ddot{U}_-[V]$	Deviation of the Electrode OCV from the Nernst Isotherm.
$\hat{\theta}(x)[mol\ m^{-3}]$	Average lithium concentration
	Subscripts
+/-/e	Positive electrode/Negative Electrode/Separator

Table 1 – The list of the dimensional parameters is reported with their units and description.

SYMBOL [UNITS]	DESCRIPTION
$\tilde{\varphi}[-]$	non-dimensional solid phase potential
$\theta[-]$	non-dimensional concentration
$\tilde{C}[-]$	non-dimensional liquid phase concentration
$\tilde{\chi}[-]$	non-dimensional liquid phase potential
$\tilde{x}[-]$	non-dimensional l distance
$\tilde{t}[-]$	non-dimensional time
$\tilde{Q}[-]$	non-dimensional cell capacity
$\ddot{u}_{\pm}[-]$	non-dimensional deviation of the electrode OCV from the Nernst isotherm.
$\tilde{J}[-]$	non-dimensional current

Table 2 – The list of the non-dimensional variables is reported with their units and description.

1 The state of the art on electrochemical modelling for Lithium-ion batteries

1.1. Framework and objectives

Electric vehicles (EV) are periodically promoted as a pollution-free and economic alternative to gasoline vehicles. In reality, this technology is still affected by low autonomy and the high costs [1]. For these reasons, in the past their diffusion was limited. Despites these technological challenges, the EVs are the most promising solution for: mitigating the greenhouse effect, improving air quality for the citizen and ensuring the energetic stability from oil producing regions [2]. The continuous drop in battery prices combined with the consciousness against the emissions of internal combustion engines, could boost the EV sales up to hundreds of thousands in 2020-2030 [3], [4]. The electrical vehicles program is the core of the Renault's strategical framework to achieve zero emissions in automobile transports. The objective is to guarantee, to everyone, the access to silent and emission-free vehicles with no-compromises between performances and safety. The Li-ion batteries, are one of the most promising technology able to achieve these goals. These batteries are largely diffused in consumer electronics because of their performances but, major improvements are still required to reduces costs, improving the safety and extend the lifetime for EV applications. Moreover, these batteries require expensive and time-consuming tests to ensure their safety, evaluate their performance and assess their degradation during the years [5], [6]. Thus, better methods are required to predict these information during the cell design phase [7]. Improvements for the cell design (e.g. better performances, faster charging protocols or reduced ageing) or the understanding of physicochemical phenomena, could be achieved with the support of modeling [8]. In fact, an electrochemical model could simulate the behavior of lithium ion cells by using the chemical characteristics of the compounds and the design parameters.

In this field, the Newman's model and its variants represent a reference. These models are nowadays an intense object of research and largely promoted in commercials software [9]–[11].

The growth of articles on EVs, batteries and modelling are illustrated in Figure 1. Before 1989 the numbers of articles on EVs can be neglected while a constant number of articles on non-lithium ion is observed in Figure 1(A). Then, after the introduction of the first commercial lithium ion battery by Sony in 1991, the publications on EVs increase exponentially by reaching 2000 articles only for in the last year. Thus, the articles on lithium-ion batteries follows the same exponential growth. As consequence, the general interest for new battery technologies is rising to supply the demand of electric vehicles. However, it is also evident how the development of electric vehicles is strictly connected to the introduction of lithium ion batteries. The number of papers on battery modelling is also rising but near 40 % of them, in 2016, are focused on lithium ion batteries as illustrated in Figure 1(B). Among all the publications on modeling, few hundreds concern physical based models. In conclusion, the development of modeling tools, from both industry (e.g. automotive producers and battery manufacturer) and academy (e.g. research centers) aiming to push forward the battery performances, is rapidly increasing.

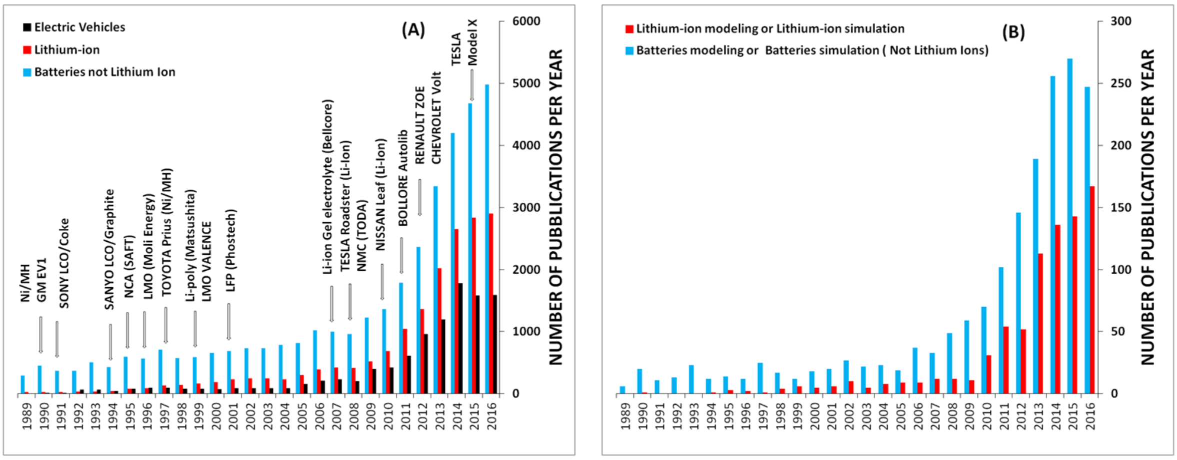

Figure 1 – The histograms in (A-B) reports the number of publications in the periods coming from 1989 to 2016. In picture (A) the publications are for keywords: “Electric Vehicles”, “Lithium-Ion”, and “batteries” that are not lithium-ion. In picture (B) are reported the number of lithium ions model and the models of batteries that are not lithium ion. (Source: Web of Science®)

During a previous Ph.D. project in Renault, a simplified electrochemical model, developed by M. Safari in 2011, was able to simulate the battery (graphite/LFP) voltage up to 1C load [12], [13]. Thus, this work, can be considered as the further step to model a lithium ion battery using the Newman’s theory to increase the comprehension on batteries and improving the performances of modelling. In fact, after the testing of some commercial software, Renault decided to develop its own tools to improve the know-how on lithium-ion battery modelling.

This work aims to develop the simplest possible electrochemical model, based on the Newman’s theory, to find a compromise between the predictability and the number of parameters. For this reason, the parameters available in literature are analysed to detect a range of values for each parameter and then investigate their contribution in the model. To generalise these results, the equations systems and the parameters are set in a dimensionless form, following an approach commonly used in fluid mechanics. Thus, the effects of each parameter are isolated in a limit case. In fact, for a limit case the parameter object of study, is the only parameter responsible for the result observed. Another question we want to answer, is how to accurately characterize the battery performances without worrying about the load history. In fact, we believe that only effective and accurate tests can be compared with the numerical simulations, while at the same time it uses only few parameters that are could be easily measured.

Thus, at the first the literature state of the art is identified and then critically discussed. An innovative non-dimensional system of equations able to generalise kinetic laws from the simulations based on the Newman's model is proposed. The values of the parameters from the literature are regrouped in a database also useful for further simulations. Commercial LG cells are electrically and physiochemically characterized to evaluate the performances and identify the parameters for the model. Thus, a new protocol aiming to accurately establish the electrical performances of the cells is proposed. Then, the electrode balancing and how the shape of the isotherms affects the estimation of the state of charge are deeply studied. Finally, in the last section the proposed non-dimensional model is solved in COMSOL for limiting cases and the kinetic limitations are generalised.

In the next section, the working principles of the lithium ion batteries are shortly exposed.

1.2. Lithium-ion working principles

The Lithium-ion battery is a complex system where mass transports and chemical reactions acts together [14]–[16]. In this section, the working principles are illustrated while the characteristics of a commercial cell are investigated in detail § 4.2. The LIB system is working because the electrodes have the ability to reversibly host lithium in their structure. The cell is a sandwich composed of three porous components, as reported in Figure 2: two electrodes and a separator placed within.

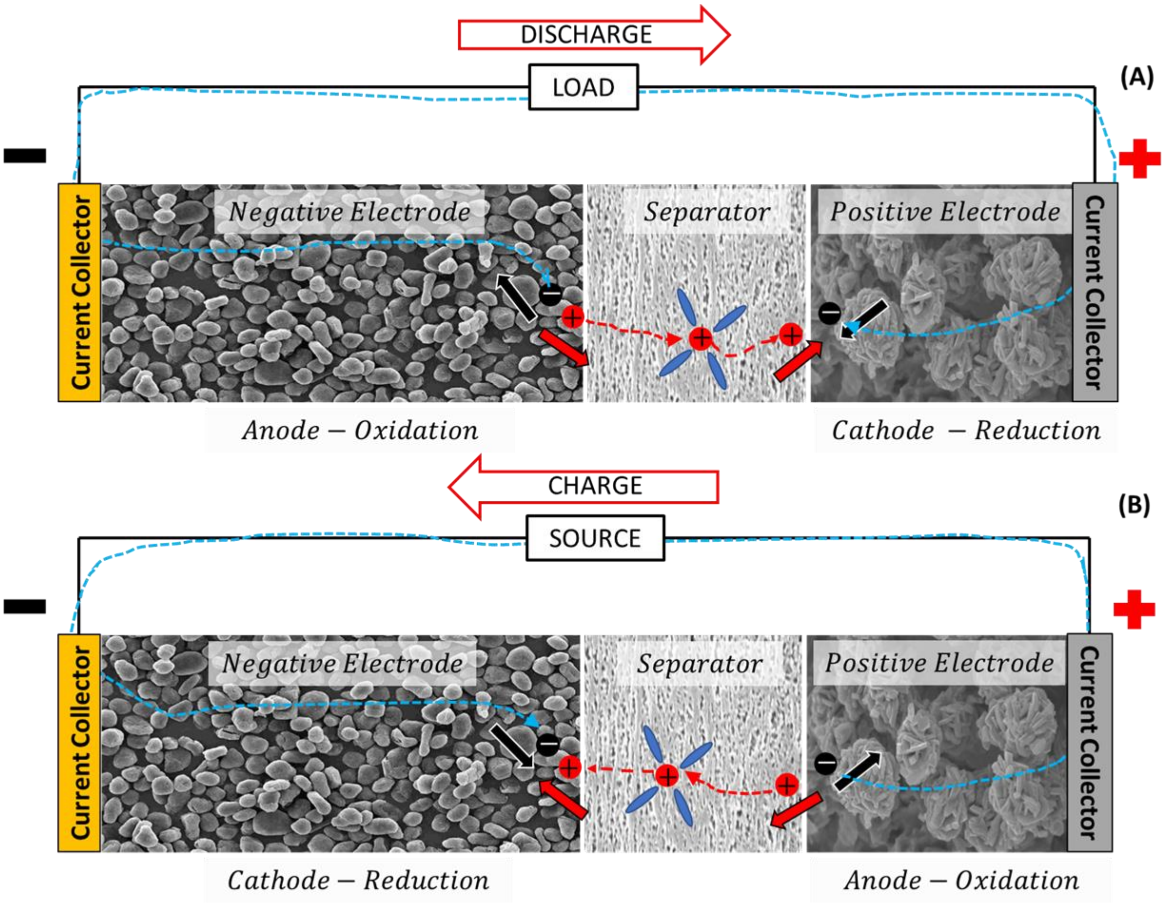

Figure 2 – The lithium ion cells is constituted of two electrodes backed on two current collectors and a separator. The working principle of a lithium ion cell is illustrated. The red circles with a plus sign represents the lithium ions, while the black circle with a minus sign represent the electrons and the blue particles is the solvent. The dashed lines in blue and red represents the path of the electron and the lithium ions, respectively.

The void spaces, in these porous structures, are filled with an electrolyte composed of a mixture of solvents, additives and a lithium salt (e.g. $LiPF_6$ in a mixture of ethylene carbonate and ethyl methyl carbonate). The purpose of the separator is to avoid the direct contact between the electrodes (in fact, this generate a short circuit) but to allow the flow of charged species. The electrodes are based on chemical compounds where the lithium can soak into them. The positive electrode is usually a lithium metal oxide, with a large choice of different chemical elements (e.g. lithium manganese oxide, lithium nickel cobalt aluminum oxide, lithium iron phosphate), while the negative electrode is usually based on carbon (or rarely other materials such as the lithium titanate). The potential of the electrodes depends on the chemical species and the amount of lithium in its structure. Since each species has a different potential, a voltage jump between the two electrodes is created. Thus, the positive electrode and the negative electrode are assigned to the compounds with the higher potential and the lower potential, respectively. Hence, the cell voltage is given by the difference between the potentials of these electrodes. The electrodes are backed on a metallic current collector, usually aluminum and copper for the positive electrode and the negative electrode, respectively. Then, an electric tab is soldered to each current collector. When these tabs are connected to a load *via* an externa wire, a flow of electrons circulates between the electrodes and thus the cell discharges, as illustrated in Figure 2 (A). Instead, when the cell is connected to an electric source the reaction is forced to reverse and consequently the cell is recharged, as illustrated in Figure 2 (B). The details of this process that produces electrons circulating in an external circuit are explained in the followings.

Either during the cell charge or discharge, lithium-ions intercalate in one electrode and deintercalated from the other. Thus, the ions shuttles between the electrodes creating a flow of charged species in the electrolyte. At the same time, this reaction of intercalation requires the participations of electrons: when an ion of lithium leaves the host structure of the electrode, an electron moves in the external circuit in direction of the other electrode. In parallel, an electron from the external circuit react with the lithium ion to intercalate in the host structure in the other electrode. Thus, a net flow of electric charges is moving: ions in the electrolyte and electrons in the external cables and electrodes.

The working principle of any electrochemical system is based on the possibility that a chemical species exists under two different forms. These two species are called oxidant and reductant, indicated by “Ox” and “Red” respectively. The transformation of the matter from “Ox” to “Red” goes *via* the electron shift at the atomic level, the so called redox reaction. When a chemical element (i.e. lithium) of this compound loses one electron this species undergoes to oxidation, instead, the reduction occurs, when the species gains an electron.

Consequently, the overall reaction splits into two simultaneous half-reactions:

$$\begin{cases} Li\Theta_S \xrightarrow{ox} Li^+ + \Theta_S + e^- \\ Li^+ + \Theta_S + e^- \xrightarrow{red} Li\Theta_S \end{cases} \qquad \text{Eq. 1}$$

where Θ_S is the host site in the latex of the insertion material. The complete redox reaction is then:

$$Li^+ + \Theta_S + e^- \underset{ox}{\overset{red}{\rightleftharpoons}} Li\Theta_S \qquad \text{Eq. 2}$$

In this system, the electro-chemical reactions occur at the interface between the solid and the liquid phases. The porous structure of the electrodes, guarantees a higher active surface compared to a bulky electrode having the same dimensions. Consequently, the electrodes in lithium ion cells are porous, because higher is the active surface and higher is the power density.

During the charge, most of the lithium in the positive electrode leaves the host structure and goes into the host structure of the negative electrode. If the negative electrode is made of lithium metal, the lithium ions are simply deposed on its surface. To reduce the formation of dendrites (i.e. the deposition of solid lithium over the electrodes when their potential is close to zero), that could generate short circuits, the lithium metal is replaced with the less performant graphite as a negative electrode. In fact, the graphite has a lower specific capacity but because of its slightly higher potential than lithium metal, the lithium deposition is disfavored. However, another inconvenient on graphite, is that during the first lithiation the potential decreases and the electrolyte reacts with the carbon on the surface creating new compounds and releasing gas, such as CO_2. This process is accompanied by a non-reversible consumption of lithium ions that remains trapped in these compounds. Thus, the surface of the active material is covered with the so-called solid electrolyte interface (SEI). This layer is composed of a mixture of lithium carbonates and many other complex compounds [17]–[30]. Fortunately, it constitutes a barrier between the active material and the electrolytes, preventing further reactions between the electrode and the electrolyte. However, the SEI (that is mostly formed during the first charge of the battery), could be broken up and it is subject to degradation due to both current and temperature cycling. Consequently, the SEI is re-formed at each time that the electrode's surface is directly exposed to the electrolyte. One of the major degradation of the battery is attributed to the non-stability of SEI resulting in the direct contact between the graphite the electrolyte. Thus, the re-decomposition of the electrolyte creates a new layer of SEI to fill the cracks in the old SEI. This overview illustrates how the involved phenomena are complex and mutually coupled. Thus, an appropriate model is required to develop new cells and to simulate their behavior when they are integrated in a system (such as the EVs powertrain).

1.3. Lithium-ion battery modelling

The main purpose of modeling is to develop a mathematical representation able to simulate a system behavior. In lithium ion batteries, many complex phenomena are involved such as: the mass transport, migrations of ions, red-ox reactions (i.e. transformations of the chemical compounds when they react with electrodes) and side reactions. The current collectors can be neglected since their conductivity is orders of magnitude higher than the values of active materials or electrolytes as reported in § 3.5. Thus, the potential drop in the collectors may be reasonably neglected. For these reasons, any proposed model can partially describe its behavior.

In recent years, many models are developed for different purposes [31], [32], such as the integration of a battery in a more complex electrical system (e.g. a EV powertrain) or to focus into the internal physics (e.g. mass transport and chemical reactions). Some niche models are based on stochastics, artificial neural networks or the fuzzy logic [33]–[36]. These approaches are not based on the physics of the system, but they still can reproduce its behavior. Thus, it is possible to divide all these models in two families based on: the phenomenology or the physics of the system. The phenomenological models can reproduce the battery behavior (i.e. the voltage drop under an external load) after a test campaign aiming to characterize electrically the cell performances in several operating conditions (e.g. temperature, state of charge, degradation, etc.). These models includes, as an example, empirical equations (Shepherd in 1965 [37]) and equivalent electric circuits. Instead, the electrochemical model describes the physics of the involved phenomena, such as (the list is not exhaustive): diffusion of ions, mechanical strain, charge transfer and migrations of ions.

However, some hybrid models containing elements of both families can also be found, as an example: the model developed by Rakhmatov & Vrudhula 2001 [38] contains the diffusion of lithium in the solid phase and the empirical Peukert's law, or the transmission line model that uses electric lumped elements to simulate the porous electrodes [39], [40].

Today, when real time computations are required (e.g. in the battery management systems, BMS), the simple approach with the equivalent electrical circuit is usually preferred [41], [42]. In fact, in EVs is important to know, the battery state of charge, power fade, capacity fade, and instantaneous available power, that are used by the battery management systems (BMS) to estimate the present operating condition of the battery packs. This is achieved by adding the control theory to an equivalent electrical circuit. The equivalent electrical circuit is composed of several lumped circuital elements (e.g. voltage generators, resistors, capacitors). The values of this elements are estimated with experiments and electrical tests [43], [44]. However, these components are usually functions of the state-of-charge (SOC), state of health (SOH) and temperature[45]–[48]. It should be mentioned that many researches are implementing simplified electrochemical models (e.g. single particle or linearizing the charge transfer relationship, cf. § 1.4) with a control systems in the BMS [49]–[52]. The transmission line model (TLM), uses circuital elements disposed in the configuration illustrated in Figure 3 [39], [53]–[57]. In this schematics, the resistances are attributed to electrode and electrolyte conductivity, while the lithium diffusion in the electrodes and the charge transfer kinetics are represented by non-constant and frequency dependent impedances [58]. Like in phenomenological models, these elements are influenced by the battery state of charge, the temperature and the state of degradation.

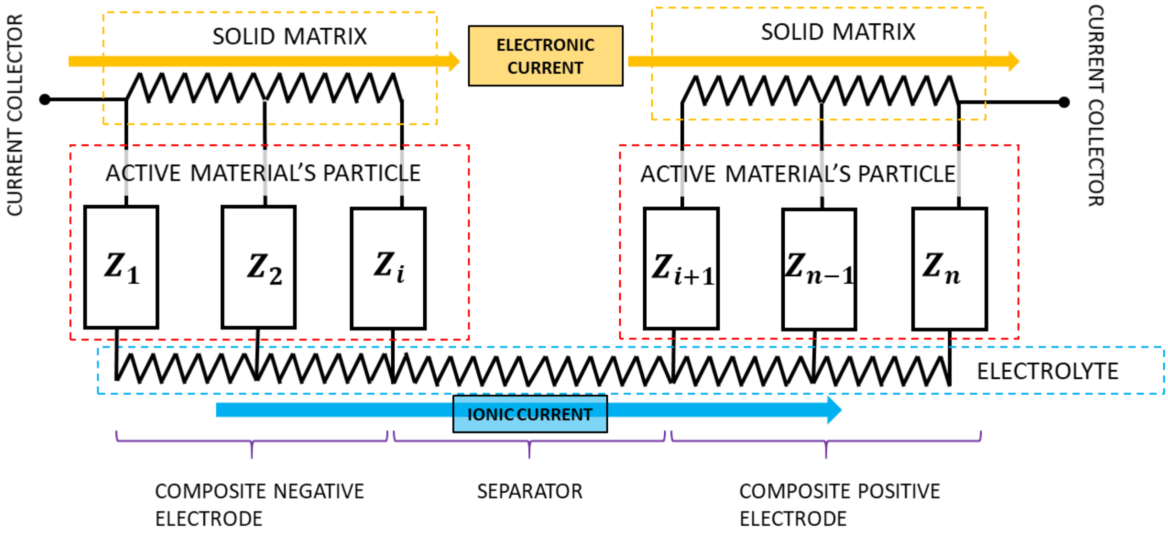

Figure 3 – The transmission line model (TLM) is a representation of the porous electrode where horizontal resistors represent the ohmic resistance in the solid phase and liquid phase while the impedances $Z_1, Z_2, Z_i, \dots, Z_{i+1}, Z_{n-1}, Z_n$ represent the kinetic resistance and the diffusion in the solid phase [59]. The arrows indicate where the electrons and ions circulate.

While the phenomenological based models are used to characterize existing cells, the electrochemical models could be used to design new cells [15], [60], [61]. In the electrochemical models, the mass transport and reaction kinetic are described in a system of partial differential equations. The objective is to predict the internal variables such as the lithium concentrations and the electrical potentials. At least one spatial dimension is required, such as the cell cross section, as indicated in Figure 5. The physical and mathematical background was established by J. Newman and its research group at Berkeley University in the '90 [62], [63]. The mathematical system of equations is available in several books such as: *Advances in Lithium-Ion Batteries, 2002* [16]. The original formulation is based on a pseudo two-dimensional geometry, where one dimension is used for the lithium diffusion inside the active material and the other for the transport of charge species in the cell cross section. In the last decades, many variants of that model have been produced, extending the equations system to 3D (three dimensional) geometries to simulation the thermal fluxes, as an example [64].

More complex and simpler models than the Newman's P2D are the so-called multi-scales and the single particle, respectively. The multi-scales model introduce several spatial and time dimensions where different physical phenomena acts [32], [65], [66]. On the other side, the single particle represents the porous electrode with a bulky spherical particle [67].

While research group of J. Newman created a free software in Fortran called Dualfoil, many commercial tools are now proposed. Among them we can mention the *Batteries & Fuel cells package for* Comsol Multiphysics®, *Battery Design Studio®* developed by CD-Adapco and Fire® from AVL [9]. The large number of parameters that is required in the original model is maintained and even increased. A critical review on the models is proposed in § 2.2.

In summary, in the last years, most of the effort from scientist and engineers, for the electrochemical models was to: (i) increase the complexity to describe more phenomena, (ii) simplify the physics to reduce the calculation time for real time applications. Consequently, we decided to work to simplify the Newman's model, whitout any changes in its electrochemical foundamentals.

1.4. Review on electrochemical models

In recent years, many works dealt with variants and improvements of the P2D original model from J. Newman and his co-workers [15], [61], [68]–[77]. The initial set of equations is extended by including thermal effects by Bernardi et al. 1985 [78], [79], the ageing by Darling et al. 1998 [80], [81] or the mechanical deformations/swelling by Christensen et al. 2006 [82], [83].

A synthetic review of the recent advances on electrochemical models representing the state of the art is reported:

- *Barai 2015* [84]: effect of the particles sizes on the mechanical degradation of the active material in the negative electrode;
- *Miranda 2015* [85]: effects of thickness, porosity and tortuosity of the separator membrane to battery performances;

- *Suthar 2015* [86]: mechanical stress induced by the lithium intercalation considers the capacity fade for different values of porosity, SEI growth, lithium plating;
- *Zhao 2015* [87]: P2D electrochemical model is coupled with a double layer capacitance and a 3D thermal model;
- *Ecker 2015* [88] : simulations are based on the measurement of the parameters in prismatic cells made by Kokam® ;
- *Cobb 2014* [89]: effect of porosity and tortuosity;
- *Chandrasekaran 2014* [90], [91]: performance of a graphite-NMC cell and lithium plating induced by fast galvanostatic charge;
- *Kim 2014* [92]: The performance of prismatic GS-Yuasa LEV50 50-Ah NMC with a 3D thermal model;
- *Zhang 2014* [93]: degradation of a graphite/LCO during the cycling at high temperature;
- *Legrand 2014* [94]: How to maximize the charging rate and avoiding the lithium plating;
- *Legrand 2014* [95]: proposed electrochemical model includes the double layer capacitance;
- *Sikha et al. 2014* [96]: original model uses a 2D geometry including the strain and stress effects to study a nanowire electrode;
- *Cobb 2014* [97]: evaluation of performances for a 3D printed electrode;
- *Mao 2014* [98]: simulations of short circuits in a MCMB/ LCO cell;
- *Ferrese 2014* [99], [100]: The PDE equations system for Li-Metal/LCO cells is solved with COMSOL to investigate the concentration of lithium along the negative electrode/separator interface during the cell cycling.
- *Northrop 2014* [101]: computational time efficiency during the simulations;
- *Fu 2013* [102]: mechanical stresses and heat fluxes for pouch C/LMO cells are studied during cycling;
- *Guo 2013* [103], [104]: The electrochemical model and the thermal model are solved in a decoupled equation system to study a battery module;
- *Ji 2013A* [105]: A model containing a double layer capacitance is used to investigate different heating strategies for sub-zero temperatures to predict Lithium-plating;

- *Ji 2013B* [106]: A thermal-electrochemical model implemented in a commercial software is used to validate the discharge rates of 18650 type cells for temperatures ranging from −20°C to 45°C;
- *Christensen 2013* [107]: performances of 18650 cells cooled by natural and forced convection are studied;
- *Lin 2013*[108]: A degradation model including SEI growth, manganese dissolution and electrolyte decomposition for a C/LMO cell is developed;
- *Awarke 2013* [81]: A P3D-thermal model including the SEI growth for a 40 Ah Li-ion during cycling of pouch cells;
- *Reimers 2013* [109]: electrochemical model PDE equations system is proposed in a decoupled form;
- *Zavalis 2012* [110]: The short-circuits are investigated in a prismatic cell having C/NCA electrodes;
- *Less 2012* [111]: The study is focused on the correlation between the geometrical scales of the structure, the material anisotropic properties, and the geometrical morphology of the electrodes compared with the macroscopic battery performances;
- *Ferrese 2012* [112]: The growth of dendrites in a 2D geometry of Li-Metal/LCO;
- *Chandrasekaran 2011*[113]: The performances of cell having Li-Metal and a blend of graphite and silicon as negative and positive electrode, respectively;
- *Jannesari 2011* [114]: The effect of SEI thickness variation across electrodes depth;
- *Martínez-Rosas 2011* [72]: An equation system with dimensionless spatial coordinates and algebraic approximations is developed;
- *Christensen 2010* [115] : diffusion equation induced by mechanical stress is introduced in Dualfoil®;
- *Stephenson 2007* [116]: The study is focused on the transfer of electrons between particles having different: sizes, materials and contact resistances of carbon additive;
- *Stewart 2008* [117]: The different results associated to the salt activity between the concentrated solution and dilute solutions are compared;
- *Nyman 2010* [73]: A The current load profile “EUCAR” is simulated for NCA cells;

The new electrochemical models are likely to consider: thermal balance, side reactions and solid mechanics. In additions, as the computational power increases, the dimensions of the geometry increase from 1D to 3D or considering a real electrode scanned with the tomography. Consequently, the number of parameters required are increasing but many of them are still not accurately measured. In fact, most these studies and models uses the fitting over many parameters. However, as the number parameters increases if they are poorly measured, they can be compensated with additional terms obtained from the fitting. In conclusion, it is not guaranteed that the fitted parameters are physically consistent. This reflect the conclusions previously discussed by Hemery 2013 in his Ph.D. manuscript [118]. Thus, as the mathematical complexity increases the battery voltage is simulated more precisely but is not assured that the other variables are correct such as the gradients of concentrations [119]. The aim of this work is to simplify as much as possible the Newman's model without losing its physical nature in order to understand meaning of each parameter and their role in the overall system.

1.5. Tests and simulations

In the literature, the majority of real EVs driving cycles are simulated with equivalent electrical circuits or simplified physical models (i.e. ODE instead of PDE) [49], [120]. In fact, a real driving profile contains charges (during the regenerative brake) and pulse-rest periods (acceleration). Thus, the thermal fluxes generated can be consistent and the values of the parameters used in the Newman's model are not constant. For this reason, more than 25 parameters must be measured for each cell. Another difficulty is to deal with a non-accurate estimation of the state of charge (SOC). In fact, the most common estimator is based on the coulomb counting method (affected by measurement errors due to current sensor and integrations errors) that are amplified when it is applied to dynamic current profiles.

However, the diffusion of Newman's based models are rapidly rising in recent years, but they still represent a minority [73], [121]–[123].

In addition, only few studies are focused on galvanostatic charges or pulse-rest periods [80], [124]. In fact, the constant voltage charge phase is difficult to simulate because it requires different boundary conditions [125], or as an alternative, a complex control feedback able to deal with current while it maintains the voltage constant could be used but it complexifies the study[63].

In conclusion, most studies are based on galvanostatic discharges, as example reported in Figure 4 (A), where different discharge rates are simulated at 273 K and compared with experiments for a graphite/NCA cell. The figure illustrates that the higher is the C-rate, the higher the errors are over the voltage while at 0.1C the rated capacity deviates from the experiment. In fact, at high current rate and low temperature the kinetic limitations are very important and the simulations are more complex (Doyle et al. 1996 [126]).

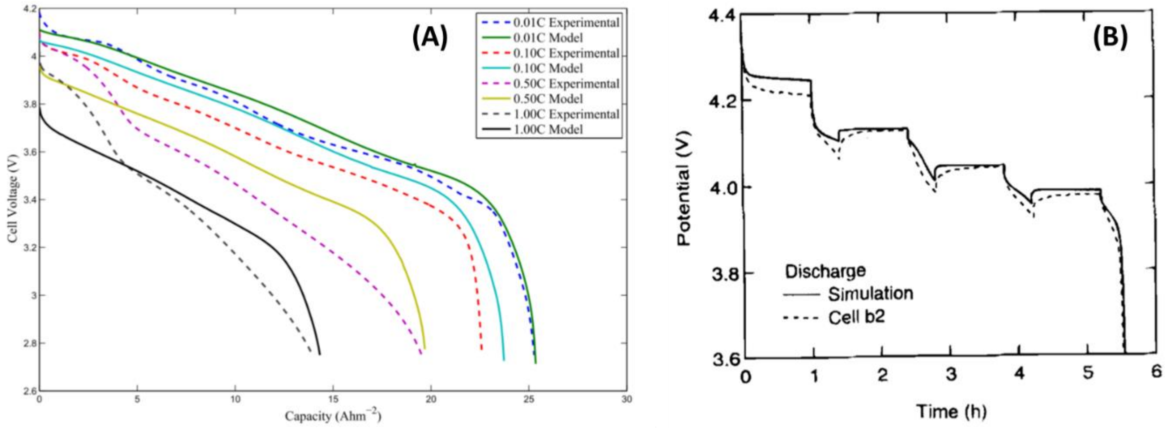

Figure 4 – (A) The discharge voltages as function of the specific capacity are measured (dashed curves) and simulated (solid curves) 273 K for several C-rates [127]: 0.01C, 0.1C, 0.5C and 1 C. (B) The voltage during the GITT as a function of the test time (in hours) is are measured (dashed line) and simulated (solid line) [80].

The pulse rest sequences are studied by Darling et al. 1998 using the Newman's model [80], for a Li-metal/LMO cell. The simulations and experiments reported in Figure 4 (B) are performed with four C/2-rate pulses followed by 1 hour of rest period. The deviations of the simulated voltages from the experiments, evidences the complexity in the battery modeling. In fact, large voltage errors after the relaxation are found even in recent papers [88]. These voltage mismatches after the relaxation could be attributed to a non-accurate estimation of time constants of the model.

In the next chapter, the literature is critically reviewed to identify some non-physical features or some methodologies that are in contrast with the Newman's P2D model.

2 Electrochemical equations system

In this chapter, the Newman's model is introduced, and the related literature is critically reviewed. The main features contrasting with the original model and rickety assumptions on the involved electrochemical phenomena are discussed. Then, a dimensionless PDE model is proposed aiming to reduce as much as possible the number of parameters. Finally, the dimensional and the dimensionless models are compared.

The basis for modeling the porous electrodes has been reviewed by Newman and Tiedemann in 1975 [128]. The porous electrodes are represented as a superposition of two macro-homogenous and continuous phases that coexist in every point of the cell. These phases are either solid or liquid. Furthermore, the solid phase is represented with spheres, attributed to particles of the active materials.

In Figure 5 the schematics of the li-ion cell in the Newman's vision of a cell is reported. It is constituted of: the negative electrode, the separator and the positive electrode, respectively with their thickness in the x-axis direction, and the particles of the active materials having an average radius R_+. Finally, the currents in the solid phase, liquid phase and at the interfaces are indicated with i_s, i_l, j_+ and j_-, respectively. The current in the solid phase is carried out by electrons while the current in the liquid phase is carried out by ions. In all the points of the electrodes, the discharge current is the sum between the electronic and the ionic currents. Consequently, the electronic current is predominant near the current collector, while it is absent in the separator.

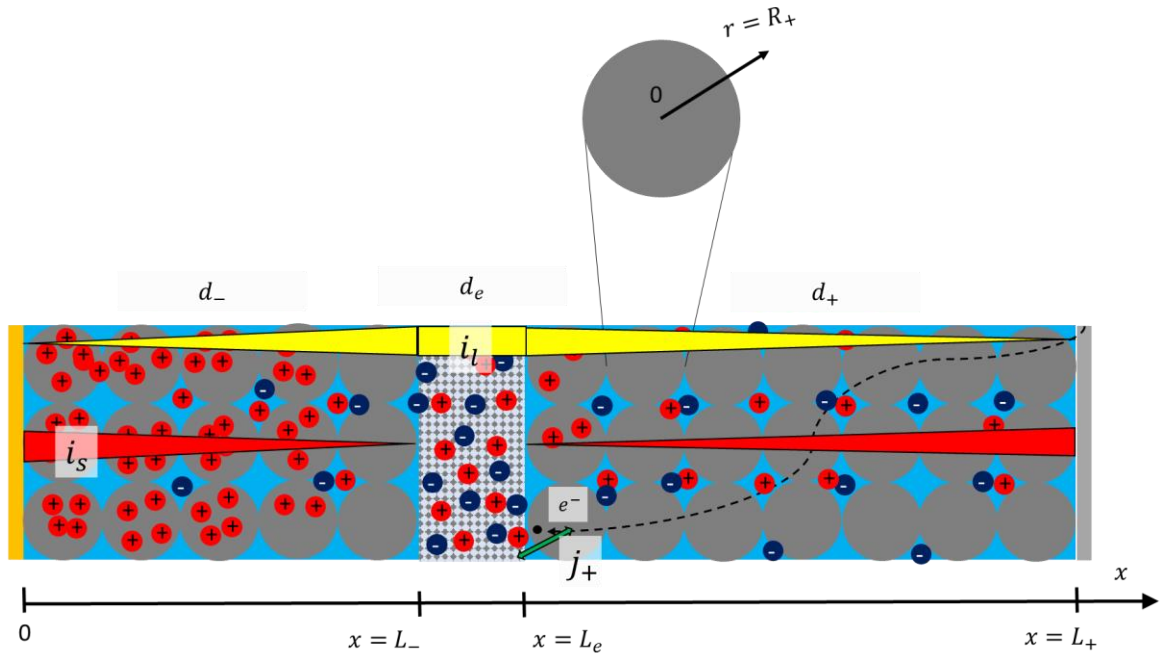

Figure 5 – A lithium-ion cell is illustrated according the Newman's model. The x-axis (cartesian coordinate) indicates the distance of any point from the negative current collector $(x = 0)$. Instead, the r-axis (spherical coordinate) indicates the distance in active material's particles from the core of the particle $(r = 0)$ to the surface $(r = R_+)$. The interface between the solid phase and electrolyte phase is at $r = R_+$. Similarly, the sign + can be replaced with – for the negative electrode.

As stated before, the model assumes a macro-homogeneous phase where the physical and chemical properties are averaged on a reference volume. The reference volume, is small compared with the dimension of the electrodes but large compared with the dimension of the pores[129]. This representation is convenient because it disregards the exact position of the particles or the real shape of either particles and pores. Furthermore, the complex structure of a porous electrode is reduced to a two-dimensional representation: one representing the "macro" domain (i.e. the x-axis direction) and the other represents "micro" domain associated to the particles radius. The macro domain is extended along the cell thickness while the micro domain is defined along the radius of the particles. Consequently, because two geometrically 1-dimensional axes are coupled, this model is called pseudo-2D.

The movement of ions in the electrolyte is driven by migration and the diffusion (since the convection is neglected because the medium is not moving), that are described with the mass transport law (cf. Eq. 14). The phenomenon of migration is associated to charged species moving under an electric field. Instead, the diffusion is related to any species driven by a concentration gradient. The solid phase and the liquid phase are coupled *via* mass balances and the kinetic reaction rate, which depends on the potential difference between the phases (cf. Eq. 13).

The reaction in lithium-ions cells is an insertion, in the site of the host matrix, of lithium ions from the electrolyte that react with the electrons in the porous electrode (cf. Eq. 9). The reactions occurring at the solid-electrolyte interface, as shown in Figure 6, are not constant across the electrode because they are function of the local potential and the local concentration in both phases. The relationship between the overpotential and the current density is expressed by the Butler-Volmer law (cf. Eq. 11). In insertion electrodes, the potential varies with the concentration of the inserted lithium and in the electrolyte (cf. Eq. 43).

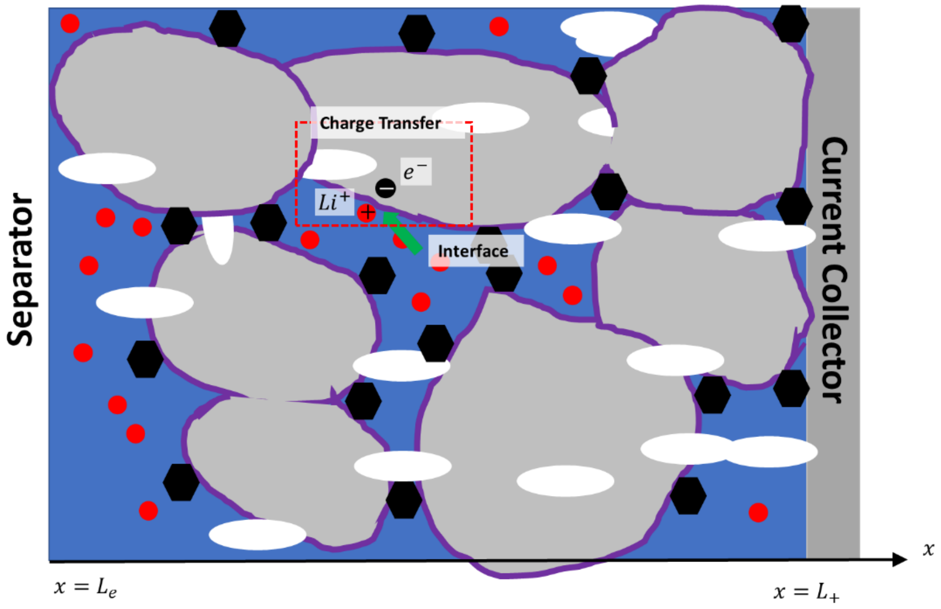

Figure 6 – The picture shows a section of the positive electrode where are reported: in red the lithium ions, in the black hexagons are conductivity enhancer in carbon, in the binder, in grey the active materials' particle and the small black particle the electron. In blue is depicted the electrolyte and in violet the interface solid phase – liquid phase.

The phases are assumed electrically neutral, this means that the volume of the double layer is small relative to the pore volume.

The geometry influences the mathematical behavior of the physical system: the diffusion is expressed in spherical coordinates while the mass transport in the electrolyte uses planar coordinates. This representation is valid since the thickness is small compared to the cell cross section area and the particles are smaller than the electrodes thickness (cf. Table 39) .

The model deals with these complex interactions and describes the overpotential vs. current density relationships generated by the mass transport (i.e. a gradient of concentration of charges species coupled to an electric field in two phases) and the charges transfers (i.e. occurring at the interface between the solid and the liquid phases).

Herein, we consider the basic Newman's model for Li-ion battery rocking-chair with porous electrodes and the electrolyte is described as a dilute solution. In literature, the authors are used to present their system of equations with the concentrate solution, but in practices because some parameters are not identified such as, as an example, the thermodynamic factor (cf. Eq. 3) [117]:

$$1 + \frac{d \ln \gamma_{\pm}}{d \ln m} \qquad \text{Eq. 3}$$

where $\gamma_{\pm}$ is the activity coefficient and m the molality of the concentration.

Thus, in several articles, the electrolyte is assumed ideal (i.e. $\gamma = 1$, the activity is equal the concentration) [117], [130], [131]. In fact, the values of the mutual diffusivities of the species involved (cations, anions, and solvent) $D_{0+}, D_{0-}, D_{\pm}$ are generally not determined.

In summary, the hypothesis assumed in our model are:

- no swelling in the electrode during the intercalation;
- no convection during the electrolyte mass transport;
- electrolyte diffusivity and the transport number are constant [132];
- electrolyte is diluted, i.e. $\gamma = 1$ [133];
- electrolyte is binary, i.e. only Lithium ions or cations;
- relation between mobility and diffusion is given by the Nernst-Einstein relation, i.e. $\frac{\mathrm{u_i}}{\mathrm{D_i}} = \frac{\mathrm{F}}{\mathrm{RT}}$;
- effective solid phase diffusivity is constant [134];
- contribution of the double layer is neglected. Double layer effects occur on millisecond time scale and can be neglected for current pulses with frequency lower than 100 Hz [59], [135] ;

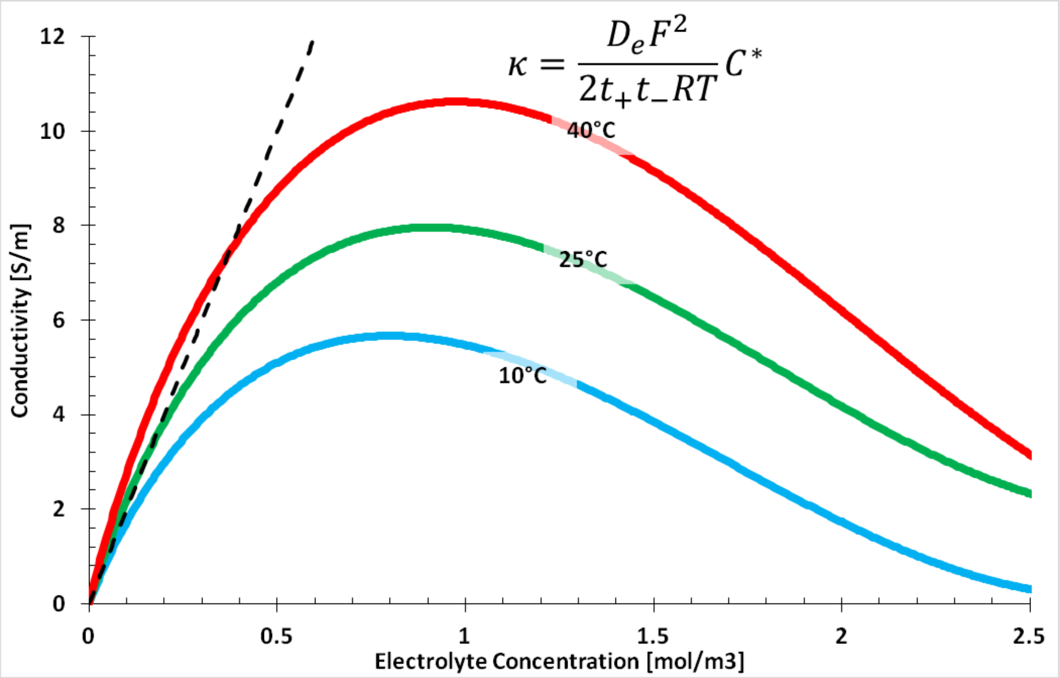

Figure 7 – The conductivity as a function of the concentration in the model reported by Lundgren et al. 2015 [136] for 10°C, 25°C and 40°C. The dashed straight line, represent the linear relationship used in the proposed model.

Moreover, the diffusivity, transport number and conductivity are assumed functions of the concentration, in many papers. However, how these parameters affect the potential in either solid and liquid phase is not discussed [91], [137]. Furthermore, in some cases, the experimentally fitted law used in the model for the electrolyte conductivity are not defined when concentration drops to zero [88], [138]. In fact, if the concentration is zero the conductivity must fall to zero. In Figure 7 is reported the conductivity measured by Lundgren et al. 2015 [136] for different temperatures of LiPF6 in EC:DEC. In this figure, the dashed lines represent the linear approximation used in the present model for the conductivity as $\kappa = \frac{D_e F^2}{2t_+ t_- RT} C^* \; [S/m]$ (cf. Eq. 21).

It should be noted that when the concentration is close to zero the conductivity is not influenced by temperature. This fact can be used to generalize the conclusions of the simulation described in §6.1.2, when the electrolyte mass transport is discussed.

Some considerations are about the limitations induced by ionic conductivity that justify the use of this approximate relation (cf. Eq. 21) are discussed in the following. Because of the mass conservation, when in the electrolyte the concentration drops in one point, in another point it rises. The conductivity in both cases decreases as observed in Figure 7, but as reported in Eq. 7,when the concentration drops to zero, the local electrolyte potential seriously increases, inducing a major drop in the cell voltage. Consequently, with these hypothesis, we focus on the limitations associated to very low concentration because the ionic conductivity is a major limiting factor when the local concentration drops to zero. Nevertheless, we changed the values of the conductivity to see how it affects the resulting polarization.

2.1. Newman's PDE equations system (diluted solutions)

In this section, the classical Newman's PDE model for a diluted electrolyte is introduced.

The material balance of the lithium ions is for the positive electrode

$$\varepsilon_{+,l}\frac{\partial C}{\partial t} = D_{eff,+}\frac{\partial^2 C}{\partial x^2} + (1 - t_+)a_+ j_+ \qquad \text{Eq. 4}$$

where $C\ [mol/m^3\ ]$ is the concentration in the electrolyte, $\varepsilon_{+,l}[-]$ the matrix porosity, $D_{eff,+}[m^2/s]$ the effective diffusivity of the ions in the porous matrix, $t_+[-]$ the transport number of cations of the electrolyte, $a_+[m^2/m^3\ ]$ the specific active area and $j_+[A/m^2\ ]$ is the charge transfer current. From here the subscript $+$ is referred to parameters for the positive electrode but the same results can be obtained with the – subscript that is associated to the negative electrode. The active surface area per unit volume, where reaction occurs for the porous electrode, is related to the active material sphere's radius:

$$a_+ = \frac{3\varepsilon_{+,s}}{R_+} \qquad \text{Eq. 5}$$

The charge transfer current is related to the divergence of the current density in the solution phase:

$$a_+ j_+ = \frac{1}{F}\frac{\partial i_l}{\partial x} \qquad \text{Eq. 6}$$

The potential in the solution phase of the porous electrode is given by

$$\frac{\partial \varphi_l}{\partial x} = -\frac{i_l}{\kappa} + \frac{2RT}{F}(1 - t_+)\frac{\partial \ln C}{\partial x} \qquad \text{Eq. 7}$$

where $\varphi_l[V]$ is the liquid phase potential, $\kappa[\mathrm{S/m}]$ the electrolyte conductivity, $i_l[A/m^2]$ the ionic current, $T[K]$ the temperature, $R[\mathrm{J/(mol\ K)}]$ and $F[\mathrm{C/mol}]$ are respectively the gas constant and the Faraday's constant.

The potential in the electrode phase follows Ohm's law

$$\frac{\partial \varphi_s}{\partial x} = -\frac{i_s}{\sigma_+} \qquad \text{Eq. 8}$$

where $\sigma_+[S/m]$ is the effective conductivity for the solid matrix that is results of the mixture of the poor conductive active material and the highly conductive black carbon.

The superficial current density in the two phases is conserved through a charge balance, which leads to

$$I = i_s + i_l \qquad \text{Eq. 9}$$

with $i_s[A/m^2]$ the electronic current, $i_l[A/m^2]$ the ionic current and $I\ [A/m^2\ ]$ the cell current density (cf. Figure 5).

The diffusion of the lithium in the host matrix is

$$\frac{\partial C_s}{\partial t} = -D_{S,+}\left(\frac{\partial^2 C_S}{\partial r^2} + \frac{2}{r}\frac{\partial C_S}{\partial r}\right) \qquad \text{Eq. 10}$$

where $C_s[mol/m^3\ ]$ is the concentration of lithium in the active material's particles, r the radius of the particles and $D_{S,+}[m^2/S]$ is the effective solid phase diffusivity in the positive electrode.

The charge-transfer reaction has the form $Li\Theta_S \rightleftharpoons Li^+ + \Theta_S + e^-$ (cf. § 2.3.1) and the kinetics of this process is described by the Butler-Volmer relation:

$$j_+ = j_0\left(e^{\alpha\frac{F}{RT}\eta} - e^{-(1-\alpha)\frac{F}{RT}\eta}\right) \qquad \text{Eq. 11}$$

where the exchange-current density is:

$$j_0 = Fk_+^*\left(C_{S+,max} - C_s\right)^{\alpha} C_S^{(1-\alpha)} C^{\alpha} \qquad \text{Eq. 12}$$

where $k_+^*[m/s]$ is the reaction rate constant, $\eta[V]$ the overpotential, the $C_{S,max}[mol/m^3\ ]$ the maximum concentration in the solid phase, α the kinetic transfer coefficient, $C[mol/m^3\ ]$ and $C_S[mol/m^3\ ]$ the concentration of lithium in the liquid and solid phase, respectively. The Eq. 11 looks like a classical Butler-Volmer equation, however a special attention is required for $j_0[A/m^2\ ]$ because it is not a constant. In fact, it depends on the local concentrations in both solid and liquid phases at the interface on the particle's surface.

The local value of the surface overpotential is defined as:

$$\eta = \varphi_s - \varphi_l - E_{ocv} \qquad \text{Eq. 13}$$

and consequently, the overpotential is governed by:

$$\frac{\partial \eta}{\partial x} = -\frac{I}{\sigma} + i_l\left(\frac{1}{\sigma} + \frac{1}{\kappa}\right) - \frac{2RT}{F}(1 - t_+)\frac{\partial \ln C}{\partial x} \qquad \text{Eq. 14}$$

The apparently simple expression Eq. 14 hides few complexities since the ionic conductivity κ is not a constant like the electronic conductivity σ.

2.2. Critical review of the literature

The system of equations reported in literature, as observed by Ramos 2015, are sometimes reported with mistakes or altered by excessive mathematical manipulations [139]. Indeed, the system of equations could be both physically and mathematically incorrect. Some inconsistencies about the systems of equations and boundary founds in the literature are reported:

- Ramos 2015 observes that systematically the boundary conditions reported have wrong signs [139]. This suggest that the equations are copied from other articles;
- A linearized Butler–Volmer equation (for low overpotentials) or the Tafel approximation (valid for high overpotentials) are assumptions not verified [81], [92] ;
- For the mass transport equation, the second term on the right-hand side of Eq. 7 and Eq. 14 is often wrongly written in the literature as $(1-t_+)$ or $(1-2t_+)$ instead of the correct $2(1-t_+)$ [69], [133], [139]–[141] ;
- In some cases, the reference value of potential at some point x is not set and then the PDE equation system does not have a unique solution [139];
- The use of the external current as a boundary instead of the current density is mathematically incorrect, because the system is not well-posed [139];
- The Butler-Volmer has a wrong expression of the overpotential in [72];
- The exchange current density i_0 is used as a fitting parameter, while it depends of the local concentration [13];

A summary about the parameters used in the models reported in the literature:

- The kinetic constant rate is not measured k_0, while Ecker et al. 2015 [142] attempt to measure the exchange-current density i_0 with a complex method;
- The kinetic constant rate of the Butler-Volmer equation is usually reported with wrong units instead of $[A.m^{-2+6\alpha_a+3\alpha_c}.mol^{-2\alpha_a-\alpha_c}]$ [143];
- The conductivity is either non-zero [85] or not defined [142] when the concentration drops to zero;
- The electrolyte conductivity is kept constant [144] (however the author explains this uncommon assumption);

- The active surface area is used as a fitting parameter while the particles radius is constant [73], [145];
- The expression of the concentrated binary electrolyte is derived for a constant transference number at first but then it is replaced with a transference number that is a function of the concentration [146];
- The isotherm (or OCV) of the electrodes is not a function of the lithium on the particles surface but depends on the average concentration in the electrode [73], [146];
- The electronic conductivity is not constant but depends on the concentration (but not from the measurements) [147];
- The concentrated solution theory is incoherently used with a an activity coefficient equal to zero [104];
- The rated capacity at C/2-rate is higher than C/8-rate, indicating that the simulations are performed on poor measurements [148];
- The parameters used for a liquid electrolyte are from the measurements from a polymer electrolyte [141], [149];
- The anodic (α_a) and cathodic (α_c) charge transfer coefficient of the Butler-Volmer kinetic law, cannot be measured with the actual knowledge. Their sum must be equal to unity and for symmetrical reasons, they are usually assumed to 0.5. However, some exceptions are reported in Ecker et al. 2015 (P2) [88] and Chandrasekaran et al. 2010 [150], where different values are chosen;
- The exchange current density is written without the kinetic rate constant [151];
- The kinetical rate constant k_0 is not constant but it is a function of the applied current I by Safari [12];

The discussion is now focused on the effective properties of the electrolyte in a porous electrode. In fact, the tortuosity and the porosity affect the diffusion path of the electrodes: higher the tortuosity and slower is the diffusion of lithium ions in the electrolyte, for the same porosity. The concept of porosity is explained with the examples of the two electrodes with different porosity reported in Figure 8. The figure illustrates on the left side an electrode with big particles, while at the right side, the spaces between the large particles are filled with smaller ones. For the same volume of reference, the amount of electrolyte is higher in the electrode with high porosity.

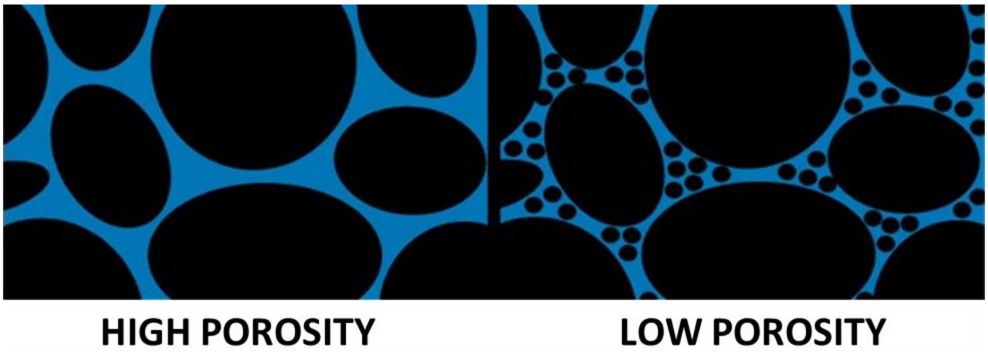

Figure 8 – Two electrodes with different porosities are illustrated: on the left side, the porosity is higher than at the right side.

The other parameter affecting the mass transport properties in the electrolyte is the tortuosity, as illustrated in Figure 9. One of the possible definition for the tortuosity is the ratio between the distance L_0 (indicated with the green arrows) and the effective path of the ions L (indicated with the dashed line) done during their diffusion:

$$\tau = \frac{L}{L_0} \qquad \text{Eq. 15}$$

This picture illustrates different situations having different shape and orientation of the particles of the active material in electrodes with the same porosity:

- In Figure 9 (A) thin and longitudinally oriented: the path of the ions is not perturbated and the tortuosity is one;
- In Figure 9 (B) spherical and homogeneous and homogeneously distributed: this situation represents the approximation given by the Bruggeman relation (cf. Eq. 16);
- In Figure 9 (C) spherical but non-homogeneous and sparse: the sphericity of the particles ensures a low tortuosity;
- In Figure 9 (D) thin and orthogonally oriented: the path of the ions is the larger and the consequent tortuosity is high;

The Bruggeman relation (cf. Eq. 16) connect the tortuosity with the porosity:

$$\tau = \varepsilon^{\beta} \qquad \text{Eq. 16}$$

where β is the Bruggeman exponent and ε the porosity. For a matrix composed of monodisperse spherical particles of uniform size (Figure 9 (B)), it has been empirically measured that $\beta \approx 0.5$. The case reported in Figure 9 (C-D) are the most realistic and they could not respect the Bruggeman relation.

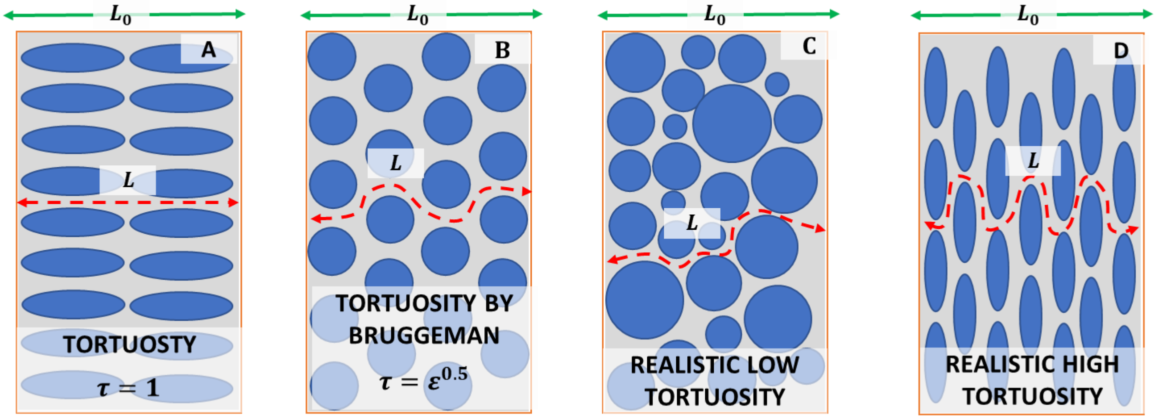

Figure 9 – In the four different electrodes reported, they have the same thickness L_0 (indicated with the green arrows), the same volume and porosity but different shapes of the active material (depicted in blue). The red dashed lines indicated the path of ions diffusing from one side to the other.

This value is usually reported in literature, but sometimes other values could be found for fitting reasons [116], [152], [153]. In one case, as an example, two different Bruggeman exponents are used: one for effective electrolyte conductivity and the other for the effective electrolyte diffusivity [154]. However, the assumptions of $\beta \neq 0.5$ could be in contrast the assumptions of spherical particles [155], while the distribution of particles with different sizes size may be in contrast with the hypothesis of a macro-homogeneous electrode.

The effective electrolyte diffusivity and effective electrolyte conductivity are expressed, respectively as [156], [157]:

$$\begin{cases} D_{eff} = \dfrac{\varepsilon D}{\tau} \\ \kappa_{eff} = \dfrac{\varepsilon \kappa}{\tau} \end{cases} \quad \text{Eq. 17}$$

where ε is the porosity (the amount of void space in the electrode) and τ the tortuosity. The effective electronic conductivity is usually measured on a fraction of the porous matrix [49], and is an averaged value between the active material conductivity and the conductivity of the black carbon (i.e. additive for increasing the conductivity). This assumption may neglect some privileged conductivity path in the electrode, such as percolating issues. However, Guo et al. 2013 [103] and Amiribavandpour et al. 2015 [149] have used the Bruggeman relation that is an unusual way to deal with the effective electron transport properties because it is usually assumed that electrons are not affected by the path in the solid matrix.

The temperature dependence of the parameters is usually performed via an Arrhenius like function where the required activation energies for these descriptions are roughly measured [142] and in others are adjusted with the experiences [158].

The film or SEI resistance, and the inter-particle contact resistance are introduced in many papers [116] in order to improve the fit with the experiences, but they are not measured.

In the next section, the proposed electrochemical equations system is illustrated and compared with the Newman's model.

2.3. The system of equations proposed in this study

In this section, the system of PDEs with its boundary conditions and the initial values of the model are derived. The general framework of this model is based on classical thermodynamics of irreversible systems, describing the mass transports (migration and diffusion), and the kinetics describing the charge transfer.

The current in discharge is $I > 0$ for convention, and the subscript + represents a property associated to positive species and the subscript – is associated to a negative species. The variables in this model are: the concentration and the potential in both solid phase and electrolyte, C, C_S, W, V.

The bulk electrolyte properties are defined as:

- Transport numbers are

$$t_+ = \frac{u_+}{u_+ + u_-} \qquad \text{Eq. 18}$$

and

$$t_- + t_- = 1 \qquad \text{Eq. 19}$$

where u_+ and u_- are the ionic mobility of the cations and ions, respectively.

- Average liquid phase diffusion coefficient:

$$D_e = \frac{2D_+D_-}{D_+ + D_-} = 2t_-D_+ = 2t_+D_- \qquad \text{Eq. 20}$$

- Linear approximation of the electrolyte conductivity is in a specific point x at the instant of time t :

$$\kappa = \frac{\mathrm{D_e F^2}\, C}{\mathrm{2t_+t_-RT}} \qquad \text{Eq. 21}$$

Consequently, at the equilibrium the ionic conductivity, from Eq. 21 is in each point

$$\kappa^* = \frac{\mathrm{D_e F^2\, C^*}}{\mathrm{2t_+t_-RT}} \qquad \text{Eq. 22}$$

First of all, for the liquid phase in the separator, the volume mass balance equations (continuity equations) are written in plane 1D geometry as:

$$\begin{cases} \varepsilon_l \dfrac{\partial C_+}{\partial t} = -\dfrac{\partial N_+}{\partial x} \\ \varepsilon_l \dfrac{\partial C_-}{\partial t} = -\dfrac{\partial N_-}{\partial x} \end{cases} \qquad \text{Eq. 23}$$

where ε_l is the porosity of the separator, that is the fraction of the volume where the mass transport act.

The molar flux of ions by considering only diffusion and migration is written as:

$$\begin{cases} N_+ = -D_+ \dfrac{\partial C_+}{\partial x} - u_+ C_+ \dfrac{\partial V}{\partial x} \\ N_- = -D_- \dfrac{\partial C_-}{\partial x} + u_- C_- \dfrac{\partial V}{\partial x} \end{cases} \qquad \text{Eq. 24}$$

where V indicates the liquid phase potential. According to Nernst-Einstein relation:

$$\begin{cases} \varepsilon_l \dfrac{\partial C_+}{\partial t} = D_+ \dfrac{\partial^2 C_+}{\partial x^2} + D_+ \dfrac{F}{RT} \dfrac{\partial}{\partial x}\left(C_+ \dfrac{\partial V}{\partial x}\right) \\ \varepsilon_l \dfrac{\partial C_-}{\partial t} = D_- \dfrac{\partial^2 C_-}{\partial x^2} - D_- \dfrac{F}{RT} \dfrac{\partial}{\partial x}\left(C_- \dfrac{\partial V}{\partial x}\right) \end{cases} \qquad \text{Eq. 25}$$

The consequence of the electroneutrality is that the concentration of cations and anions are the same. Then Eq. 25 became

$$\begin{cases} \varepsilon_l \dfrac{\partial C}{\partial t} = D_+ \dfrac{\partial^2 C}{\partial x^2} + D_+ \dfrac{F}{RT} \dfrac{\partial}{\partial x}\left(C \dfrac{\partial V}{\partial x}\right) \\ \varepsilon_l \dfrac{\partial C}{\partial t} = D_- \dfrac{\partial^2 C}{\partial x^2} - D_- \dfrac{F}{RT} \dfrac{\partial}{\partial x}\left(C \dfrac{\partial V}{\partial x}\right) \end{cases} \qquad \text{Eq. 26}$$

Then the sum between the upper equation in Eq. 26 multiplied per D_- and the lower equation in Eq. 26 multiplied per D_+ gives:

$$(D_- + D_+)\varepsilon_l \frac{\partial \mathrm{C}}{\partial \mathrm{t}} = 2D_+D_- \frac{\partial^2 \mathrm{C}}{\partial \mathrm{x}^2} \qquad \text{Eq. 27}$$

Similarly, the difference between the upper equation in Eq. 26 multiplied *per* D_- and the lower equation in Eq. 26 multiplied *per* D_+ gives:

$$(D_- - D_+)\varepsilon_l \frac{\partial C}{\partial t} = 2D_+D_- \frac{F}{RT} \frac{\partial}{\partial x}\left(C \frac{\partial V}{\partial x}\right) \qquad \text{Eq. 28}$$

Consequently, two equations, considering the properties of Eq. 20, are derived:

$$\begin{cases} \varepsilon_l \dfrac{\partial \mathrm{C}}{\partial \mathrm{t}} = \mathrm{D_e} \dfrac{\partial^2 \mathrm{C}}{\partial \mathrm{x}^2} \\ (\mathrm{t}_- - \mathrm{t}_+)\varepsilon_l \dfrac{\partial \mathrm{C}}{\partial \mathrm{t}} = \mathrm{D_e} \dfrac{\mathrm{F}}{\mathrm{RT}} \dfrac{\partial}{\partial \mathrm{x}}\left(\mathrm{C} \dfrac{\partial \mathrm{V}}{\partial \mathrm{x}}\right) \end{cases} \qquad \text{Eq. 29}$$

In the porous electrodes, chemical reaction occurs (i.e. at the solid phase – liquid phase interface) so that a source term appears in the mass balance equations.

The electrochemical reaction occurring at the interface, defined by Faraday’s law, depends on local current density:

$$\begin{cases} \varepsilon_{+,l}\dfrac{\partial C_+}{\partial t} = -\dfrac{\partial N_+}{\partial x} + \dfrac{1}{F}a_+ j_+ \\ \varepsilon_{+,l}\dfrac{\partial C_-}{\partial t} = -\dfrac{\partial N_-}{\partial x} \end{cases}$$ Eq. 30

The Faraday’s equation says that where the reactions between the electrode and the solutions are, the flux of the species is related to the current of the reaction, the stoichiometry of the species involved and the related of the number of electrons in the reaction.

The current conservation is expressed by the movement of charged species:

$$I = I_l + I_S$$ Eq. 31

where I_l is the ionic current. The electronic current and I_s is defined by Ohm’s law:

$$I_S = -\sigma_+ A \frac{\partial W}{\partial x}$$ Eq. 32

where W the solid phase potential and A is the electrode surface. The electronic transport is only due to migration. The volume is electrically neutral and total current density divergence is zero (no charge accumulation). The ionic current gradient is an expression of the local current density:

$$\frac{\partial I_l}{\partial x} = a_+ A j_+ = \sigma_+ A \frac{\partial^2 W}{\partial x^2}$$ Eq. 33

The mass transport equation and the migration are derived from Eq. 30 and Eq. 33, using the same procedure used for deriving Eq. 29:

$$\begin{cases} \varepsilon_{+,l}\dfrac{\partial C}{\partial t} = D_{e,+}\dfrac{\partial^2 C}{\partial x^2} + \dfrac{t_-}{F}\sigma_+\dfrac{\partial^2 W}{\partial x^2} \\ D_{e,+}\dfrac{F}{RT}\dfrac{\partial}{\partial x}\left(C\dfrac{\partial V}{\partial x}\right) = (t_- - t_+)D_{e,+}\dfrac{\partial^2 C}{\partial x^2} - \dfrac{2t_+t_-}{F}\sigma_+\dfrac{\partial^2 W}{\partial x^2} \end{cases}$$ Eq. 34

The concentration of lithium in the solid phase is determined by the Fick’s second law:

$$\frac{\partial C_s}{\partial t} = D_{s,+}\frac{1}{r^2}\frac{\partial}{\partial r}\left(r^2\frac{\partial C_s}{\partial r}\right)$$ Eq. 35

where $D_{s,+}$ is a constant diffusion coefficient.

The boundary conditions for the diffusion in the solid phase are:

$$\begin{cases} -D_{s,+}\left(\dfrac{\partial C_s}{\partial r}\right)_{r=0} = 0 \\ -D_{s,+}\left(\dfrac{\partial C_s}{\partial r}\right)_{r=R_+} = \dfrac{1}{F}j_+ \end{cases}$$ Eq. 36

where the first condition is derived for symmetry reasons and the second one relates to the particle flux across the solid/liquid phases interface.

The boundary conditions between current collector and the electrode are obtained by setting the ionic flux to zero:

$$\begin{cases} N_{+} = 0 = \dfrac{I_l}{FA} = \dfrac{I}{FA} + \dfrac{\sigma_{+}}{F}\left(\dfrac{\partial W}{\partial x}\right)_{x=L_{+}} \\ N_{-} = 0 \end{cases} \qquad \text{Eq. 37}$$

consequently, the boundary conditions at the positive collector are:

$$\begin{cases} \dfrac{F}{RT} C \left(\dfrac{\partial V}{\partial x}\right)_{x=L_{+}} = 0 \\ \left(\dfrac{\partial C}{\partial x}\right)_{x=L_{+}} = 0 \\ \sigma_{+}\left(\dfrac{\partial W}{\partial x}\right)_{x=L_{+}} = -\dfrac{I}{A} \end{cases} \qquad \text{Eq. 38}$$

The boundary conditions between the positive electrode and the separator are obtained by setting the flux continuity:

$$\begin{cases} N_{+}|_{x^{+}=L_e} - N_{+}|_{x^{-}=L_e} = \dfrac{I_S}{FA} = 0 = -\dfrac{\sigma_{+}}{F}\dfrac{\partial W}{\partial x} \\ N_{-}|_{x^{+}=L_e} - N_{-}|_{x^{-}=L_e} = 0 \end{cases} \qquad \text{Eq. 39}$$

Where the exponent $+$ and $-$ for the x variable represent, respectively the right side and left side of the frontier. Hence, the boundary conditions at separator side are:

$$\begin{cases} -D_{e,+}\frac{F}{RT} C \left(\dfrac{\partial V}{\partial x}\right)_{x^{+}=L_e} = -D_e \frac{F}{RT} C \left(\dfrac{\partial V}{\partial x}\right)_{x^{-}=L_e} \\ -D_{e,+}\left(\dfrac{\partial C}{\partial x}\right)_{x^{+}=L_e} = -D_e\left(\dfrac{\partial C}{\partial x}\right)_{x^{-}=L_e} \\ \left(\dfrac{\partial W}{\partial x}\right)_{x^{+}=L_e} = 0 \end{cases} \qquad \text{Eq. 40}$$

The initial conditions are:

- Homogeneous concentration in each phase;
- The phases are equipotential and

$$\begin{cases} \varphi_{+} - \chi = \ddot{U}_{+} \\ \varphi_{-} - \chi = \ddot{U}_{-} \end{cases} \qquad \text{Eq. 41}$$

where $\ddot{U}_{+}$ and $\ddot{U}_{-}$ are the isotherms of the electrodes.

The local current density can be written in the general Butler-Volmer form:

$$j_+ = Fk_+^{*\prime}\left(\theta e^{\alpha\frac{F}{RT}(W-V-\ddot{U}_+)} - \frac{C}{C^*}(1-\theta)e^{-(1-\alpha)\frac{F}{RT}(W-V-\ddot{U}_+)}\right)_{r=R} \qquad \text{Eq. 42}$$

where θ is the concentration normalized with the maximum concentration in the solid phase and $\ddot{U}_+(\theta)$ is the deviation of a real isotherms from the ideal isotherm described by the Nernst law:

$$\ddot{U}_+(\theta) = U_+(\theta) + \frac{RT}{F}\ln\frac{\theta}{1-\theta} \qquad \text{Eq. 43}$$

where $U_+(\theta)$ is the measured electrode's open circuit voltage.

This equation describes the faradaic charge transfer from the matrix to the solution. The kinetic constant dimensions are $k^{*\prime}\left[\frac{mol}{m^2 s}\right]$ or $k^*\left[\frac{m}{s}\right]$ or $k^{*\prime\prime}\left[\frac{m^{2.5}}{mol^{0.5}s}\right]$ are found in literature and can be obtained:

$$k^{*\prime} = k^* C_{S,max} = k^{*\prime\prime} C_{S,max}\left(C^*\right)^{\alpha} \qquad \text{Eq. 44}$$

2.3.1 Comparison with Newman

Most of equations used in this work are similar to Newman's but some differences are associated to the different definition of the potential. This different definition affects the expression of the electrolyte potential and the Butler-Volmer equation.

In fact, the definition of the potential is referred to an ideal electrode (constant potential) in the proposed PDE equations system, while in Newman's model the potential is referred to a lithium electrode that is a pseudo reference because the potential depends on the nearby concentration of charged species. The potential in the Newman's model can be expressed as:

$$\varphi_l = V + \frac{RT}{F}\ln\frac{C}{C^*} + const. \qquad \text{Eq. 45}$$

Potential in the electrolyte

Some mathematical manipulations are required to transform the electrolyte potential Eq. 7 into Eq. 34. Combining Eq. 7 and Eq. 45 it is obtained:

$$\frac{\partial V}{\partial x} + \frac{RT}{F}\frac{\partial \ln C}{\partial x} = -\frac{i_l}{k} + \frac{2RT}{F}(1-t_+)\frac{\partial \ln C}{\partial x} \qquad \text{Eq. 46}$$

Then introducing the conductivity defined in Eq. 21:

$$\frac{\partial V}{\partial x} = -\frac{i_l}{D_e F}\frac{2t_+t_-}{C}\frac{RT}{F} + \frac{RT}{F}(t_- - t_+)\frac{1}{C}\frac{\partial C}{\partial x}$$

Eq. 47

The simplifications of Eq. 47 leads to:

$$D_e\frac{F}{RT}C\frac{\partial V}{\partial x} = -\frac{2t_+t_-}{F}i_l + (t_- - t_+)D_e\frac{\partial C}{\partial x}$$

Eq. 48

Then differentiating Eq. 48 is:

$$D_e\frac{F}{RT}\frac{\partial}{\partial x}\left(C\frac{\partial V}{\partial x}\right) = -\frac{2\mathrm{t}_+\mathrm{t}_-}{F}\frac{\partial i_l}{\partial x} + (t_- - t_+)D_e\frac{\partial^2 C}{\partial x^2}$$

Eq. 49

Than according to Eq. 33

$$D_e\frac{F}{RT}\frac{\partial}{\partial x}\left(C\frac{\partial V}{\partial x}\right) = -\frac{2\mathrm{t}_+\mathrm{t}_-}{\mathrm{D_e}F}\sigma_+\frac{\partial^2 W}{\partial x^2} + (t_- - t_+)D_e\frac{\partial^2 C}{\partial x^2}$$

Eq. 50

And simplifying the Eq. 34 is obtained.

Butler-Volmer

In insertion mechanism one of the redox species is an insertion compound like graphite or lithium oxides. In this case, the complete redox reaction is:

$$Li^+ + \Theta_S + e^- \underset{ox}{\overset{red}{\rightleftharpoons}} Li\Theta_S$$

Eq. 51

where Θ_S is the host site in the latex of the insertion compound material.

The current density equation reported here is obtained from Eq. 11 and Eq. 12:

$$J_+ = Fk_+^*(C_{s+,max} - C_s)^\alpha C_s^{1-\alpha}C^\alpha\left(e^{\alpha f\eta} - e^{-(1-\alpha)f\eta}\right)$$

Eq. 52

where $f = \frac{F}{RT}$. The expression of the overpotential is obtained using the combinations of Eq. 45, Eq. 13 and Eq. 43:

$$\eta = W - V - \frac{RT}{F}\ln\frac{C}{C^*} - \ddot{U}_+ - \frac{RT}{F}\ln\frac{\theta}{1-\theta}$$

Eq. 53

Consequently, Eq. 52 becomes:

$$J_+ = Fk_+^*C_{s+,max}(1-\theta)^\alpha\theta^{1-\alpha}C^\alpha\left(\left(\frac{C}{C^*}\right)^{-\alpha}\left(\frac{1-\theta}{\theta}\right)^{-\alpha}e^{\alpha f(W-V-\ddot{U})} - \left(\frac{C}{C^*}\right)^{1-\alpha}\left(\frac{1-\theta}{\theta}\right)^{1-\alpha}e^{-(1-\alpha)f(W-V-\ddot{U})}\right)$$

Eq. 54

then simplifying:

$$J_+ = Fk_+^*C_{s+,max}C^\alpha\left[\theta e^{\alpha f(W-V-\ddot{U})} - \frac{C}{C^*}(1-\theta)e^{-(1-\alpha)f(W-V-\ddot{U})}\right]$$

Eq. 55

2.3.2 Non-dimensional PDE equations system (positive and negative porous electrodes)

The PDE equations system, uses 25 parameters: 21 are reported in Table 3 and 4 are reported in Table 4. Consequently, an opportune strategy is required to reduce the number and facilitate the generalizations of the results. In fact, a non-dimensional equation system, allows to identify the role and isolate the influence of each parameter in the model. The same strategy is commonly applied in fluid mechanics, where some characteristic parameters such as the numbers of Reynolds, Prandtl, Grashof, and many others are identified. The schematics of the cell with the distances and the thicknesses is reported in Figure 10 (A).

SYMBOL [UNITS]	DESCRIPTION
$D_{S,+}\ , D_{S,-}\ [m^2 s^{-1}]$	Solid phase diffusivity
$D_{+,}, D_{-}, D_e [m^2 s^{-1}]$	Effective ions diffusivity in the electrolyte
$\sigma_{+}, \sigma_{-} [S\ m^{-1}]$	Electronic conductivity solid matrix
$d_{+}, d_{-}, d_e [m]$	Electrode and separator thickness
$R_{+}, R_{-} [m]$	Active material's Particles size
$C^{*} [mol\ m^{-3}]$	Initial Li^{+}concentration
$C_{s+,max}, C_{s-,max} [mol\ m^{-3}]$	Maximum Li concentration in the active material
$\varepsilon_{+,s}, \varepsilon_{-,s} [m^3\ m^{-3}]$	Active material volume fraction
$\varepsilon_{+,l}, \varepsilon_{-,l} [m^3\ m^{-3}]$	Electrode porosity (electrolyte volume fraction)
$k_{+}^{*}, k_{-}^{*} [mol\ m^{-2} s^{-1}]$	Reaction rate constant

Table 3 – The list of the dimensional parameters is reported with their units and description. The subscripts +/-/e are associated to positive electrode/negative electrode/separator, respectively.

The kinetic transfer coefficient α_{+} and α_{-} are assumed equal to 0.5 and not calculated as a design parameter. The surface is not considered directly as a parameter because all the others are defined per unit of surface. The temperature is considered constant to 25°C.

SYMBOL [UNITS]	DESCRIPTION
$t_+[adim]$	Transport number of lithium ions
$\theta_{+,c}$, $\theta_{-,c}[adim]$	Initial positive/Negative electrode stoichiometry at the charged state
$\Delta E^0[V]$, $\frac{F}{RT}\Delta E^0[adim]$	Difference between the electrodes isotherms

Table 4 – The list of parameters the are still required after the dimensionless equations system are reported with their units and description.

In Table 4, is reported only the difference between the two electrodes isotherms ΔE^0. If the isotherms are obtained with the Nernst law, they are characterized by the difference between the equilibrium potentials.

casein reality, the isotherms of the electrodes are defined with more parameters depending of the method used (e.g. interpolating function, look-up table, etc.). Anyway, disregarding the method used the isotherms increase the number of parameters equally in both Table 3 and Table 6.

Many different choices for non-dimensional parameters are possible. In the proposed dimensionless equations system, the effective ion diffusivity in the positive electrode is used to derive all the other dimensionless parameters. The non-dimensional variables are listed in Table 5.

UNIT/DEFINITION	DESCRIPTION
$\theta = \frac{c_{s+}}{c_{+,s,max}}$ *in (+);* $\theta = \frac{c_{s-}}{c_{-,s,max}}$*in (-)*	Solid concentration
$\tilde{C} = \frac{C}{C^*}$	Liquid phase concentration
$\tilde{\varphi} = \frac{F}{RT}\,\varphi$	Solid phase potential
$\tilde{\chi} = \frac{F}{RT}\,\chi$	Liquid phase potential
$\tilde{r} = \frac{r}{R_+} = \frac{r\,a_+}{3\,\varepsilon_{+,s}}$ *in (+) ,*$\tilde{r} = \frac{r}{R_-} = \frac{r\,a_-}{3\,\varepsilon_{-,s}}$ *in (-)*	Particle radius
$\tilde{x} = \frac{x}{d_+}$ *in (+);* $\tilde{x} = \frac{x}{d_e}$ *in (sep) ;* $\tilde{x} = \frac{x}{d_-}$ *in (-)*	Cell distance
$\tilde{t} \,=\, t\,\frac{1}{\varepsilon_{+,l}}\,\frac{D_+}{d_+^2}$	Time

Table 5 – Non-dimensional variables

The schematics of the cell with the distances and the thicknesses in the dimensionless system is reported in Figure 10 (B). It should be noted that the dimensionless thicknesses are equal to 1 for each component. The non-dimensional current is expressed as $\tilde{j} = j\,\frac{d_+}{D_+ F C^*}$, hence the non-dimensional capacity is the product between the non-dimensional current and the non-dimensional time: $\tilde{Q} = \tilde{j}\tilde{t}$.

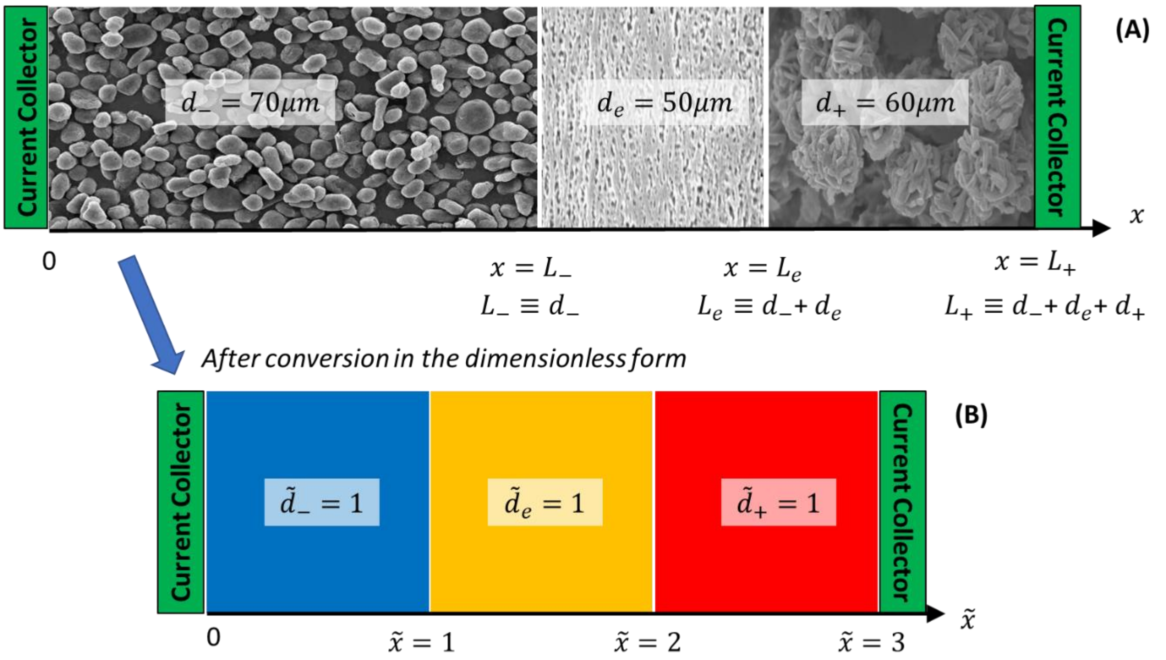

Figure 10 – In figure (A) is reported the schematics of complete cell with the thickness and distances for the negative electrode, separator, and positive electrode. In figure (B) is reported the equivalent complete cell transformed by using the dimensionless thickness.

These non-dimensional variables are associated to 12 non-dimensional parameters reported in Table 6 plus the parameters reported in Table 4. Consequently, the 25 parameters in the dimensional equations systems are reduced to 16.

$A_{1+} = \frac{RT}{F}\,\frac{\sigma_+}{D_+\,F\,C^*}$	$A_{1-} = \frac{RT}{F}\,\frac{\sigma_-}{D_-\,F\,C^*}$
$A_{2+} = \varepsilon_{+,s}\,\frac{D_{s,+}}{D_+}\,\frac{C_{s,max,+}}{C^*}\left(\frac{d_+}{R_+}\right)^2$	$A_{2-} = \varepsilon_{-,s}\,\frac{D_{s,-}}{D_-}\,\frac{C_{s,max,-}}{C^*}\left(\frac{d_-}{R_-}\right)^2$
$A_{3+} = \frac{\varepsilon_{+,s}}{\varepsilon_{+,l}}\,\frac{C_{s,max,+}}{C^*}$	$A_{3-} = \frac{\varepsilon_{-,s}}{\varepsilon_{-,l}}\,\frac{C_{s,max,-}}{C^*}$
$A_{4+} = \frac{a_+ d_+^2\,k_+^*}{D_+}\,\frac{C_{s,max,+}}{C^*}$	$A_{4-} = \frac{a_- d_-^2\,k_-^*}{D_-}\,\frac{C_{s,max,-}}{C^*}$
$A_{5e} = \frac{1}{\varepsilon_{+,l}}\,\frac{D_+}{D_e}\left(\frac{d_e}{d_+}\right)^2$	$A_{6e} = \frac{D_+}{D_e}\,\frac{d_e}{d_+}$
$A_{7-} = \frac{\varepsilon_{-,l}}{\varepsilon_{+,l}}\,\frac{D_+}{D_-}\left(\frac{d_-}{d_+}\right)^2$	$A_{8-} = \frac{D_+}{D_-}\,\frac{d_-}{d_+}$

Table 6 – Non-dimensional parameters for porous electrodes

The parameters A_{1+} and A_{1-} , as an example, associate the electronic conductivity of the porous matrix, the effective electrolyte diffusivity, the temperature and the initial electrolyte salt concentration.

The non-dimensional PDE equations system is reported in Table 7 for the porous electrodes and separator.

	Electrolyte concentration
$A_{7-}\frac{\partial \tilde{C}}{\partial \tilde{t}} - \frac{\partial^2 \tilde{C}}{\partial \tilde{x}^2} = (1-t_+)\, A_{1-}\frac{\partial^2 \tilde{\varphi}}{\partial \tilde{x}^2}$	Negative electrode
$\frac{\partial \tilde{C}}{\partial \tilde{t}} - \frac{\partial^2 \tilde{C}}{\partial \tilde{x}^2} = (1-t_+)\, A_{1+}\frac{\partial^2 \tilde{\varphi}}{\partial \tilde{x}^2}$	Positive electrode
$A_{5e}\frac{\partial \tilde{C}}{\partial \tilde{t}} = \frac{\partial^2 \tilde{C}}{\partial \tilde{x}^2}$	Separator
	Electrolyte potential
$\frac{\partial}{\partial \tilde{x}}\left(\tilde{C}\frac{\partial \tilde{\chi}}{\partial \tilde{x}}\right) = (t_- - t_+)\frac{\partial^2 \tilde{C}}{\partial \tilde{x}^2} - 2\, t_+ t_-\, A_{1-}\frac{\partial^2 \tilde{\varphi}}{\partial \tilde{x}^2}$	Negative electrode
$\frac{\partial}{\partial \tilde{x}}\left(\tilde{C}\frac{\partial \tilde{\chi}}{\partial \tilde{x}}\right) = (t_- - t_+)\frac{\partial^2 \tilde{C}}{\partial \tilde{x}^2} - 2\, t_+ t_-\, A_{1+}\frac{\partial^2 \tilde{\varphi}}{\partial \tilde{x}^2}$	Positive electrode
$\frac{\partial}{\partial \tilde{x}}\left(\tilde{C}\frac{\partial \tilde{\chi}}{\partial \tilde{x}}\right) = (1-2t_+)\frac{\partial^2 \tilde{C}}{\partial \tilde{x}^2}$	Separator
	Solid phase potential
$J_{BV,-} = \frac{A_{1-}}{A_{8-}}\frac{\partial^2 \tilde{\varphi}}{\partial \tilde{x}^2}$	Negative electrode
$J_{BV,+} = A_{1+}\frac{\partial^2 \tilde{\varphi}}{\partial \tilde{x}^2}$	Positive electrode
	Exchange current density
$J_{BV,-} = \frac{A_{4-}}{A_{8-}}\left(\theta e^{\alpha(\tilde{\varphi}-\tilde{\chi}-\ddot{u}_-)} - (1-\theta)\,\tilde{\mathrm{C}}\, e^{-(1-\alpha)(\tilde{\varphi}-\tilde{\chi}-\ddot{u}_-)}\right)_{\tilde{r}=1}$	Negative electrode
$J_{BV,+} = A_{4+}\left(\theta e^{\alpha(\tilde{\varphi}-\tilde{\chi}-\ddot{u}_+)} - (1-\theta)\,\tilde{\mathrm{C}}\, e^{-(1-\alpha)(\tilde{\varphi}-\tilde{\chi}-\ddot{u}_+)}\right)_{\tilde{r}=1}$	Positive electrode
	Solid phase diffusion
$A_{3-}\, A_{7-}\frac{\partial \theta}{\partial \tilde{t}} = A_{2-}\frac{1}{\tilde{r}^2}\frac{\partial}{\partial \tilde{r}}\left(\tilde{r}^2\frac{\partial \theta}{\partial \tilde{r}}\right)$	Negative electrode
$A_{3+}\frac{\partial \theta}{\partial \tilde{t}} = A_{2+}\frac{1}{\tilde{r}^2}\frac{\partial}{\partial \tilde{r}}\left(\tilde{r}^2\frac{\partial \theta}{\partial \tilde{r}}\right)$	Positive electrode

Table 7 – Porous electrode and porous separator non-dimensional PDE equation system

The terms for the exchange current are defined as:

$$\begin{cases} a_-\, d_-\, \tilde{J}_- = \frac{A_{1-}}{A_{8-}}\frac{\partial^2 \tilde{\varphi}}{\partial \tilde{x}^2} \equiv J_{BV,-} \\ a_+\, d_+\, \tilde{J}_+ = A_{1+}\frac{\partial^2 \tilde{\varphi}}{\partial \tilde{x}^2} \equiv J_{BV,+} \end{cases} \qquad \text{Eq. 56}$$

The boundary conditions are reported in Table 8:

Negative Electrode/Current Collector	**Positive Electrode/Current Collector**
$\begin{cases} -A_{1-}\left(\frac{\partial\tilde{\varphi}}{\partial\tilde{x}}\right)_{\tilde{x}=0} = A_{8-}\,\tilde{j} \\ \left(\frac{\partial\tilde{C}}{\partial\tilde{x}}\right)_{\tilde{x}=0} = 0 \\ \left(\frac{\partial\tilde{\chi}}{\partial\tilde{x}}\right)_{\tilde{x}=0} = 0 \end{cases}$ $\tilde{\varphi}(x=0)=0$	$\begin{cases} -A_{1+}\left(\frac{\partial\tilde{\varphi}}{\partial\tilde{x}}\right)_{\tilde{x}=3} = \tilde{j} \\ \left(\frac{\partial\tilde{C}}{\partial\tilde{x}}\right)_{\tilde{x}=3} = 0 \\ \left(\frac{\partial\tilde{\chi}}{\partial\tilde{x}}\right)_{\tilde{x}=3} = 0 \end{cases}$
Negative Electrode/Separator	**Positive Electrode/Separator**
$\begin{cases} \left(\frac{\partial\tilde{\varphi}}{\partial\tilde{x}}\right)_{\tilde{x}=1^-} = 0 \\ A_{6e}\left(\frac{\partial\tilde{C}}{\partial\tilde{x}}\right)_{\tilde{x}=1^-} = A_{8-}\left(\frac{\partial\tilde{C}}{\partial\tilde{x}}\right)_{\tilde{x}=1^+} \\ A_{6e}\left(\frac{\partial\tilde{\chi}}{\partial\tilde{x}}\right)_{\tilde{x}=1^-} = A_{8-}\left(\frac{\partial\tilde{\chi}}{\partial\tilde{x}}\right)_{\tilde{x}=1^+} \end{cases}$	$\begin{cases} \left(\frac{\partial\tilde{\varphi}}{\partial\tilde{x}}\right)_{\tilde{x}=2^+} = 0 \\ A_{6e}\left(\frac{\partial\tilde{C}}{\partial\tilde{x}}\right)_{\tilde{x}=2^+} = \left(\frac{\partial\tilde{C}}{\partial\tilde{x}}\right)_{\tilde{x}=2^-} \\ A_{6e}\left(\frac{\partial\tilde{\chi}}{\partial\tilde{x}}\right)_{\tilde{x}=2^+} = \left(\frac{\partial\tilde{\chi}}{\partial\tilde{x}}\right)_{\tilde{x}=2^-} \end{cases}$
Particle Surface/Negative Electrode	**Particle Surface/Positive Electrode**
$\begin{cases} \left(\frac{\partial\theta}{\partial\tilde{r}}\right)_{\tilde{r}=0} = 0 \\ 3\,A_{2-}\left(\frac{\partial\theta}{\partial\tilde{r}}\right)_{\tilde{r}=1} = -A_{1-}\frac{\partial^2\tilde{\varphi}}{\partial\tilde{x}^2} \end{cases}$	$\begin{cases} \left(\frac{\partial\theta}{\partial\tilde{r}}\right)_{\tilde{r}=0} = 0 \\ 3A_{2+}\left(\frac{\partial\theta}{\partial\tilde{r}}\right)_{\tilde{r}=1} = -A_{1-}\frac{\partial^2\tilde{\varphi}}{\partial\tilde{x}^2} \end{cases}$

Table 8 – Boundary Conditions

Finally, the initial conditions are reported in Table 9.

$\theta = \theta_{-,c}$	Negative electrode stoichiometry
$\theta = \theta_{+,c}$	Positive electrode stoichiometry
$\tilde{C} = 1$	Electrolyte concentration
$\tilde{\varphi} = 0$	Negative electrode solid phase potential
$\tilde{\chi} = -\ddot{u}_- - \ln\frac{1-\theta_{-,c}}{\theta_{-,c}}$	Electrolyte liquid potential
$\tilde{\varphi} = \ddot{u}_+ + \ln\frac{1-\theta_{+,c}}{\theta_{+,c}} + \tilde{\chi}$	Positive electrode solid phase potential

Table 9 – Initial Conditions

The capacity of the cell depends of the initial (charged) state of charge of the electrodes according the relation:

$$\tilde{Q} = \min\left(A_{3-}\frac{A_{7-}}{A_{8-}}\,\theta_{-,c}\ ;\ (1-\theta_{+,c})\,A_{3+}\right) \qquad \text{Eq. 57}$$

The mass conservation law for the ions of lithium in the liquid phase is:

$$\frac{A_{7-}}{A_{8-}}\int_0^1 \tilde{C}d\tilde{x} + \frac{A_{5e}}{A_{6e}}\int_1^2 \tilde{C}d\tilde{x} + \int_2^3 \tilde{C}d\tilde{x} = \frac{A_{7-}}{A_{8-}} + \frac{A_{5e}}{A_{6e}} + 1 \qquad \text{Eq. 58}$$

The average insertion state in every particle is:

$$\hat{\theta}(\tilde{x}) = 3\int_0^1 \theta(\tilde{r},\tilde{x})\tilde{r}^2 d\tilde{r} \qquad \text{Eq. 59}$$

and the state of charge in the whole positive electrode is:

$$\theta_+ = 3\int_0^1\int_0^1 \theta(\tilde{r},\tilde{x})\tilde{r}^2 d\tilde{r}\, dx \qquad \text{Eq. 60}$$

As an example, the 24 values (the isotherms are not reported) in Table 10 are obtained from the literature [72] and the corresponding non-dimensional parameters are reported.

$D_{s,-} = 10^{-13}\ \mathrm{m^2\ s^{-1}}$	$C^* = 870\ \mathrm{mol\ m^{-3}}$
$D_{s,+} = 10^{-13}\ \mathrm{m^2\ s^{-1}}$	$R_- = 11\ \mu\mathrm{m}$
$d_- = 72\ \mu m$	$R_+ = 5\ \mu\mathrm{m}$
$d_+ = 61\ \mu m$	$\varepsilon_{-s} = 0{,}60$
$d_e = 20\ \mu m$	$\varepsilon_{+s} = 0{,}62$
$C_{s,max-} = 30\,000\ \mathrm{mol\ m^{-3}}$	$\varepsilon_{-l} = 0{,}32$
$C_{s,max+} = 50\,000\ \mathrm{mol\ m^{-3}}$	$\varepsilon_{+l} = 0{,}24$
$\theta_{-,c} = 0{,}8$	$k_-^* = 3.10^{-9}\ \mathrm{m\ s^{-1}}$
$\theta_{+,c} = 0{,}4$	$k_+^* = 3.10^{-9}\ \mathrm{m\ s^{-1}}$
$\sigma_- = 4\ Sm^{-1}$	$D_e = 10^{-10}\ \mathrm{m^2\ s^{-1}}$
$\sigma_+ = 0{,}5\ Sm^{-1}$	$D_- = 2.10^{-11}\ \mathrm{m^2\ s^{-1}}$
$t_+ = 0{,}4$	$D_+ = 10^{-11}\ \mathrm{m^2\ s^{-1}}$

Table 10 – The parameters from the table are obtained from the literature [93]. The thickness of the separator is not reported in the article and it is assumed.

The other derived parameters such as active surface, and the capacity are calculated and reported in Table 11. The specific capacity is $27{,}8\,\mathrm{Ah\,m^{-2}}$ and the reference current is $1\tilde{J} \approx 14.3\,A\,m^{-2}$ corresponding to C/2.

$a_- = \frac{3\varepsilon_{-s}}{R_-} = 2.10^5\,m^{-1}$	$\kappa^* = \frac{D_e F^2 C^*}{RT}\frac{1}{2t_+t_-} = 0{,}7\,S\,m^{-1}$
$a_+ = \frac{3\varepsilon_{+s}}{R_+} = 4.10^5\,m^{-1}$	$\frac{Q_{e+}}{A} = \varepsilon_{+l}\,d_+F\ C^* = 0{,}34\,\mathrm{Ah\,m^{-2}}$
$\frac{Q_+}{A} = 50{,}7\ \mathrm{Ah\,m^{-2}}$	$\frac{Q_-}{A} = 34{,}7\,\mathrm{Ah\,m^{-2}}$
$\frac{Q_{max}}{A} = \frac{Q_-}{A}\,\theta_{-,c} = 27{,}8\,\mathrm{Ah\,m^{-2}}$	$1\,\tilde{\varphi} \approx 25\,mV$
$1\tilde{J} \approx 14.3\,A\,m^{-2}$	$1\tilde{t} \approx 89\,s$

Table 11 – The derived parameters, the capacity and the reference values are calculated.

The dimensionless parameters are reported:

$A_{1-} = 68$	$A_{1+} = 13$
$A_{2-} = 4.9$	$A_{2+} = 45$
$A_{3-} = 65$	$A_{3+} = 150$
$A_{4-} = 5.0$	$A_{4+} = 21$
$A_{7-} = 1{,}2$	$A_{5e} = 0{,}053$
$A_{8-} = 0{,}77$	$A_{6e} = 0{,}039$

Table 12 - These are the non-dimensional parameters obtained from [93].

2.3.3 Non-dimensional PDE equations system for the Li-metal foil negative electrode

The number of parameters is additionally reduced by studying the “half-cell” configuration. In this case, the negative electrode is a lithium metal foil. Consequently, the parameters A_{2-}, A_{3-}, A_{7-} and A_{8-} are not defined, while parameters A_{1-} and A_{4-} are replaced with the parameters L_{1-} and L_{4-} respectively. The new table of non-dimensional parameters is:

$A_{1+} = \frac{RT}{F}\,\frac{\sigma_+}{D_{e+}\,F\,C^*}$	$A_{3+} = \frac{\varepsilon_{+,s}}{\varepsilon_{+,l}}\,\frac{C_{s,max,+}}{C^*}$
$A_{2+} = \varepsilon_{+,s}\,\frac{D_{s,+}}{D_+}\,\frac{C_{s,max,+}}{C^*}\left(\frac{d_+}{R_+}\right)^2$	$A_{4+} = \frac{a_+ d_+^2\,k_+^*}{D_{e+}}\,\frac{C_{s,max+}}{C^*}$
$A_{5e} = \frac{1}{\varepsilon_{+l}}\,\frac{D_{e+}}{D_e}\left(\frac{d_e}{d_+}\right)^2$	$L_{1-} = \frac{RT}{F}\,\frac{\sigma_-}{D_{e-}\,F\,C^*}\,\frac{d_+}{d_-}$
$A_{6e} = \frac{D_{e+}}{D_e}\,\frac{d_e}{d_+}$	$L_{4-} = \frac{d_+\,k_-^*}{D_{e+}}$

Table 13 – Non-dimensional parameters for a positive porous electrode and a lithium metal foil at the negative electrode.

As it is reported in Table 13, the number of parameters is reduced to 11 (8+3), and their effect on the rated capacity are detailed in § 6.

The non-dimensional PDE equations system is reported in for the positive porous electrode and the lithium foil at the negative electrode.

	Electrolyte concentration
$A_{7-}\,\frac{\partial \tilde{C}}{\partial \tilde{t}} \;-\; \frac{\partial^2 \tilde{C}}{\partial \tilde{x}^2} \;=\; (1-t_+)\,A_{1-}\,\frac{\partial^2 \tilde{\varphi}}{\partial \tilde{x}^2}$	Negative Electrode
$\frac{\partial \tilde{C}}{\partial \tilde{t}} \;-\; \frac{\partial^2 \tilde{C}}{\partial \tilde{x}^2} \;=\; (1-t_+)\,A_{1+}\,\frac{\partial^2 \tilde{\varphi}}{\partial \tilde{x}^2}$	Positive Electrode
$A_{5e}\,\frac{\partial \tilde{C}}{\partial \tilde{t}} \;=\; \frac{\partial^2 \tilde{C}}{\partial \tilde{x}^2}$	Porous Separator
	Electrolyte potential
$\frac{\partial}{\partial \tilde{x}}\left(\tilde{C}\,\frac{\partial \tilde{\chi}}{\partial \tilde{x}}\right) \;=\; (t_- - t_+)\,\frac{\partial^2 \tilde{C}}{\partial \tilde{x}^2} \;-\; 2\,t_+ t_-\,A_{1-}\frac{\partial^2 \tilde{\varphi}}{\partial \tilde{x}^2}$	Negative Electrode
$\frac{\partial}{\partial \tilde{x}}\left(\tilde{C}\,\frac{\partial \tilde{\chi}}{\partial \tilde{x}}\right) \;=\; (t_- - t_+)\,\frac{\partial^2 \tilde{C}}{\partial \tilde{x}^2} \;-\; 2\,t_+ t_-\,A_{1+}\frac{\partial^2 \tilde{\varphi}}{\partial \tilde{x}^2}$	Positive Electrode
$\frac{\partial}{\partial \tilde{x}}\left(\tilde{C}\,\frac{\partial \tilde{\chi}}{\partial \tilde{x}}\right) \;=\; (1-2t_+)\,\frac{\partial^2 \tilde{C}}{\partial \tilde{x}^2}$	Porous Separator
	Solid phase potential
$-\;L_{1-}\,\frac{\partial \tilde{\varphi}}{\partial \tilde{x}} = \tilde{j}$	Negative Electrode
$\frac{\partial \tilde{\varphi}}{\partial \tilde{x}} \;=\; -\,\frac{A_{4-}}{A_{1-}}\,\left(e^{\alpha(\tilde{\varphi}-\tilde{\chi}-\ddot{u}_-)} - \;\tilde{C}e^{-((1-\alpha)(\tilde{\varphi}-\tilde{\chi}-\ddot{u}_-)}\right)$	Positive Electrode
	Exchange current density
$\tilde{j} \;=\; L_{4-}\left(e^{\alpha(\tilde{\varphi}-\tilde{\chi}-\ddot{u}_-)} - \;\tilde{C}e^{-((1-\alpha)(\tilde{\varphi}-\tilde{\chi}-\ddot{u}_-)}\right)$	Negative Electrode
$J_{BV,+} \;=\; A_{4+}\left(\theta e^{\alpha(\tilde{\varphi}-\tilde{\chi}-\ddot{u}_+)} - (1-\theta)\,\tilde{C}\,e^{-(1-\alpha)(\tilde{\varphi}-\tilde{\chi}-\ddot{u}_+)}\right)_{\tilde{r}=1}$	Positive Electrode
	Solid phase diffusion
$A_{3-}\,A_{7-}\,\frac{\partial \theta}{\partial \tilde{t}} = \;A_{2-}\,\frac{1}{\tilde{r}^2}\,\frac{\partial}{\partial \tilde{r}}\left(\tilde{r}^2\,\frac{\partial \theta}{\partial \tilde{r}}\right)$	Negative Electrode
$A_{3+}\,\frac{\partial \theta}{\partial \tilde{t}} = \;A_{2+}\,\frac{1}{\tilde{r}^2}\,\frac{\partial}{\partial \tilde{r}}\left(\tilde{r}^2\,\frac{\partial \theta}{\partial \tilde{r}}\right)$	Positive Electrode

Table 14 – Porous electrode and porous separator non-dimensional PDE equation system

The terms for the exchange current are defined as:

$$\begin{cases} a_+\,d_+\,\tilde{j}_+ = \;A_{1+}\,\frac{\partial^2 \tilde{\varphi}}{\partial \tilde{x}^2} \equiv J_{BV,+} \end{cases} \qquad \text{Eq. 61}$$

The boundary conditions at the negative current collector for lithium negative electrode foil are:

	Negative Electrode / Current Collector
	$\begin{cases} -A_{1+}\left(\frac{\partial\tilde{\varphi}}{\partial\tilde{x}}\right)_{\tilde{x}=3} = \tilde{j} \\ \left(\frac{\partial\tilde{C}}{\partial\tilde{x}}\right)_{\tilde{x}=3} = 0 \\ \left(\frac{\partial\tilde{\chi}}{\partial\tilde{x}}\right)_{\tilde{x}=3} = 0 \end{cases}$ $\tilde{\varphi}(\mathrm{x}=0) = 0$
Separator/Negative Electrode	**Positive Electrode/Separator**
$\begin{cases} \left(\frac{\partial\tilde{C}}{\partial\tilde{x}}\right)_{\tilde{x}=1^+} = -A_{6e}\,(1-t_+)\,\tilde{j} \\ \left(\tilde{C}\,\frac{\partial\tilde{\chi}}{\partial\tilde{x}}\right)_{\tilde{x}=1^+} = -A_{6e}\,(1-t_+)\,\tilde{j} \end{cases}$	$\begin{cases} \left(\frac{\partial\tilde{\varphi}}{\partial\tilde{x}}\right)_{\tilde{x}=2^+} = 0 \\ A_{6e}\left(\frac{\partial\tilde{C}}{\partial\tilde{x}}\right)_{\tilde{x}=2^+} = \left(\frac{\partial\tilde{C}}{\partial\tilde{x}}\right)_{\tilde{x}=2^-} \\ A_{6e}\left(\frac{\partial\tilde{\chi}}{\partial\tilde{x}}\right)_{\tilde{x}=2^+} = \left(\frac{\partial\tilde{\chi}}{\partial\tilde{x}}\right)_{\tilde{x}=2^-} \end{cases}$
	Particles Surface / Electrode
	$\begin{cases} \left(\frac{\partial\theta}{\partial\tilde{r}}\right)_{\tilde{r}=0} = 0 \\ 3A_{2+}\left(\frac{\partial\theta}{\partial\tilde{r}}\right)_{\tilde{r}=1} = -A_{1-}\frac{\partial^2\tilde{\varphi}}{\partial\tilde{x}^2} \end{cases}$

Table 15 – Boundary Conditions for the “Half-Cell”

Finally, the initial conditions are

$\theta = \theta_{+,c}$	Positive electrode stoichiometry
$\tilde{C} = 1$	Electrolyte concentration
$\tilde{\chi} = -\ddot{u}_-$	Electrolyte liquid potential
$\tilde{\varphi} = 0$	Negative electrode solid phase potential
$\tilde{\varphi} = \ddot{u}_+ + \ln\frac{1-\theta_{+,c}}{\theta_{+,c}} + \tilde{\chi}$	Positive electrode solid phase potential

Table 16 – Initial Conditions for the “Half-Cell”

The conservation of the lithium charged species in the electrolyte is expressed as:

$$\frac{A_{5e}}{A_{6e}}\int_1^2 \tilde{C}d\tilde{x} + \int_2^3 \tilde{C}d\tilde{x} = \frac{A_{5e}}{A_{6e}} + 1 \qquad \text{Eq. 62}$$

3 Analysis of the parameters from literature

The values of the parameters obtained from the literature are discussed in this chapter. In fact, most of these parameters are assumed or fitted with simulations but only some of them are measured.

A similar work was performed by Arunachalam et al. 2015 [159] by reporting tables containing some of the required parameters. In the present chapter, all the required parameters are reported for both dimensional and the dimensionless PDE systems (§ 2.3.3). Because of the large number of parameters in this database an estimation of their range is permitted.

The ionic conductivity κ, the diffusivity D and the transport (or transference) number of cations t_+, are the macroscopic parameters that describes the property of the electrolyte mass transport. These values change when the medium is filling the porous structure of the cell. Consequently, several correction factors are introduced to deal with the porosity and the tortuosity. Usually, the Bruggeman relation (cf. § 2.2) is widely used to estimate the effective transport properties but other relations could be used as investigated by Cobb and Bae 2014 [156]. The transport properties in the solid phase are regulated by the diffusivity D_s and the conductivity κ. In literature, these parameters could be functions of both concentration and temperature.

In Table 17 the parameters from the literature are reported by assigning a different color for each parameter according to the source. Thus, the chemical compounds related to Table 17 for the electrodes and the electrolytes are reported in Table 18. The fitting (e.g. using a regression method [109], [160]) with the simulations used by the authors, can be useful to identify some parameters, but it leads to non-general results because of the fitting ambiguities and the poor accuracy. It is worth mentioning that, even when the values are measured they are commonly adjusted to obtain better simulations[88], [142].

	D_e	σ_-	σ_+	d_-	d_e	d_+	R_-	R_+	$D_{s,-}$	$D_{s,+}$	β_-	β_e	β_+	t_+	C^*	$Cs_{max,-}$	$Cs_{max,+}$	$\varepsilon_{s,-}$	ε_-	ε_e	$\varepsilon_{s,+}$	ε_+	$k_{0,+}$	$k_{0,-}$	κ_e
Albertus_2008 [161]	L	A	A	F	A	F	L	L	L	L	L	L	L	L	L	L	L	L	L	L	L	L	A	A	L
Albertus_2009 [162]	L	L	L	A	A	A	A	A	L	L	L	L	L	L	A	L	L	A	A	A	A	A	L	L	L
Awarke_2013 [81]	L	A	A	L	L	L	L	L	L	L	F	F	F	L	L	L	L	A	A	A	A	A	F	F	L
Christensen_2013 [107]	L	A	A	A	A	A	A	A	A	A	A	A	A	A	A	A	A	A	A	A	A	A	A	A	L
Cobb_2014 [156]	L	A	A	A	A	A	A	A	A	A	A	A	A	L	A	A	A	A	A	A	A	A	A	A	L
Darling_1997 [154]	L	L	L	A	A	A	A	A	A	A	A	A	A	L	A	A	A	A	A	A	A	A	A	A	L
Darling_1998 [80]	L	L	L	A	A	A	A	A	F	F	A	A	A	L	A	A	A	A	A	A	A	A	F	F	L
Ecker_2015 [88], [142]	M	M	M	M	M	M	F	M	L	L	M	M	M	L	M	M	M	M	M	M	M	M	F	F	M
Ferrese_2012 [112]	L	L	L	M	M	M	L	L	L	L	L	L	L	L	L	L	L	L	L	L	L	L	L	L	L
Ferrese_2014 [99]	L	L	L	M	M	M	L	L	L	L	L	L	L	L	L	L	L	L	L	L	L	L	L	L	L
Fu_2014 [163]	A	A	A	A	A	A	A	A	A	A	A	A	A	A	A	A	A	A	A	A	A	A	A	A	A
Guo_2013 [103], [104]	L	A	A	A	A	A	A	A	A	A	A	A	A	L	A	A	A	A	A	A	A	A	A	A	L
Jsari_2011 [114]	F	L	L	L	L	L	F	F	L	L	L	L	L	L	L	L	L	F	F	F	F	F	A	A	F
Ji_2013 [105]	L	L	L	M	M	M	A	A	L	L	L	L	L	L	M	L	L	L	M	M	L	M	F	F	L
Kim_2014 [92]	L	L	L	L	L	L	L	L	L	L	L	L	L	L	L	L	L	L	L	L	L	L	L	L	L
Kumaresan_2008 [164]	L	L	L	A	A	A	A	A	F	L	F	F	F	F	A	A	A	A	A	A	A	A	F	F	L
Zhang_2014 [93]	F	A	A	A	A	A	F	F	F	F	A	A	A	A	F	A	A	F	F	F	F	F	F	F	F
Legrand_2014 [95]	L	L	L	L	L	L	L	L	L	L	L	L	L	L	L	L	L	L	L	L	L	L	L	L	L
Martínez-Rosas_2011 [72]	L	L	L	L	L	L	L	L	L	L	L	L	L	L	L	L	L	L	L	L	L	L	L	L	L
Ning_2004 [165]	A	A	A	A	A	A	A	A	A	A	A	A	A	A	A	A	A	A	A	A	A	A	A	A	A
Nyman_2010 [73]	L	L	L	L	L	L	L	L	L	L	L	L	L	L	L	L	L	L	L	L	L	L	L	L	L
Barai_2015 [84]	L	L	L	L	L	L	L	L	L	L	L	L	L	L	L	L	L	L	L	L	L	L	L	L	L
Prada_2013 [166]	L	A	A	M	M	M	M	M	A	L	L	L	L	L	A	L	L	A	A	A	A	A	A	A	L
Ramadass_2003	A	A	A	A	A	A	A	A	A	A	A	A	A	A	A	A	A	A	A	A	A	A	F	F	L
Ramadass_2004	A	A	A	A	A	A	A	A	A	A	A	A	A	A	A	A	A	A	A	A	A	A	A	A	L
Sikha_2004 [145]	A	A	A	A	A	A	A	A	A	A	A	A	A	A	A	A	A	F	F	F	F	F	A	A	L
Stephenson_2007 [116]	A	A	A	A	A	A	A	A	A	A	A	A	A	A	A	A	A	A	A	A	A	A	F	F	L
Suthar_2015 [86], [158]	L	L	L	A	A	A	A	A	L	L	A	A	A	L	L	L	L	L	L	L	L	L	L	L	L
Lin_2013 [108]	A	A	A	A	A	A	A	A	A	A	A	A	A	A	A	A	A	A	A	A	A	A	A	A	A
Zavalis_2012 [110]	L	A	L	L	L	L	L	L	L	L	L	L	L	L	L	L	L	L	L	L	L	L	L	L	L
Zhao_2015 [87]	L	L	L	L	L	L	L	L	L	L	L	L	L	L	L	L	L	L	L	L	L	L	L	L	L

Table 17 – The parameters used in the Newman's model for each reference are reported with a color-map according their source: in blue if the authors take the value from another article (L), in yellow if they are assumed either by the author or they are not explicated (A), in red if values are fitted by the author (F), in green if they are measured by the author (M).

NAME	ELECTROLYTE COMPOSITION	ACTIVE MATERIAL COMPOUNDS	REFERENCE
Albertus_2008	LiPF$_6$ in EC/DMC	C/LMO and LTO/LFP	[161]
Albertus_2009	LiPF$_6$ in a 1:2 EC/DMC	Li-M/NCA+LMO	[162]
Awarke_2013	LiFP$_6$ salt, EC/EMC and PVDF polymer matrix	C/NMC	[81], [131]
Christensen_2013	N.C.	C/LCO	[107], [131]
Cobb_2014	EC/PC/DMC	Li-M/LCO	[156], [117]
Darling_1997	LiClO$_4$ in PC	Li-M/LMO	[154], [167]
Darling_1998	LiClO$_4$ in PC	Li-M/LMO	[80] , [167]
Ecker_2015	BASF (LP50)	C/NCO KOKAM 7.5 Ah	[88], [142]
Ferrese_201(2/4)	N.C.	Li-M/CoO$_2$	[112], [99]
Fu_2014	EC/DMC	C/NMC	[135]
Guo_2013	N.C.	C/NCA LG pouch	[103]
Jsari_2011	EC/PC/EMC/DEC 30:5:35:30	C/LCO	[114], [168]
Ji_2013	20% EMC, 20% EC and 60% DMC	C/NMC	[106]
Kim_2014	LiPF$_6$ in EC/DEC	C/NMC	[92]
Kumaresan_2008	LiPF$_6$ salt, EC/PC/EMC/DEC	MCMB/LCO	[164] , [131]
Zhang_2014	EC/DMC	MCMB/LCO	[93]
Legrand_2014	N.C.	C/LMO, LCO, LNO	[95], [135]
Martínez_Rosas_2011	LiPF$_6$ in a EC/DMC 2:1	C/LMO	[72]
Ning_2004	EC	MCMB/LCO	[165]
Nyman_2010	LiPF$_6$ in EC/EMC 3:7, MAG-10	C/NCA	[73]
Barai_2015	N.C.	C+NMC	[84]
Prada_2013	N.C.	C/LFP	[169],[170]
Ramadass_2003	LiPF$_6$ in EC/DMC	C/LCO	[171]
Ramadass_2004	EC mixture	C/LCO	[172]
Sikha_2004	LiFP$_6$ salt, EC/DMC	C/LCO	[145]
Stephenson_2007	EC/DEC 1:1 (w)	Li-M/LCO	[116]
Suthar_2015	N.C.	C/LCO	[86]
Lin_2013	1 M LiPF$_6$ in EC/DMC	C/LMO	[108]
Zavalis_2012	EC/EMC 3:7 |MAG-10	MCMB/NCA	[110]
Zhao_2015	2M LiPF$_6$ salt in 1:2 v/v EC/DMC	C/LMO	[87]

Table 18 – The references are listed with the respective composition of the electrolyte and the active material.

3.1. Electrolyte conductivity

The electrolyte conductivity can be measured with the conductivity meter or the impedance spectroscopy [131], [136], [173]–[175]. The electrolyte is a medium constituted of a mixture of solvents, a lithium salt and many additives. In the literature, LiPF$_6$ is the most used salt. Instead the solvent could be a mixture of ethylene carbonate (EC), ethyl methyl carbonate (EMC), diethyl carbonate (DEC), dimethyl carbonate (DMC) and propylene carbonate (PC). Yet, the exact, composition in a commercial cell, is usually not communicated by the manufacturer. Consequently, it is difficult to use the values reported in literature and the electrolyte must be analyzed by modeler but still some additives can be poorly detected.

In Figure 11 (A-B) are reported the conductivities for various solvents, when the salt concentration ranges between 0.4 and 1 M [175]: EMC, EC/DMC, EC/EMC, PC/EC/DMC and PC/EC/EMC. At the concentration of 1M, for most solvents the conductivity is found ranging between 1.2 and 1.8 S/m at 50°C Figure 11 (A). Instead, at -40°C, for the same concentration of 1M, the conductivity is 10 times smaller, i.e. approximately 0.1 S/m, Figure 11 (B).

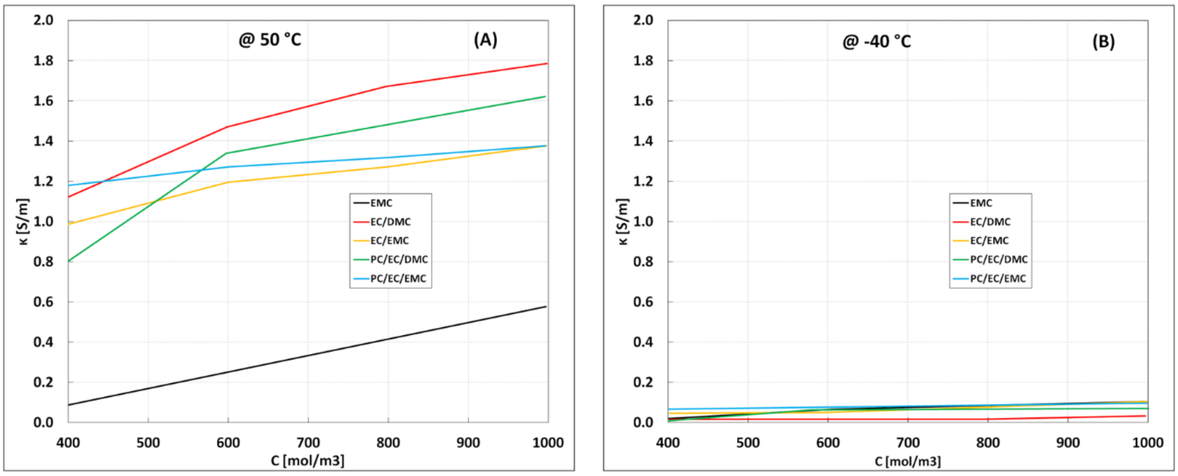

Figure 11 – The conductivity for different electrolytes containing a $LiPF_6$ salt, is reported for concentrations ranging from 0.4 M to 1 M. In (A) the measurements are conducted at 50°C, while in (B) they are conducted at -40°C.

The conductivity as a function of the concentration is reported in Figure 12 and Figure 13. In Figure 12 the conductivity is measured at 25°C while in Figure 13 the measurements are reported for 10°C and 45°C. The maximum conductivity is reached when the concentration is approximately 1M. Physically, when the concentration is zero, the conductivity is zero, but a non-physical offset is introduced by some authors to deal with the numerical stability of the solver.

For most electrolytes at 1 M, the conductivity is approximatively 1 S/m at 25°C (Figure 12), while the conductivity measured by Lundgren et al. 2015 [136], for a EC/DEC electrolyte, is 8 times higher. The EC/DEC electrolyte seems to depend more on temperature rather than the PC/EC/DMC reported by Valøen & Reimers 2005 [131].

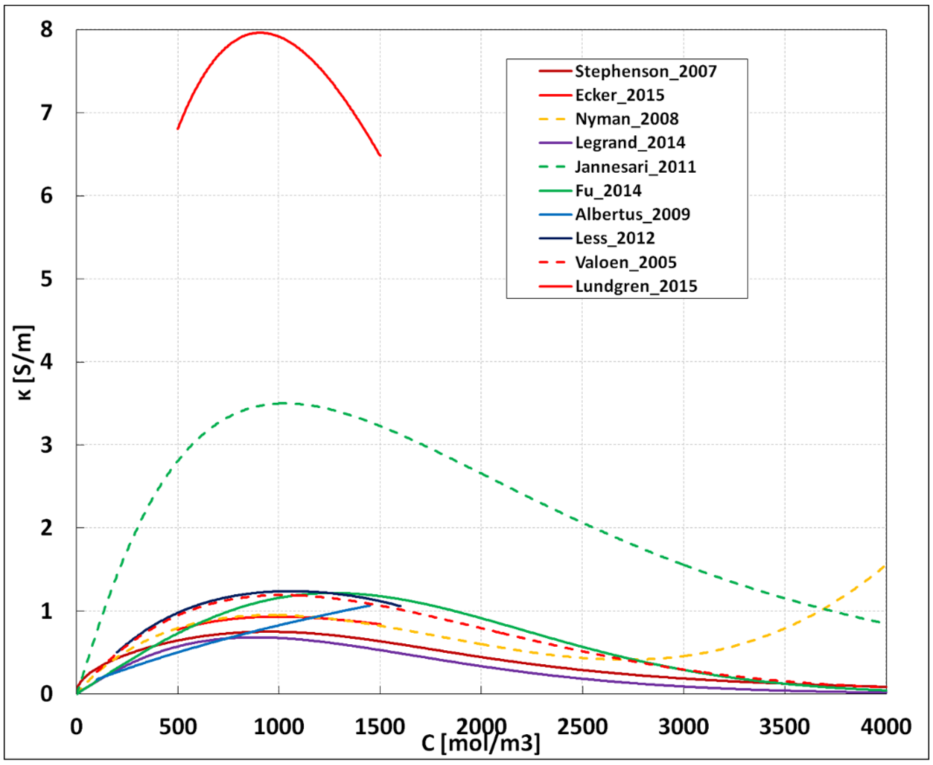

Figure 12 – The conductivity as a function of the concentration is reported for 25°C. The composition of the electrolyte and the references are reported in Table 19.

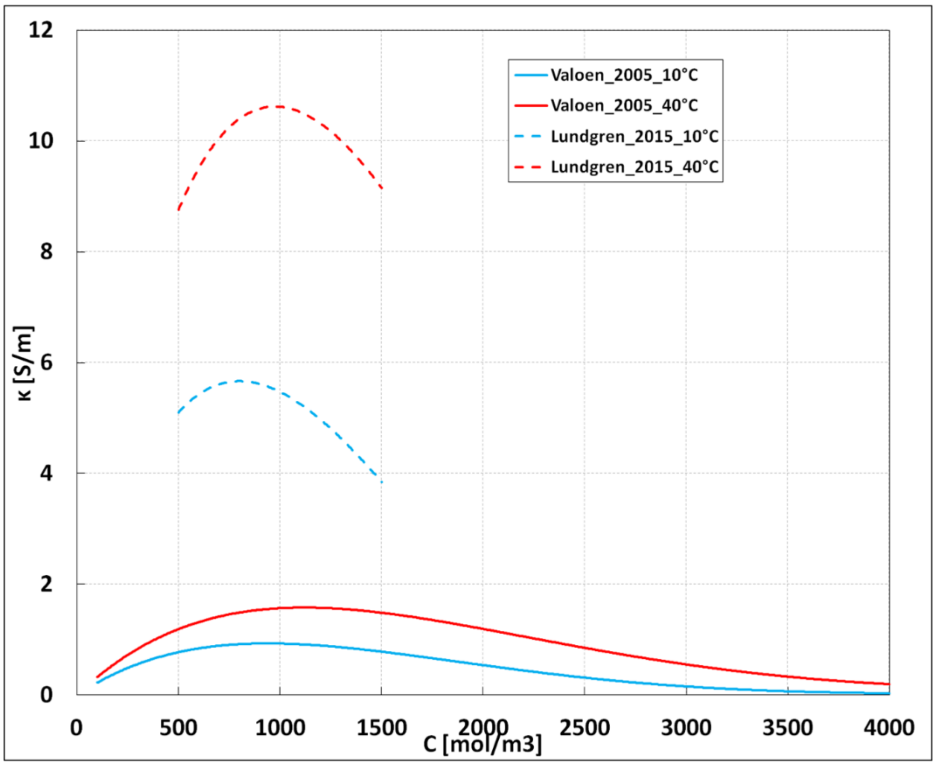

Figure 13 –The conductivity as a function of the concentration is reported for both 10°C and 45°C. The composition of the electrolyte and the references are reported in Table 19.

ID	COMPOSITION	RANGE OF CONCENTRATION	REFERENCE
Stephenson_2007	EC/DEC 1:1 (w)	Non-physical offset when concentration goes to 0 for the solver's numerical stability	[116]
Ecker_2015	BASF (LP50)	From 0.5 to 1.5 M	[88]
Nyman_2008	EC/EMC 3:7	From 0.2 and 2.0 M	[110], [174]
Legrand_2014	N.C.	N.C	[95], [135]
Jsari_2011	EC/PC/EMC/DEC 30:5:35:30	N.C.	[114], [168]
Fu_2014	EC/DMC	N.C.	[135]
Albertus_2009	EC/DC 1:2 (v)	From 0.1 to 1.45 M	[162]
Less_2012	EC/DMC 3:7	From 0.2 to 1.60 M	[111]
Valoen_2005	PC/EC/DMC 10:27:63 (vol. %) - Mitsubishi	From 0.1 to 4.0 M	[81], [86], [131], [164]
Lundgren_2015	EC/DEC 1:1 (w)	From 0.5 to 1.5 M	[136]

Table 19 – The list of references with the identification name, the composition, the range of concentration where the conductivity is defined, and the references are reported.

The values of the conductivity reported by Guo 2013 [103], Doyle 1996 [176] and Christensen 2013 [107] are some orders of magnitude far from the values reported in Figure 12 and Figure 13. In details, the electrolyte from Doyle et al. 1996 [176], is a liquid-polymer matrix system consisting of a mixture of EC/DMC (2:1 v/v and 1:2 v/v) having a much smaller conductivity than a pure liquid electrolyte.

In Figure 14 (A-B) the conductivity is reported for the initial concentration of the simulation: in most cases 1M. The electrolyte conductivity κ_e of the pure species and its associated conductivity κ_D calculated by using Eq. 21 are reported in Figure 14 (A). In most cases, these values are very close, indicating the good approximation with the measurements. This fact also suggests that the diffusivity can be calculated by knowing the electrolyte conductivity, that is much easier to be measured.

The effective conductivity of the electrolyte obtained when the electrolyte fills the pores in the matrix $\kappa_{eff,-}$, $\kappa_{eff,e}$, $\kappa_{eff,+}$ at 1M is reported in Figure 14 (B). The relationship used to calculate the effective conductivity (e.g. by considering Bruggeman relationship between porosity and tortuosity) suggests that conductivity in the separator is higher than in the electrodes.

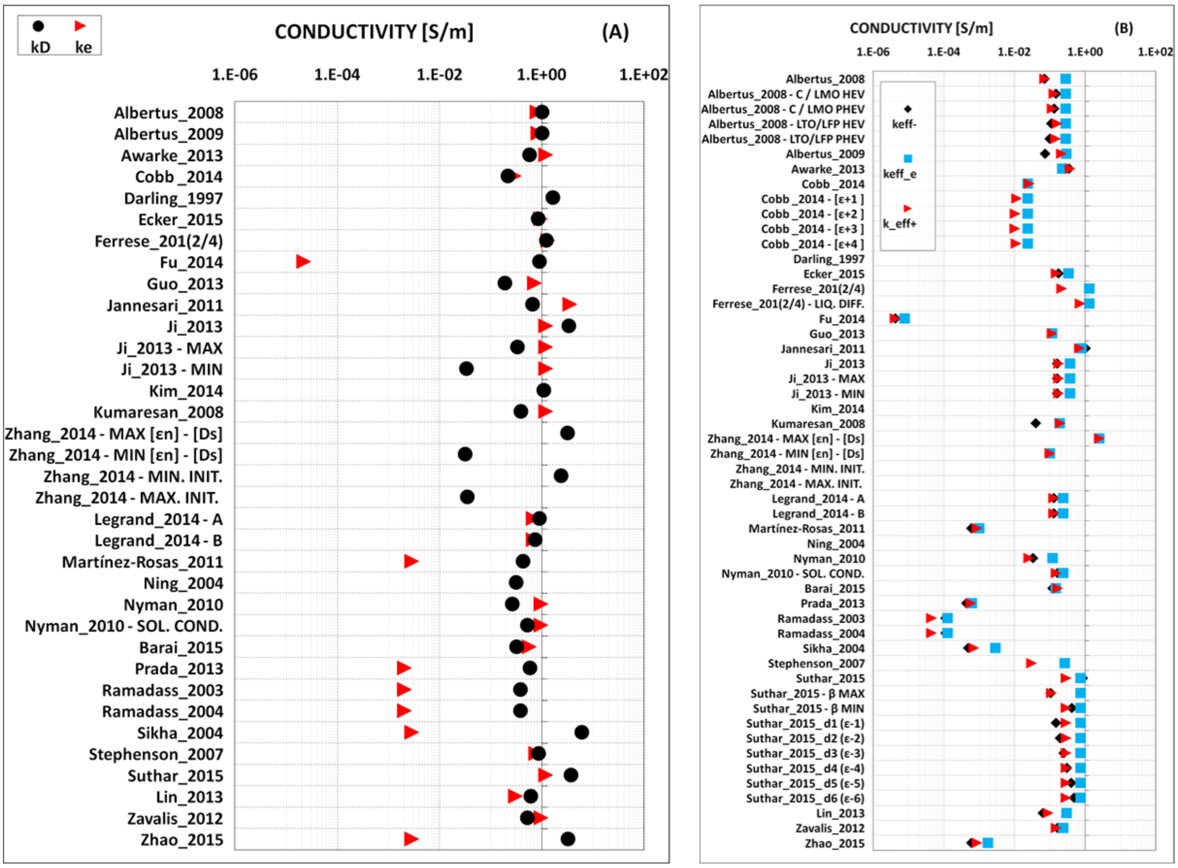

Figure 14 – The conductivity κ_e is referred to pure electrolyte species and κ_D is the conductivity calculated with the value of the diffusivity is reported in (A), while in (B) is reported the effective conductivity $\kappa_{eff,-}$, $\kappa_{eff,e}$, $\kappa_{eff,+}$ associated to negative electrode, separator and positive electrode, respectively.

3.2. Electrolyte diffusivity

The diffusivity of lithium ions in the solvent is measured for examples with the Pulse Field Gradient PFG - NMR, the UV/vis absorption or a concentration cell [131], [136], [177]. In the concentration cell, two lithium metal electrodes are immersed in the electrolytes: at the beginning the concentration of lithium is the same in the proximity of both electrode, after applying a constant current for a predetermined amount of time, the concentration in the proximity of one electrode is much higher than the other. Thus, the potential is then measured during the relaxation and the diffusion coefficient is then extracted with an appropriate mathematical theory.

The diffusivities are plotted in Figure 15 (A-C) at 25°C, 10°C and 40°C, respectively. These expressions are obtained by fitting an expression on the measurements on a limited range of concentration. We extrapolate the values of the diffusivity from 0M to 4M, because they are crucial when limitations occur. In fact, the diffusivity at higher and lower concentration is more difficult to obtain experimentally, but it is a crucial parameter when kinetic limitations occur.

ID	COMPOSITION	RANGE OF CONCENTRATION	REFERENCE
Suthar_2015	N.C.	N.C.	[86]
Nyman_2008	EC/EMC 3:7	From 0.2 and 2.0 M	[174]
Valoen_2005	PC/EC/DMC 10:27:63 (vol. %) - Mitsubishi	From 0.1 to 4.0 M	[131]
Guo_2013	N.C.	N.C.	[103]
Albertus_2009	EC/DC 1:2 (v)	From 0.1 to 1.45 M	[162]
Lundgren_2015	EC/DEC 1:1 (w)	From 0.5 to 1.5 M	[136]
Christensen_2013	EC/DEC	N.C.	[107]

Table 20 – The list of references with the identification name, the composition, the range of concentration where the diffusivity is defined, and the references are reported.

The composition of the electrolytes and their range of concentration when the diffusivity is measured is reported in Table 20.

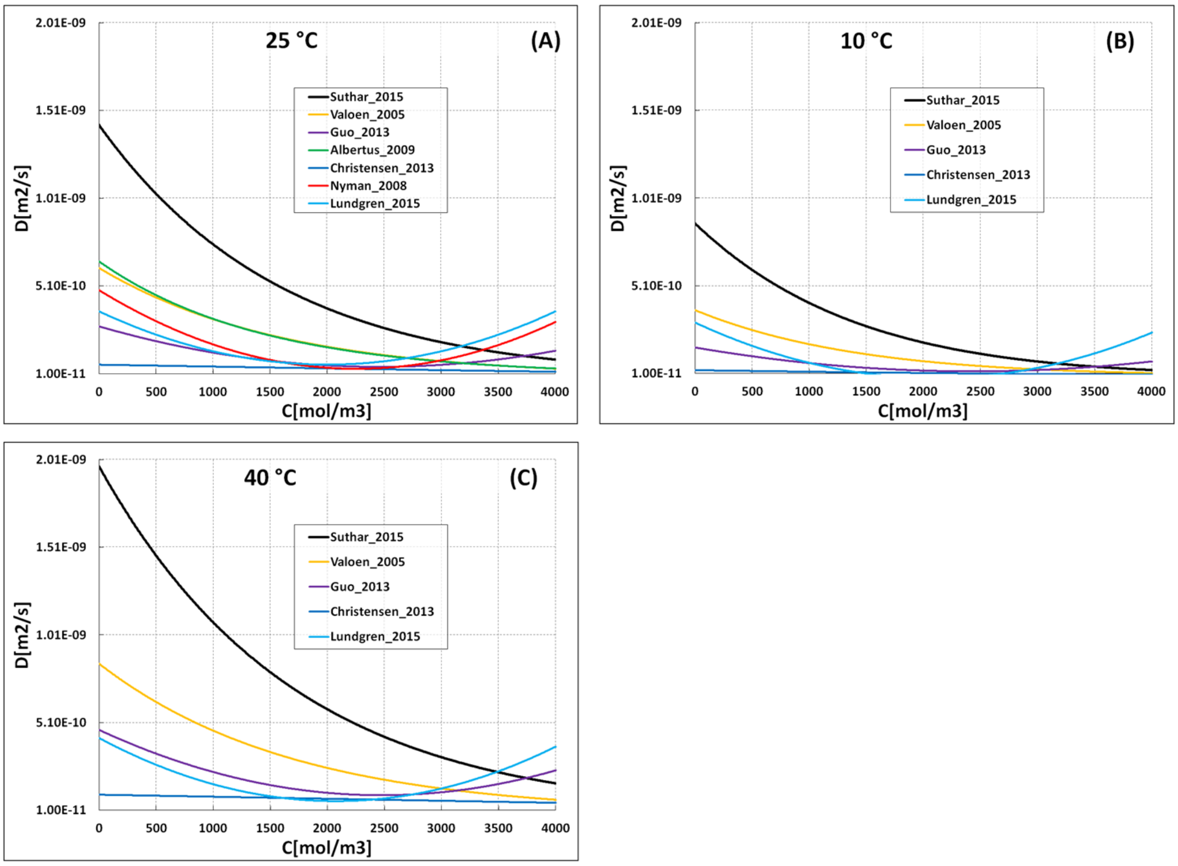

Figure 15 – Diffusivity from the equations available in literature @ 25°C (A), 10 °C (B) and 40°C (C) for concentrations ranging from 0 M to 4 M.

The diffusivity reported by Suthar et al. 2015 [86] is higher at least of one order of magnitude than the others. The composition is not known but the authors used the values from Subramanian et al. 2009 [68]. In this case, the diffusivity doubles when the temperature increases from 10°C to 40°C. Instead, the other electrolytes are less influenced by the temperature.

Two different trends are found for the diffusivity: in the references Valøen and Reimers 2005 [131] and Albertus et al. 2009 [162] the diffusivity is higher when the concentration is close to zero, and then it decreases monotonically, while in the references Nyman et al. 2008 [174] and Lundgren et al. 2015 [136] the diffusivity has a "*U*" shaped profile with the same values at 0M and 4M.

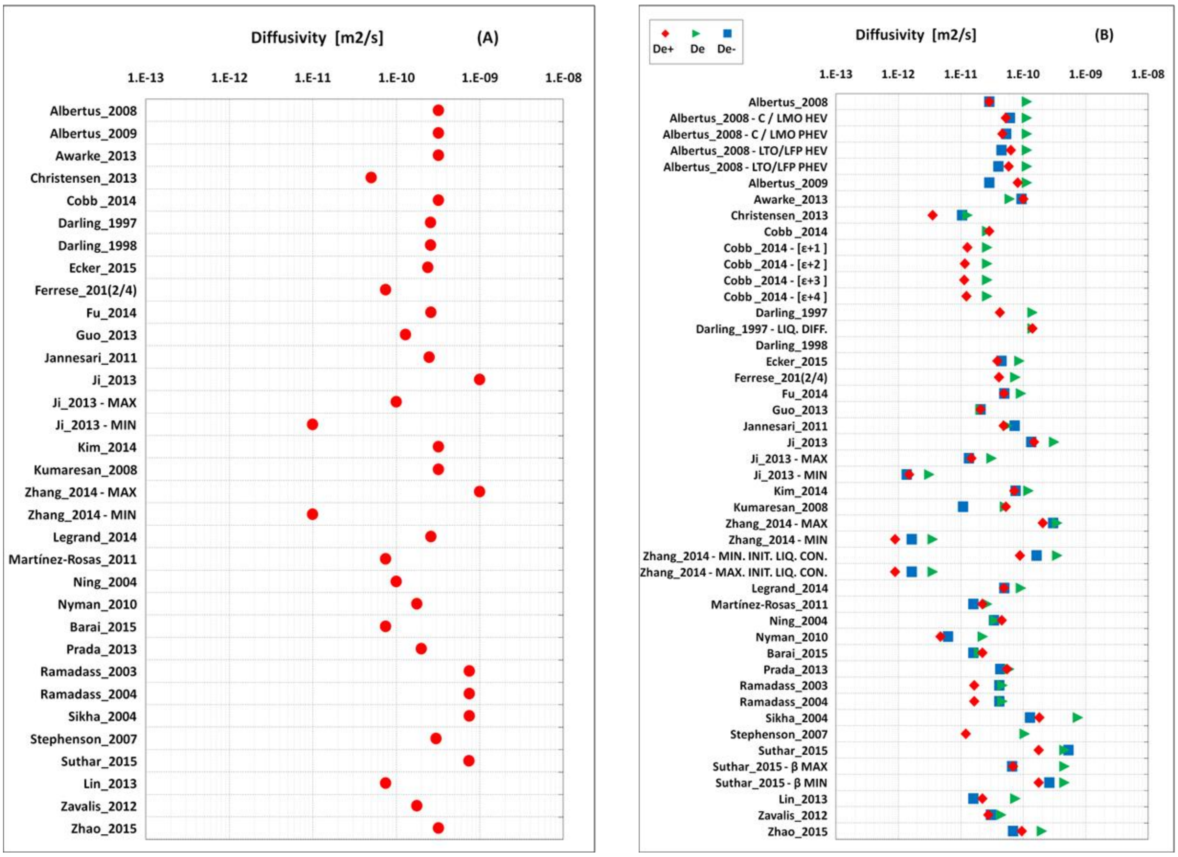

Figure 16 – Diffusivity from at 1M concentration and 25°C. In (A) the diffusivity of the pure electrolyte is reported, while in (B) the effective electrolyte diffusivity when the electrolyte fills the porous electrodes is reported using the Bruggeman approximation.

In Figure 16 (A-B) is reported the electrolyte diffusivity at 25°C for the pure electrolyte and the effective diffusivity dealing with the porous structure. These diffusivities are reported from models that uses a constant diffusivity, or they are calculated for the initial salt concentration. The values of the porosity, initial concentration and Bruggeman exponents, used for calculating the effective diffusivity, are reported in § 3.7. The references and the composition, when available, are reported in Table 18.

The diffusivity in pure electrolyte ranges between $10^{-9}[m^2/s]$ and $10^{-10}[m^2/s]$, while a large dispersion is observed for effective diffusivity (i.e. mediated with the values of tortuosity, porosity and Bruggeman): from $10^{-9}[m^2/s]$ to $10^{-12}[m^2/s]$ and the average diffusivity is $5 \cdot 10^{-11}[m^2/s]$.

3.3. Transport number

The lithium ion transport number (or transference number) can be determined with two techniques: the moving boundary method or the Hittorf method[131], [174], [177]. The moving boundary method consists to measure the speed of displacement of the boundary between two solutions generated by an applied electric current. Instead, the Hittorf method is based on the measurements of the variation of ion concentration in the proximity of the electrodes. The transport number is reported in Figure 17(A-B) as a function of the concentration for three temperatures: 25°C, 10°C and 40°C [131], [174], [177]. These picture illustrates the different behavior on the values from literature: in Nyman 2010 (EC/EMC 3:7) [73] and Lundgren 2015 (EC/DEC 1:1) [136] the transport number decreases monotonically while the opposite behavior is reported by Guo 2013 [103]. However, in the last reference, the composition is not communicated. It is worth mentioning that the transport number measured by Lundgren 2015 [136] is defined for a concentration from 0.5 M to 1.5 M.

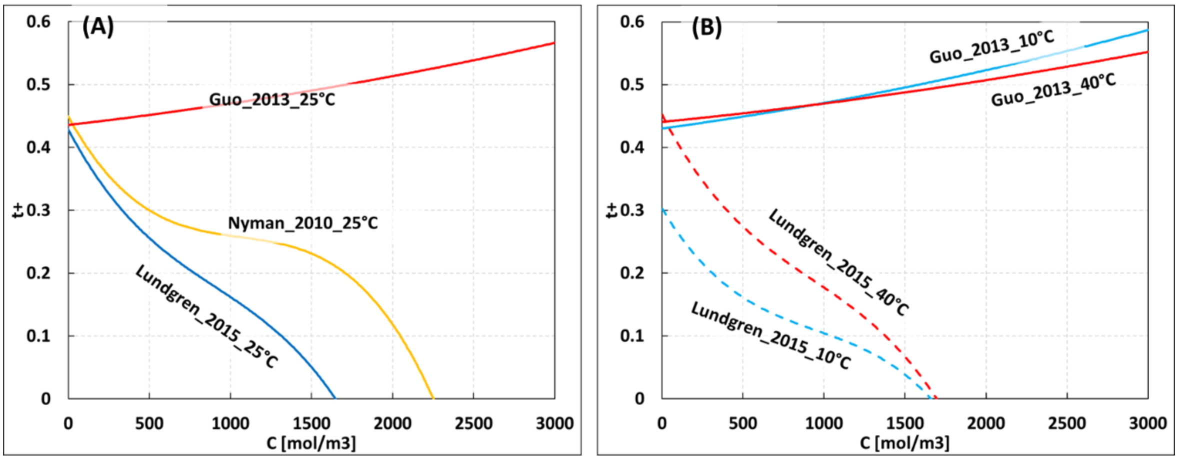

Figure 17 – The transport number as a function of the electrolyte concentration at 25°C in (A) and for both 10°C and 40°C in (B).

The transport numbers reported in Figure 18 are mostly from papers where they are considered constant or they are calculated at 1M. The references and the compositions, when available, are reported in Table 18. The transport number is almost close to 0.37 despites the different solvents.

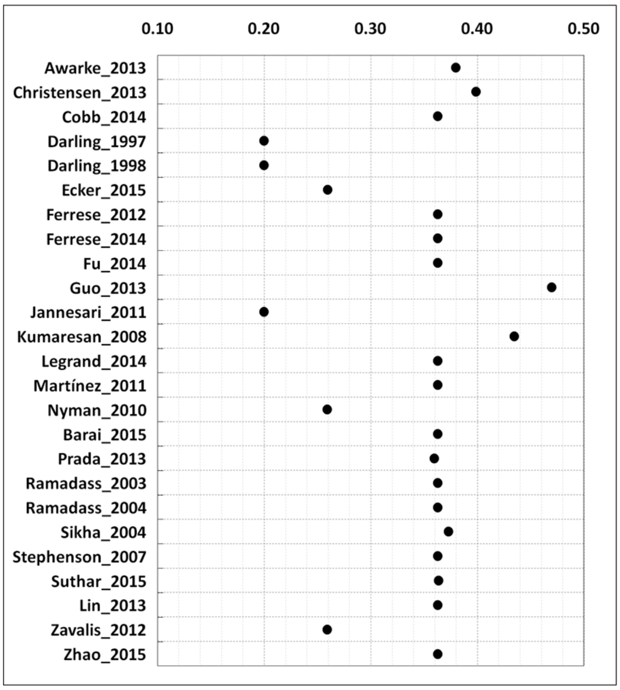

Figure 18 – Transference number are reported for $LiPF_6$ in different solvents at 25°C for a concentration of 1M.

3.4. Solid phase diffusivity

The solid phase diffusivity is measured with several techniques such as the GITT (intermittent current steps), the PITT (intermittent potential steps), the EIS (impedance spectroscopy using a current signal) or EVS (impedance spectroscopy using a voltage signal) [111], [135], [142], [178]–[185]. Each of them have advantages and drawbacks but a large inaccuracy on the measurements is found. The most pertinent method to apply for the solid phase diffusivity measurements is the subject of intense researches [111], [186].

Many authors report the solid phase diffusivity as a function of the Li-ions concentration in the solid phase at the solid/liquid phase interface or its average in the electrode (such as the DOD). Thus, the diffusivities are plotted in Figure 19 with the functions reported by Ji et al. 2013 (Graphite/NMC) [106]. The reference P. Barai et al. 2015 (Graphite/NMC) [84] and Albertus et al. 2009 [162] (blend positive electrode of LMO and NCA).

These values are far (several orders of magnitude) from the values measured by Levi & Aurbach 1997 [187] and Ecker 2005 [142].

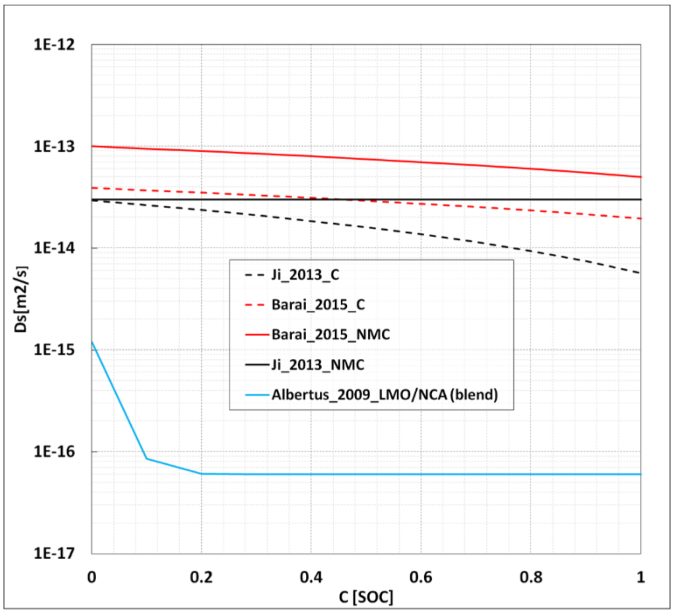

Figure 19 – Electrode material diffusivity as a function of the intercalated concentration at the surface.

Furthermore, the diffusivity is usually reported as a monotonous function of the temperature[188], as illustrated in Figure 20 for the values reported by Suthar 2015 [86], Subramanian 2007 [189]) and Kumaresan 2008 [164].

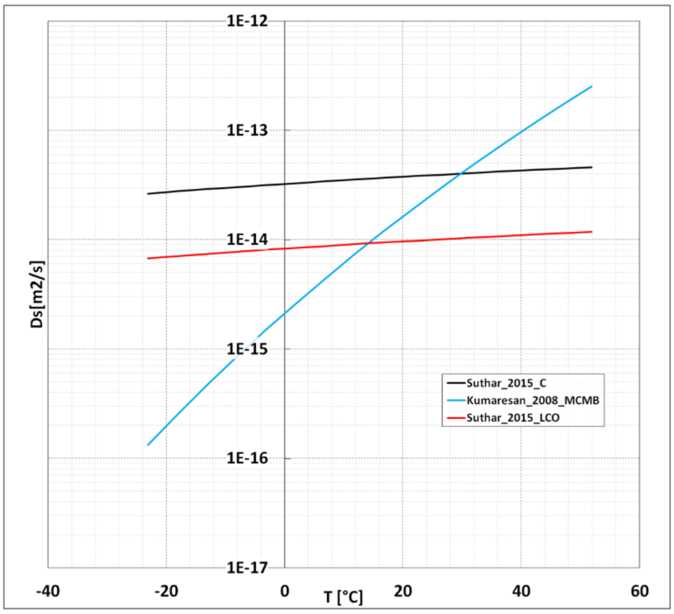

Figure 20 – Solid phase diffusivity as a function of the temperature for the graphite (values from Suthar 2015 [86] and Kumaresan 2008 [164]) and lithium cobalt oxide from Suthar 2015.

In Figure 21 is reported the diffusivity (the references and compounds are indicated in Table 18) when it is assumed as a constant. In average, the values range between $10^{-13}[m^2/s]$ and $10^{-15}[m^2/s]$, but an extremely large dispersion is also observed, since the values are from $10^{-7}[m^2/s]$ and $10^{-19}[m^2/s]$, indicating the solid phase diffusion as one of the poorly measured parameter. We can attribute this dispersion to both the techniques used for the measurements and the mathematical model used to extrapolate these values. These aspects are discussed more in details in § 6.2.

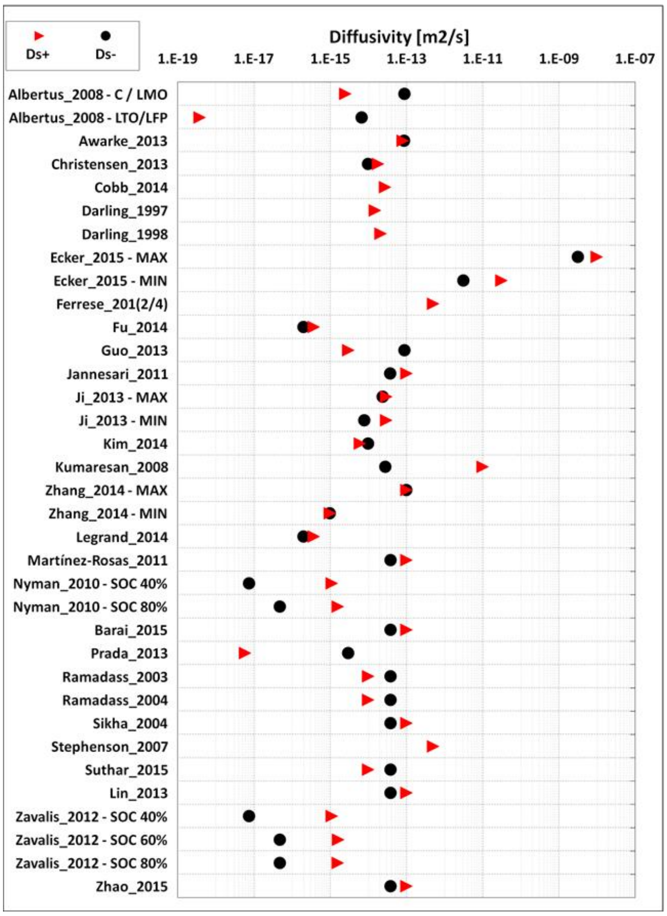

Figure 21 – Values of the solid phase diffusion coefficient reported from articles using a constant diffusivity.

3.5. Solid phase conductivity

The porous electrode matrix conductivity is generally measured with a four-point probe technique [142]. Since the lithium oxide compounds are poorly conductive, the conductivity of the positive electrode mostly depends on the amount of black carbon and if it is homogeneously distributed. Nevertheless, the conductivity can be a function of the state of lithiation as reported by Park et al. 2010 [190].

The conductivities found in the literature for the negative and positive electrode material are reported in Figure 22 (A-B). In Figure 22 (A) the conductivity of the electrodes solid matrix is presented. In Figure 22 (B) the effective conductivity is calculated through the volume fraction or the Bruggeman relation. In fact, in some papers the electrode conductivity is corrected by considering the active material volume fraction, the tortuosity and porosity. Thus, a Bruggeman like approach is also used to calculate the effective conductivity.

The graphite conductivity is extremely variable with 3 to 4 orders of magnitude according to the considered references. Furthermore, the measures reported by Ecker et al. 2015 [142] before and after the SEI formation are $139.91 \pm 34.2 [mS/cm]$ and $1.11 \pm 0.7 [mS/cm]$, respectively. We can conclude that large variations occur in conductivity before and after the SEI formation and the accuracy is very poor. The same poor accuracy is evidenced for positive electrode (NCO) having a conductivity of $680.67 \pm 442.7 [mS/cm]$ [142].

The electronic conductivity could be a function of the particle size and distribution as studied for the $\mathrm{LiFePO_4}$ by N. Zhao et al. 2015 [188], with variations of 4 orders of magnitude through the particle size range.

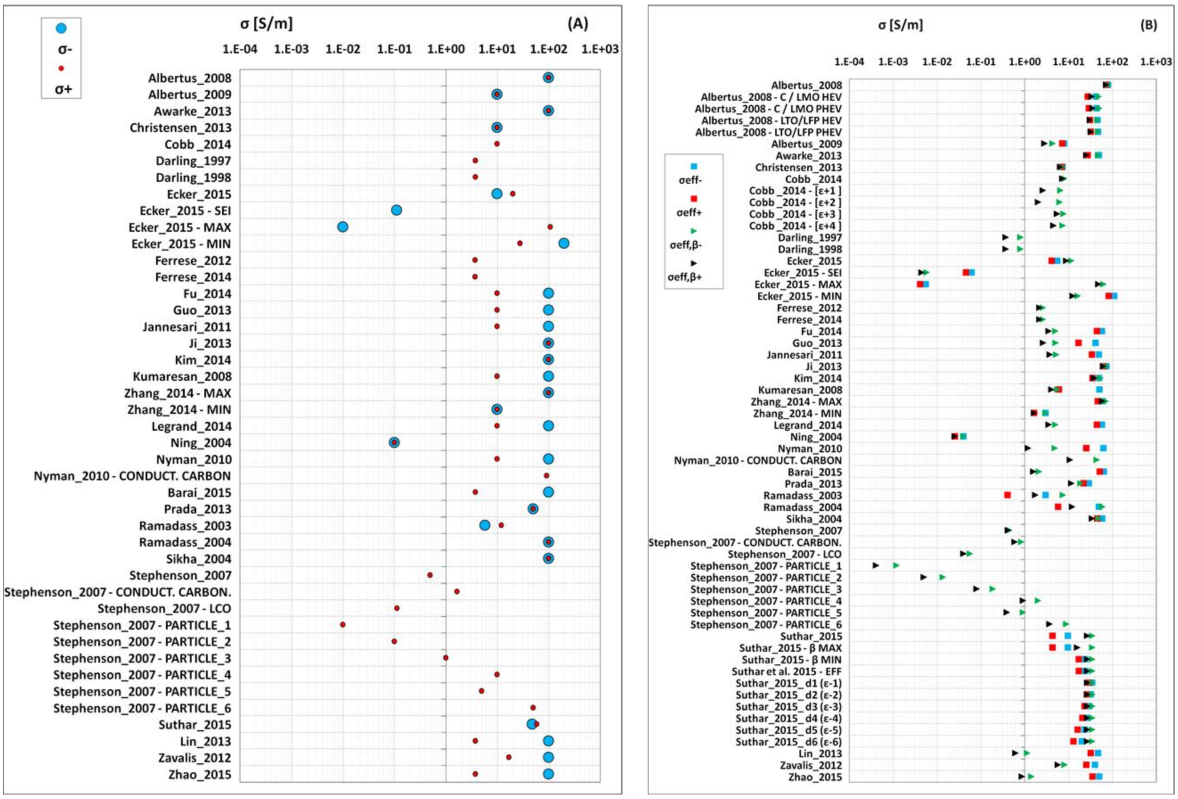

Figure 22 – The positive and negative electrode conductivities are reported in (A). The effective conductivity corrected with the active material volume fraction and the “Bruggeman” relationship are shown in (B).

One of the most studied compound is the LCO, but there is not a complete agreement on its conductivity: in most cases it is assumed at $100 [S/m]$ in others at $10 [S/m]$. The list of the whole references and chemistries are reported in Table 18. Comparing Figure 22 (A) and Figure 22 (B) we can conclude that the conductivity is assumed to be high for almost all the compounds, but it is later adjusted to fit the experiments. Then, the effective conductivity is usually comprised between $1\ [S/m]$ and $10\ [S/m]$.

3.6. Kinetic reaction rate constant

The kinetic reaction rate constant of Li insertion, to the authors knowledge, still cannot be measured in a complex system like lithium ion batteries. Consequently, it is mostly a fitting parameter. Furthermore, to complexify the situation, the authors use slightly different formulations of the Butler-Volmer kinetic equation (e.g. Tafel or linear approximations) and consequently the unit associated to this constant is different according to the considered reference (cf. Eq. 11, Eq. 12). Thus, it is hard to compare the values found in the literature, because they must be converted in the same units. For some papers, we could deal such conversions and the results are reported in Figure 23. The composition of the materials used is reported in Table 18. As we can see, the only conclusions that can be stated is that these values are far orders of magnitude from each other.

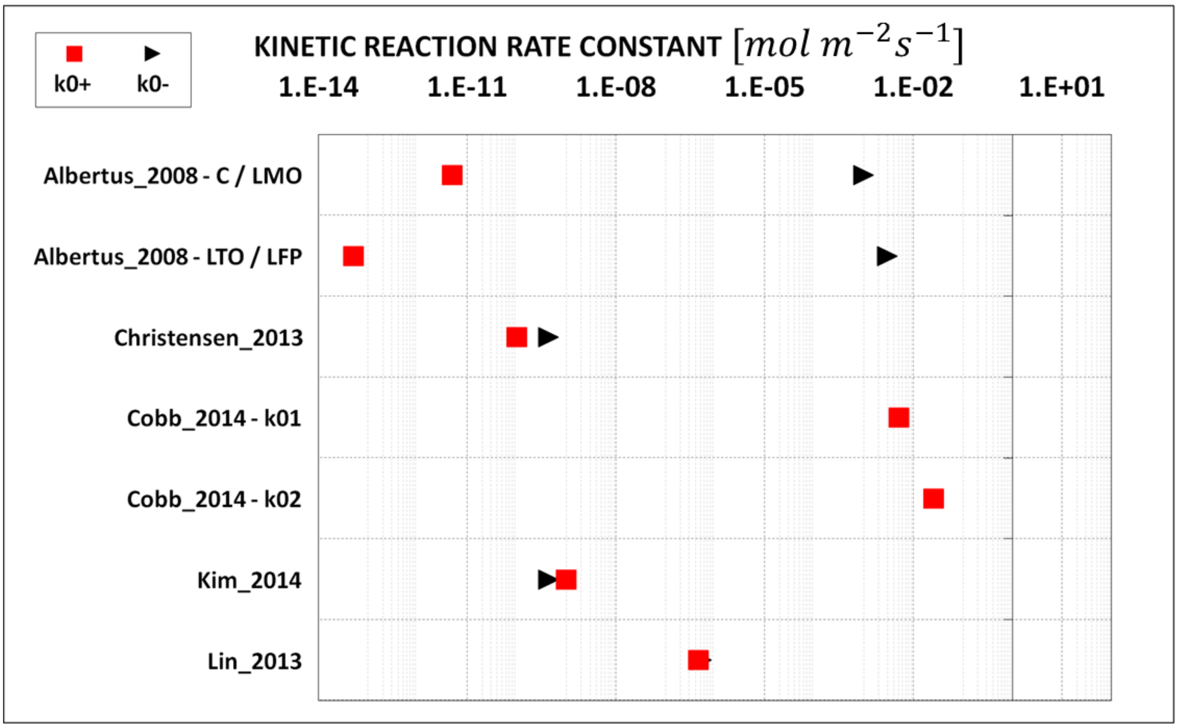

Figure 23 – Kinetic reaction rate constants converted in the same units.

It is worth mentioning that in many articles, the kinetic constant rate k_0^* is meaningless since the fitting was performed on the current density i_0, that depends on the local Li concentration.

3.7. Dimensional design parameters

In this section are reported the remaining design parameters collected from the literature. They are different for each cell, but their reports could be useful to estimate time constants and having reference parameters, but also observe which cells are most simulated as an example, power (thin electrodes, small particles, etc..) or energy cells (high active material volume fraction, thick electrodes, etc..).

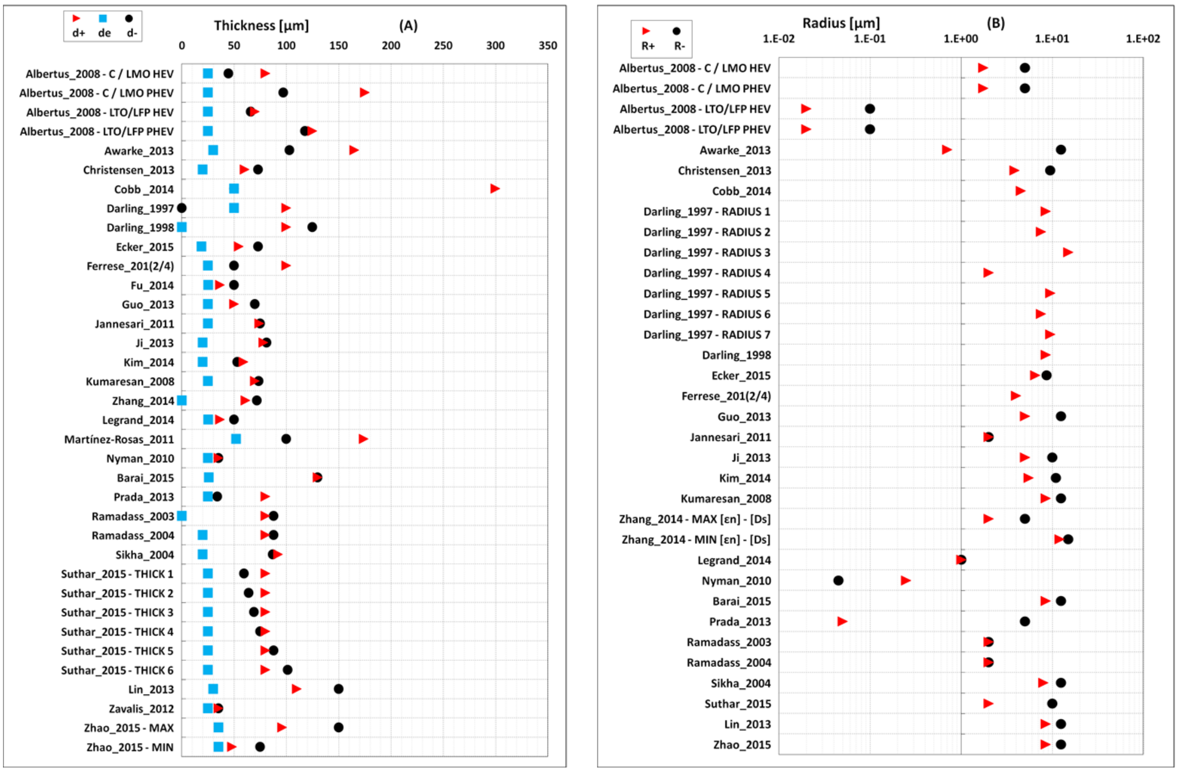

Figure 24 – The thickness of the electrodes and the separator are reported in (A), while the particles' radii of the active materials are reported in (B).

In Figure 24 (A-B) the thicknesses of the electrodes, separators and the radius of the active material's particles are reported. As an example, if we assume $100\ [\mu m]$ as thickness of the electrode and the particles radius of $10\ [\mu m]$, then only 10 particles constitutes the electrode. This situation may be adverse for a macro-homogeneous model where the presence of many particles is assumed.

In Figure 25 the Bruggeman's correction factors are reported. This theory was developed to understand how the oil diffuses in sedimentary rocks for the oil drilling in rocky sands containing oil. For spherical particles, the values are close to 1.5, different values can be coherently used by changing the shape of the active materials particles. Instead, in many cases the Bruggeman's exponent is used as a global fitting parameter because it changes both liquid phase diffusivity and electronic conductivity.

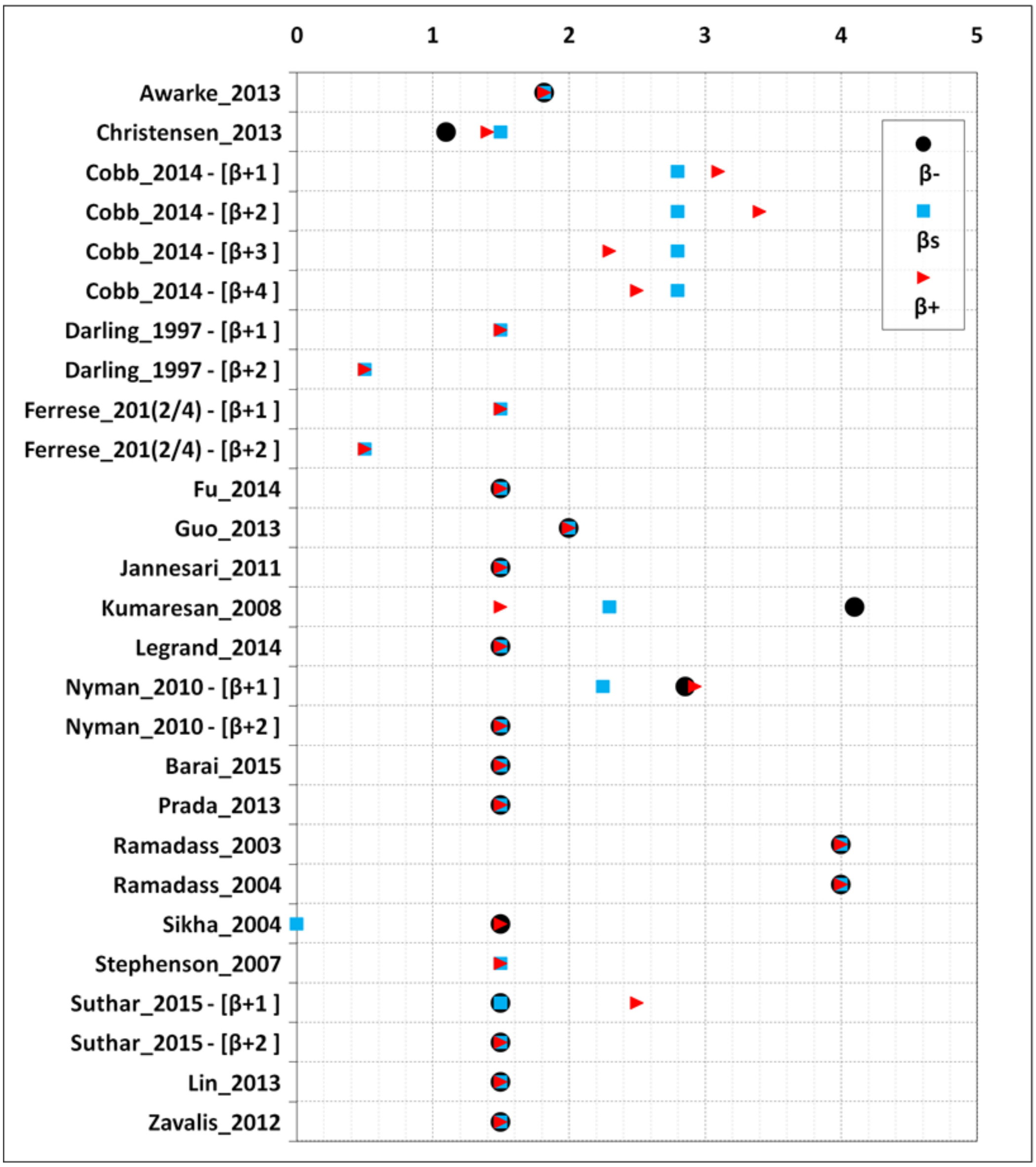

Figure 25 – The Bruggeman's correction factors are reported.

In Figure 26 (A) is reported the initial concentration in the electrolyte, that is usually assumed to 1M. Then, the maximum solid phase concentration is reported in Figure 26 (B). It should be noted that for the same material such as the graphite, different values are reported by *Kumaresan_2008* and *Guo_2008*. Probably because the values are not correctly calculated. Finally, in Figure 27(A-B) the porosity and the active material are shown. These parameters usually do not consider the inclusions (i.e. percentile of porosity non-connected) and fracture/non-connected active material (i.e. percentile of active material volume fraction non-connected). For such reasons, these parameters are, in practices, non-easily measurable.

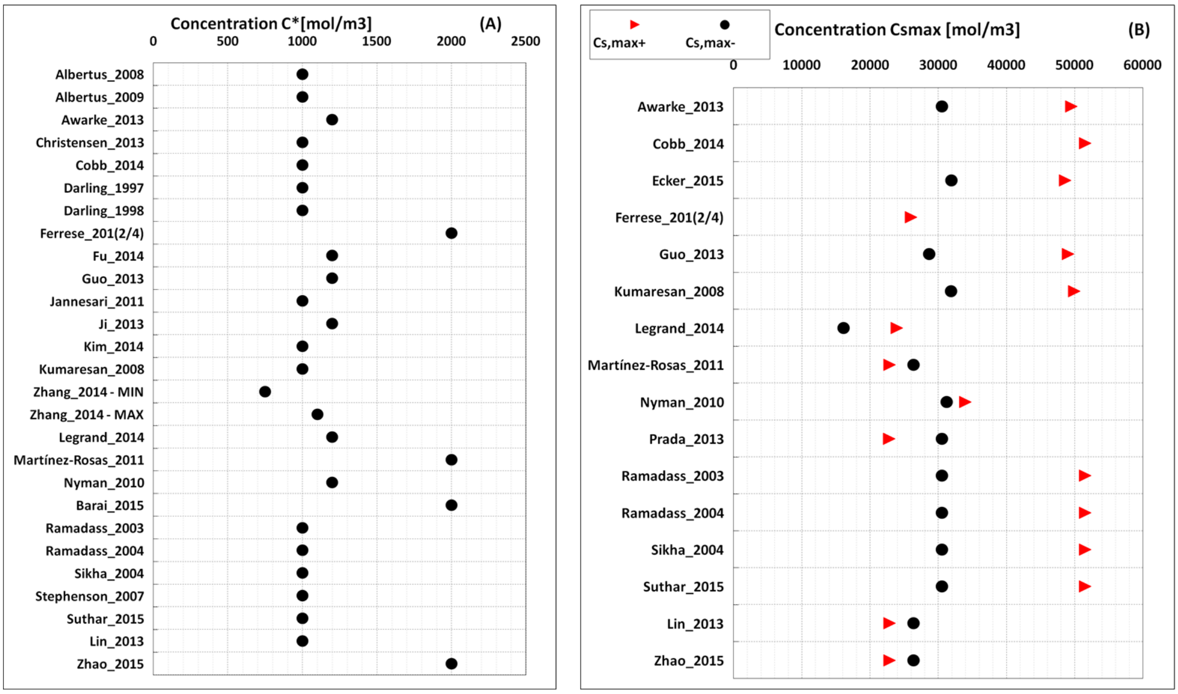

Figure 26 – In (A) the initial concentration in the electrolyte and in (B) the maximum concentration in the active materials are reported.

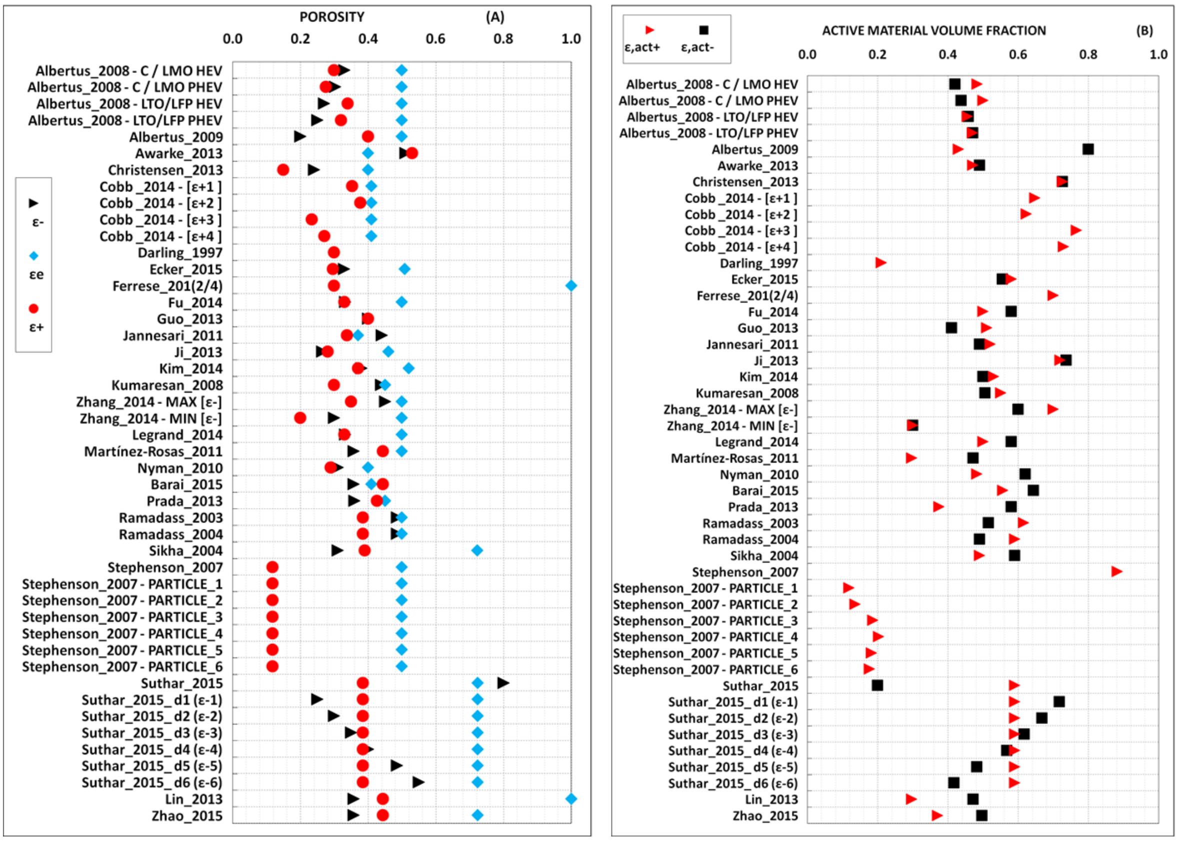

Figure 27 – The porosity and the active material volume fraction are reported in (A) and (B), respectively.

3.8. Dimensionless parameters

Finally, all the parameters found in literature (Table 18) and reported in the previous chapters, are converted in the dimensionless parameters use in the model reported in § 2.3.2.

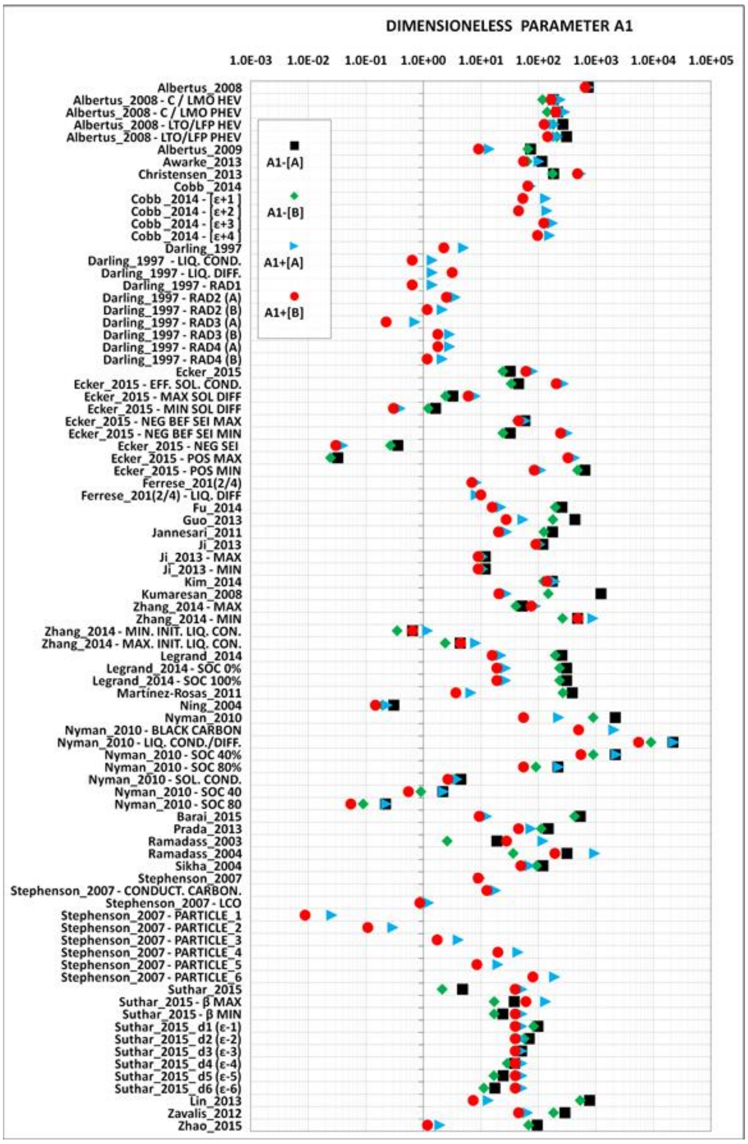

Figure 28 – The parameters A_1 are reported using both relation described by Eq. 63 and Eq. 64 .

The first parameter illustrated in Figure 28 is A_1 associated to electronic conductivity. Two values for each electrode are calculated because the effective electronic conductivity can be calculated using:

$$\sigma_{eff,+} = \sigma_+ \varepsilon_+ \tag{Eq. 63}$$

or

$$\sigma_{eff,+} = \sigma_+ \varepsilon_+^{\beta_+} \tag{Eq. 64}$$

The same equations are obtained for the negative electrode by substituting the subscript $+$ with the subscript $-$. Since some authors uses eithers Eq. 63 or Eq. 64, we decided to calculate both. As we can see, the calculation mode influence can be neglected compared to the range of variation for A_1 from 1 to 1000, in most of the cases.

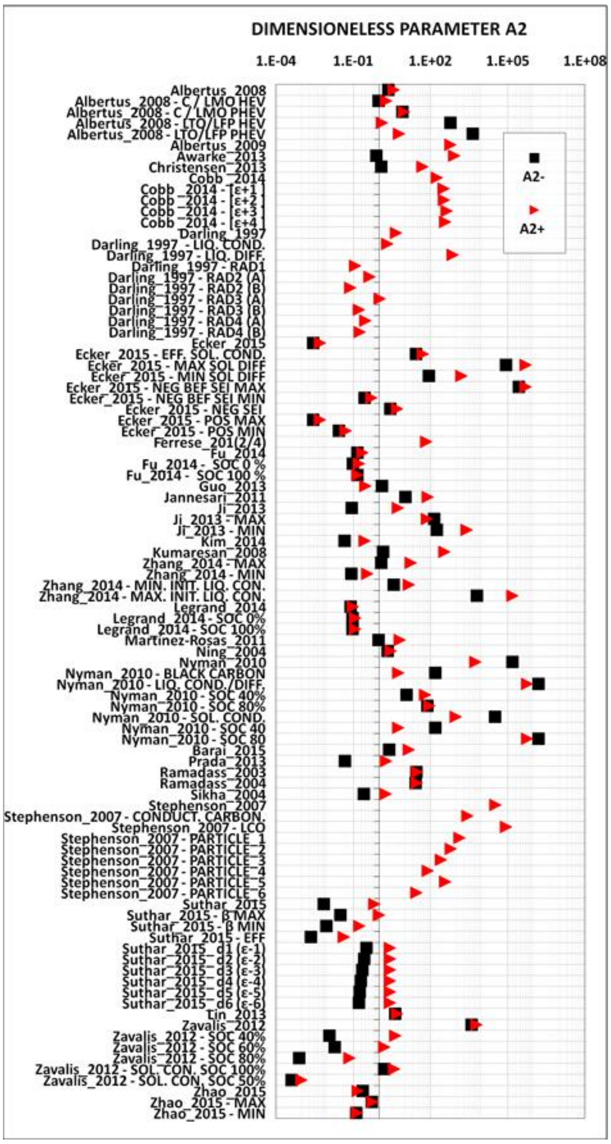

Figure 29 – The dimensionless parameter A_2 associated to solid phase diffusivity is reported.

The dimensionless parameter A_2 associated to solid phase diffusivity is reported in Figure 29. Many authors, focus their studies on “half-cell” configuration, and consequently more values are available for the parameter associated to positive electrode A_{2+}. However, the negative electrode is usually the graphite but a large variation on A_{2-} of 4 to 5 orders of magnitude can be observed.

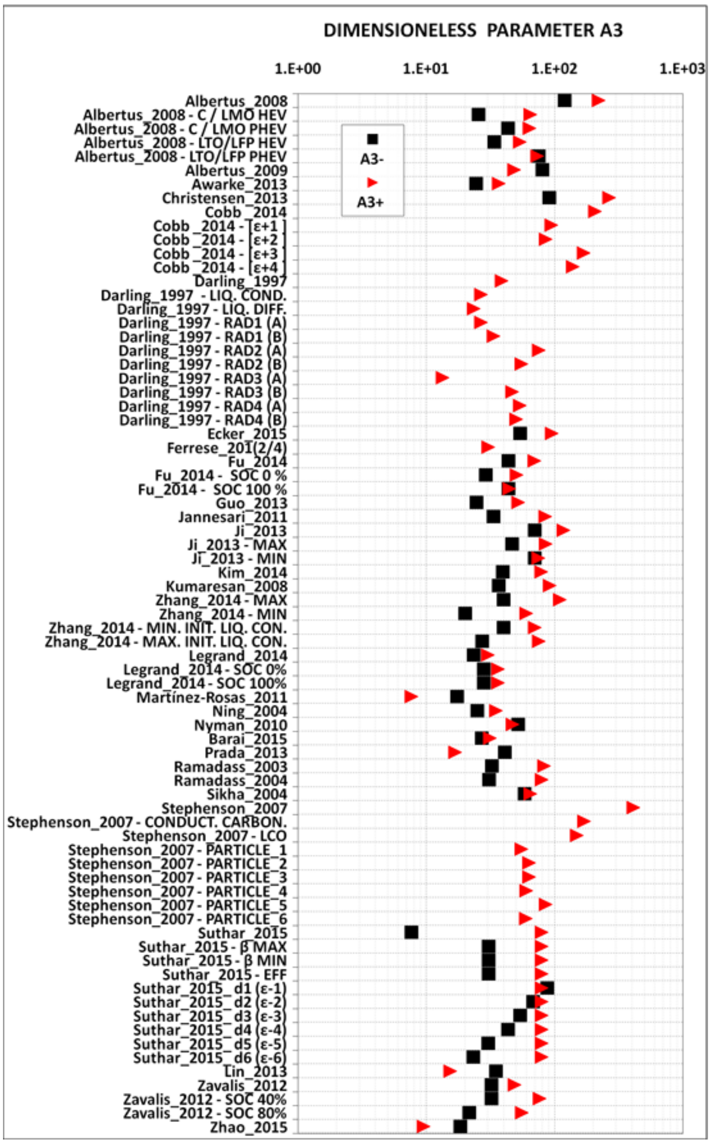

Figure 30 – The dimensionless parameter A_3 is associated to the amount of active material in the electrode.

The dimensionless parameter A_3, reported in Figure 30, is associated to the amount of active material in the electrode. For this parameter, there is a small dispersion, since the dimensional parameters that defines A_3 are close in the literature.

The dimensionless parameter A_4 associated to reaction rate kinetics is reported in Figure 31. The values are found in a wide range, but they are surprisingly extremes, i.e. very large or very small.

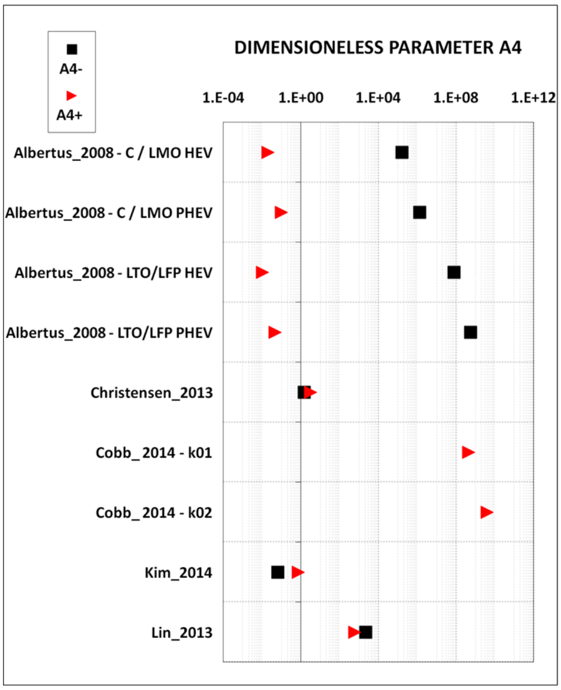

Figure 31 – The parameter A_4 is associated to the kinetic reaction rate.

Finally, the remaining parameters A_5, A_6, A_7, A_8 are reported. They mostly deal with the properties of the separator and they are concentrated in a small range from 1 to 0.1.

In conclusion, the parameters with large dispersion are A_2 then A_1. Instead, the parameters A_5, A_6, A_7, A_8 and A_3 are closer. The parameter A_4 is affected by the lack of measurement of the kinetic constant rate, that justifies the 12 orders of magnitude of variations between the references.

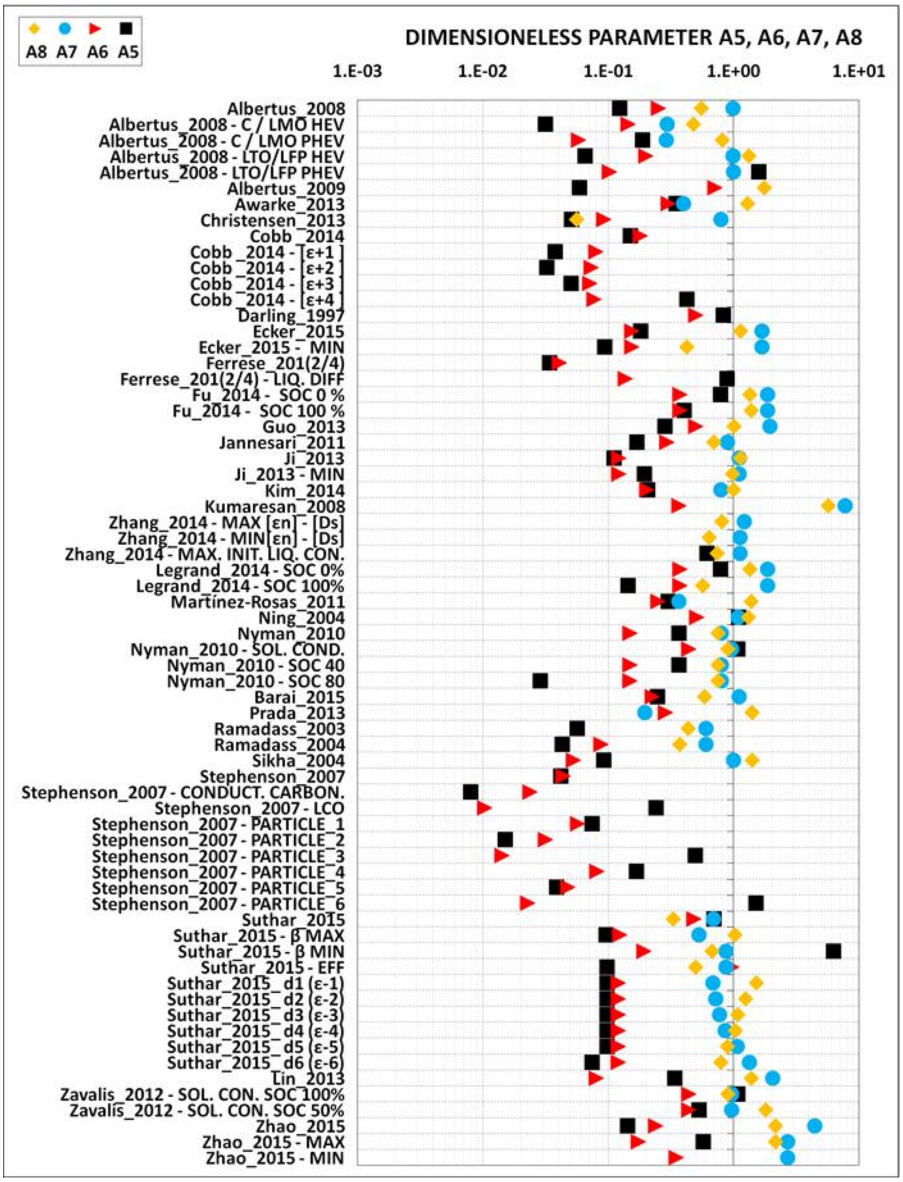

Figure 32 – The parameters A_5, A_6, A_7, A_8 are reported.

3.9. The ageing effect on parameters

Some considerations on the evolution of the parameters because of the battery degradation are reported in this section. Considering the difficulties, to properly measure the parameters for a fresh cell, it seems logical that for aged cell, it would be even more complex because of the cell history and considering the different mixed aging conditions[191]–[194]. However, some qualitative trend can be considered by resuming the studies on aging available in literature. In fact, the degradation affects: the capacity fade (i.e. State-Of-Health reduction) and the ohmic drop (i.e. rising of internal resistance).

Capacity

The capacity decreases because of:

- Lithium losses. Consequently, the stoichiometry of the electrodes at the charged and discharged state of the complete cell shift [108], [195]–[197]. This may be attributed to:
    - The deposition of lithium in metallic or lithium metal plating over the negative electrode surface. This lithium will not likely participate anymore to intercalation reactions. Furthermore, these depositions create very dangerous safety issues;
    - The SEI growth. The reactions between the negative electrode and the electrolyte creates compounds tramping the lithium in the structure. These compounds may affect the electrodes porosity by filling up the pores and reducing the active surface, creating an insulating barrier between the solid and electrolyte interfaces[198], [199]. Consequently, the reaction rate kinetics will be affected, and a reduction of its value is observed most of the time [20], [200];
- Loss of the active material/Loss of hosting capacity [115], [201]. This may be attributed to:
    - Dissolution of the chemical elements constituting the active material;
    - Structural degradation or irreversible phase changes due to high insertion of lithium (overcharge) or poor insertion of lithium (under-discharges);
    - Particle’s isolation because of side reactions between the binder and the solvent of the electrolyte [202];
    - The particle cracking due to mechanical stress generated by the lithium swelling during the intercalation process[75], [86], [114];
    - The active material delamination due to reactions of the electrolyte during the SEI growth. This may generate the expansion of gasses in the active material structure leading to exfoliations.
    - Underutilization of the active material because of the drift of the stoichiometry [203]–[206]. The discharge may be limited at the beginning by the negative electrode but later by the positive electrode as a consequence of the negative electrode degradation[201].

Internal resistance and impedance

The internal resistance (i.e. the ohmic drop during current loads) or the impedance (applying alternating signals of currents) increases (or impedance). This may be the consequence of a sluggish diffusion of lithium in active material [207] and in the electrolyte [84], [93], [166], [208]–[210]. The conductivity decreases as well in the electrolyte and in the solid matrix [197], [211]. This may be attributed to

- Passivation films at the active particle surface (SEI);
- Lower active surface due to SEI growth and lithium plating [212];
- Loss of electrical contact between the particles (side reactions between the electrolyte and the black carbon, cracking and fracture in the particles and in the porous matrix).
- Reduction of concentration of Lithium ions in the liquid phase at the equilibrium [199].

Many of these hypotheses are still object of intense research and studies, for this reason the simulations in § 6 will be focused in situations where the smaller number of parameters can influence the results to obtain general rules. The analysis of the literature conducted in this chapter allowed to estimate the approximative value expected for each parameter (for either in dimensional and dimensionless model) and not only which one is accurately measured, but also how they depend from other variables such as temperature, local concentrations and their evolution during time (ageing and degradation).

In conclusion, the parameters found in the literature are in some cases poorly measured and in most cases assumed or fitted. Thus, further researches are required to understand how the measurements (e.g. theoretical approximations, testing conditions, instruments and methods) should coherently connect the parameters used in the electrochemical models (e.g. Newman's model).

The next chapter is focused in the determination of the performance of the cells by optimizing the protocols and the identification of some parameters (e.g. electrode's thicknesses, compositions, particle's radii) that are useful for the simulations of commercial LGC MH18650 cells.

4 Electrical and physicochemical characterizations

In this chapter the electrical and physicochemical characterizations of the cell are detailed. The openings and the chemical analysis are conducted by Renault's experts. The devices used to perform the electrical tests are constituted of 3 battery cyclers able to perform impedance spectroscopy and deliver currents up to 20 A for a total of 72 channels from Bio-Logic Instruments® and 6 climatic chambers from different suppliers. In the climatic chamber, shown in Figure 33, it is illustrated how the cells and the electrical harness are arranged during the tests.

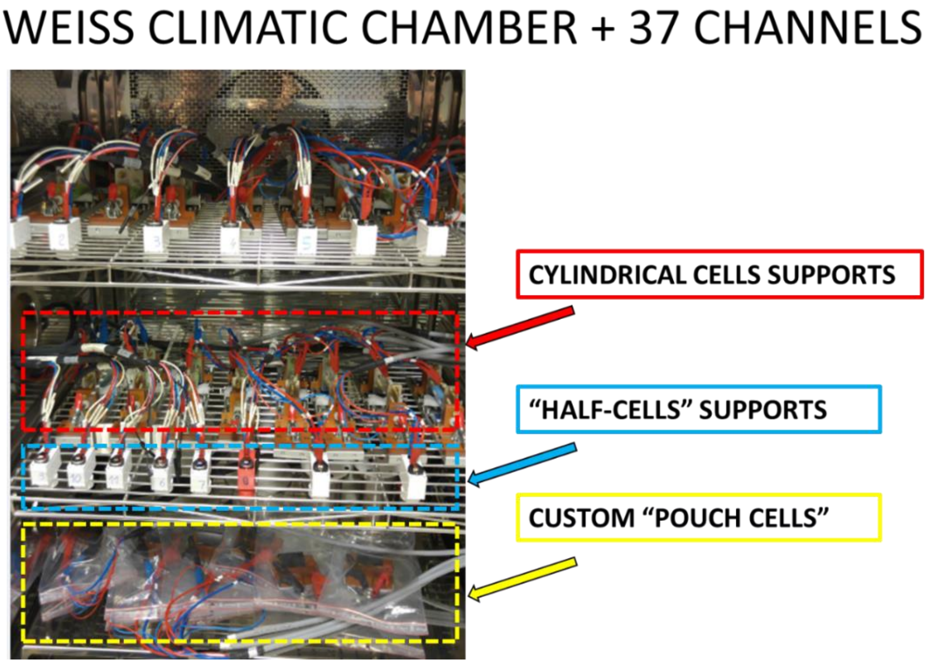

Figure 33 – The picture shows a Weiss® secured climatic chamber having 600L of volume. The different cell supports are provided from Arbin Instruments® for the cylindrical cells while the "coin" shape cells are made in-house via 3D printers.

4.1. Electrical characterization

Electrical tests are required to assess the battery performances and comparing it with the simulations. Before entering in the details of the testing procedures and protocols, the concepts of rated current and rated capacity are introduced.

The rated current is indicated with "xC", where x is a real number. This value represents the theoretical current required to completely discharge the cell in 1/"x" hours. Thus, the measured capacity at the end of the discharge is called the rated capacity. Furthermore, for a discharge current “small” [1] enough, the rated capacity is indicated as the nominal capacity and the voltage during the discharge is close to OCV.

The rated capacity is then normalized using the nominal capacity as reference, defining the DOD: a real number varying between 0 and 1. Consequently, this method is used to benchmark cells having different capacities, different chemical compounds or manufacturing processes.

In the next sections the reproducibility of C-rate characterizations and the cell voltage behaviour are discussed.

4.1.1 Reproducibility analysis of a test protocol for galvanostatic discharges

The purpose of this procedure is to guarantee the reproducibility of the measured voltage and rated capacity during galvanostatic discharges. The correct protocol is attained after two failure attempts described in the followings.

Accelerated C-rate Characterization Protocol

In Figure 34 is reported the applied current profile to characterize the C-rate capability for a commercial cell having the voltage cut-off reported by the manufacturer between 4.2 V and 2.5 V. After the galvanostatic charge, once the upper cut-off voltage is reached, the charge continues with a constant voltage until the cut-off current to 50 mA is reached, as reported in the datasheet. The overall test time is shortened by setting the charge and discharge at the same C-rates and the rest time limited to 30 minutes.

The test is repeated twice for the cell n°01. After the first test the cell is degraded by 0.69 %, as a consequence the time duration to complete the test is reduced from 92h to 90h.

---

[1] The current applied for discharge the cell can be considered “small” when the measured capacity is reasonably equal to the measured capacity obtained with a smaller current and the polarization can be neglected. As an example, we suggest a C-rate smaller than C/24 inducing a polarization, when the current is switched on, smaller than 5mV

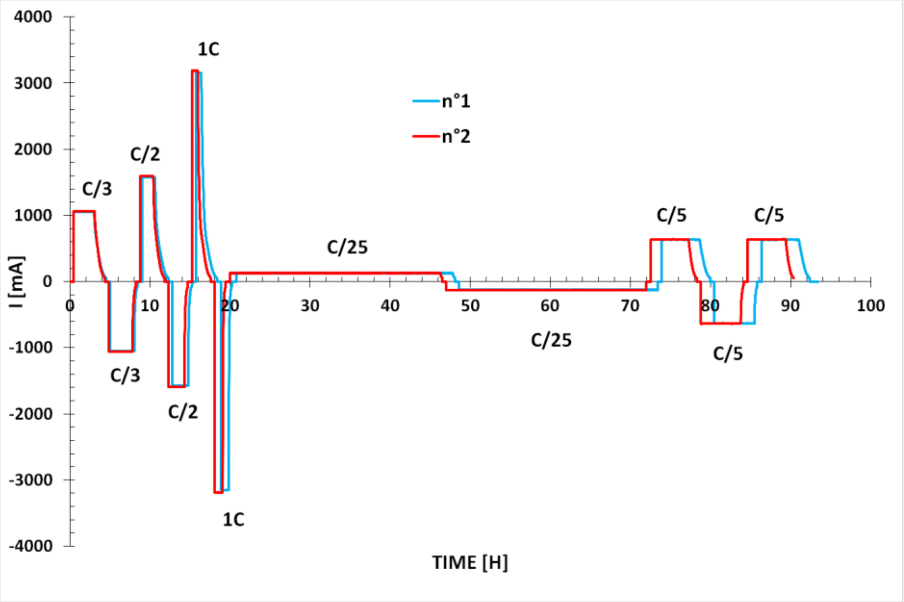

Figure 34 – The picture reports the current profile in mA and the expected test duration in the abscises for the cell n°01 and 25°C the test n°1 in blue is for the fresh cell and in red is reported the test n°2.

The test showing the discharge voltage as a function of the capacity for different C-rate is reported in Figure 35.

As the capacity rated at C/25 is lower than the capacity rated at C/5, that is not physically possible, because the rated capacity at lower rate is inferior than the capacity rated for a higher rate. In conclusion, the protocol applied is not satisfying and the results are not accurate enough.

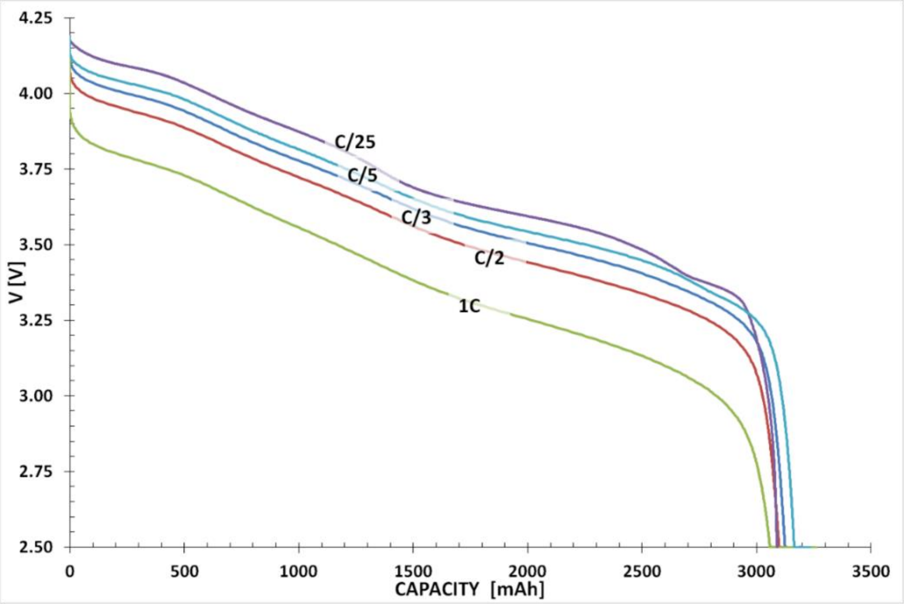

Figure 35 – The discharge voltage as a function of the capacity for different C-rates is reported for the test n°1.

Homogeneous C-rate Characterization Protocol

The next protocol reported in Figure 36, based on the experience of the previous protocol reports more coherent rated capacities. For the C-rate capability in charge, the discharge rate is fixed to C/3 while for the C-rate capability in discharge the charge rate is fixed to C/3, for symmetry.

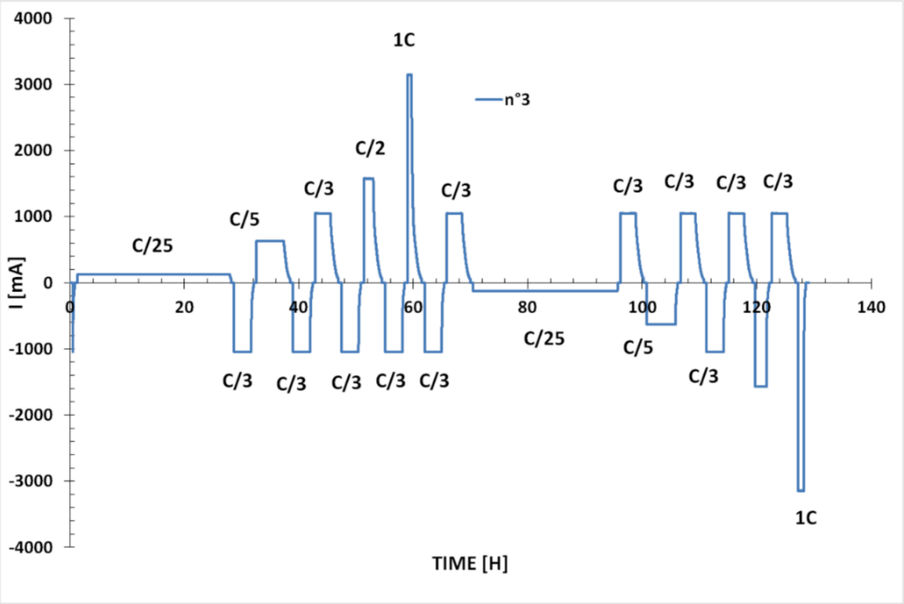

Figure 36 – The picture reports the current profile in mA and the expected test duration in the abscises for the test n°3 of the cell n°01 performed at 25°C. The test protocol uses a fixed discharge rate to C/3 for the charge rate characterization and a fixed charge rate to C/3 for the discharge rate characterization.

Thus, the discharge voltage as a function of the capacity for different C-rate is reported in Figure 37. The results are more accurate because the capacity measured behave as expected with the higher quantity of charge measured at lower discharge rate. However, as discussed just below, the dispersion in terms of ohmic drop is still elevate and consequently even this protocol is not satisfying.

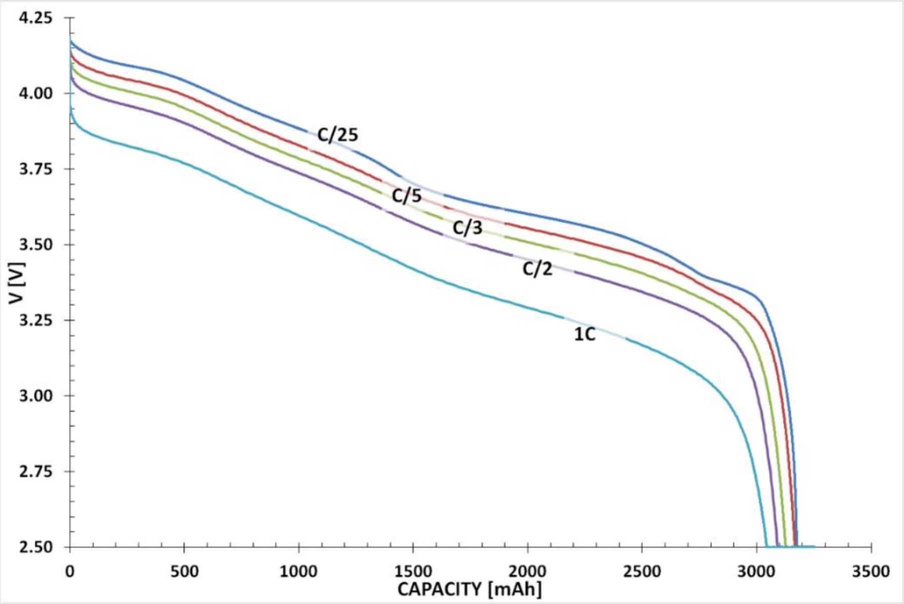

Figure 37 – The discharge voltage as a function of the capacity for different C-rates is reported test n°3.

In fact, the test is repeated twice and the discharge voltages at 1C rate are reported in Figure 38. The rated capacities are very close, but the ohmic drops are still different. In fact, the lithium ions batteries, like most of the batteries, are influenced by their load history[213]. This behaviour is mitigated with the protocol proposed in the next section.

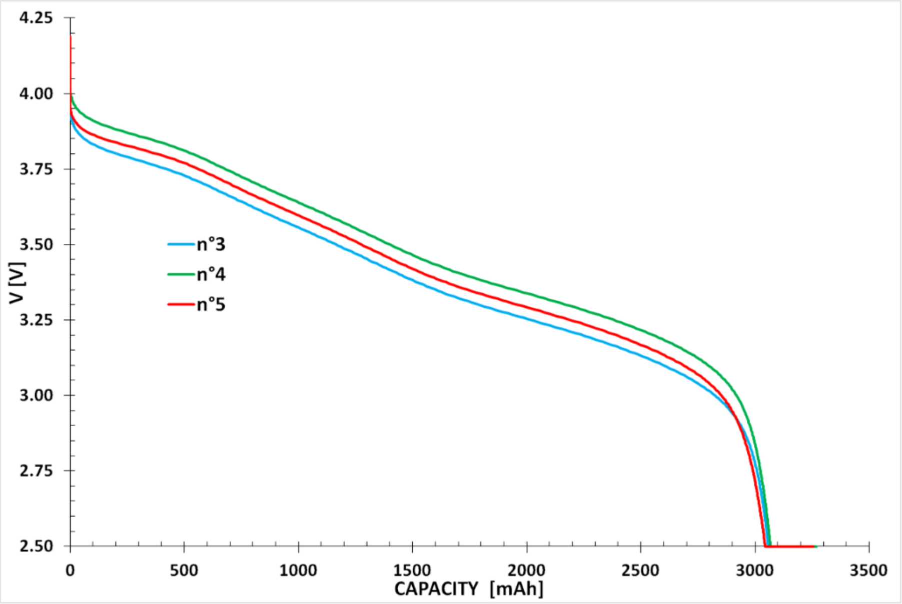

Figure 38 – The discharge voltage as a function of the capacity for 1C rate is reported test n°3, n°4 and n°5.

Optimized C-rate Characterization Protocol

The most accurate C-rate characterization protocol is finally reported in Figure 39. Thus, the 5 steps constituting the protocols are reported:

- Step 1 – The initial rest period ensures the stabilization of the cell temperature is stabilized and the initial equilibrium of the battery;
- Step 2 – Charge-discharge sequences at C/3 are reproduced 4 times to stabilize the capacity. In fact, after long rest periods a fluctuation in the rated capacity can be found;
- Step 3 – The nominal battery capacity is measured at C/12 using the Battery Capacity Determination feature implemented in Bio-Logic® Instrument;
- Step 4 – The battery is charged at C/3 till 4.2 V followed by a constant voltage charge until the current drops to 50 mA. Then the cell is discharged at “x”C-rate (where “x” stands for the C-rate that we want to characterize during this test);
- Step 5 – A loop of 3 charge-discharge sequences at C/3 is performed to reset the battery “history”. After, the protocol is set back to Step 4 for 4 times. Finally, the sequence is repeated for 2 times from the beginning.

Between each step, the pause ends when the voltage variation is smaller than 1mV per hour. In the most favorable condition, such as after a slow C-rate, the pause duration is 1 hour.

The discharge cut-off voltage is set to 1.75V for these cells that are usually limited to 2.5 V.

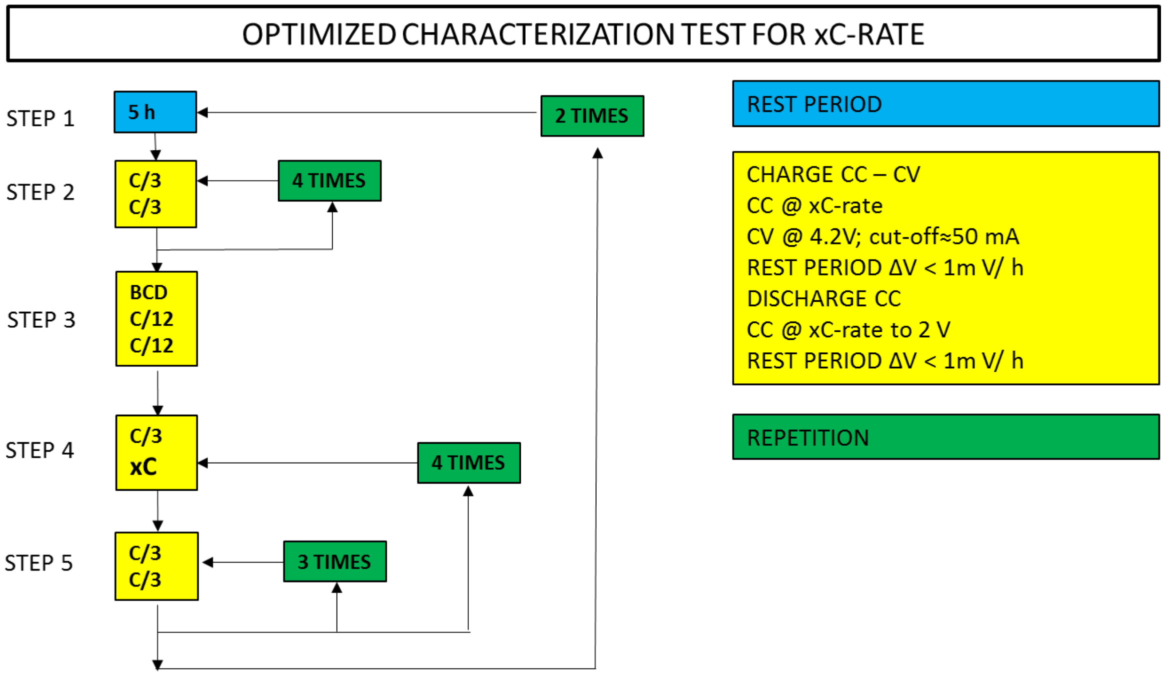

Figure 39 – The optimized characterization test *per* xC-rate is reported. The amount of time required to characterize the cells at 1C-rate is approximately 450 hours.

The results in Figure 40, shows the excellent stability and the rated capacity is almost unchanged for the following C-rates: C/3, C/2, 1C, 2C and 3C. This test is repeated 5 times for the same cell n°28 at 25°C. Furthermore, the cell shows an initial voltage dip when the cell was tested (i.e. 24 months after the reception of the cell's batch). This behaviour was not observed when the batch of cells was received.

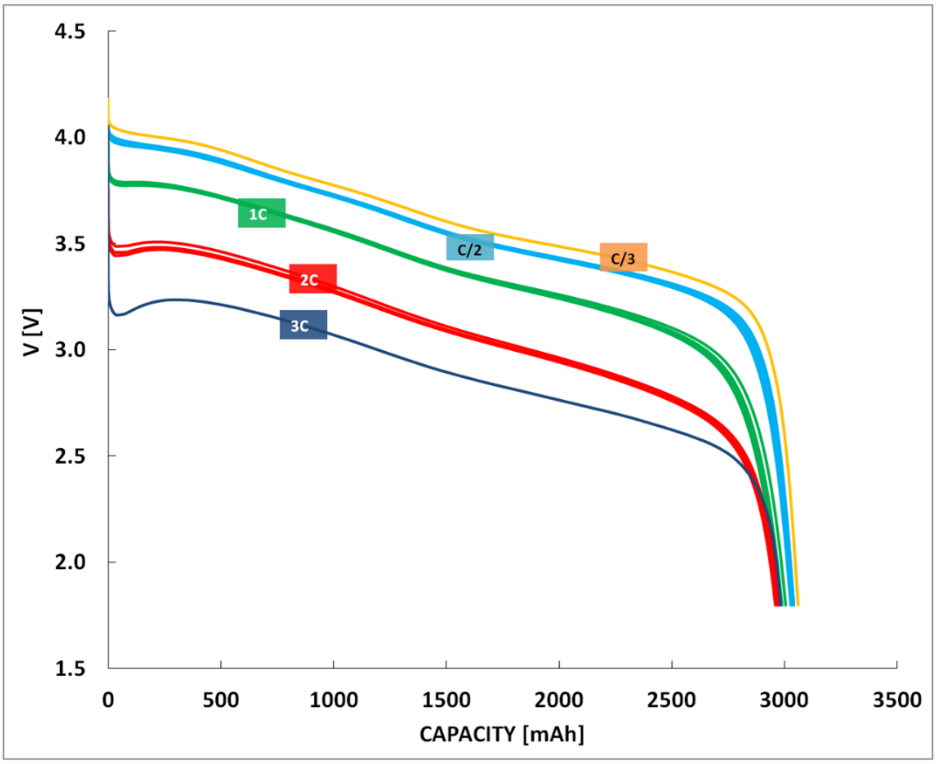

Figure 40 – The discharge voltage as a function of the capacity is reported for different C-rates: C/3, C/2, 1C, 2C and 3C. The cell is the n°28 tested for the first time 24 months after the reception at 25°C.

Very small variations in the rated capacity are appreciated:

- the rated capacity at C/2 is 2.5 % ± 0.4 % smaller than at C/12;
- the rated capacity at 1C is 3.9 % ± 0.8 % smaller than at C/12;
- the rated capacity at 2C is 4.3 % ± 1.7 % smaller than at C/12;

In conclusion, higher is the C-rate and larger is the spread of measured capacity and lower is the rated capacity.

The electrical characterizations described in the next chapter were realized before the validation of the test described here. Consequently, the rated capacity may be not extremely accurate, but the results and the conclusions are qualitatively effective.

4.1.2 Voltage dip during galvanostatic discharges

A curious voltage dip at the beginning of the discharge is investigated during these tests, from two different manufacturers (i.e. Panasonic and LG Chemical), depending of C-rates, Temperatures, SOC and SOH. According to the manufacturer’s datasheet of LG-Chemical cells, the maximum current the cell can sustain continuously is 10 A (i.e. ~3.5C), while in these tests, currents up to 19 A are applied. The sequence of the C-rate profile is schematically reported in the Appendix 8.7.

Purpose of this protocol is to assess the cell performances from 1C to 6C, where high kinetic limitations occur. Indeed, simulations below 1C where performed during a previous project by Safari 2011 in partnership with Renault [12].

The discharge voltage is reported at 25°C in Figure 41 (A) and then at 0°C Figure 41 (B) for cell n°26 at BOL. However, at lower temperature, the formation of a characteristic voltage is observed as the current rate increases. In both cases the rated capacity is inversely proportional to C-rates, which is more pronounced at low temperature, as expected. Furthermore, at low temperature the voltage is distorted because of major kinetic limitations (i.e. combination of diffusion, migration and charge transfer).

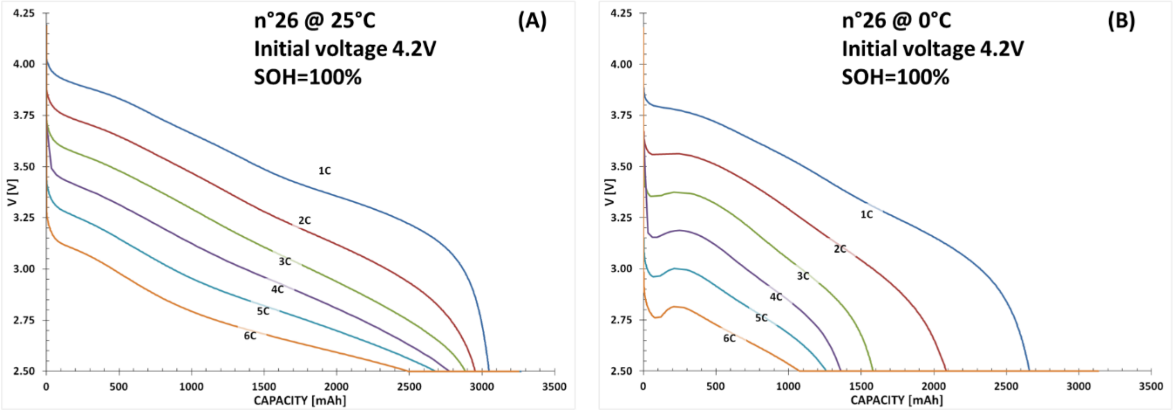

Figure 41 – The cell n°26 is tested at BOL at 25°C (A) and 0°C (B). The discharge voltage as function of the quantity of charge is reported. The end of charge voltage is 4.2 V.

Cell n°01 is cycled at C/10 at 25 °C from 4.2 V to 2.5 V for 30 days, reducing the SOH to 97 %. The cell is then characterized at 25°C between 4.2 V and 2.5 V,Figure 42 (A), evidencing a voltage dip at the beginning of the discharge at 4C, 5C and 6C rates. The test is then performed between 3.9 V and 2.5 V, Figure 42 (B), but in this condition, the voltage dip is not observed.

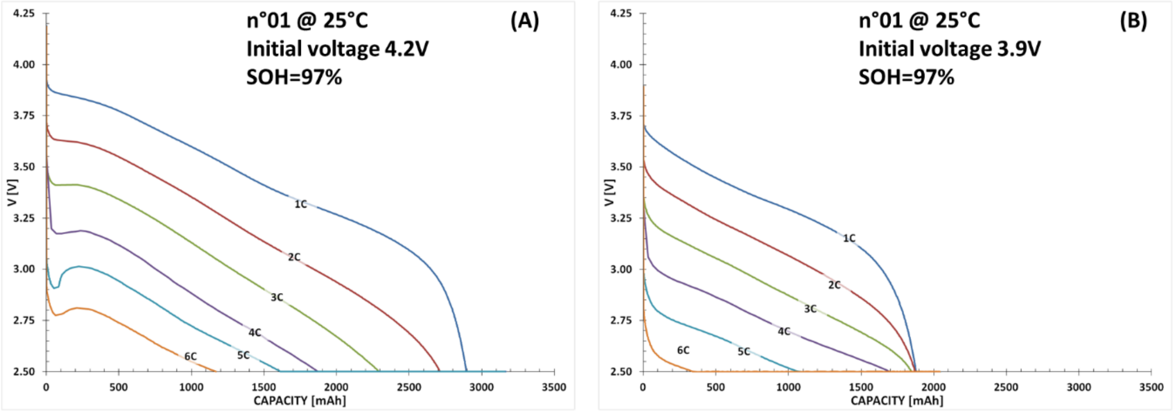

Figure 42 – The cell n°01 is tested at 97 % of SOH at 25°C, using and end of charge voltage of 4.2 V (A) and 3.9 V (B). The discharge voltage as function of the delivered quantity of charge is reported.

The cell n° 12 is characterized at BOL & 0°C, from 4.2 V to 2.5 V Figure 43 (A) and from 3.9 V and 2.5 V in Figure 43 (B), observing the voltage dip only in the first case.

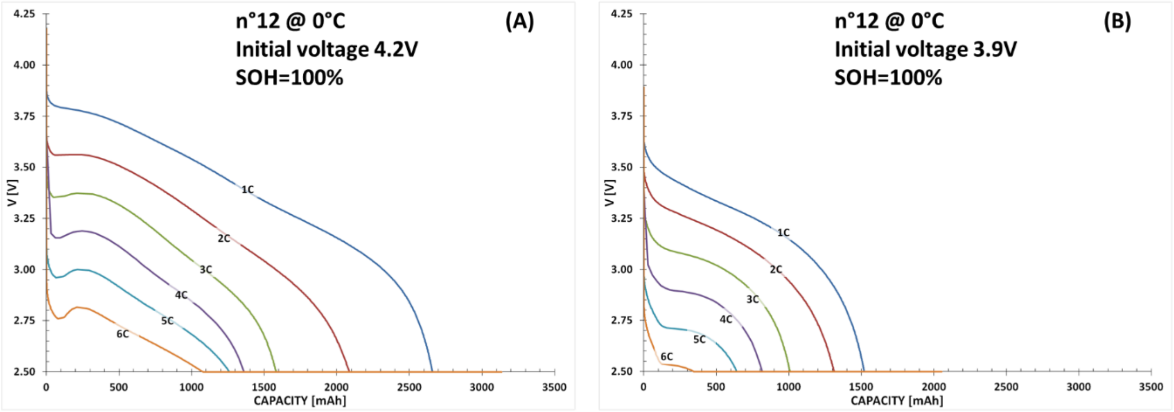

Figure 43 – The cell n°12 is tested at BOL at 0°C, using and end of charge voltage of 4.2 V (A) and 3.9 V (B). The discharge voltage as function of the delivered quantity of charge is reported.

In conclusion, both SOC and SOH influences the voltage dip at the beginning of the discharge more than temperature or kinetic limitations in contrast with the conclusions found in literature [214]–[216]. The initial voltage dip is known in lead acid batteries as “coup-de-fouet”, but is not extensively investigated in lithium ion cells [217]–[223]. This phenomenon can be attributed to the terms of concentration observed in the Butler-Volmer relationship (cf. Eq. 11, Eq. 12). However, more detailed studies are required to understand this behavior.

4.1.3 Galvanostatic discharge to 0.05 V

In this section is studied the behaviour the cell discharge using a lower cut-off voltage than the usual values set to 2.5 V. In fact, the voltage knee (evidenced in the red dashed circle in Figure 44) at the end of discharge is not observed for rates higher than 2C, as seen in Figure 41 and Figure 42, when the cut-off is limited to 2.5 V [217]. For this reason the end of discharge voltage cut-off is set to 0.05 V to observe the voltage knee and the related degradation.

The current profile in term of C-rate and the synthetic sequence are reported in Appendix 8.8.

In order to compare the discharge rates, the charge conditions are the same. The discharge voltage as a function of charge is reported in Figure 44, for the following discharge rates: C/25, C/10, C/3, C/2, 1C, 2C, 3C, 4C and 5C. The rated capacity at 5 C is 93.75 % of the capacity measured at C/25, indicating the presence of kinetic limitations. However, the voltage knee proving the end of discharge is observed, we suggest reducing the end of discharge cut-off voltage to measure the rated capacity at high C-rates. In literature is reported that at low voltages the electrolyte oxidation and structural degradation may occurs [224]. However, this condition is maintained in the proposed test protocol only for a short time. In literature similar tests was reported by Broussely 2005 where the SAFT VLE 45 Ah cell was discharge to 0.7 V [225].

In conclusion the rated capacities measured with a cut-off of 0.05 V are very close of the rated capacities evaluate with a cut-off of 1.75 V. Meanwhile, the degradation with a 1.5 V cut-off should be smaller than a 0.05 V cut-off.

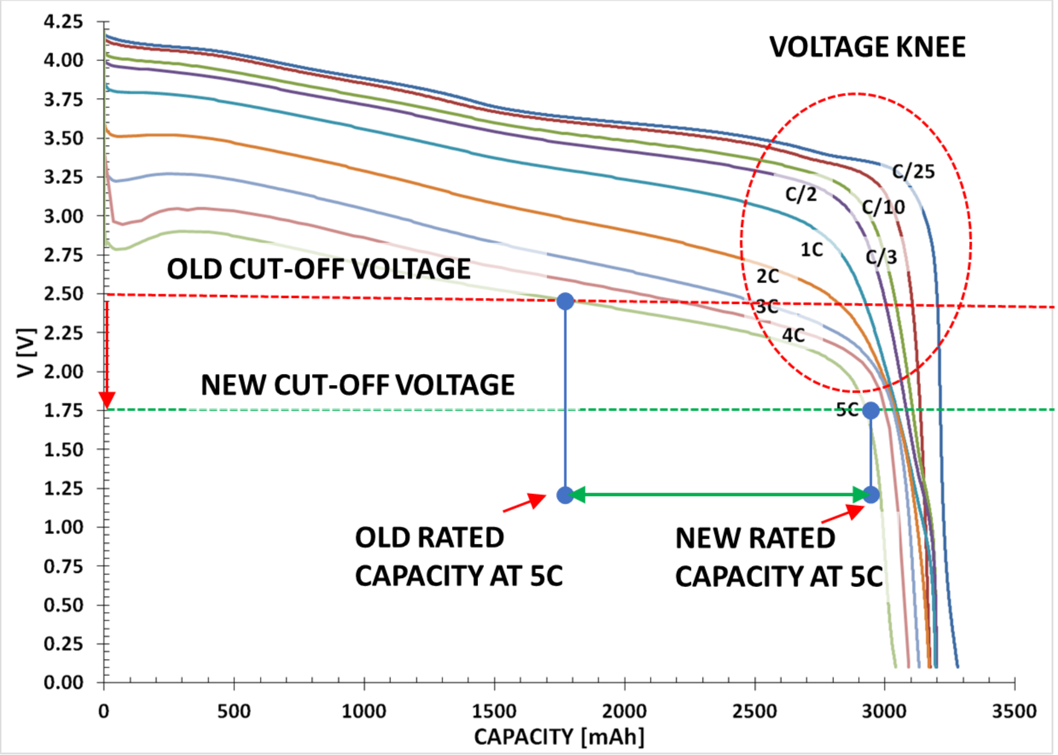

Figure 44 – The discharge voltage as function of the capacity is reported for different C-rates when the cell n°31 is discharged to 0.05 V. The red dashed circle indicates the voltage knee at the end of the discharge. The dashed lines indicate the old cut-off voltage at 2.5V and the new cut-off voltage at 1.75V respectively. The green arrow indicates the rated capacity at 5C with the old cut-off voltage and the new cut-off voltage respectively.

The rated capacities are calculated at the intersection between the discharge voltage and the cut-off voltage (dashed lines). The red dashed lines indicate the old cut-off voltage at 2.5 V while the green dashed line indicate the new cut-off voltage at 1.75V. It is evident that the new cut-off guarantees a higher rated capacity at the end of the discharge and the voltage knee. The general study conducted in § 6 evidences that are dominant kinetic limitation can be attributed to electronic limitations in these LG cells.

This protocol is repeated 4 times to assess the battery SOH measured with the capacity measured at C/3 as reported in Figure 45, respectively. Moreover, the degradation accelerates after each test of 0.6 %, 0.7 % and 1 %. Obviously during a prolongated cycling at this low voltage, the degradations may be enhanced[30], [213], [226], But it is not investigate because the test aim only to characterize the C-rate.

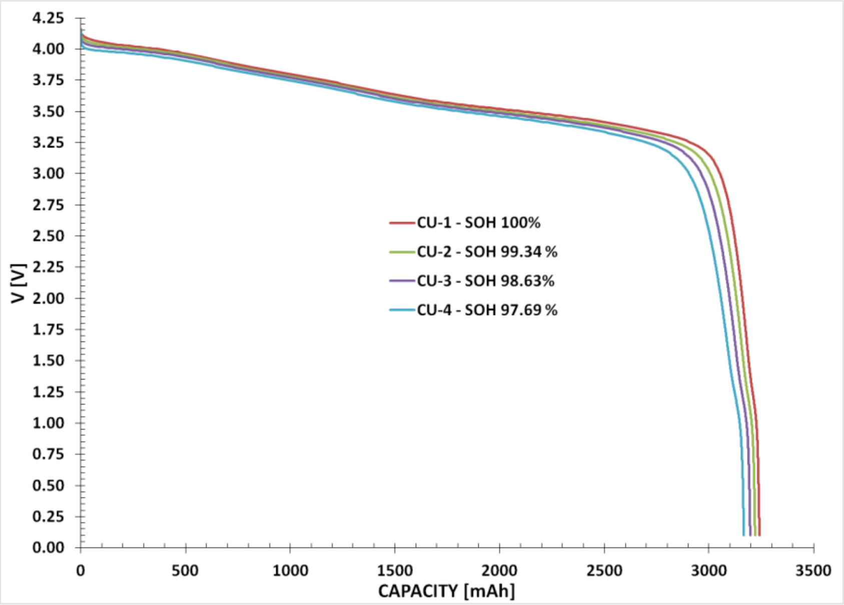

Figure 45 – The discharge voltage is reported as a function of the capacity for the C/3 discharges used to calculate the battery capacity before each test sequences. The state of health is reported and calculated using the first rated capacity at C/3 as reference.

In conclusion, if the voltage knee is not observed, then the cut-off voltage should be reduced if this procedure doesn’t affect significantly the degradation. This procedure is helpful for the understanding of kinetic limitations, improving the modelling and investigates the electrodes chemistries. The objective of chapter xxx is to investigate the characteristics of this abrupt potential drop that is usually observed when the battery is close to the end of discharge.

4.2. LGC INR18650MH1 chemical characterization

The cell is opened to characterize compounds and chemistries to obtain useful parameters (e.g. electrode thickness, particles size, porosity, etc.) for the simulations.

<u>Radiography (X-Ray)</u>

The radiography is an imaging technique using electromagnetic radiation to observe the internal structure of an object. This non-destructive technique is used to measure the dimensions of the electrodes and prevent the electrodes short circuits during the opening of the cell steel case opening. In Figure 46, the radiography on LGC 18650 cells is reported and the components such as security cap, the negative electrical tab connection and the rolling tube are shown.

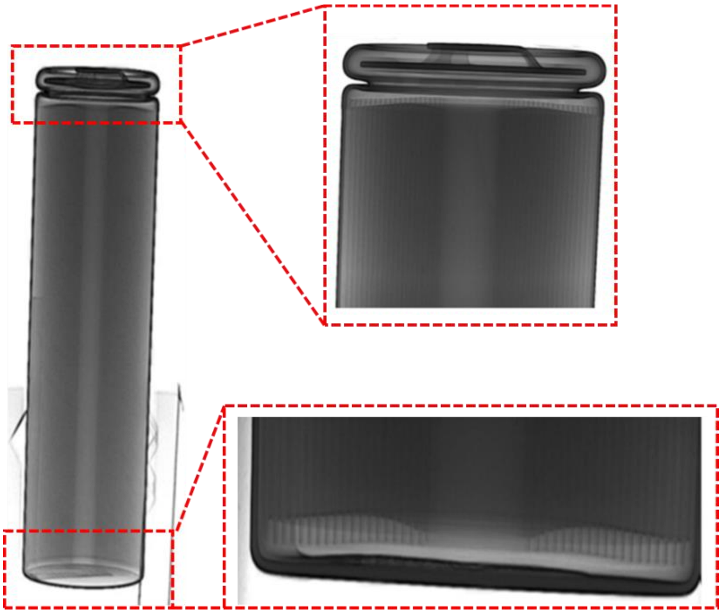

Figure 46 – The X-ray radiography of the LGC INR18650MH1 shows the details of the vent tap and the bottom of the negative tab side.

Cylindrical Cell Case Openings

The bottom of the cell is catted with a mandrel and the negative tab connection is removed as reported in Figure 47. During this procedure, the weight and thickness of the casing are measured and reported in Table 21. The amount of electrolyte in the cell is too small to be recovered.

Figure 47 – The cutting sequence with the successive measures of the casing thickness and weight are reported from the upper-left picture in clockwise order.

Dimensions MH18650	**mm**	**Positive Electrode**	**mm**	**Surface**	**mm^2**
Diameter	18.23	Inner Length	638	Inner	37004
Height	64.32	Outer Length	650	Outer	37700
Case Thickness	0.27	Height	58	Total	74704
		Collector Length	690	Collector	40020
		Negative Electrode	**mm**	**Surface**	**mm^2**
		Inner Length	677	Inner	40620
		Outer Length	621	Outer	37260
		Height	60	Total	77880
		Collector Length	690	Collector	40020

Table 21 – Dimension and sizes measured for the positive electrode, negative electrode and separator. The surfaces are calculated.

Because of the cell rolling process the surface on each side of the electrodes has a different area, and the dimension of the separators are different. It's worth mentioning that the negative electrode surface is 3176 mm^2 higher than the positive electrode, suggesting that the amount of active material in this electrode is higher. Hence, the capacity in the negative electrode should be slightly higher than in the positive electrode. The mass of each component is reported in Table 22, where the electrolyte mass is estimated from the wet and the differences between dried components.
For this reason, the electrodes are dumped in a solvent and the obtained solution is analyzed with mass spectrometry to identify the composition, as reported in Table 25.

Weight	***grams***
Casing	8.27
Positive Electrode (double coating)	17.39
Positive Current Collector (Aluminum)	2.01
Negative Electrode (double coating)	10.63
Negative Current Collector (Copper)	3.82
Separator # 1	0.90
Separator # 2	0.78
Total	43.80
Total MH18650	46.81
Electrolyte	3.01

Table 22 – Resume the weight for each component.

Optical microscope

The optical microscope uses the visible light and a system of lenses to magnify the samples and capture the images. This instrument is used to measure the thicknesses of the electrodes and the radii of the active materials particles. In Figure 48 and Figure 49 are reported the pictures of the electrodes and the separator, respectively.

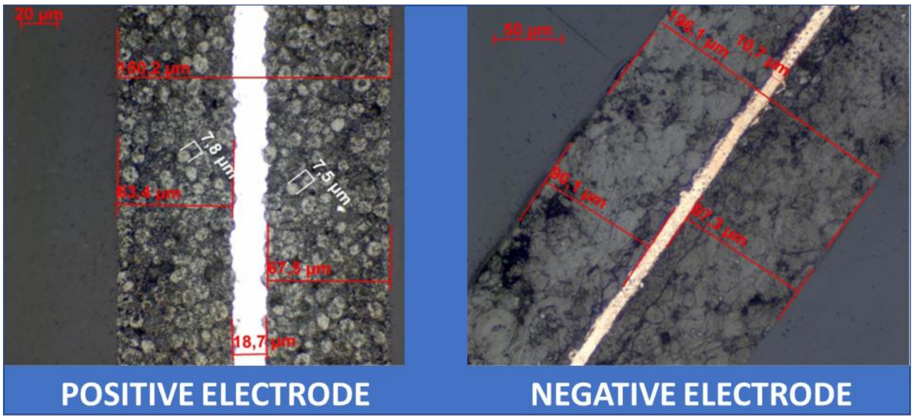

Figure 48 – The images shows the sizes of the double coating electrodes and the radii of the active material particles.

The thickness of the electrodes, their densities and the porosity are reported in Table 23. The porosity is calculated considering the density of the active material, the weight and the volume of the electrodes. Consequently, pore inclusions (i.e. pores where the electrolyte is in a confined space between the active material's particles) is not considered. The total thickness (double coating) of the positive electrode is ~7 time higher than its current collector while this ratio is ~17 for the negative side.

Positive Electrode	**µm**	**Densities**	**mg/cm^2**	**Porosity [%]**
Side # 1	63.4	One Side coating	23.7	22.19
Side # 2	67.5	Collector	4.38	
Collector	18.7	Collector + double coating	50.58	
Total	150.2			
Negative Electrode	**µm**	**Densities**	**mg/cm^2**	**Porosity [%]**
Side # 1	90.1	One Side coating	15.28	30.50
Side # 2	97.3	Collector	7.09	
Collector	10.7	Collector + double coating	37.64	
Total	196.1			

Table 23 – The thickness of the electrodes, density and porosity.

Between the separator and the negative electrode, an alumina layer (~3 µm) is observed. It is usually applied to prevent dendrites and consequently the short circuits.

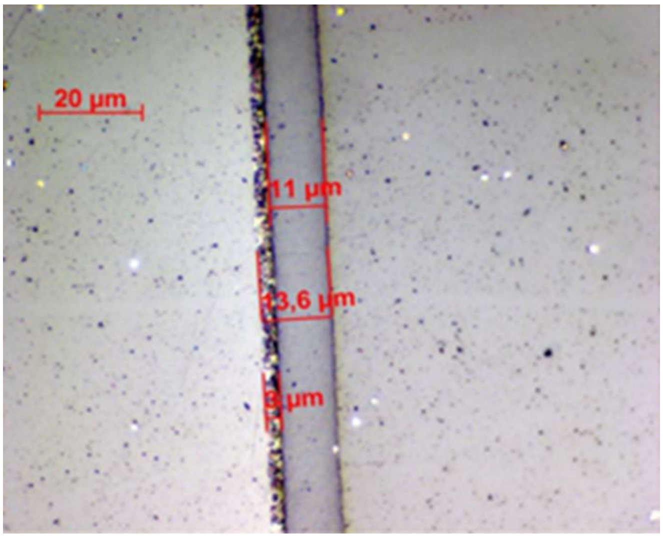

Figure 49 – The image show the thickeness of both separator and its alumina coating. The composition of the alumina coating is verified with the XEDS analysis.

Scanning electron microscope with X-ray microanalysis SEM/XEDS

A scanning electron microscope (SEM) is a type of microscope that produces images of a sample by scanning it with a focused beam of electrons. It is used to evaluate the sample's surface topography and composition, as shown in Figure 50, for the positive and the negative electrode respectively.

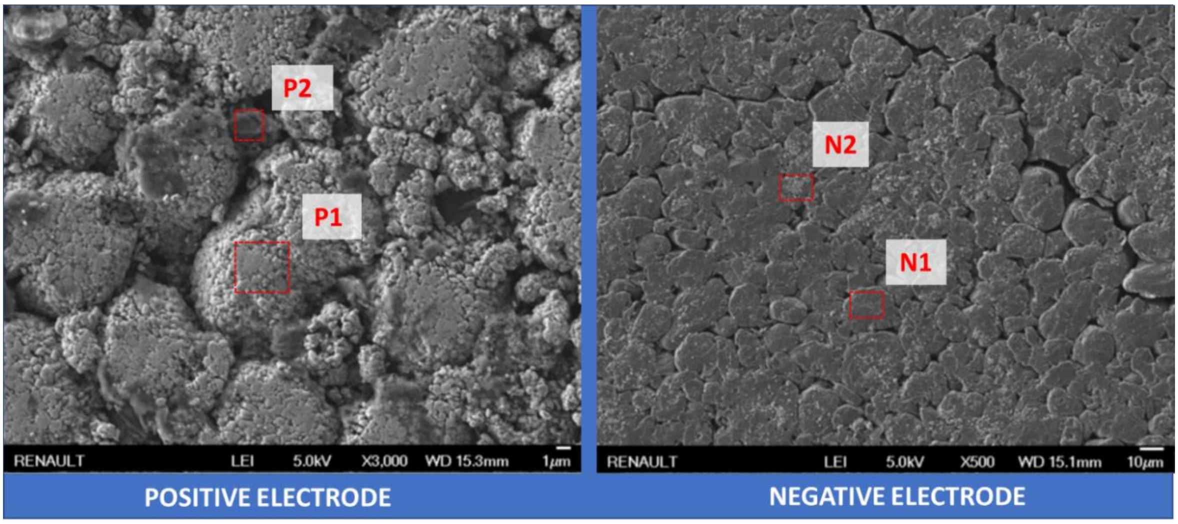

Figure 50 – The picture illustrates the electrodes surface morphology obtained with the SEM. The evidenced points are analysed with the XEDS in order to identify their chemical composition.

The size of the grains ranges between $10\ \mu m$ and $30\ \mu m$ for the negative electrode, while positive electrodes are composed of conglomerates of particles smaller than $0.5\ \mu m$ in macro-grains with sizes between $5\ \mu m$ and $15\ \mu m$. Consequently, we can estimate using the values reported in Table 23 the presence of 4 to 13 particles in the positive electrode thickness while there are 3 to 9 particles in the negative electrode thickness. In fact, the highest the number of layers of particles and the closer are the samples with the macro-homogeneous assumption in the Newman's model, as in this case each particle is equally supplied by electrons and reactants.

The point P1, in Figure 50 is analyzed with the XEDS and the signal is show in Figure 51 evidencing the presence of Nickel, Manganese and Cobalt (NMC). Other elements found in significate amounts are oxygen and calcium because of the carbonates formed during the reduction of the solvent.

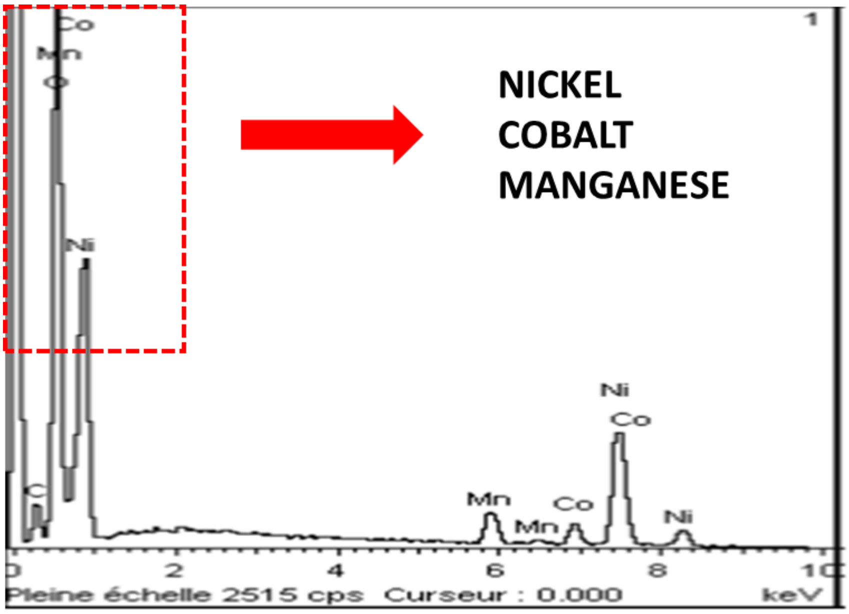

Figure 51 – The results of the EDS analysis over the sample P1 showing the presence of Nickel Manganese Cobalt. The x-axis indicates the applied energy in keV and the y-axis the reponse.

The XEDS in point P2 identifies black carbon that is used as conductivity enhancer. In point N1 is found high presence of carbon while in N2 is identified the aluminum, migrated from the alumina coating.

X-ray Diffraction (XRD) & X-ray fluorescence (XRF)

The samples of positive and negative electrodes are set to 2.5 V vs Li-Metal and to 1.5 V vs Li-Metal, respectively, before to be analyzed with the XRD. The results confirm the presence of the elements constituting the NMC for the positive electrode and carbon for the negative electrode. Traces of other elements, such as copper, are attributed to migration of atoms from the current collector.

The percentage of elements constituting the positive electrodes, suggest that the compounds is the NMC 811, as reported in Table 24.

Element	*Concentration [%]*
Nickel	56.2
Oxygen	18.0
Cobalt	7.04
Manganese	6.41

Table 24 - Composition of the positive electrode elements obtained with the XRF.

Conclusions

The results of the chemical characterization are resumed in Table 25.

Positive electrode	
Active compound	96 % Nickel-Manganese-Cobalt (NMC 811)
	Particle radius from 5 to 15 µm
Conductivity enhancer	2 % Carbon
Binder	2 % PVDF
Negative electrode	
Active compound	98 % Graphite
	Particle radius from 10 to 30 µm
Other	2 % CMC/SBR
Separator	
Composition	PE – High Density
Manufacturing	Wet process
Electrolyte	
Salt	LiPF6
Solvent	DMC, DEC, EC, PC
Additive	Trichlorobenzene (probably)

Table 25 – Resume of the chemical analysis

Finally, in Table 26, are resumed the parameters that are here measured and are later used for the simulations reported in Appendix 8.6.

	Summary of the physical parameters measured
$R_+ = 10\ \mu m$	Radii of the positive electrode active material's particles
$R_- = 20\ \mu m$	Radii of the negative electrode active material's particles
$d_+ = 65\ \mu m$	Thickness of the positive electrode
$d_- = 65\ \mu m$	Thickness of the negative electrode
$d_s = 11\ \mu m$	Thickness of the separator
$S = 750\ cm^2$	Total surface of the electrodes
$\varepsilon_{+l} = 22\ \%$	Positive electrode porosity
$\varepsilon_{-l} = 30\ \%$	Negative electrode porosity
$\varepsilon_{+s} = 75\ \%$	Positive electrode active material volume fraction
$\varepsilon_{-s} = 68\ \%$	Negative electrode active material volume fraction

Table 26 – The parameters measured in Renault and used for the simulations are here summarized.

5 Electrode balancing

In this chapter is studied how the shape of the isotherms influences the capability to estimate the state of lithiations in the electrodes at the charged and discharged state in the complete cell. They play a major role on the battery performances because the electrode balancing is affected and are not constant during the battery lifetime. This is one of the first task to be completed for the electrochemical model because it affects both OCVs and the parameters that are function of the state of charge, such as the solid phase diffusivity, as discussed in § 3. The states of lithiations are a non-directly accessible parameter in the complete cell. Thus, a method for their estimation is required. At the beginning of this study, two simple isotherms based on the Nernst law are considered and then by scaling up the complexity of the isotherms a method is proposed to evaluate the accuracy of the fitting process for the fresh and aged cells introduced in the previous chapter. The fitting method is applied to the identification of the stoichiometry in each electrode in the complete cell.

5.1. Introduction to electrode balancing

The electrode balance is usually reported in literature as the negative electrode (Q_-) and the positive electrode (Q_+) capacities ratio [227] . In addition, the electrode balance is also influenced by the state of lithiation in each electrode. When a fresh cell is assembled, the negative electrode is completely delithiathed and the positive electrode is lithiated. A new cell is assembled entirely discharged and the voltage is the lowest possible. Then, during the first charge, as it was discussed in § 1.2, the solid electrolyte interface (SEI) is formed. In this layer composed of many compounds such as the lithium carbonates, some ions of lithium are trapped within. Even if few ions are trapped, this side reaction by itself induces the state of lithiation to shift. In other words, at the same equilibrium potential, the states of lithiation in both electrodes changes after side reactions. Consequently, for the same operating voltage window (e.g. from 4.2 V to 2.5 V), the stoichiometry shifts, and this can have consequences on the amount of that is used in the electrodes.

Furthermore, during battery life many other side effects occur such as the deformation of the structure, the dissolution, fracture of the active material, enhancing the shifting the electrodes stoichiometry. In conclusion, the knowledge of the stoichiometry is requested to identify the limiting electrode and preventing the underuse of the active material or preventing the lithium deposition over the surface of the negative electrode during the charge. The lithium deposition is an important issue for the cell performance and safety because short circuits may occur. The methodology used by author’s in the literature to identify the stoichiometry is not completely clear. Thus, a method for their identification and the accuracy determination is proposed and discussed in the next sections.

5.2. Introduction to isotherms and the states of lithiation in either complete cell and “half-cell” configurations

In this section, we focus the discussion on the state of lithiation of the electrodes and how they influence the OCV in the complete cell. The concepts of “half-cell” and then the hypothesis supporting this study is introduced.

It is useful to disassemble a complete cell to measure the isotherm of its electrodes. The electrodes are reassembled in a cell with a lithium metal foil as counter electrode i.e. the so called “half-cell”. The term “positive electrode” and negative electrode remains assigned to the lithium metal oxide electrode and to the carbon-based electrode to avoid confusion.

Herein, the hypotheses are discussed. In fact, the quantity of charge is the cell capacity if no parasitic reaction occurs. For this reasons, the concept of coulombic efficiency is usually introduced to deal with the side reactions [228], [229]. Then a very small current is applied to let the system in equilibrium upon measuring the isotherm.

In conclusion, we assume that no side reactions occur during the measure (cf. Eq. 67) and the isotherms are accurately measured.

For the graphite, the “rocking chair” reaction is reported in Eq. 65:

$$xLi^+ + C_6 + xe^- \leftrightarrows Li_xC_6$$

Eq. 65

Where $0 < x < 1$ is the electrode stoichiometry defined with the reference to C_6.

The case for the lithium metal oxide $LiCoO_2$ is different: lithium ions are deintercalated as the Co^{3+} is oxidized into Co^{4+} while the intercalation the Co^{4+} is reduced into Co^{3+} according to Eq. 66:

$$LiCoO_2 \leftrightarrows yLi^+ + Li_yCoO_2 + ye^-$$

Eq. 66

Where $0.3 < y < 0.9$ is the stoichiometry window defined with the reference to Co [63]. The reactions in Eq. 65 and Eq. 66 are the half-reactions taking places in the electrode when the complete cell is charged.

First of all, the attention is focused on the characteristics of the positive electrode isotherm, illustrated in Figure 52. The equilibrium potential, measured in the half-cell configuration, is reported as a function of the stoichiometry. For LCO chemistries, the cell potential is usually limited between 4.3 V and 3.0 V. For higher and lower values of the voltage, the crystalline structure of the lithium oxides may be damaged. Furthermore, many side reactions are possible at higher voltage such as the oxidation of the electrolyte. Consequently, we attribute at the maximum voltage (e.g. 4.3 V) the minimum state of lithiation y_{min} while at the minimum voltage (e.g. 3.0 V) is associated the maximum state of lithiation y_{max}. When the battery cycles between these voltage cut-off, as illustrated in Figure 52, the state of lithiation varies from y_{min} to y_{max} and the reversible quantity of charge measured is Q_+.

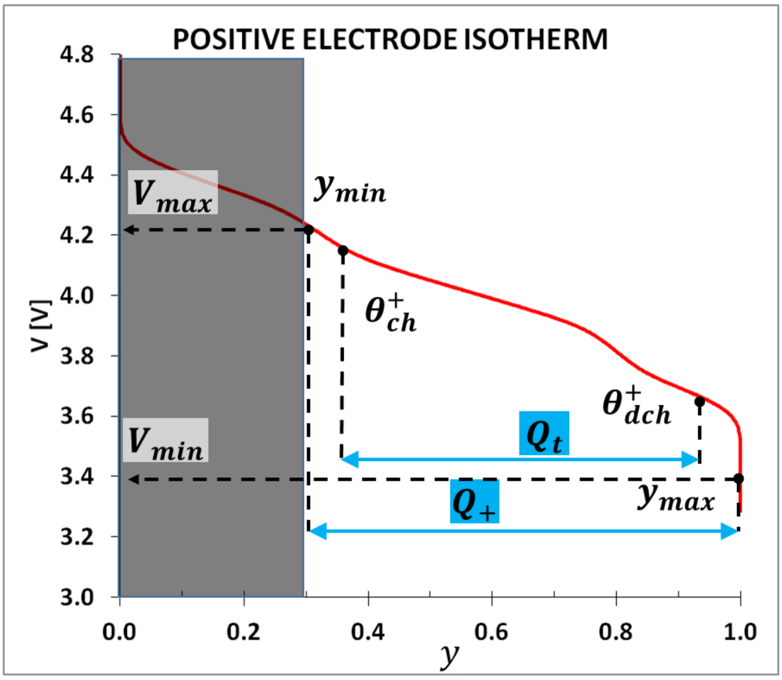

Figure 52 – The positive electrode isotherm is reported in the half cell configuration as function of the state of lithiation. The symbols y_{min} and y_{max}, indicates the minimum and the maximum state of lithiation available without inducing side reactions. The states of lithiation y at the charged and the discharged state, when the electrode is assembled in the complete cell configuration are θ^+_{ch} and θ^+_{dch}, respectively. The quantity of charge measured between the voltage cut off corresponding at the state of charges y_{min} and y_{max} is Q_+. Similarly, the capacity measured between θ^+_{ch} and θ^+_{dch} is Q_t, corresponding at the complete cell total capacity. The values of potential associated to y_{min} and y_{max} are respectively V_{max} and V_{min}.

This analysis continues by considering the complete cell configuration reported in Figure 53(A), where the open circuit voltage measured with quasi-static discharge between V_{max} and V_{min} is reported as a function of the DOD (the depth of discharge). The DOD is defined as fraction of the total quantity of charge $\mathrm{Q_t}$.. When the battery is fully charged, the state of lithiation for the positive electrode is indicated with θ_{ch}^{+}, while for the negative electrode is indicated with θ_{ch}^{-} ,as reported in Figure 53 (B). Therefore, when the battery is discharged, the states of lithiation are θ_{dch}^{+} and θ_{dch}^{-}, for the positive electrode and the negative electrode, respectively. Thus, with this notation there is an agreement between the charged and the discharged state of lithiation for both electrodes. Furthermore, a mathematical artifice for the negative electrode indicating the state of lithiation as $\theta^{-} = 1 - x$ is introduced. The symbol x indicates the stoichiometry in the negative electrode having the same meaning of y for the positive electrode. When the OCV of the complete cell cycles, the state of lithiations in the electrodes moves from $\theta_{ch}^{\pm}$ to $\theta_{dch}^{\pm}$. As consequence, for both electrodes their capacity Q_{+} and Q_{-} is inferior or equal to Q_{t}.

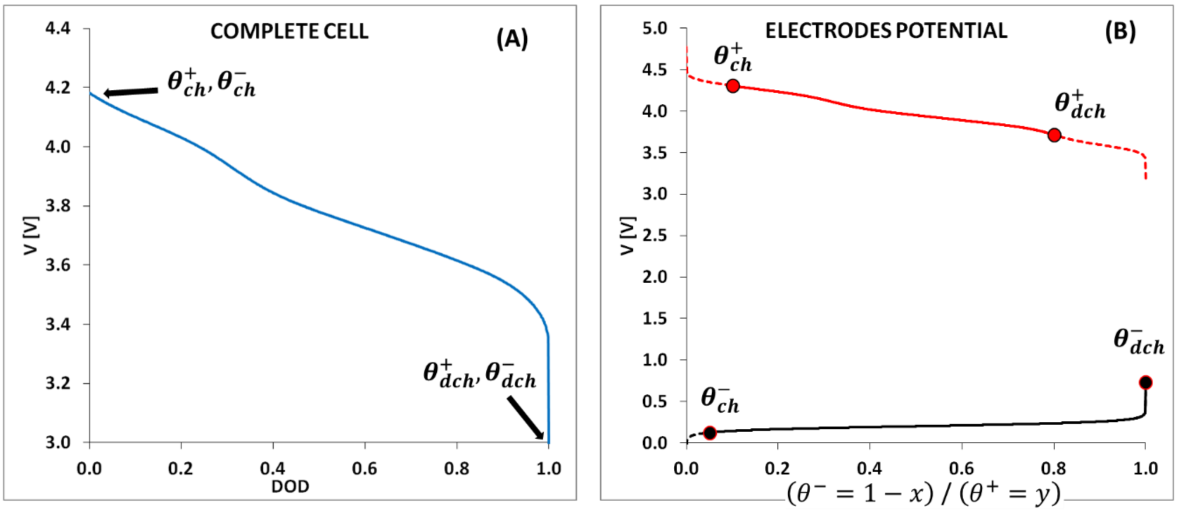

Figure 53 – (A) The cell voltage is reported as a function of the normalized quantity of charge DOD, where Q_{t} is the rated capacity. In (B) the isotherm of the electrodes reports the associated state of lithiation when the complete cell is charged rather discharged.

In a complete cell, the states of charge at the maximum and minimum voltage are determined by 6 parameters: Q_{+}, Q_{-} , $\theta_{dch}^{+}, \theta_{ch}^{+}$, $\theta_{dch}^{-}, \theta_{ch}^{-}$. However, these parameters are not independent because of the relation between capacity and the state of lithiation:

$$Q_{t} = Q_{+}(\theta_{dch}^{+} - \theta_{ch}^{+}) = Q_{-}(\theta_{dch}^{-} - \theta_{ch}^{-})$$

Eq. 67

Consequently, the independent parameters to be evaluated are 4 (for example $\theta_{dch}^{+}, \theta_{ch}^{+}, \theta_{dch}^{-}, \theta_{ch}^{-}$), but they can be reduced to 2 (i.e. $\theta_{ch}^{+}, \theta_{ch}^{-}$) if the capacities of the electrodes Q_{+} and Q_{-} are measured in the half-cell configuration. In this latter case, the states of lithiation at the end of discharge can be determined:

$$\begin{cases} \theta_{dch}^{+} = \dfrac{Q_t}{Q_+} + \theta_{ch}^{+} \\ \theta_{dch}^{-} = \dfrac{Q_t}{Q_-} + \theta_{ch}^{-} \end{cases} \qquad \text{Eq. 68}$$

A method to estimate the states of lithiation (i.e. $\theta_{dch}^{+}, \theta_{ch}^{+}, \theta_{dch}^{-}, \theta_{ch}^{-}$) without opening the cell and measuring the capacity of each electrode is proposed in the next chapters. This method can also be applied to track the shift of these parameters during the cell fading. Herein, for generality, the four states of lithiations $\theta_{dch}^{+}, \theta_{ch}^{+}, \theta_{dch}^{-}, \theta_{ch}^{-}$ are unknown parameters.

5.3. How the shape of the isotherms influences the accuracy on the initial states of lithiation

In a complete cell configuration, the states of lithiation in either electrode are unknown even if they were measured in each electrode before the assembling. Indeed, the irreversible side reactions occurring on the electrodes on the first cycle, shifts these values when the electrodes are assembled, as stated in § 5 and § 5.2. These values are estimated by matching the cell open-circuit voltage with the difference between the isotherms according to Eq. 69 [176].

$$\min\{E_{meas}(DOD) - [E_{+}(\theta^{+}) - E_{-}(\theta^{-})]\} \qquad \text{Eq. 69}$$

where $\theta_{dch}^{+} < \theta^{+} < \theta_{ch}^{+}$ and $\theta_{dch}^{-} < \theta^{-} < \theta_{ch}^{-}$, and $0 < DOD < 1$.

Before to discuss about the accuracy on the estimated states of lithiation, we discuss about different techniques for the isotherm analysis. Many studies have been reported using the incremental capacity (IC) and differential voltage (DV) [196], [228]–[239].

These two approaches are equivalent because they arrange differently the slope of the same isotherms, i.e. $\frac{dQ}{dV}\ vs\ V$ (IC) and $\frac{dV}{dQ}\ vs\ Q$(DV). When the modulus of the change of the potential rises, a peak is observed, that is attributed to a phase transformation. Without entering in these details, many studies use the IC and DV curves to analyses how these peaks shift with the degradation of lithium ions batteries. Additional information about these methods are reported in Appendix 8.3. We focus now the discussion on the accuracy of the measurement of the identified states of lithiation [240]. In this paragraph is explained why a good fit between the measured OCV and the reconstructed OCV does not guarantee *a priori* the correct identification of the states of lithiation. Since the Nernst law represents the simplest isotherm, it can be used to illustrate the ambiguity of the fitting method.

In a complete cell (Figure 54), the capacity is limited at least by the capacity of one of the electrodes, creating four different scenarios, reported in Figure 55:

- (A) end of charge limited by positive electrode while end of discharge limited by the negative electrode;
- (B) end of charge limited by negative electrode while end of discharge limited by positive electrode;
- (C) end of charge and end of discharge limited by positive electrode;
- (D) end of charge and end of discharge limited by negative electrode.

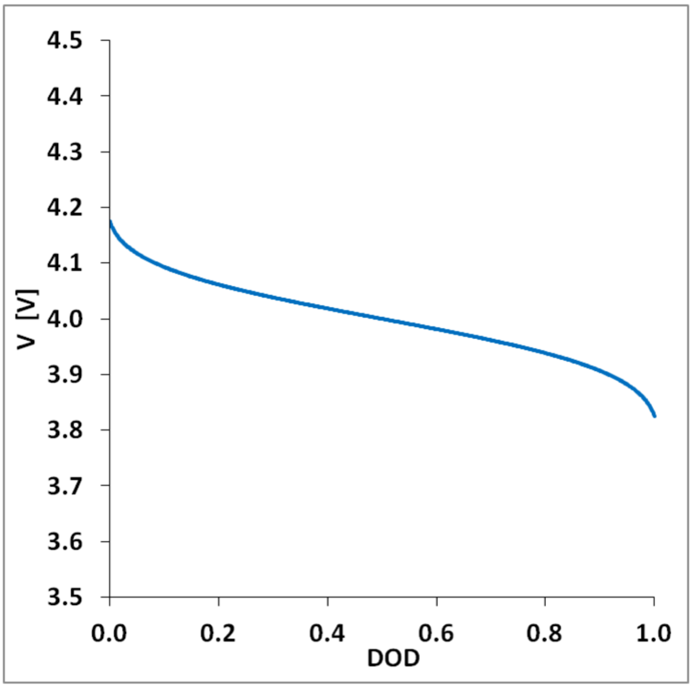

Figure 54 – The OCV of complete cell is obtained with the four scenarios in Figure 55 (A)-(D) associated to the electrodes' isotherms initial and final states of charge.

The four different scenarios reported in Figure 55 (A)-(D), lead to the same isotherm in the complete cell (Figure 54). Consequently, the estimated states of lithiation are not accurate. This situation is caricatural because of the simplicity of the isotherms, but it illustrates well the problematics behind any fitting process. Which electrodes limit the charge and which one the discharge is not usually known.

For this scope, we consider a reference cell having a Nernst isotherm for the electrodes and the states of lithiation: $\theta^{+}_{ch,ref} = 0.01$, $\theta^{+}_{dch,ref} = 0.99$, $\theta^{-}_{ch,ref} = 0.1$ and $\theta^{-}_{dch,ref} = 0.90$. This OCV is then compared with a cell having the same Nernstian isotherms and different states of lithiation to evaluate the error different the states of lithiation.

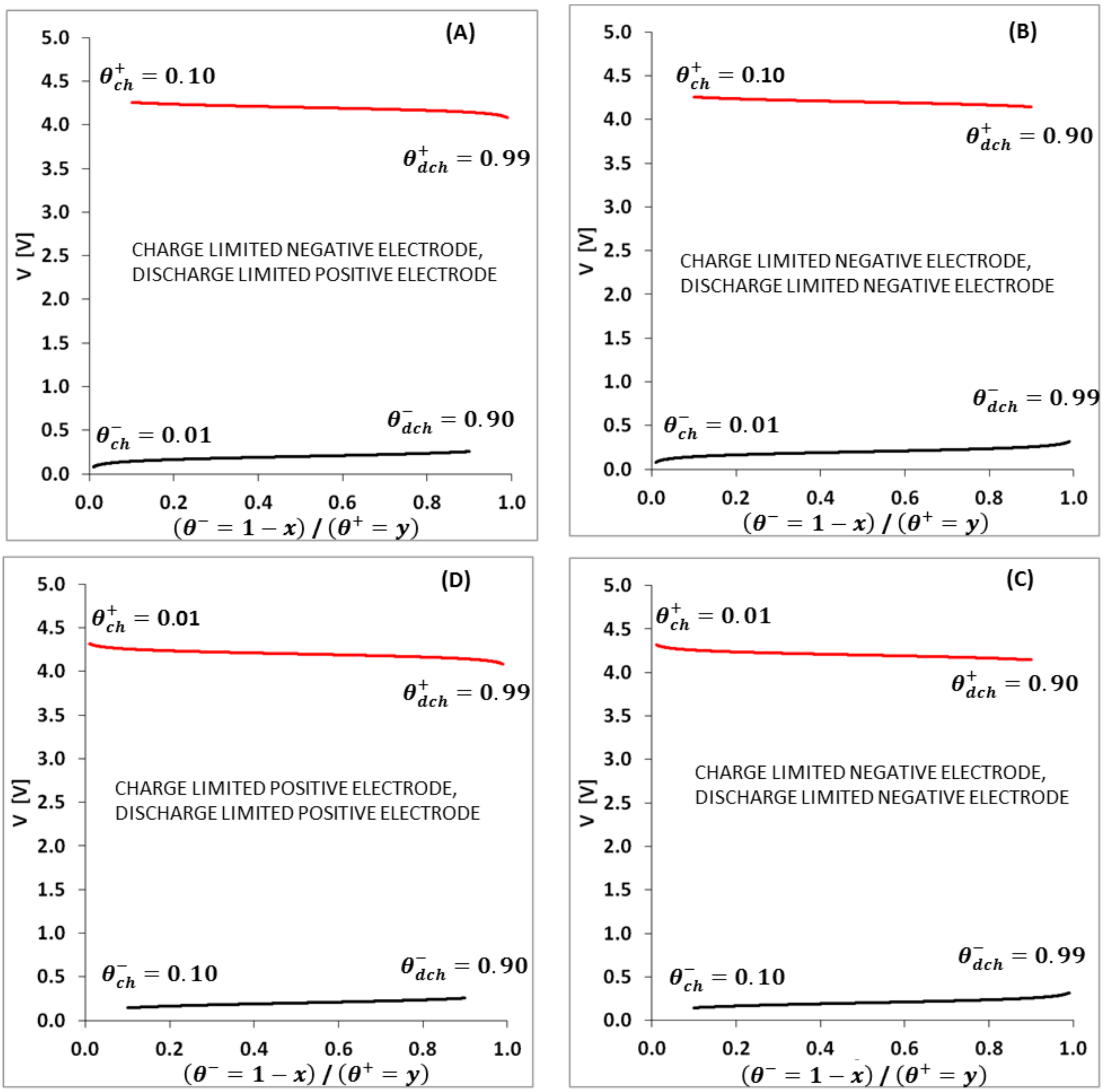

Figure 55 – The potential of the isotherms is reported for the electrodes as a function of the state of lithiation. The four-major combinations of charge and discharge limitation are illustrated.

The quantity of charge transferred the electrodes Q_t, depends of the capacity of each electrode and the variation from the charged to discharged state, as reported in Eq. 67:

$$Q_t = Q_+\left(\theta^+_{dch,ref} - \theta^+_{ch,ref}\right) = Q_-\left(\theta^-_{dch,ref} - \theta^-_{ch,ref}\right) \qquad \text{Eq. 70}$$

In the Nernstian case investigated up to now, the reference complete cell OCV is

$$U_r = \left(E^+_0 + \frac{RT}{F}\log\frac{1-\theta^+_r}{\theta^+_r}\right) - \left(E^-_0 + \frac{RT}{F}\log\frac{\theta^-_r}{1-\theta^-_r}\right) \qquad \text{Eq. 71}$$

A similar equation can be written for the fitting cell with the unknown states of lithiation

$$U = \left(E_0^+ + \frac{RT}{F}\log\frac{1-\theta^+}{\theta^+}\right) - \left(E_0^- + \frac{RT}{F}\log\frac{\theta^-}{1-\theta^-}\right) \qquad \text{Eq. 72}$$

The function of the voltage error between these OCVs can be determined analytically as:

$$U_{error}(DoD) = U_r - U = \frac{RT}{F}\log\left(\frac{\theta^-\theta^+(1-\theta_r^-)(1-\theta_r^+)}{\theta_r^-\theta_r^+(1-\theta^+)(1-\theta^-)}\right) \qquad \text{Eq. 73}$$

The states of lithiation are then obtained by minimizing the error:

$$V_{error} = \min(\max(U_r(\theta_{ch}^+, \theta_{dch}^+, \theta_{ch}^-, \theta_{dch}^-) - U(DOD))) \qquad \text{Eq. 74}$$

In Figure 56 is reported V_{error} as a function of θ_{ch}^+ , where *per* construction for $\theta_{ch}^+ \equiv \theta_{ch,ref}^+$, hence $V_{error} = 0\ mV$. As an example, for a $\theta_{ch}^- = 0.05$ the other 3 parameters are optimized (i.e. θ_{dch}^+, θ_{ch}^+, θ_{dch}^-) to minimize this error (i.e. ~ 7 mV). In other words, there is no combinations of θ_{dch}^+, θ_{ch}^+, θ_{dch}^- when $\theta_{ch}^- = 0.05$ that could provide an error, inferior to 7 mV. For any value of DOD, the error is compared between 0mV and 7 mV. At least two combinations of the 4 parameters ($\theta_{ch}^+, \theta_{dch}^+$, $\theta_{ch}^-, \theta_{dch}^-$) leads to coincident OCVs. Furthermore, if we consider acceptable an error of 10 mV $(i.e. V_{error} = 10\ mV)$, represented in the picture Figure 56 (A) to Figure 56 (D) by the dashed red lines, many combinations of these parameters are acceptable.

It should be noted that the curves are flickering as consequence of the discretized number of combinations used. Thus, they become smoother as the path of the samples decreases.

In conclusion, the shape of the isotherm affects directly how the state of charge of the electrodes at the charged are estimated, even for small error between the measured and the fitted OCV.

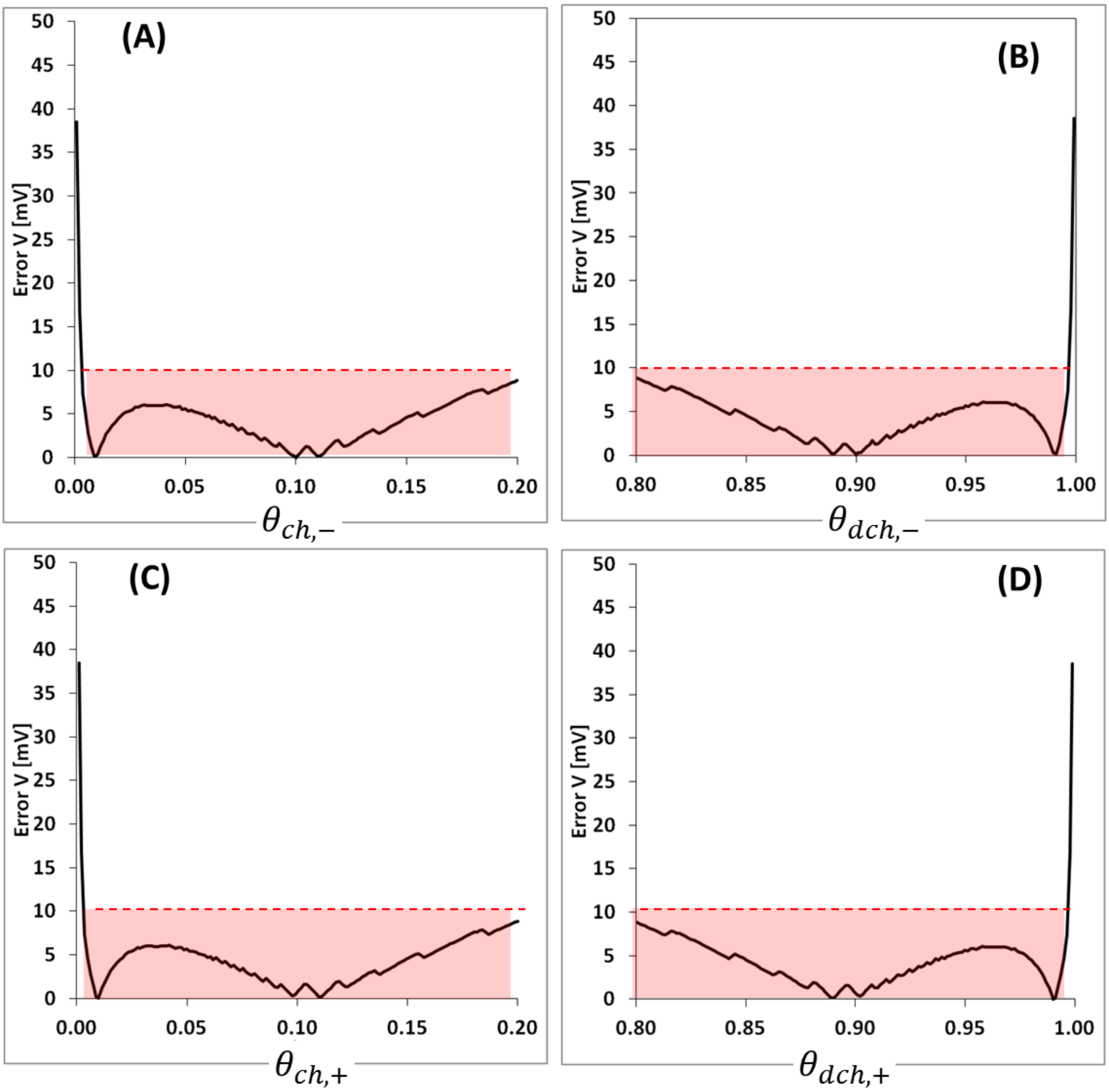

Figure 56 – In each of picture is reported the maximum error in terms of the voltage between the reconstructed OCV(DOD) and the reference OCV(DOD) obtained with two Nernstian electrodes isotherms. Furthermore, the reconstructed OCV is obtained with the best combination of 3 parameters when the 4th is parameter.

In the next case illustrated in Figure 57, the isotherms are complex enough to guarantee a good accuracy. the positive electrode has two sharp voltage steps in θ_{s1}^{+} and θ_{s2}^{+} , respectively.

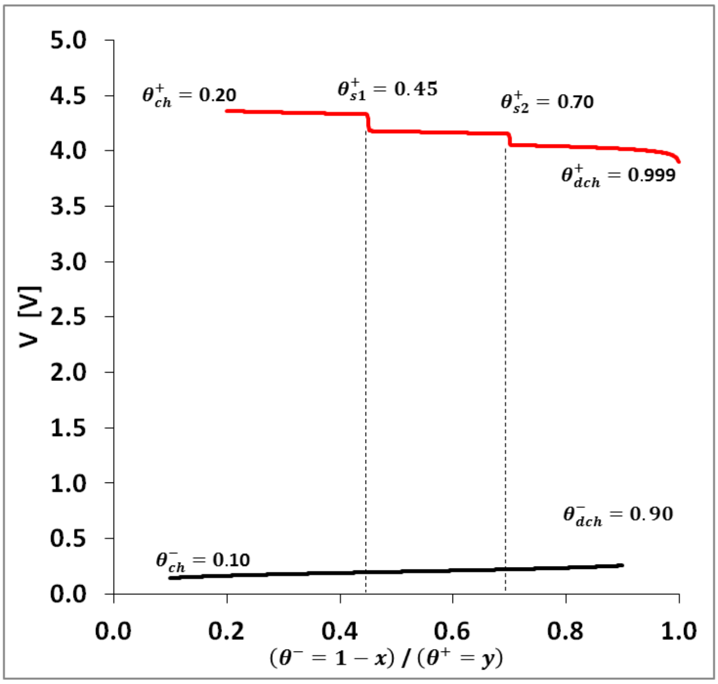

Figure 57 – The isotherms in either electrodes are based on the Nernst law but for the positive electrode is modified with two sharp voltage steps in $\theta^+_{s1} = 0.45$ and $\theta^+_{s2} = 0.7$.

The reference OCV as a function of the quantity of charge is reported in Figure 58.

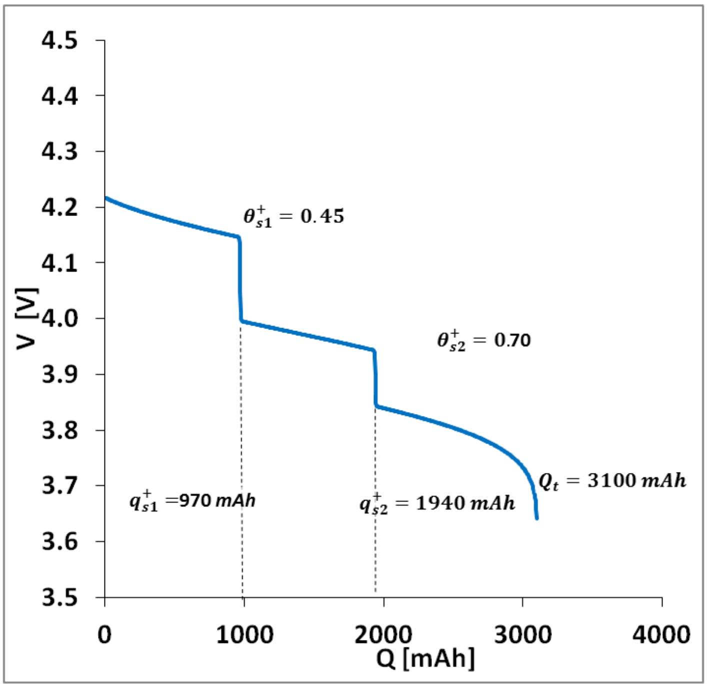

Figure 58 – The complete cell isotherm reported as a function of the quantity of charge. The capacity is $Q_t = 3100\, mAh$, and the sharp voltage steps are detected in $q^+_{s1} = 970\, [mAh]$ and $q^+_{s2} = 1940\, [mAh]$.

The total capacity is Q_t and the voltage steps are in $q^+_{s1}\, [mAh]$ and $q^+_{s2}\, [mAh]$. In this situation, it is possible to associate the state of lithiation θ^+_{s1} and θ^+_{s2} with the quantity of charge q^+_{s1} and q^+_{s2} with the equation Eq. 75:

$$\frac{\theta_{dch}^{+} - \theta_{s2}^{+}}{Q_t - q_{s2}^{+}} = \frac{\theta_{s2}^{+} - \theta_{s1}^{+}}{q_{s2}^{+} - q_{s1}^{+}} = \frac{\theta_{s1}^{+} - \theta_{ch}^{+}}{q_{s1}^{+}} \qquad \text{Eq. 75}$$

From Eq. 75 it is possible to explicit the state of lithiation for the positive electrode at the charged and discharged state as:

$$\begin{cases} \theta_{dch}^{+} = \dfrac{\theta_{s2}^{+} - \theta_{s1}^{+}}{q_{s2}^{+} - q_{s1}^{+}}(Q_t - q_{s2}^{+}) + \theta_{s2}^{+} \\ \theta_{ch}^{+} = -\dfrac{\theta_{s2}^{+} - \theta_{s1}^{+}}{q_{s2}^{+} - q_{s1}^{+}} q_{s1}^{+} + \theta_{s1}^{+} \end{cases} \qquad \text{Eq. 76}$$

The positive electrode capacity can also be calculated analytically, and consequently the measuring is not necessary:

$$Q_{+} = -\frac{q_{s1}^{+}}{\theta_{s1}^{+}}(1 - \theta_{s2}^{+}) + q_{s2}^{+} \qquad \text{Eq. 77}$$

Additional considerations about the error are reported in Figure 59 if θ_{ch}^{-} is smaller than $\theta_{ch,ref}^{-}$ than the error between the OCVs is positive, otherwise is negative. In conclusion, when one of the isotherm possess two voltage jumps, the state of lithiation can be accurately detected for both electrodes.

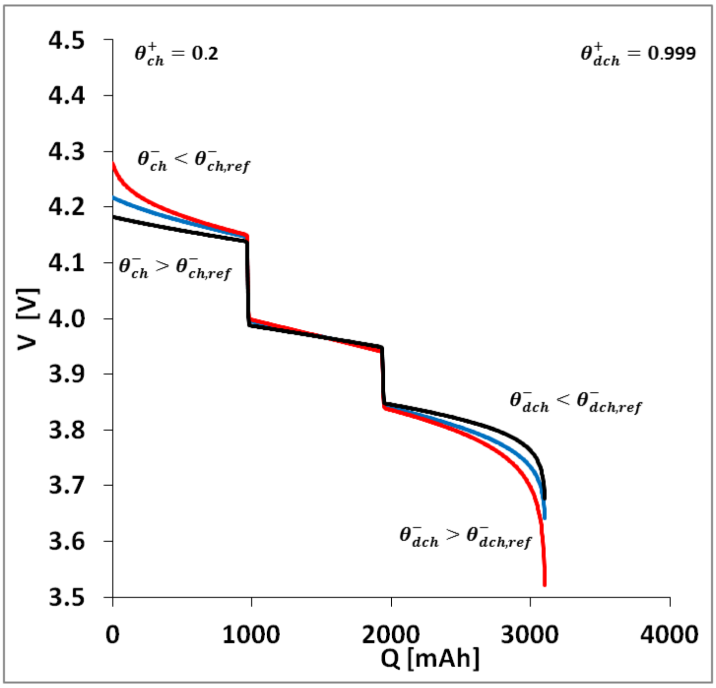

Figure 59 – The complete cell isotherm is reported with the values of the positive electrodes states of lithiations. The blue curve is measured, the red and black are drawn with different charged and discharged state of lithiation at the negative electrode.

The same procedure used to obtain the Figure 56 is now applied and illustrated in Figure 60. The charged and discharged state for the positive electrode can be detected very precisely as reported in Figure 60 (C) and Figure 60 (D). The accuracy is lower for the negative electrode, but still there is only one combination of parameters leading to $V_{err} = 0$. The ambiguity of the estimated states of charge reported in Figure 56 is now avoided.

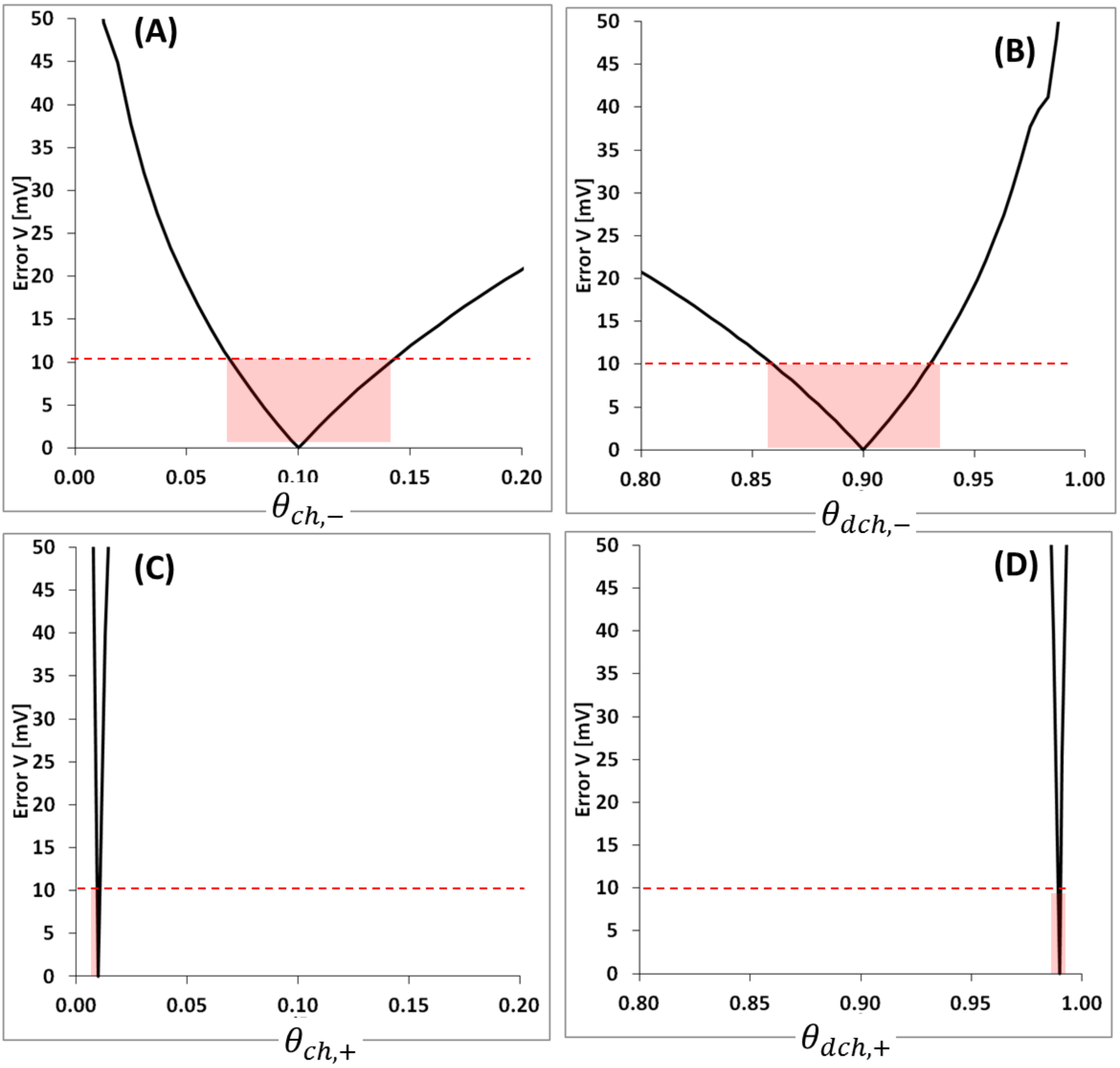

Figure 60 – In these pictures is reported the maximum error in terms of the voltage between the reconstructed OCV(DOD) and the reference OCV(DOD) obtained for a Nernstian isotherm (negative electrode) and a Nernstian isotherm having two voltage steps (positive electrode). Furthermore, the reconstructed OCV is obtained with the best combination of 3 parameters when the value of the 4th parameter is indicated in the abscises.

When the electrodes isotherms are similar to Nernst law, like in LiFePO4/LTO cells, the state of lithiation are poorly detectable. However, if one isotherm presents at least two sharp voltage steps, the initial states of lithiation are accurately identified. Between these two extreme cases, there are intermediate situations where some of the 4 parameters identified. This is for example the case if in one or both electrodes there is only one sharp voltage step. With these guidelines, the LGC cell is in investigated in the next chapter.

5.4. Identification of the state of lithiation in LGC INR18650MH1 half cell

In Figure 61 (A) are illustrated the isotherms of the LGC INR18650MH1 are measured with a current rate of C/50. The voltage thresholds are from 1.5 V to 0.05V for the negative electrode and from 4.3V to 3V for the positive electrode. The measurement of the isotherm is a difficult because the quasi-static condition is required [13], [238], [241]–[248].

The state of lithiation at 4.3 V for the positive electrode is approximatively $\theta^{+}_{max} \approx 0.3$ (as it is estimated in Appendix 8.2). However, the values of the boundary states of lithiation use the definition of § 5.2, found in literature (cf. § 3):

- For the negative electrode: $\theta^{-}_{max} = 1$ at 1.5 V and $\theta^{-}_{min} = 0$ at 0.05 V
- For the positive electrode: $\theta^{+}_{max} = 1$ at 3.0 V and $\theta^{+}_{min} = 0.3$ at 4.3 V

Slightly changes of $\theta^{+,-}_{max,min}$ doesn't affect our conclusions this method. Herein, the isotherms as a function of the state of lithiation are reported in Figure 61 (B).

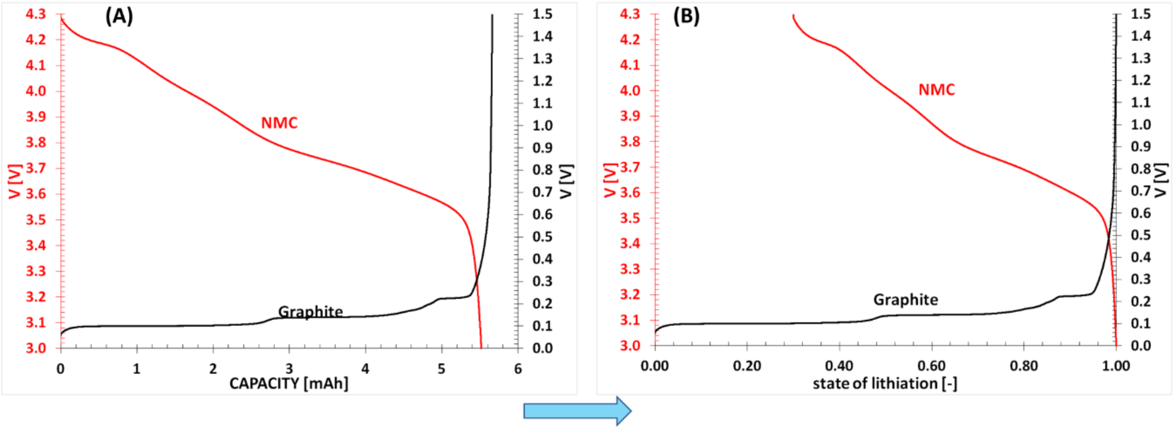

Figure 61 – The OCVs of both positive and negative electrode obtained from a LGCMH18650 are reported as a function of the quantity of charge (A) and as a function of the state of lithiation (B).

The identification of the initial and final states of charge of the electrodes of the complete cell is discussed in the followings. The same tool developed in MATLAB for the analysis performed in § 5.3 is used for this purpose. The code uses parallel computing to calculate ~100 million of combinations. In fact, for each one of the four states of charge ($\theta^{+}_{ch}, \theta^{+}_{dch}, \theta^{-}_{ch}, \theta^{-}_{dch}$) 100 values are considered:

- For the negative electrode between 0.95 and 1 for θ^{-}_{dch} and between 0 and 0.2 for θ^{-}_{ch} ;

- For the positive electrode between 0.95 and 1 for θ^+_{dch} and between 0.3 and 0.35 θ^+_{ch} ;

In Figure 62 in red is reported the measured OCV, while the fitted OCV is dashed. For this set of parameters: $\theta^+_{ch} \cong 0.305$, $\theta^+_{dch} \cong 0.975$, $\theta^-_{ch} \cong 0.030$, $\theta^-_{dch} \cong 0.998$ the maximum absolute error is $\sim 4.3\ \mathrm{mV}$ (while the accuracy of measurement is 2mV) and a root squared error $\mathrm{R}^2 = 0.9997$. Despites this very good fitt the identified values require an additional study to evaluate how an error on their estimation affects the fitting. For example, we need to know how the OCV is if θ^+_{ch} is few per cent higher or lower than the estimated value. Therefore, this study is conducted to evaluate the accuracy for each one of the states of charge.

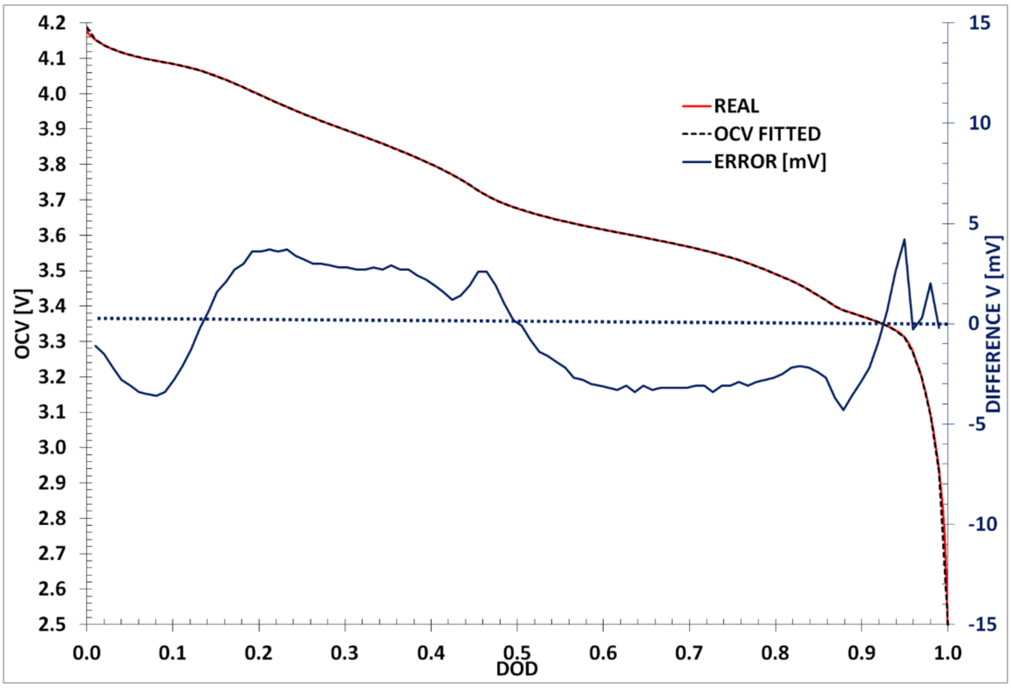

Figure 62 – The measured OCV and the reconstructed OCV using the proposed method is reported as a function of the DOD by using Eq. 72. The difference between these OCVs, obtained with Eq. 73, is reported in the second axis and the dashed blue line represent the zero.

Figure 63 (A-D) illustrates the evolution of one of the maximum error between the measured OCV and the reconstructed OCV as a function of the state of charge by minimizing the error associated to the other three parameters. The maximum error is reported in (A) and (B) for the parameters $\theta_{ch,-}$ and $\theta_{dch,-}$, respectively, while the error associated to $\theta_{ch,+}, \theta_{dch,+}, \theta_{dch,-}$ and $\theta_{ch,+}, \theta_{dch,+}, \theta_{ch,-}$ respectively, is minimized. Similarly, the maximum error is reported in (C) and (D) for the states of $\theta_{ch,+}$ and $\theta_{dch,+}$, respectively, while the error associated to $\theta_{ch,-}, \theta_{dch,+}, \theta_{dch,-}$ and $\theta_{ch,+}, \theta_{dch,-}, \theta_{ch,-}$, respectively is minimized. In conclusion, the most critical parameter is $\theta_{ch,-}$ because different values lead to the same error in the complete cell. Even though graphite isotherms have 3 voltage plateaus the state of charge at the charged state are poorly identified. In fact, the transitions between plateaus are smooth and the voltage steps are too small to provide enhanced accuracy.

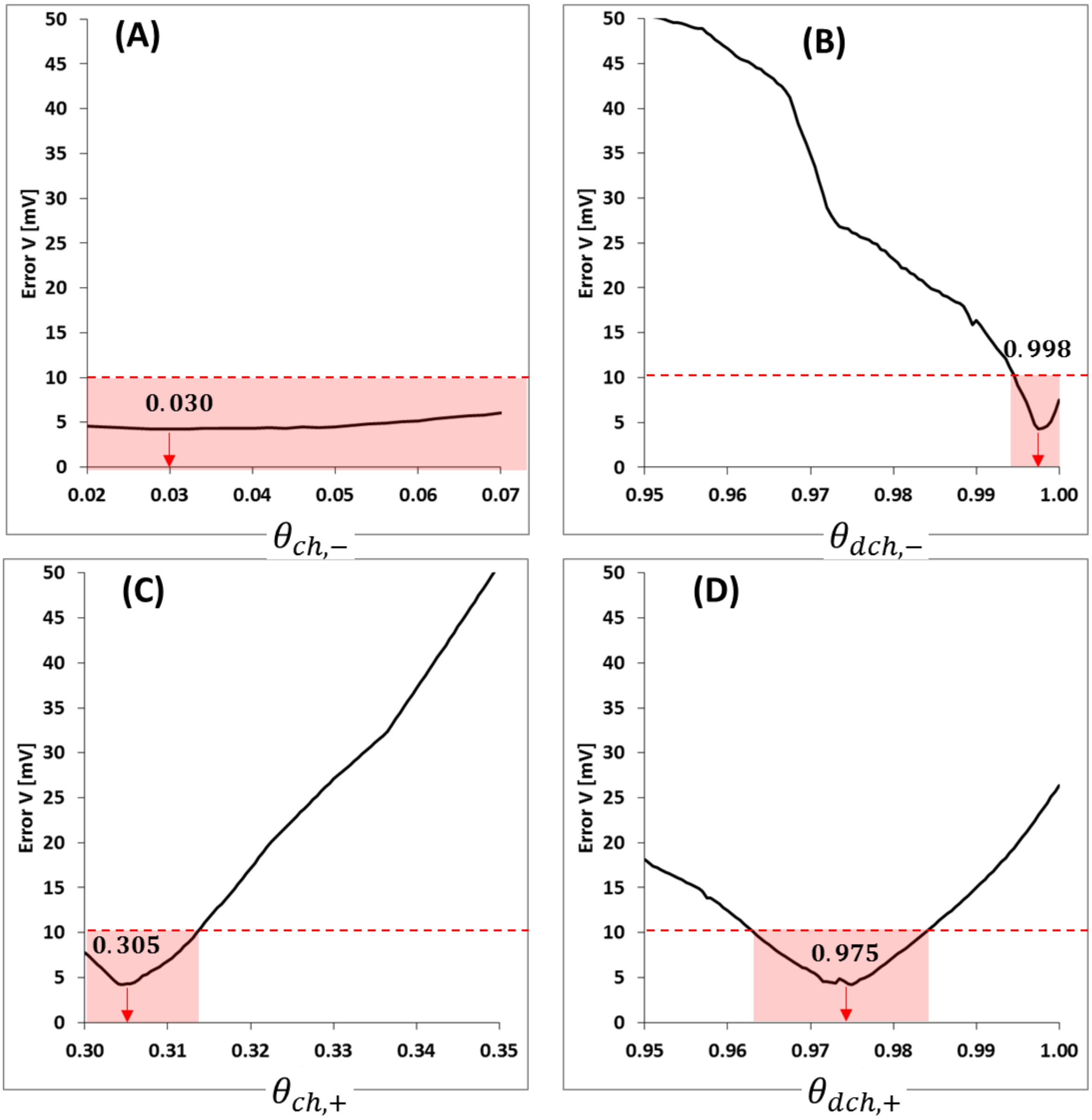

Figure 63 – The errors reported is the maximum error measured on the curve between the measured OCV and the fitted OCV, for the studied LGMH18650. In the abscises indicates the parameters analyzed and in the ordinates the maximum error over the curves, when the other parameters are optimized for the minimum error.

The uncertainties of the estimated state of charges at 4.2 V and 2.5 V illustrated in Figure 63 (A-D) with an accuracy of 10 mV are reported in Table 27.

$\Delta\theta_{ch,-}$	$\Delta\theta_{dch,-}$	$\Delta\theta_{ch,+}$	$\Delta\theta_{dch,+}$
0 – 0.12	0.995 – 1	0.3 – 0.313	0.963 – 0.984

Table 27 – The range of uncertainties $\Delta\theta$ over the state of charges at the charged and discharged state having an accuracy of 10 mV between the reference OCV and the reconstructed OCV for the cell characterized in § 4.2.

This procedure is then applied to 11 LGC INR18650MH cells at beginning-of-life and after aging from the same batch. The intention is to observe if the states of charges are similar in all the cells, and their accuracy. Furthermore, the goal for the aged cell investigation is to observe their evolutions.

The OCV, measured at C/25 shows in Figure 64 (A), the dispersion in terms of capacity in this batch is close to 3%. The result after the normalization of the capacity is reported in Figure 64 (B).

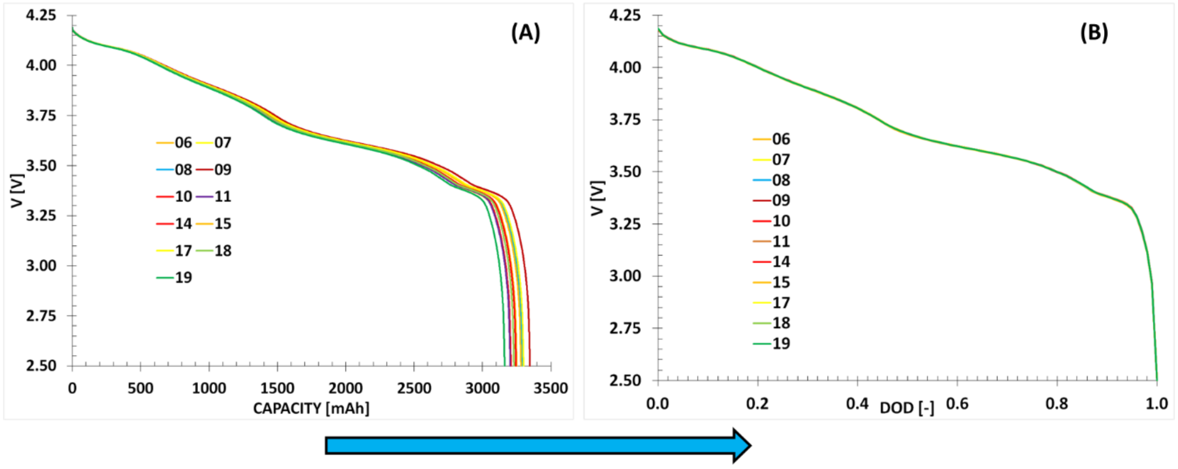

Figure 64 – The discharge voltage at a C/25 rate is reported as a function of the measured capacity (A) for the different cells. The discharge capacity is normalized with the measured capacity at the end of each discharge (B).

In Figure 65(A) are reported the differences between the OCV as a function of the DOD from the cell n°9 and the cells previously reported in Figure 64(B). The different discharge curves ca be superposed when they are normalized using the definition of DOD. In fact, the dispersion (i.e. voltage difference between al the discharge curves) is less than 2 mV in the DOD range from 0.05 to 0.95. In fact, 2 mV represents the sensibility of the instrument. In Figure 65 (B) is reported the differential voltage as a function of the DOD. Even in this case the differential voltage is very similar for these cells. Consequently, is not possible with this approach to demonstrate that the states of charges are different.

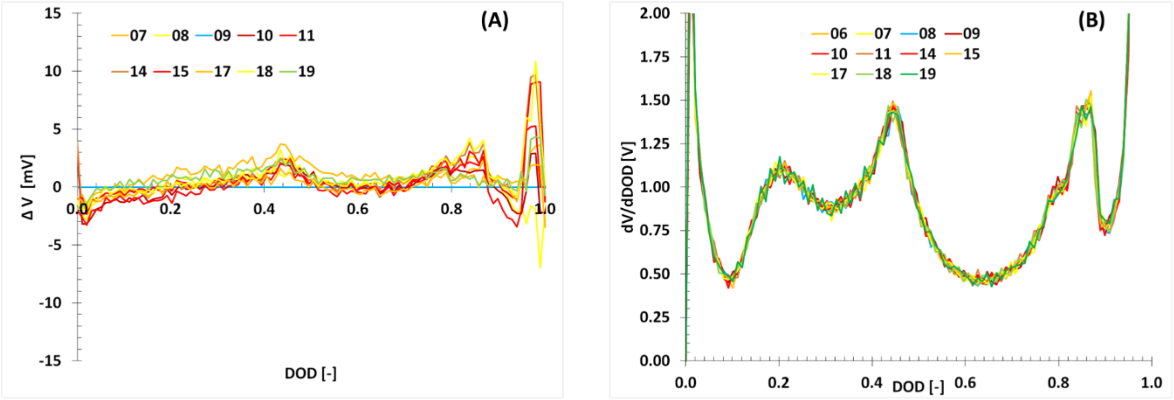

Figure 65 – In (A) is reported the voltage difference from the OCV normalized of the cell n°9, used as reference cell, and the voltage of the other cells. Instead, in (B) the differential voltage is reported for all the cells as a function of the DOD.

The capacity dispersion and weight are analysed in this section. Their nominal values are 3200 mAh and 49 gr, respectively. Instead, the measurement performed on 10 cells belonging to the same batch, shows that the average capacity and weight are 3242 ± 92 mAh (or ± 2.8%) and 47 ± 0.059 gr (or ± 0.12 %), respectively.

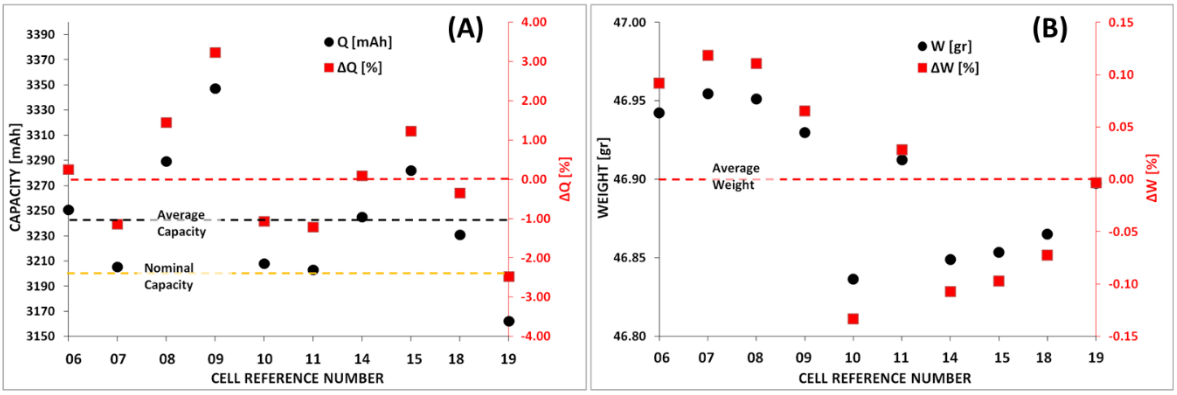

Figure 66 – In (A) and (B) are reported, in the main axis, for the fresh cells the capacity [mAh] and the weight [gr] respectively. In the second axis are reported, the percentile variations of capacity and weight using their respective average values: 3242 mAh and 46.90 gr.

In Figure 66 are reported their capacity and weight, percentile variation of capacity and weight from the average. It should be noted that cells n°07 and n°10 have a similar weight, but their capacity is respectively the highest and lowest. The connection between the capacity and the weight is thus not obvious. This can be attributed to the effect of particle connection, quantity of black carbon and binder, pore inclusions and percolations.

The capacity of these cells is measured after 3 years of aging in calendar at 25°C and 50% of DOD for the cells n°14 and n°06. Instead, the cell n°09 cycled for 1 month at C/3, 25 °C from DOD 0 to 100 % and then aged in calendar at 25°C and 50% of DOD for 3 years. In these conditions, the SOH become 91%, 96% and 98 %, for the cell n°09, n°14 and n°06, respectively. In Table 28 is resumed the capacity before and after aging:

CELL NUMBER	Q @ BOL [mAh]	Q @ SOH [mAh]	ΔQ [mAh]
09	3347	3050	-298
06	3251	3175	-74
14	3245	3127	-119

Table 28 – The capacity for the cells at the beginning of life and after the degradation is reported.

The method is then applied to identify the possible drift in the electrodes balancing. In Table 29 are reported the uncertainty for the four states of charge having an accuracy of 10 mV. Surprisingly these values are the same in these aged cells.

$\Delta\theta_{ch,-}$	$\Delta\theta_{dch,-}$	$\Delta\theta_{ch,+}$	$\Delta\theta_{dch,+}$
0 – 0.20	0.99 – 1	0.3 – 0.32	0.95 – 0.98

Table 29 – The range of uncertainties over the state of charges at the charged and discharged state having an accuracy of 10 mV between the reference OCV and the reconstructed OCV.

In literature, the degradation is commonly attributed to graphite electrode, however with this results we cannot confirm nor deny this conclusion [203], [206].
In conclusion, two different situations are identified:

- $\theta_{ch,-}$ has a poor accuracy;
- $\theta_{dch,-}$, $\theta_{ch,+}$ and $\theta_{dch,+}$ are accurately measured but it is not possible to identify significant variations after the aging. However, this conclusion should be verified after a more severe aging;

Therefore, more cells are required to observe the stoichiometry drift in aged cells. In conclusion, the proposed method can identify the stoichiometry but is not able to identify the variation of the parameters after the aging. We are confident that harsher ageing protocol are going to lead to detectable variations. Nevertheless, the aging effects are evident at high C-rates on the polarization, as reported in Figure 41 (A) and Figure 42 (A).
In the next paragraph, another strategy is illustrated to investigate the influence of ageing on the stoichiometry.

5.5. The aging scenarios

The method described in the previous section was not able to identify the effect of the degradation on the states of charge. For this reason, several scenarios are created to simulate how the stoichiometry affect the OCV. The isotherms of the electrodes, obtained from the LGC INR18650MH1 are reported in Figure 61.

Case 1: $\theta_{ch}^{-} \uparrow$

In the first case, the state of lithiation in the negative electrode at the charged states shift to higher values after the degradation as reported in Figure 67 (A). In Figure 67 (B) is reported the shape of OCVs associate to different values of θ_{ch}^{-} and the difference between the OCV having the initial θ_{ch}^{-} and the obtained OCVs. The arrows indicate how the peaks changes for different θ_{ch}^{-}. In conclusion, the voltage at the end of the charge is lower for higher θ_{ch}^{-}.

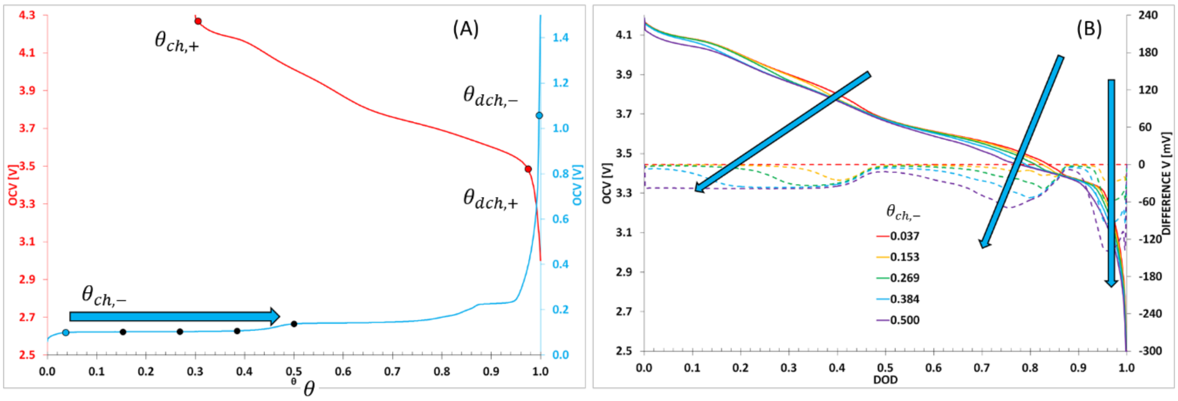

Figure 67 – The isotherms of the LGC INR18650MH1 cell are reported in (A) and the complete cell open circuit voltage and the differences between the initial OCV and OCV with shifted stoichiometry are reported in (B). The OCV reported in (B) are consequence of the shift of the θ_{ch}^{-} to higher values. The blue arrows indicate the directions of the new peaks obtained as a difference between the initial OCV and the actual OCV.

Case 2: $\theta_{ch}^{-} \downarrow$

For symmetry, in the second scenario are simulated the new OCVs when θ_{ch}^{-} decrease, as shown in Figure 68 (A-B). The variations of the new OCVs are small and the peaks in the new OCVs shifts only slightly, as indicated by the blue arrows in Figure 68 (B). It should be noted that the peaks are symmetric with the reference of previous first case.

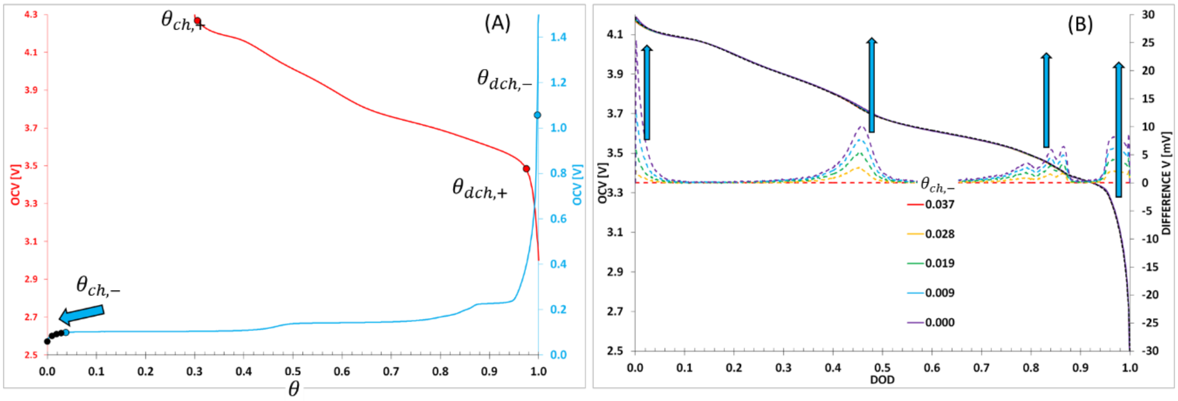

Figure 68 – The isotherms of the LGC INR18650MH1 cell are reported in (A) and the complete cell open circuit voltage and the differences between the initial OCV and OCV with shifted stoichiometry are reported in (B). This scenario illustrates the consequences on the OCV if the θ_{ch}^{-} decrease because of the cell degradation as indicated by the blue arrows.

Case 3: θ_{ch}^{+} ↑

In the next scenario, θ_{ch}^{+} increase as illustrated in Figure 69 (A-B). In this case the OCV decreases and the voltage at the end of charge decreases. This situation is not observed in the cells studied and consequently this scenario can be excluded.

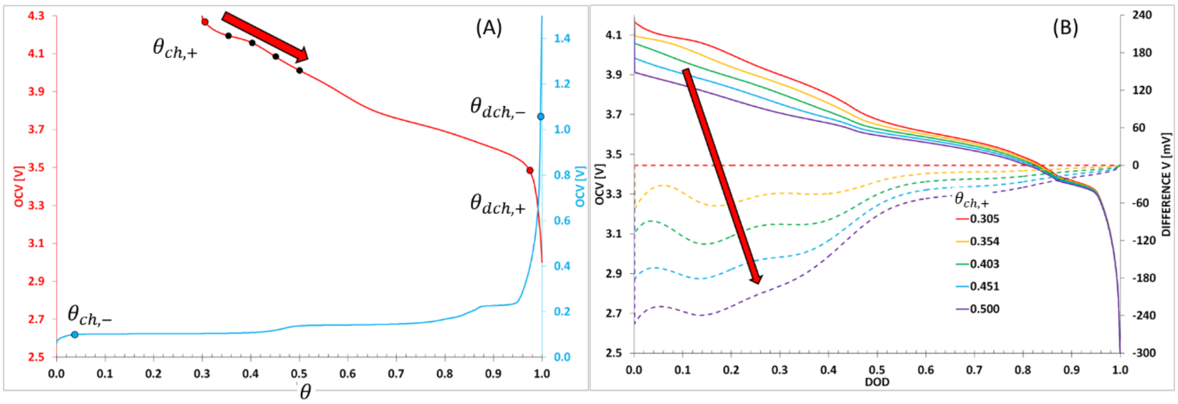

Figure 69 – The isotherms of the LGC INR18650MH1 cell are reported in (A) and the complete cell open circuit voltage and the differences between the initial OCV and OCV with shifted stoichiometry are reported in (B). This scenario illustrates the consequences on the OCV if the $\theta_{ch,+}$ increase because of the cell degradation as indicated by the red arrows.

Case 4: θ_{dch}^{+} ↓

In Figure 70 (A) is illustrated how the OCV looks like if the state of lithiation at the end of the discharge θ_{dch}^{+} decreases as indicated by the red arrow. The resulting OCVs in Figure 70 (B) indicates that the potential rises for elevate DODs. This situation is not observed in the studied cells and consequently is excluded.

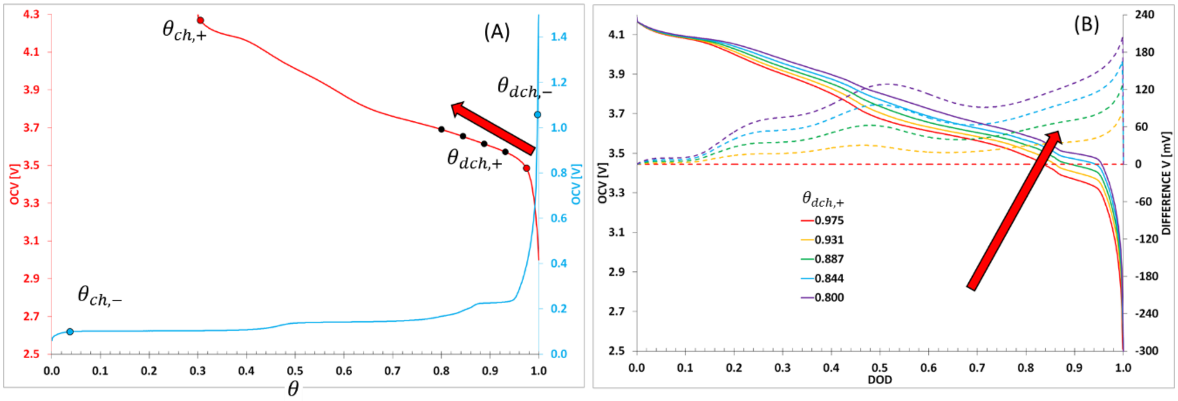

Figure 70 – The isotherms of the LGC INR18650MH1 cell are reported in (A) and the complete cell open circuit voltage and the differences between the initial OCV and OCV with shifted stoichiometry are reported in (B). This scenario illustrates the consequences on the OCV if the θ_{dch}^{+} decrease because of the cell degradation as indicated by the red arrows.

Case 5: θ_{dch}^{+} ↑

The symmetric of the previous scenario is illustrated in Figure 71(A-B). Indeed, some similarities can be found with the scenarios illustrated in Figure 68. In fact, in the present scenario, the OCV is slightly affected by the shifting of θ_{dch}^{+} to higher values.

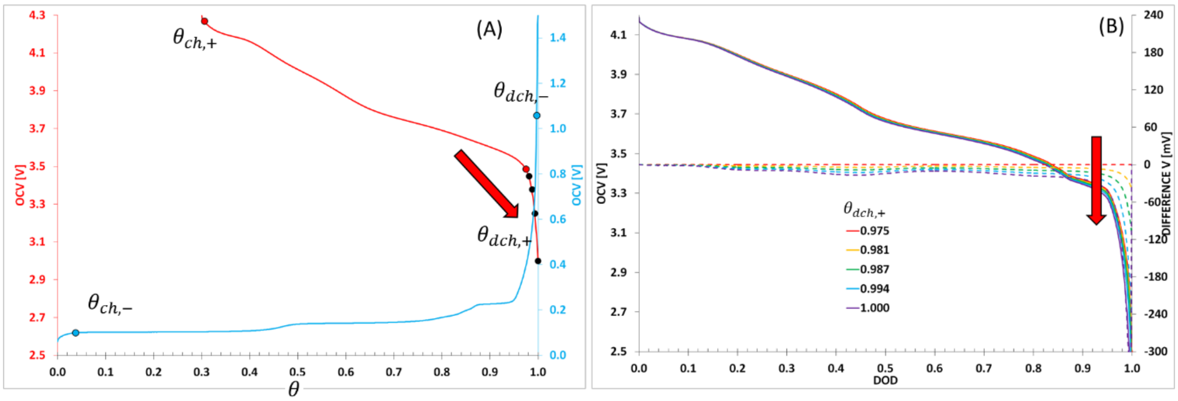

Figure 71 – The isotherms of the LGC INR18650MH1 cell are reported in (A) and the complete cell open circuit voltage and the differences between the initial OCV and OCV with shifted stoichiometry are reported in (B). This scenario illustrates the consequences on the OCV if the $\theta_{dch,+}$ increase because of the cell degradation as indicated by the red arrows.

Case 6: θ_{dch}^{+} ↑ and θ_{dch}^{-} ↓

Finally, in Figure 72 (A) a situation where both $\theta_{dch,-}$ decreases while $\theta_{dch,+}$ increases are illustrated. In fact, by considering that one of the electrode should limit the end of the discharge, θ_{dch}^{-} can decrease only if θ_{dch}^{+} increases opportunely. Thus, in this scenario, the cell becomes limited by the positive electrode after the aging.

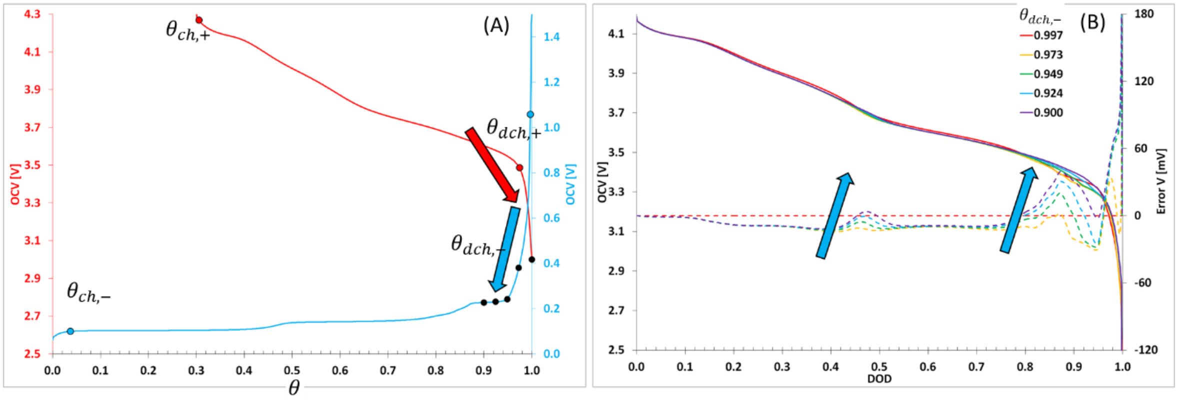

Figure 72 – The isotherms of the LGC INR18650MH1 cell are reported in (A) and the complete cell open circuit voltage and the differences between the initial OCV and OCV with shifted stoichiometry are reported in (B). This scenario illustrates the consequences on the OCV if the $\theta_{dch,+}$ increase while the $\theta_{dch,-}$ decrease because of the cell degradation as indicated by the red arrows.

In this last section, the aged cells n°09, n°06 and n°14 introduced in § 5.4 are analyzed to identify which one of the proposed scenarios is the most likely possible.

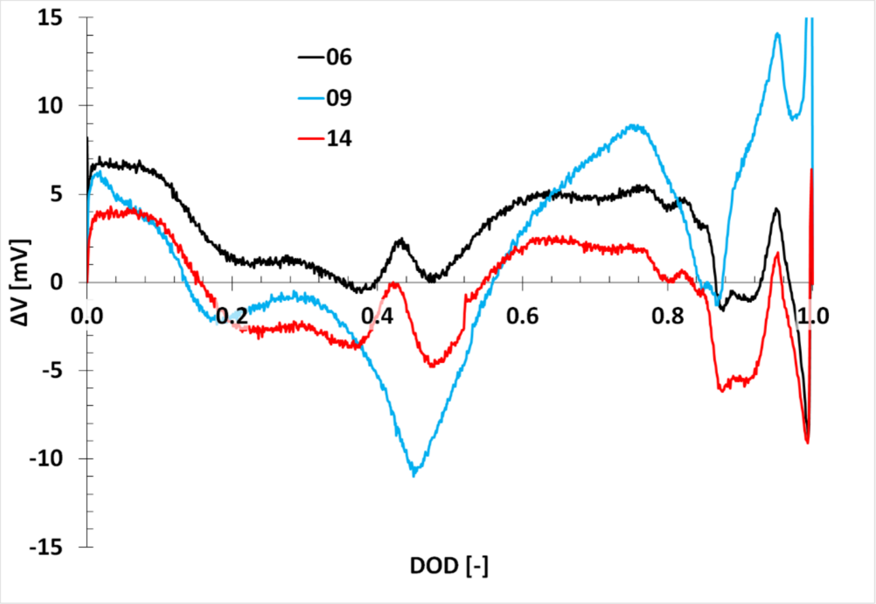

Figure 73 –The figure shows the difference between the fresh and the aged OCV (C/25) as function of the DOD for the cells n°09, n°06 and n°14.

In Figure 73 the differences between the fresh and the aged OCV are reported. The curves associated to cell n°6 and n°14 are similar, while in the n°9 different peaks are observed. This result suggests that different history of aging affects the shape of the OCV. However, this low degradation cannot provide definitive conclusions because the OCV, after aging is slightly modified. However, the first scenario discussed in Figure 67 where θ_{ch}^{-} increases seems the most possible. However, it is also realistic the θ_{ch}^{+} shifts to higher values.

6 Numerical simulations with COMSOL

The system of equations is coded in COMSOL to investigate the mass transport limitations and their effect on the rated capacity. The dedicated battery toolbox available for COMSOL was also tested but the convergence of the solution is not reached when the local concentration in the solvent is zero. This situation may occur at very high C-rates. For these reasons the system of equation is coded ex-novo using the constant coefficient form.

The 1D geometry consists of three segments: the positive electrode, the separator and the negative electrode. The geometry of the non-dimensional P2D model in COMSOL and the mesh are illustrated in Figure 74. The mesh density is higher at the boundaries: electrode/separator, electrode/current collector and the particle's surface (r=1). In the P2D model, the *x*-axis indicates the position along the width of the electrodes (i.e. the 1D electrode geometry) while the *r*-axis indicate the particles radius (i.e. the 2D particles geometry indicated with P2D). The lithium concentration is a local variable in either solid and liquid phase in the (x,r) dimensions.

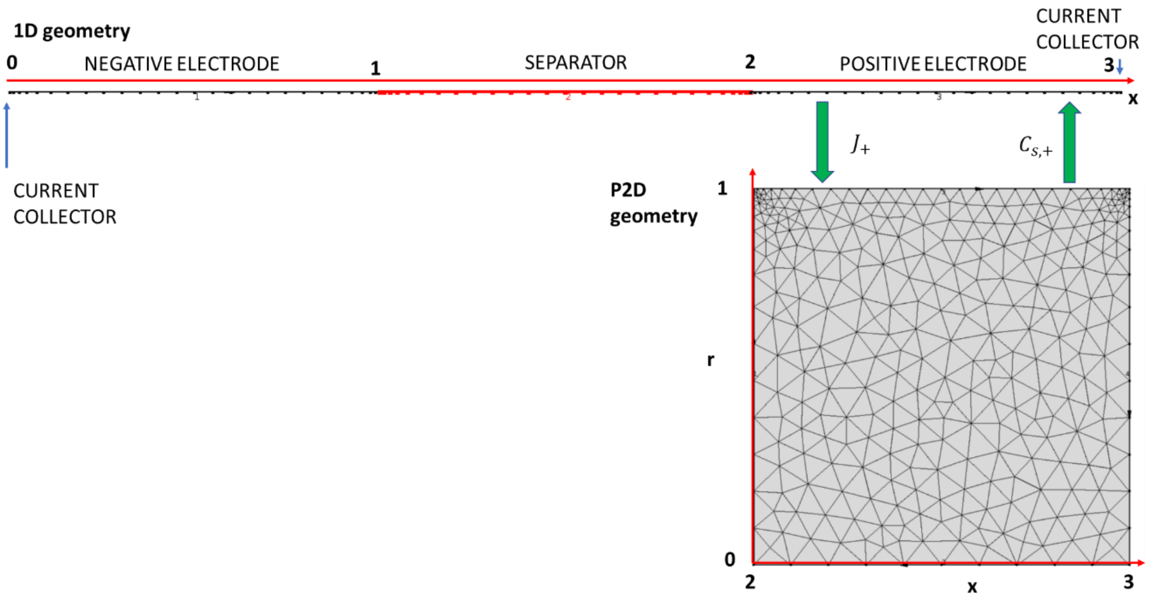

Figure 74 – The draw reports the 1D geometry with the negative electrode, positive electrode and the separator. The negative current collector is located in x=0 and the positive current collector in x=3 as indicated by blue arrows. The positive electrode in the 2D geometry is represented with the square shape: the direction x across the particles comes from x=2 to x=3 and the direction-r, inside the particle, comes from r=0 to r=1. The value of r=1 represent the surface of the particles. The green arrows indicate the variables J_+ and $C_{s,+}$ that connects the 1D geometry with the P2D geometry (i.e. the current density and concentration at the surface of the particles).

The Butler-Volmer law connects the two geometries: the flux from the 1D geometry is projected to the P2D boundary while the surface concentration from the P2D boundary is projected to the 1D geometry, as indicated by the green arrows.

The diffusion equation in the P2D geometry is modeled in COMSOL using an anisotropic diffusivity equal to zero in the x-axis direction. The reference potential (0 V) is set at the boundary of the negative current collector (x=0).

The solver in Comsol has some problems when the solid phase concentration reaches the unity (i.e. the particle is saturated in the dimensionless equation system). However, the stability of the solver is obtained with a simple variable change:

$$\theta_S = 1 - \theta_+ \qquad \textit{Eq. 78}$$

where the subscript S is for reverse solid phase concentration and the subscript + for positive solid phase concentration. The new variable reaches zero at the end of discharge (i.e. the particle's saturation). When, the solver works close to zero it is accurate because of the separation because of the separation between positive and negative values.

At the beginning of the discharge, when the current is switched on there is a numerical instability associated to the non-derivability of mathematical steps. Consequently, the use of the smoothed step transitions function "fl2hcs" creates continuous variables that can be derived twice.

The model was also coded in Matlab using the server COMSOL-Livelink, with the intention to automatize the simulations and identify the parameter's sensibility and manipulate the data for post-processing. Unfortunately, COMSOL-Livelink is found to be much slower (at least 5 times) then COMSOL, and after many tentative this approach was abandoned. In the next chapter are explained the main mass transport limitations during the galvanostatic discharges.

6.1. Galvanostatic discharges

The battery performances are usually evaluated with a sequence of discharges at constant current (i.e. galvanostatic) in a potential threshold window. In general, the measured capacity is lower as the current increases. Thus, one of the method to evaluate the cell performances is to apply a constant discharge current to associate it with the measured capacity. On the contrary, in literature, many studies are conducted on the cell polarization by fitting the simulations with the experiments rather than studying the rated capacity [91], [106], [137], [249], [250].

In the followings, the rated capacity at the end of the galvanostatic discharge reported from literature is investigated to detected possible connections with the C-rate. The discharge voltage profiles from the literature are reported in Figure 75, for a prismatic (A), cylindrical (B) and pouch cell (C).

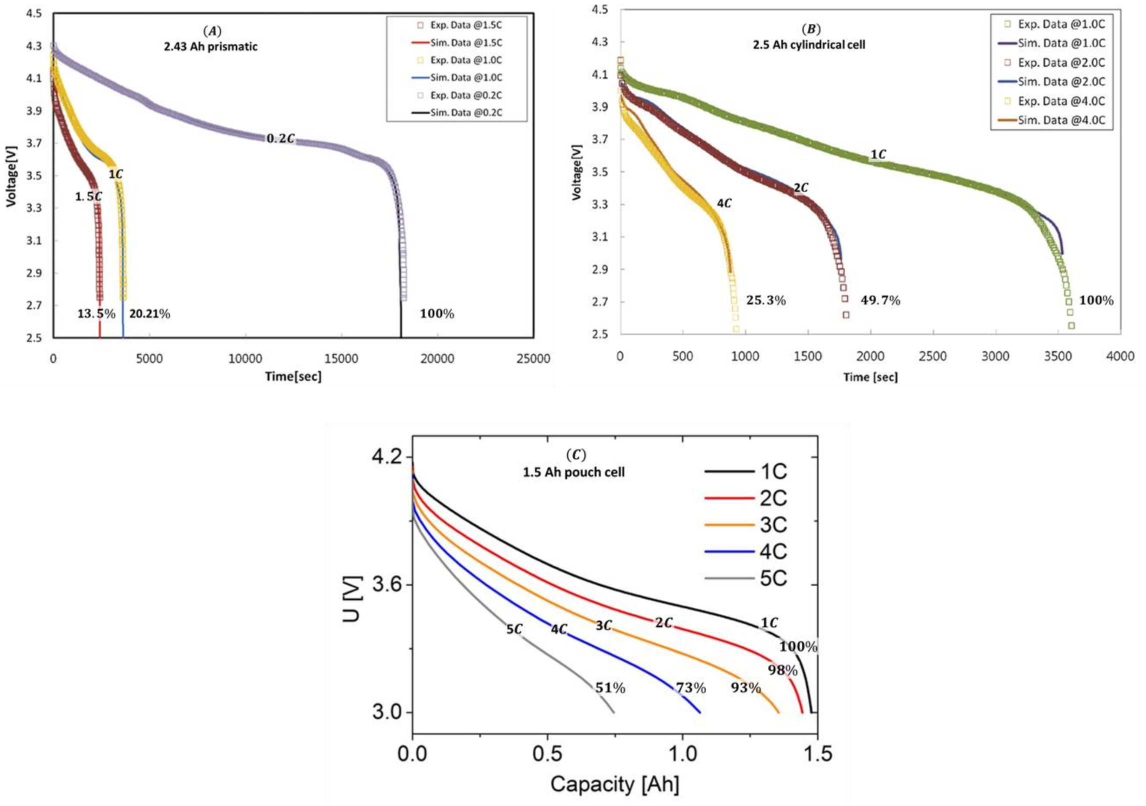

Figure 75 – The discharge voltage at 25°C for different C-rates for (A) prismatic cell, (B) cylindrical cell [155] and (C) pouch cell [214]. The figures reports in % the estimated rated capacity at the end of the discharge.

It is known that the rated capacity decreases at higher C-rate, but the inverse of the rated capacity provides information about the behaviour of the transport limitation. In fact, this trend can be attributed to one of the different possible kinetic limitation. The rated capacity and its inverse value obtained from Figure 75 are reported in Figure 76. The rated capacity decreases as the C-rate increases by following different laws. In fact, for the cells [A] and [B] the inverse of the rated capacity is linear, while in [C] it is almost for C-rate lower than 1.5 and then it decreases. The origin of the performance limitations in terms of the capacity were studied by Johns et al 2009 [251] and Cornut et al. 2015 [252]. Following their approach in Figure 76(A) is reported the rated capacity and in Figure 76(B) the inverse of the rated capacity as function of the C-rate. Considering these articles, and the results of this work detailed in the next chapters, we can speculate that the limiting factors responsible for the reduction of the rated capacity are similar in cell [A] and [B] (i.e. solid phase mass transport limitation) and a different one in cell [C] (i.e. liquid phase mass transport limitation). When no kinetic limitation occurs for the rated capacity the inverse of the capacity is constantly 1. Instead, when the liquid phase transport limitations occur, the inverse of the rated capacity form a straight line, like in the case Figure 76(B) [A] that can be eventually extrapolated to a line passing *per* zero.

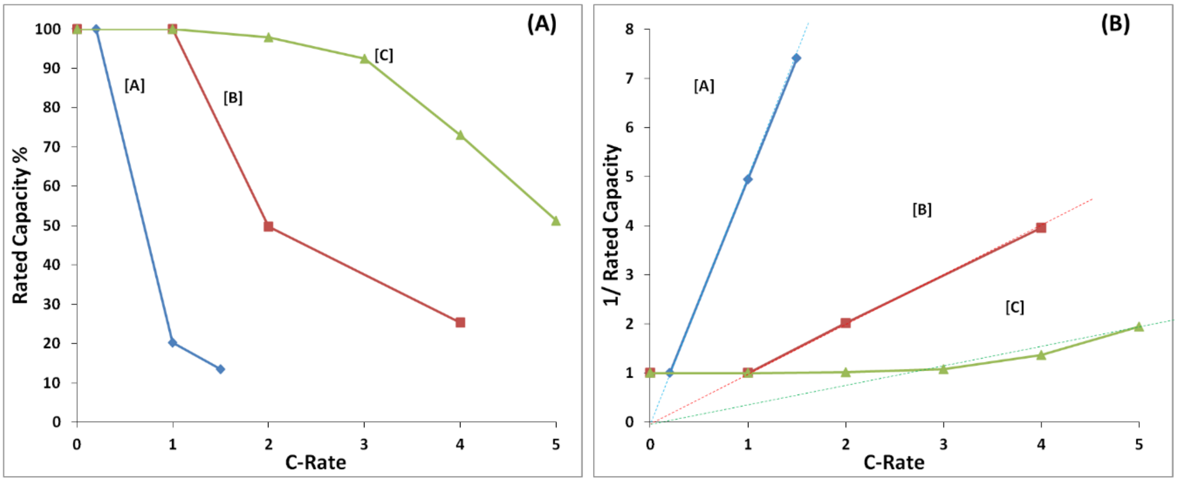

Figure 76 – The rated capacity for different C-rates for (A) prismatic cells and (B) cylindrical cells [155], while in (C) are pouch cells from [214].

More in general, how the rated capacity varies as a function of the C-rate is discussed in several articles and the rated capacity is a direct consequence of the different kinetic limitations occurring in the: electrolyte, solid phase, or particles [252][251]. These mass transport limitations, occurring during galvanostatic discharge, are discussed in detail in this chapter.

Many parameters can potentially influence the results and the rated capacity. Consequently, an opportune methodology is required to isolate the effect of each parameter, to obtain general conclusions. In practice, the number of parameters is reduced by avoiding the mass transport limitations in the negative electrode and the separator, as reported in Table 30. As consequence, the negative electrode is a lithium metal foil and the isotherm in the positive electrode is represented with the Nernst law. In Table 14 are reported the values of transport number and reaction kinetic constant that are usually found in literature (§ 3) [93].

The non-dimensional electrochemical model with the description of the PDE system and its parameters are reported in § 2.3.3.

The ratio between the quantity of charge in the solid phase and the charge in the liquid phase is expressed by the non-dimensional parameter A_{3+} (Table 31).

The parameter A_{3+}, is assumed to 100, as it is usually close to what is obtained from the literature. However, the effect of different value for the parameter A_{3+} will be discussed. The maximum concentration in the solid phase is approximately 22000 $mol\, m^{-3}$ for LFP and from 40000 to 60000$mol\, m^{-3}$ for NMC, NCA or LCO.The initial concentration in the electrolyte is approximately $1000\ mol\, m^{-3}$ according to literature. The study is focused on: kinetic limitation, electrolyte mass transport limitation, electronic transport limitation, diffusion mass transport limitation in the particles. Finally, the influence on their combinations are discussed.

CONSTANT PARAMETERS	
$L_{1-} = \frac{RT}{F}\,\frac{\sigma_-}{D_{e+}\,F\,C^*}\,\frac{d_+}{d_-} \gg 1$	$L_{1-} = 1000$
$L_{4-} = \frac{d_+\,k_-^*}{D_{e+}} \gg 1$	$L_{4-} = 1000$
$A_{6e} = \frac{D_{e+}}{D_e}\,\frac{d_e}{d_+} \ll 1$	$A_{6e} = 0.001$
$A_{5e} = \frac{1}{\varepsilon_{+l}}\,\frac{D_{e+}}{D_e}\left(\frac{d_e}{d_+}\right)^2 \ll 1$	$A_{5e} = 0.001$

Table 30 – The table shows the parameters selected in all the following simulations and their respective values. These latter were chosen for avoiding their contribution in the mass transport limitations.

Since the non-dimensional parameters are obtained using the effective diffusivity in the positive electrode, the electrolyte mass transport limitation corresponds to the study of the non-dimensional current $\tilde{\jmath}$ (§ 2.3.3). The other parameters such as A_{1+} , A_{2+} , A_{4+} are associated to electronic mass transport, diffusion in the solid phase and kinetic reaction, respectively.

CONSTANT PARAMETERS FROM LITERATURE

$$\alpha_{\pm} = 0.5$$

$$t_{+} = 0.4$$

$$A_{3+} = \frac{\varepsilon_{+s}}{\varepsilon_{+l}} \frac{C_{s,max+}}{C^{*}} = 100$$

Table 31 – The table shows the parameters selected according to literature and used in all the following simulations. In some cases, the influence of the parameter A_{3+} is discussed and its values explicated.

6.1.1 Kinetic redox limitation

In this chapter, the influences of the reaction rate kinetics constant k^{*} in the Butler-Volmer relation are studied. In this study the transport limitation in both solid and liquid phase are avoided (i.e. infinitely fast diffusion) by using the opportune values of the parameters reported in Table 32. Thus, the concentration of lithium ions in the electrolyte is constant ($C \equiv C^{*}$).

CONSTANT PARAMETERS	
$A_{1+} = \frac{RT}{F} \frac{\sigma_{+}}{D_{e+} F C^{*}} \gg 1$	$A_{1+} = 1000$
$A_{2+} = \varepsilon_{+s} \frac{D_{s+}}{D_{e+}} \frac{C_{s,max+}}{C^{*}} \left(\frac{d_{+}}{R_{p+}}\right)^{2} \gg 1$	$A_{2+} = 1000$
$A_{3+} = \frac{\varepsilon_{+s}}{\varepsilon_{+l}} \frac{C_{s,max+}}{C^{*}}$	$A_{3+} = 100$

Table 32 – The parameters reported in this table ensure that only the kinetic limitation can be observed.

In Figure 77 is reported the non-dimensional potential during the discharge as a function of the DOD for different values of the parameter A_{4+}.

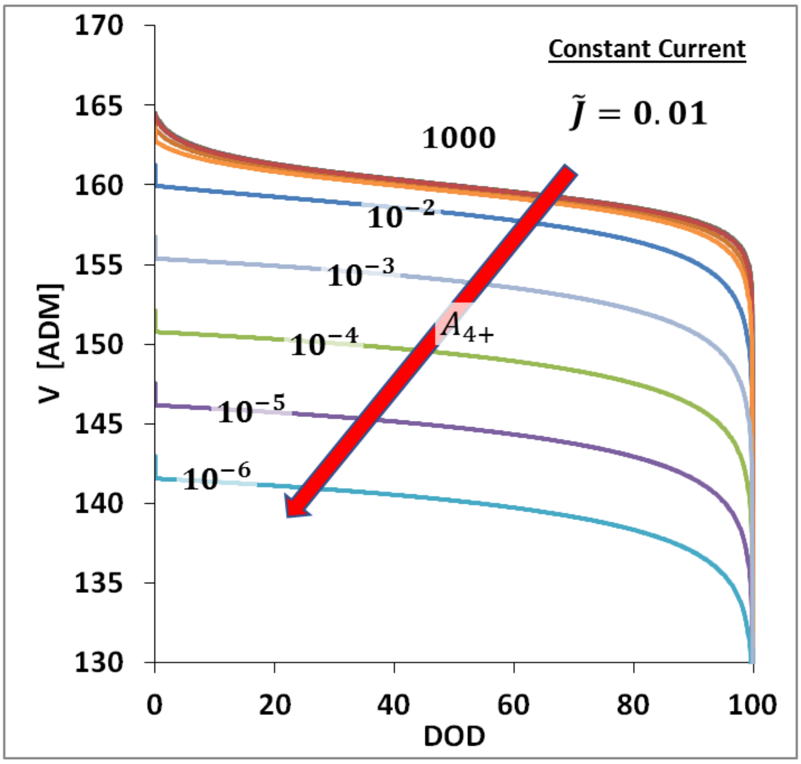

Figure 77 – The non-dimensional potential is plotted as function of the DOD for different values of the parameter A_{4+} for a fixed value of the non-dimensional current $\tilde{J} = 0.01$.

In Figure 78 is reported the discharge voltage for different values of the non-dimensional current $\tilde{J}$ for three different values of the kinetical parameter A_{4+}. The values chosen for $\tilde{J}$ are small enough to avoid transport limitation in solution: $\tilde{J}$<<3 (detailed in § 6.1.2). At the beginning the analysis focused on the evolution of the internal variables (i.e. concentration in the solid and the liquid phase) during the discharge. Then it is studied now the influence of the parameters on the polarization for a given DOD of 15%.

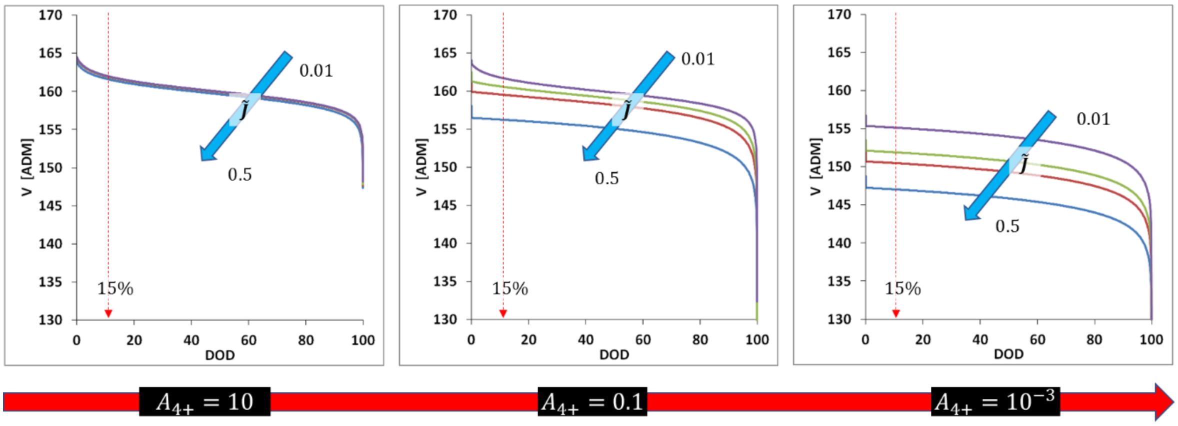

Figure 78 – The discharge voltage as a function of the DOD is reported for three values of the parameter $A_{4+} = 10, 0.1, 10^{-3}$. The values of non-dimensional $\tilde{J}$ are 0.5, 0.1, 0.05 and 0.01.
The red arrow indicate the direction of lower A_{4+} and the dashed arrow indicates the 15% of DOD.

The lithium concentration on the particle's surface is reported every 10% of DOD, across the electrode in Figure 79. The concentration is uniform in the whole section from x=2 to x=3 for any values of the parameter A_{4+}.

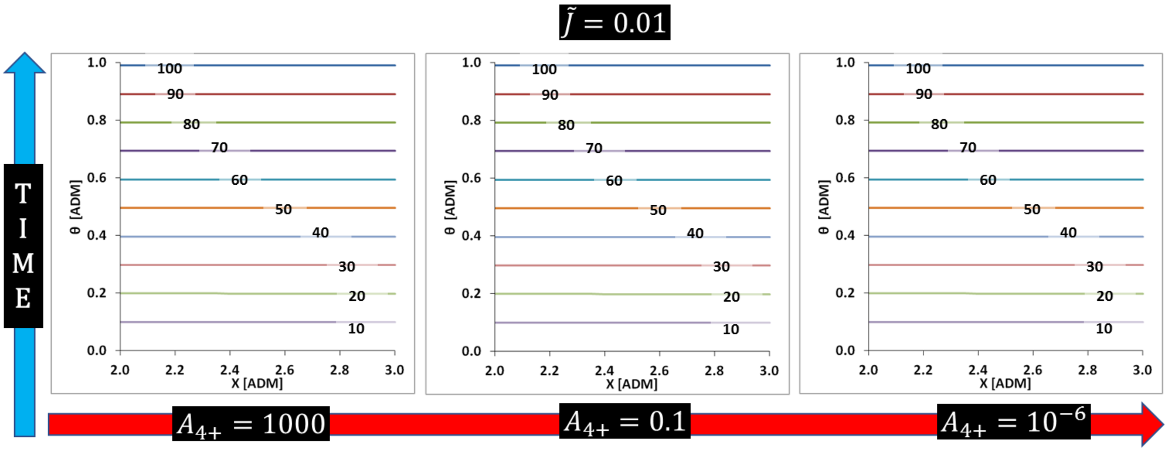

Figure 79 – The concentration of intercalated lithium across the electrode is reported every 10 % of DOD for different values of the parameter A_{4+} for a fixed value of the non-dimensional current $\tilde{J} = 0.01$. The blue arrow indicate the time direction while the red arrow indicate the direction of lower A_{4+}.

The concentration of lithium ions in the electrolyte are reported in Figure 80. The concentration is uniform and constant during the discharge.

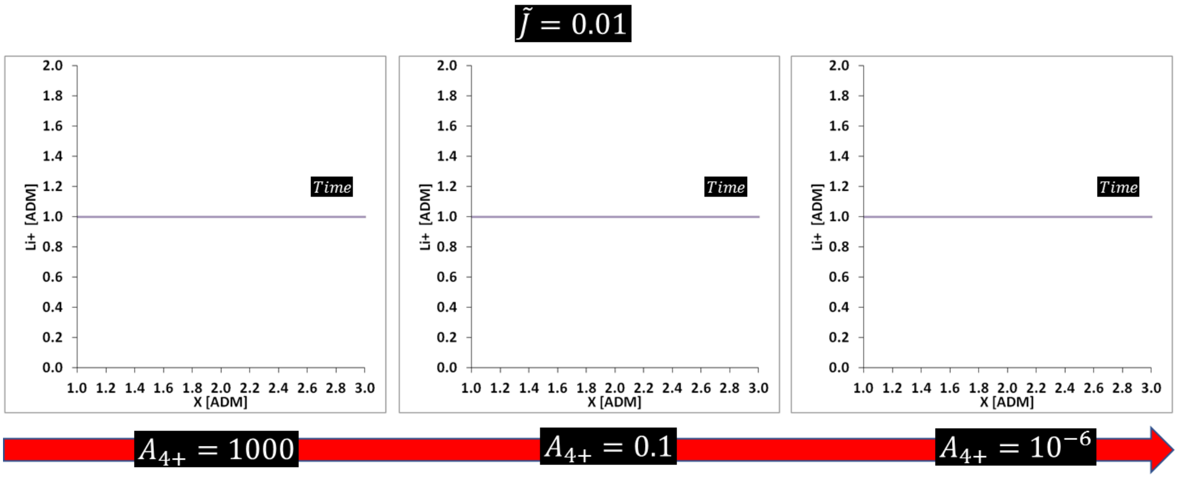

Figure 80 – The concentration of lithium ions in the separator and positive electrode are reported every 10% of DOD for different values of the parameter A_{4+} for a fixed value of the non-dimensional current $\tilde{J} = 0.01$. The red arrow indicate the direction of lower A_{4+}.

The concentration of intercalated lithium inside the particle near the separator (x=2) is reported every 10% of DOD in Figure 81. The concentration is uniform from the inner $(r = 0)$ to the surface $(r = 1)$ for any values of the parameter A_{4+}. This picture is connected at the values reported in Figure 79, inside the particle at the separator $(x = 2)$.

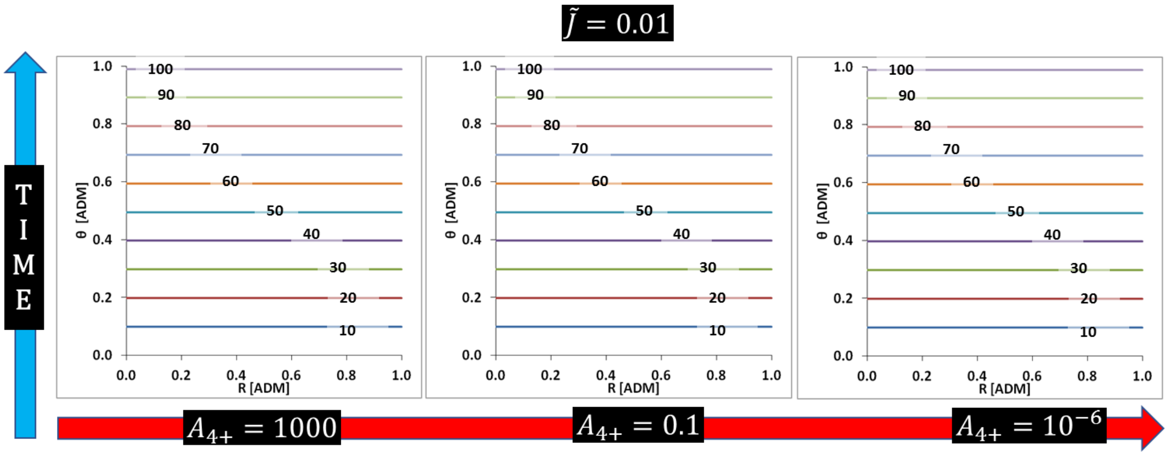

Figure 81 – The concentration as function of the radius for the particle near the separator is reported every 10 % of DOD for different values of the parameter A_{4+} and a fixed value of the non-dimensional current $\tilde{J} = 0.01$. The blue arrow indicate the time direction while the red arrow indicate the direction of lower A_{4+}.

Finally, the profile of the concentration inside the particles of the electrode at the end of the discharge are reported in Figure 82. The concentration is uniform in both dimension x (across the electrode) and r (inside the particles), showing that all the host site in the active material are used for any A_{4+}.

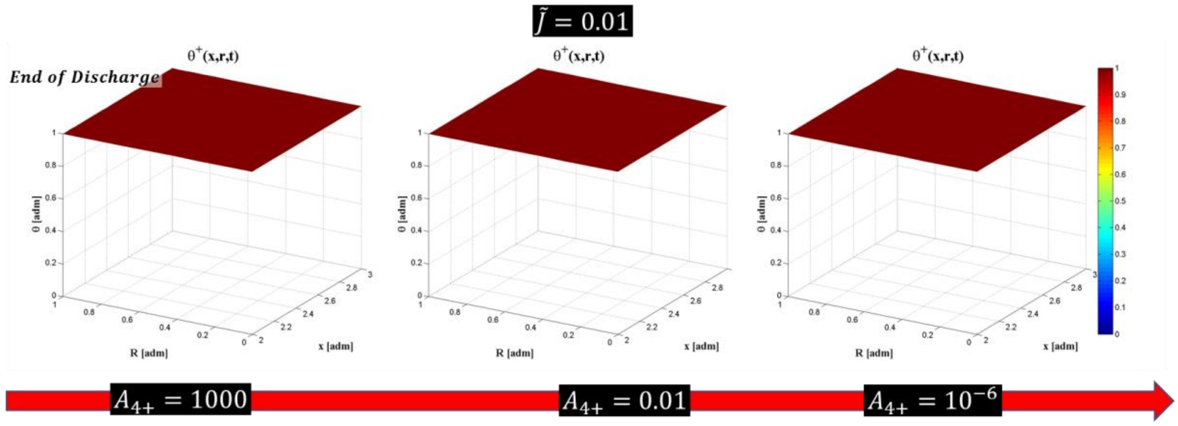

Figure 82 – The profile of the solid phase concentration in the positive electrode (the axis in the bottom of the figures are the electrode thickness and particle radii) is reported at the end of discharge. The red arrow indicate the direction of smaller A_{4+}. The non-dimensional current $\tilde{J} = 0.01$ is a fixed-value.

In conclusion, the kinetic limitation does not influence the concentration in the solid phase nor in the liquid phase, but it only increases the non-ohmic drop. The non-ohmic drop (cf. Figure 78) is not proportional to the current but the voltage drop is constantly translated during the discharge.

The non-ohmic behavior is evidenced in Figure 83, reporting the difference $\xi(\theta)$ between the potential at the equilibrium and the voltage written according to Eq. 79.

$$\xi = \frac{F}{RT}(E - E^0) \qquad \text{Eq. 79}$$

where: θ is 0.85 (i.e. DOD 15%). A logarithmic behavior for $A_{4+} < 0.5$ is observed, in line with the exponent in the Butler-Volmer kinetic law, that is poorly influenced by the θ, θ_i (the initial state of lithiation) or α (the kinetic exponential).

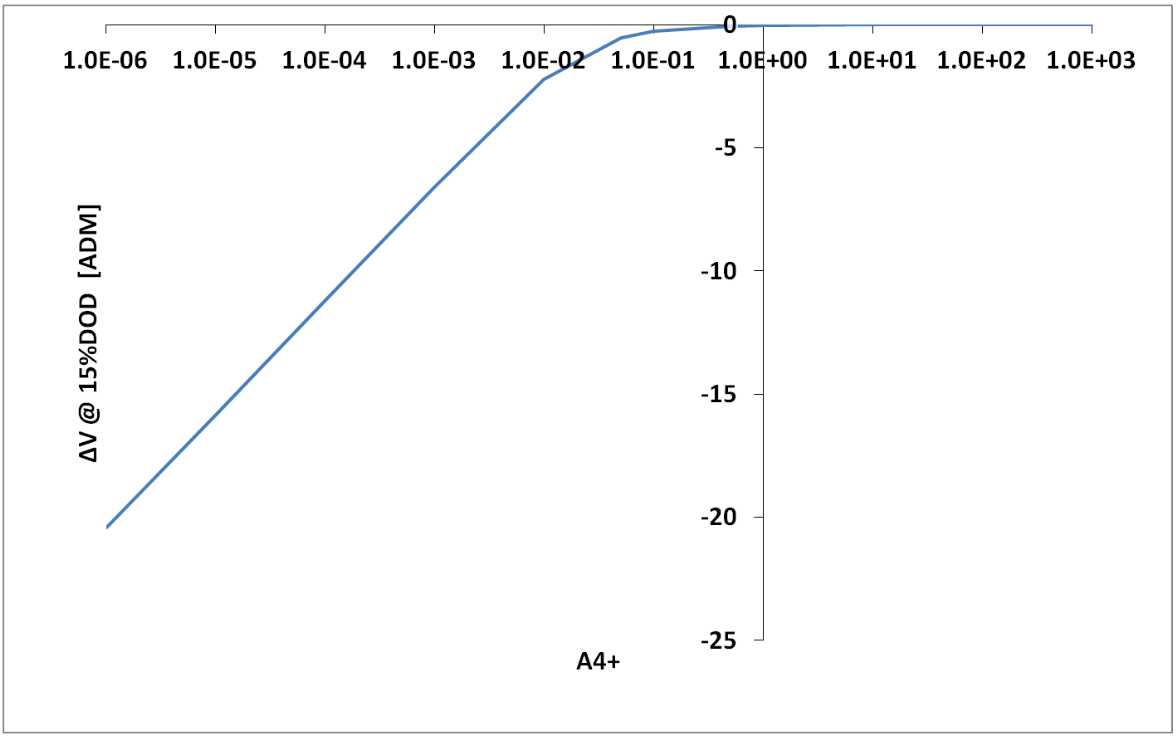

Figure 83 – The overpotential is plotted as function of kinetical parameter A_{4+} in the logarithmic axis-scale at 15% of DOD and a fixed value of the non-dimensional current $\tilde{J} = 0.01$.

The same approach is used in Figure 84 for studying the polarization at 15% of DOD as a function of the non-dimensional current $\tilde{J}$ for various parameters A_{4+}, as seen in Figure 78. The voltage drop is exponential because of the connection with the Butler-Volmer expression.

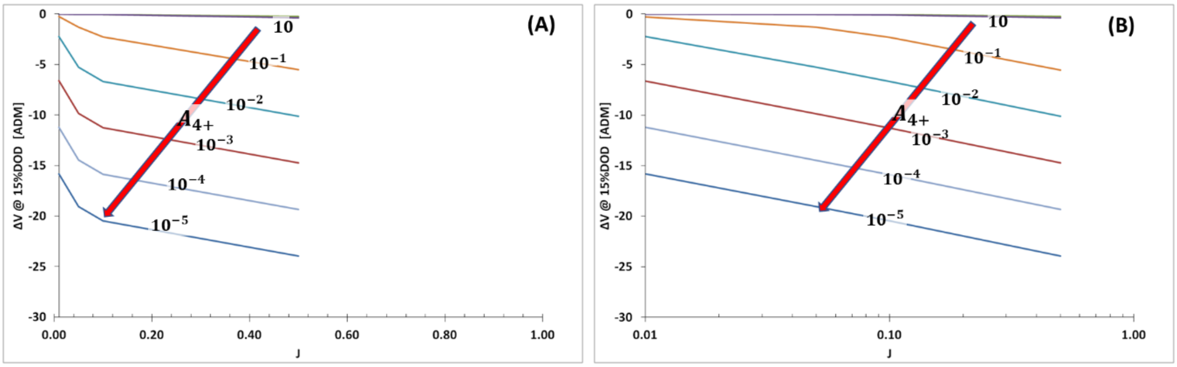

Figure 84 – The overpotential is plotted as function of the non-dimensional current $\tilde{J} = 0.01$ in the linear axis scale (A) and logarithmic axis-scale (B) at 15% of DOD for different values of the kinetical parameter A_{4+}.

These results (Figure 83 and Figure 84) are in contrast with what is obtained from experiments, in Figure 85 and Figure 86. In Figure 85, is reported the discharge voltage for the LGCMH at different current rates. Therefore, the dashed red line, indicates the values of the voltage at 500 mAh (i.e. 15% DOD), that are reported in Figure 86.

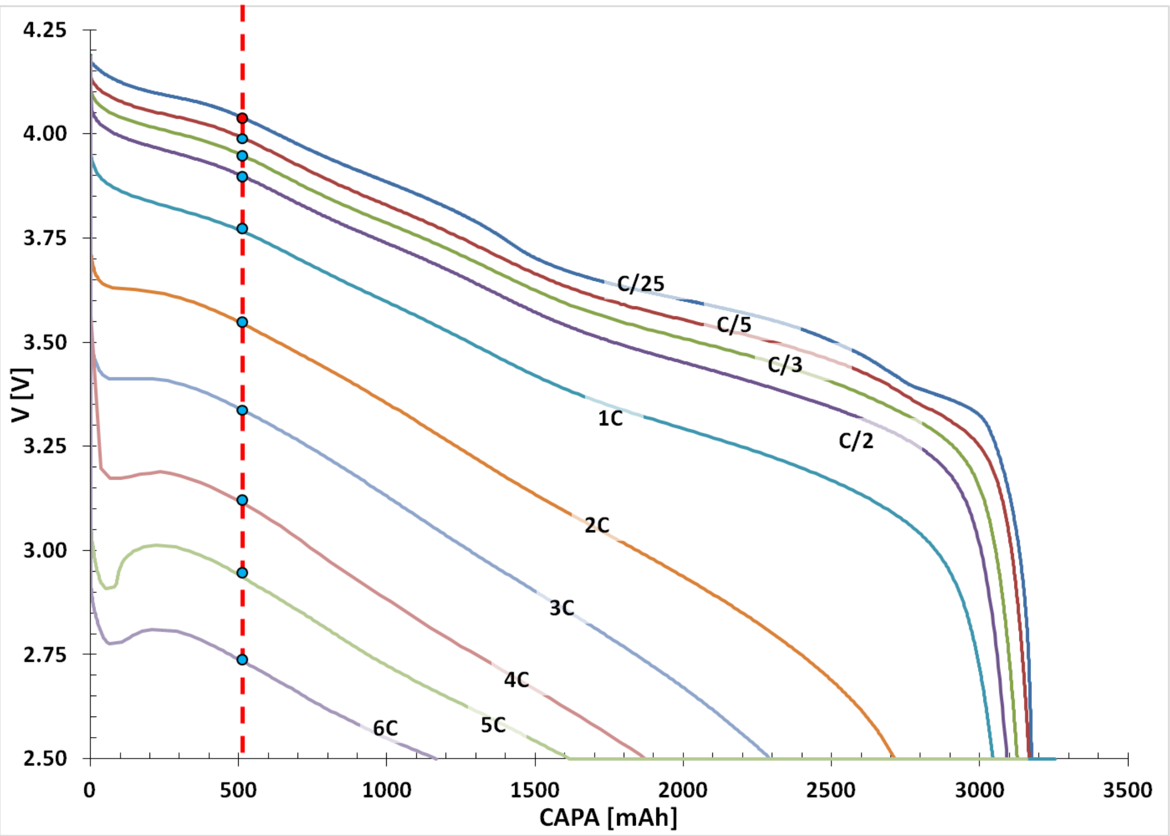

Figure 85 – The discharge voltages as a function of the rated capacity, for the LGCMH, are reported for the C-rates ranging from C/25 to 6C. The red dot indicate the refence voltage, while the blue dots are used to calculate the voltage drop.

The Figure 86 shows that for different current values the behavior is linear, while in Figure 84, the behavior was exponential.

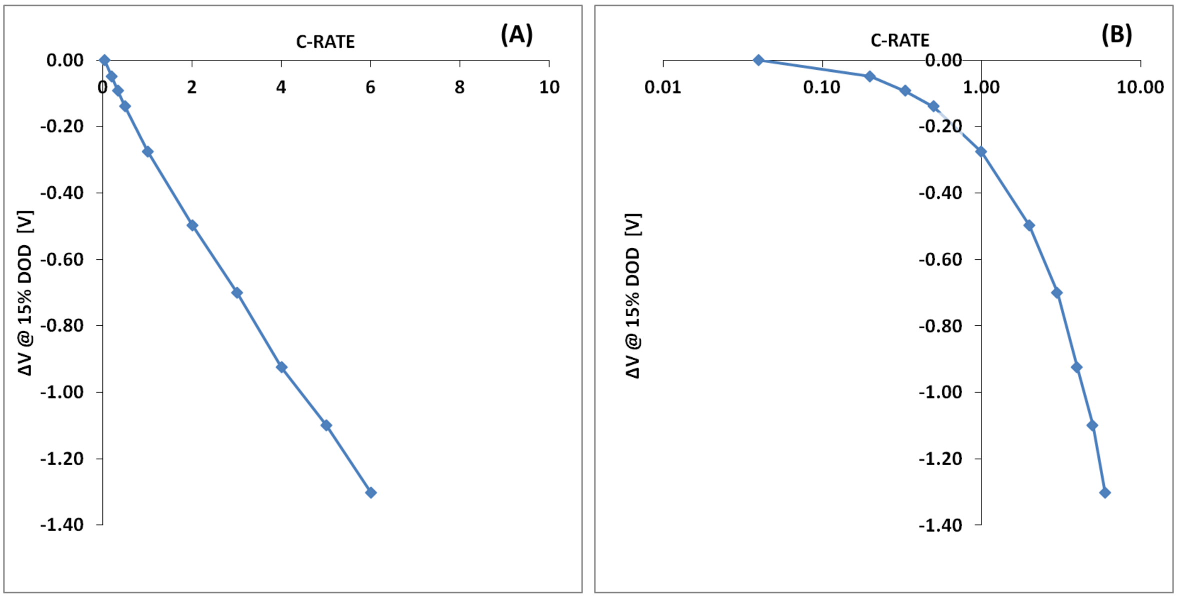

Figure 86 – The voltage drop of the LGCMH for C-rates ranging from C/25 to 6 is reported in either linear (A) and logarithmic axis scale (B) when the battery deliver @ 15% DOD.

In conclusion, the interfacial kinetics limitation is not likely playing a relevant role in the system. Consequently, while the Butler-Volmer relation is maintained, the hypothesis of reversibility is advanced. This will imply a large kinetic constant k^* and consequently $\mathrm{A}_{4+} \gg 1$ in the dimensionless PDE system.

6.1.2 Electrolyte mass transport

The effect of the electrolyte mass transport limitation is isolated with an opportune selection of the non-dimensional parameters, as reported in *Table 33*. The non-dimensional current $\tilde{j} = j\,\frac{d_+}{D_{e+}\,F\,C^*}$ is responsible for the mass electrolyte mass transport limitation in the electrolyte.

CONSTANT PARAMETERS	
$A_{1+} = \frac{RT}{F}\,\frac{\sigma_+}{D_{e+}\,F\,C^*} \gg 1$	$A_{1+} = 1000$
$A_{2+} = \varepsilon_{+s}\,\frac{D_{s+}}{D_{e+}}\,\frac{C_{s,max+}}{C^*}\left(\frac{d_+}{R_{p+}}\right)^2 \gg 1$	$A_{2+} = 1000$
$A_{4+} = \frac{a_+ d_+^2\, k_+^*}{D_{e+}}\quad\frac{C_{s,max+}}{C^*} \gg 1$	$A_{4+} = 1000$

Table 33 – The parameters reported in this table ensure that only electrolyte mass transport limitation can be observed.

The results of the simulations, for different current density rate, are presented in *Figure 87* where the battery voltage as a function of the Depth-Of-Discharge or DOD is shown. The most relevant fact is that the rated capacity depends of the applied current.

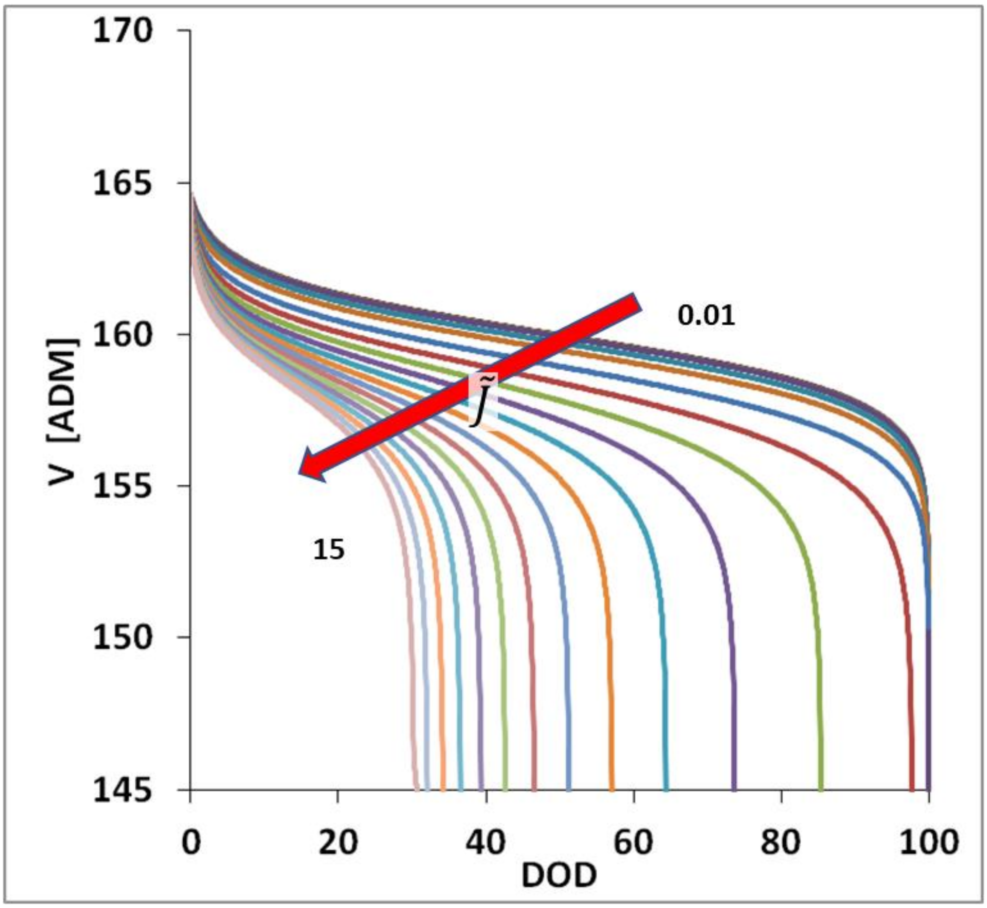

Figure 87 – The battery voltage for different currents are reported in function of the Depth-of-Discharge(DOD).

The reduction of the rated capacity is explained by observing how the concentration of lithium in both solid phase and liquid phase evolves. Across the electrode thickness, the lithium concentration on the particle's surface is reported every 10% of DOD (Figure 88). At the beginning, when the discharge current is low, the concentration of intercalated lithium is uniform along the electrode.

When the current when rise, the concentration of intercalated lithium is predominant in the particles near the separator (x=2). Furthermore, as the particles closer the separator are filled the insertion slips towards the positive current collector (x=3), where non-saturated particles are present. In fact, since the conductivity in the solid phase is large, because $A_{1+} \gg 1$, the electrons can be easily transported in the solid phase. Consequently, the different distribution of concentration in the solid phase is attributed only to the heterogeneous distribution of lithium ions in the solution.

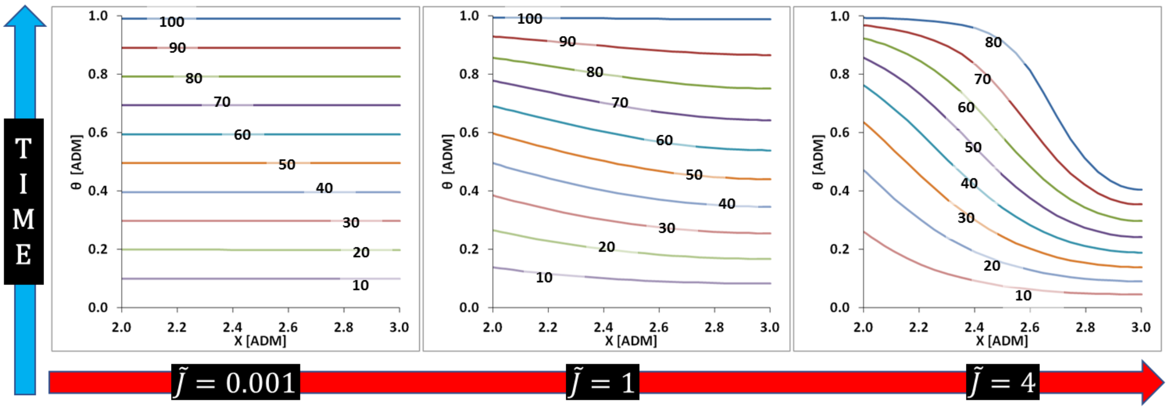

Figure 88 – The concentration of intercalated lithium across the electrode is reported every 10 % of DOD for different current rates.

In fact, the concentration of lithium ions in the electrolyte is reported in Figure 89. When the current is low, the concentration is uniform across both separator and positive electrode. Afterwards, for a high current the concentration rises in the separator and decreases in the electrode. In this condition, a quasi-steady-state of concentration of lithium is reached, because the diffusion in the electrolyte is fast enough to compensate the number of ions consumed during the intercalation. Instead, when the current is too large, the steady state cannot be achieved, and the lithium consumed cannot be replaced. Hereafter, the ions are depleted near the current collector creating a large gradient in the electrolyte concentration. Once somewhere in the electrode, the concentration of lithium ions is zero, the ohmic drop in the electrolyte becomes huge and consequently the cell voltage drops, and the discharge is immediately interrupted.

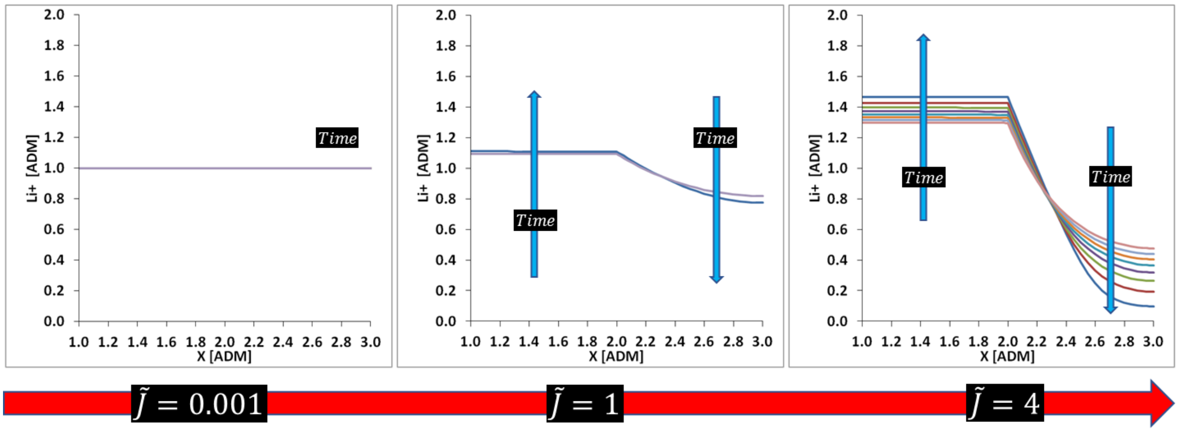

Figure 89 – The concentration of lithium ions in the separator and positive electrode are reported every 10% of DOD for different values of the non-dimensional current. The arrows indicate the evolution of the concentration during the discharge.

It should be noted, that while the concentration of lithium ions rises in the separator while it decreases in the electrode. The reason is found in the mass conservation in the liquid phase as reported in Eq. 80. Moreover, during these simulations the parameters A_{5e} and A_{6e} are equal and consequently the integral of the concentration is constantly 2 during the whole discharge.

$$\frac{A_{5e}}{A_{6e}}\int_{1}^{2}\tilde{C}d\tilde{x} + \int_{2}^{3}\tilde{C}d\tilde{x} = \frac{A_{5e}}{A_{6e}} + 1 \qquad \text{Eq. 80}$$

The profiles of concentration inside the particle near the separator (x=2) (Figure 90), is uniform as expected, because the parameter $A_{2+} \gg 1$, avoid the mass transport limitation in the solid phase.

This image can be interpreted from Figure 88, and looking on at the point near the separator (x=2), as the current increase the concentration in this particle is higher at the beginning and then, when they are filled the insertion slips to particles closer the current collector.

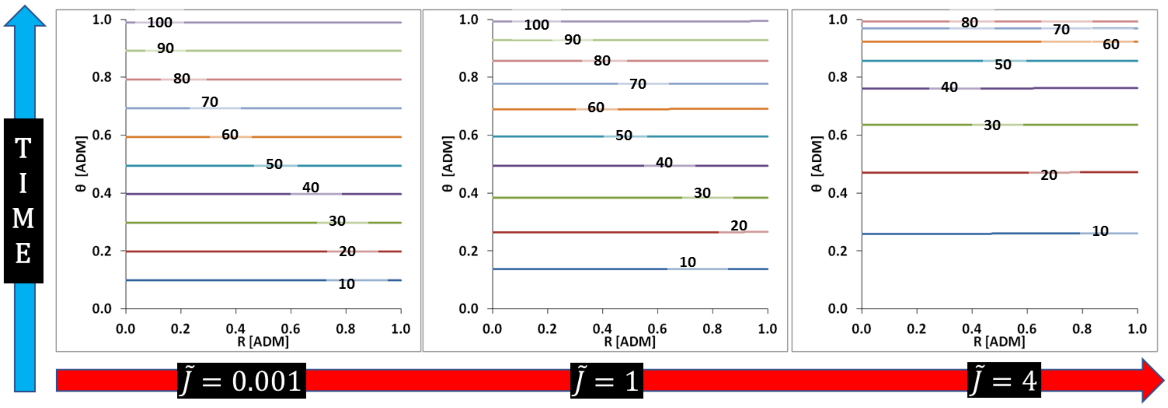

Figure 90 – The concentration as function of the radius for the particle near the separator is reported every 10 % of DOD. The blue arrow indicate the time direction while the red arrow indicate the direction of higher currents.

Finally, in Figure 91 is reported the concentration inside the positive electrode at the end of the discharge. The complete lithiation is reached for J=0.001 and J=1, while for J=4 an underutilization of the active material near the current collector is observed.

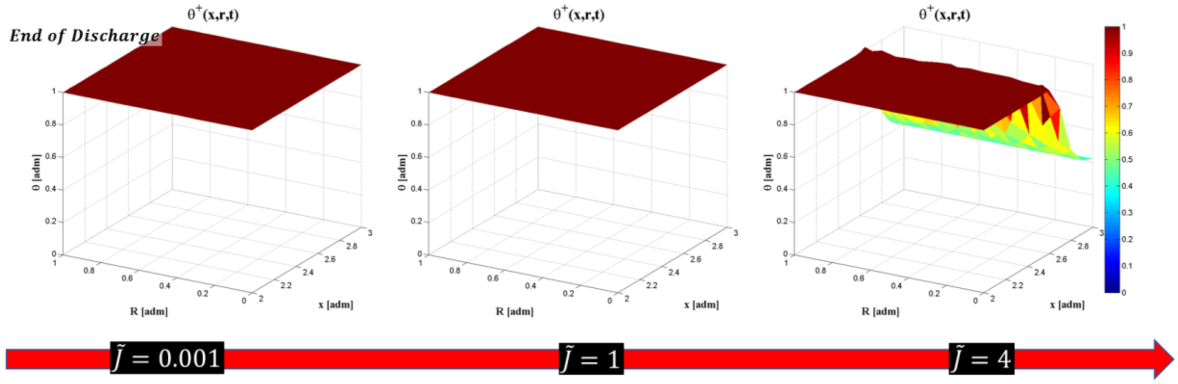

Figure 91 – The profile of the solid phase concentration in the positive electrode (the axis in the bottom of the figures are the electrode thickness and particle radii) is reported at the end of discharge. The red arrow indicate the direction of higher current densities.

The rated capacity as a function of the discharge current is reported in Figure *92* for three values of A_{3+}: 50, 100 and 200. The current reported in Figure *92*(A) is in a linear scale, while in Figure *92* (B) is logarithmic. We can conclude that A_{3+} do not influence the rated capacity.

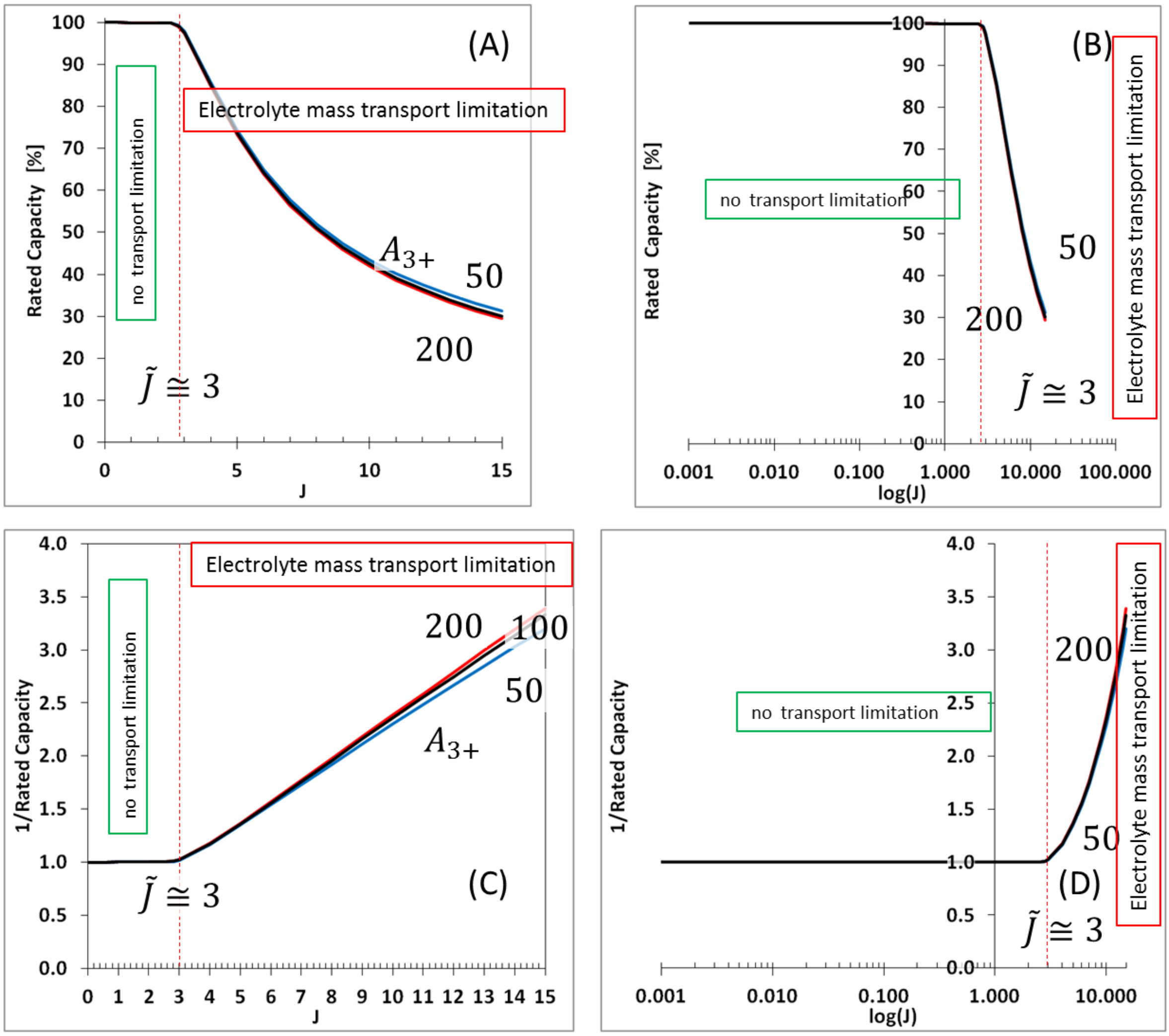

Figure 92 – The rated capacity is reported as a function of the non-dimensional current in both linear (A) and logarithmic (B) scales. The inverse of the rated capacity as a function of the non-dimensional current in linear is reported in (C) and in logarithmic axis in (D).

The effect of the electrolyte limitation on the rated capacity can be better investigated by plotting the inverse of the rated capacity as a function of the non-dimensional current in either linear scale Figure 92 (C) and logarithmic scale Figure 92 (D). When the current is close to 3 the limitation occurs and the rated capacity follows a straight line, as predicted by the analytical expression of Johns et al.[251] . This value is the frontier for the mass transport limitation i.e. for lower values the rated capacity is not affected. The shape of the curve is scarcely influenced by the parameter A_{3+} because in practices $A_{3+} \gg 1$ and we can conclude that mass transport limitation is mostly dependent of the effective electrolyte diffusivity rather than the electrode porosity. This can be explained because the large amount of the lithium ions that intercalate cannot be initially contained in the electrolyte, but they must be transported from the negative electrode through the separator.

The draw in Figure 93 , schematically illustrate the situation when the electrolyte limits the rated capacity. The lithiated particles are solid in black and the lithium ions in the electrolytes is represented in the electrodes with vertical stripes. The white color indicates the particles non-entirely lithiated and the electrolyte depleted in lithium ions. The discharge is interrupted because the particle non-entirely lithiated are surrounded with solvent without ions.

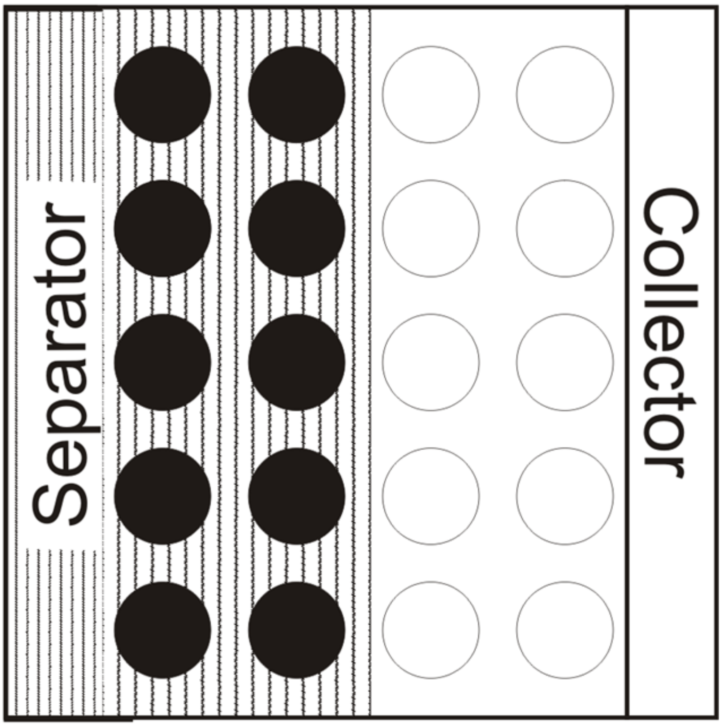

Figure 93 – The schematics of a porous electrode when mass transport limitations in electrolyte interrupt the discharge.

An equivalent electric circuit can be used for a better understating of the limitations observed and creates a bridge between the electrochemical and the electrical models. In fact, the transmission line model (TLM) is an advanced equivalent electrical circuit able to partially represent the behavior of porous electrodes, Figure 94.

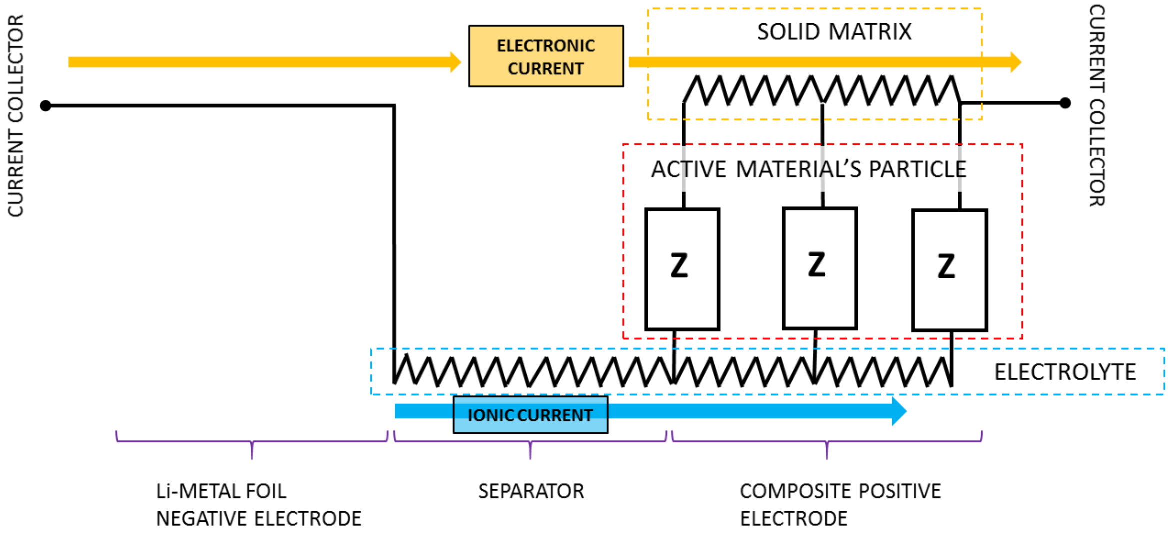

Figure 94 – The general representation of the Transmission Line Model (TLM) for the half-cell is reported. The impedances represents the diffusion in the active material particles, and the resistances the voltage drop in the electrolyte and solid phase matrix. The arrows indicate the ionic current and the electronic current, respectively.

The equivalent situation of this limit case is reported in Figure 95, where the impedances and the resistance in the solid phase can be seen as short circuits. When the particles are entirely lithiated the system act like an open circuit. Furthermore, when the mass transport limitation occurs the electrolyte resistance is seen as an open circuit because the ohmic drop becomes infinite (i.e. the lithium ions are depleted and no current can flow).

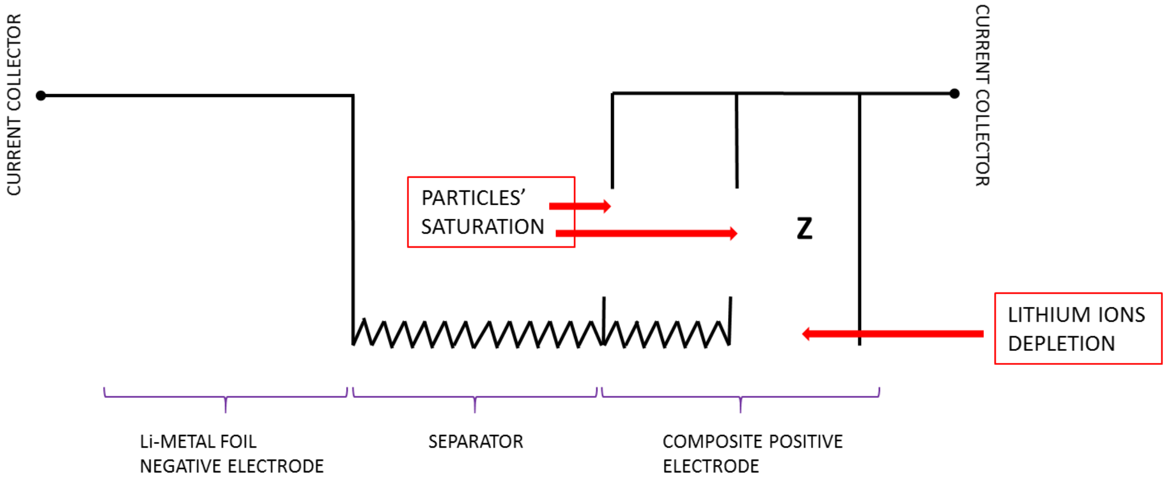

Figure 95 – The equivalent TLM is reported when the electrolyte mass transport limitation occurs.

6.1.3 Electronic transport

The electronic transport limitation is discussed in this section. A small current is applied ($\tilde{J} \ll 3$) to avoid any mass transport limitation in the electrolyte, as concluded from § 6.1.1. The other limitations are avoided with the opportune choice of the parameters reported in Table 34.

CONSTANT PARAMETERS	
$A_{2+} = \varepsilon_{+s} \dfrac{D_{s+}}{D_{e+}} \dfrac{C_{s,max+}}{C^*} \left(\dfrac{d_+}{R_{p+}}\right)^2 \gg 1$	$A_{2+} = 1000$
$A_{4+} = \dfrac{a_+ d_+^2\, k_+^*}{D_{e+}} \dfrac{C_{s,max+}}{C^*} \gg 1$	$A_{4+} = 1000$
$A_{3+} = \dfrac{\varepsilon_{+s}}{\varepsilon_{+l}} \dfrac{C_{s,max+}}{C^*} = 100$	$\tilde{J} = 0.01$

Table 34 – The parameters reported in this table ensure that only electronic transport limitation can be observed.

The simulations are performed for different non-dimensional values of the parameter A_{1+}, Eq. 81, that is associated to electronic conductivity.

$$A_{1+} = \frac{RT}{F} \frac{\sigma_+}{D_{e+}\, F\, C^*} \qquad \text{Eq. 81}$$

The voltage drop is higher for low values of A_{1+}, as expected because of the poor conductivity, but conversely, the rated capacity is not reduced (Figure 96). Since the voltage drop is proportional to the applied current it can be called as an ohmic-drop but it is not constant during the discharge. The opposite situation was observed for the kinetic limitations of section 6.1.1, where the non-ohmic drop (voltage drop non-proportional to the applied current) reproduce a voltage plateau during the discharge.

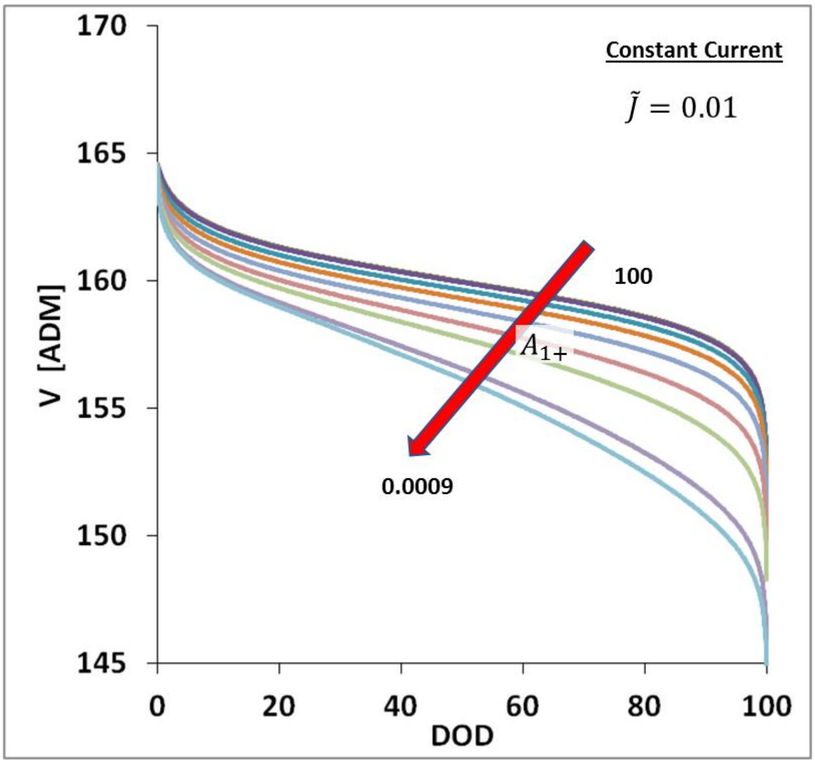

Figure 96 – The cell voltage during the discharge is reported as a function of the DOD for J=0.01.The values used for A_{1+} in the simulations are: $100, 10, 1, 10^{-1}, 10^{-2}, 5 \cdot 10^{-3}, 3 \cdot 10^{-3}, 2 \cdot 10^{-3}, 1.5 \cdot 10^{-3}, 10^{-3}, 9 \cdot 10^{-4}$.

The profiles of lithium concentration in the electrode's particles are reported in Figure 97 for A_{1+} = 10, 0.01 and 0.0009. For high conductivity, the concentration is uniform every 10% of DOD and across the entire electrode. Instead, for low conductivity, the insertion is predominant in the particles near the current collector (x=3). Once these particles are almost fully intercalated, the insertion slips toward the separator where empty particles are still available but it is required a large potential drop to move electrons at the insertion site.

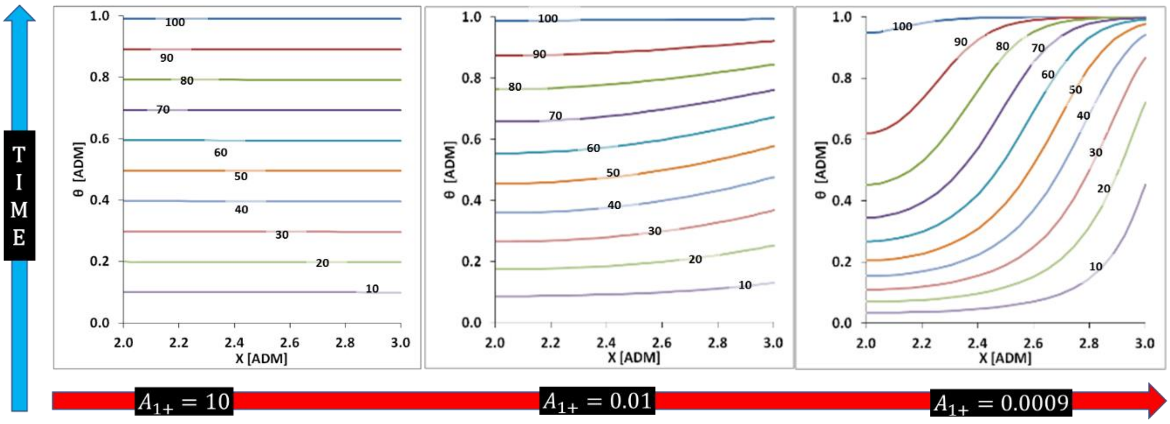

Figure 97 – The profiles of the concentration of intercalated lithium in the positive electrode are reported every 10% of DOD. The blue arrow indicates the time direction during the discharge, while the red arrow indicates the direction of lower parameters A_{1+} .

Instead, the concentration of ions in the electrolyte is constant, as expected, since this transport limitation is avoided with the chosen value of $\tilde{J}$ (Figure 98).

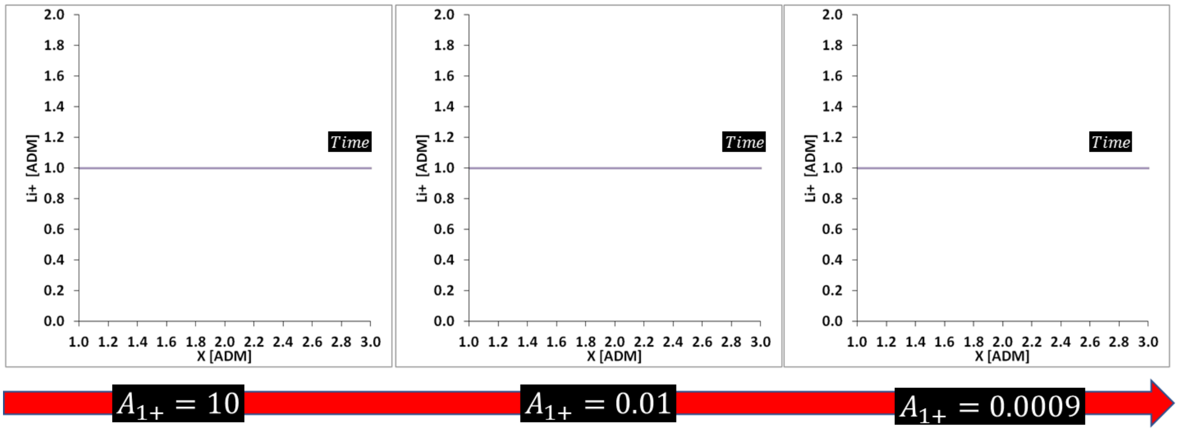

Figure 98 – The concentration of lithium ions in the electrolyte is constant during the whole discharge for any A_{1+}.

In Figure 99, is reported the concentration inside the particle close to the separator (x=2). The concentration of lithium is uniform in each particle, as expected, because no transport limitation in the particles occurs with the chosen value of A_{2+}. Instead, the concentrations between two levels of DOD are not constants, for small values of A_{1+}, as seen in Figure 97 for x=2.

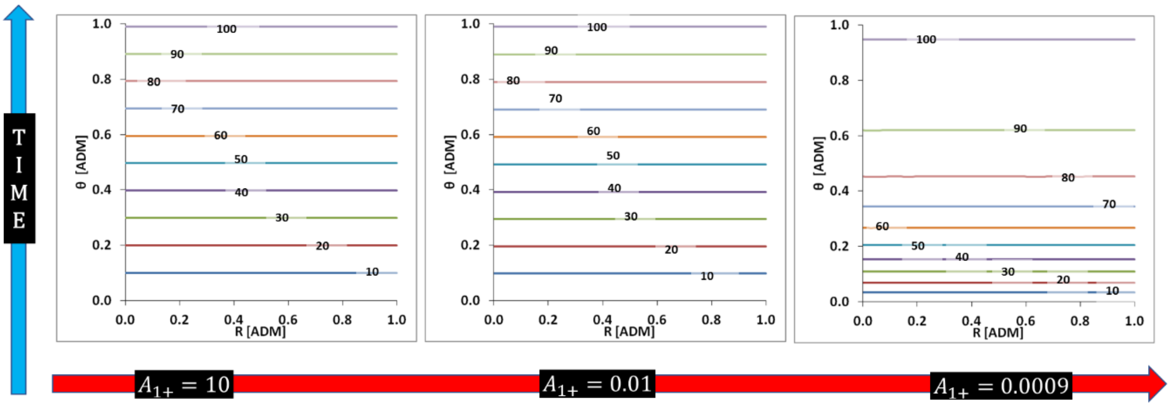

Figure 99 – The concentration as function of the radius for the particle near the separator is reported every 10 % of DOD. The blue arrow indicate the time direction while the red arrow indicate the direction of smaller A_{1+}.

In case of electron transport limitation, at the end of the discharge, all the particles reach the same state of lithiation (Figure 100). All the active material is used and consequently the rated capacity is constant for any A_{1+}.

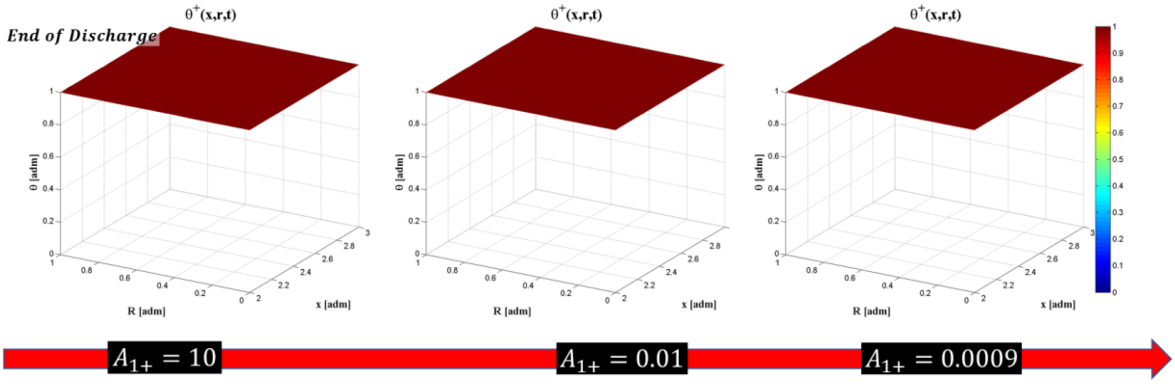

Figure 100 – The profile of the solid phase concentration in the positive electrode (the axis in the bottom of the figures are the electrode thickness and particle radii) is reported at the end of discharge. The red arrow indicate the direction of smaller A_{1+}.

Like in § 6.1.2, the so called TLM, (Figure 94) is used to explain this limit case with an electrical model.

In this case, the electrolyte resistance and the charge transfer/diffusion impedances are short circuits, because no transport limitations are involved. However, the impedances became open circuit, and no current can flow once the particles are fully lithiated.

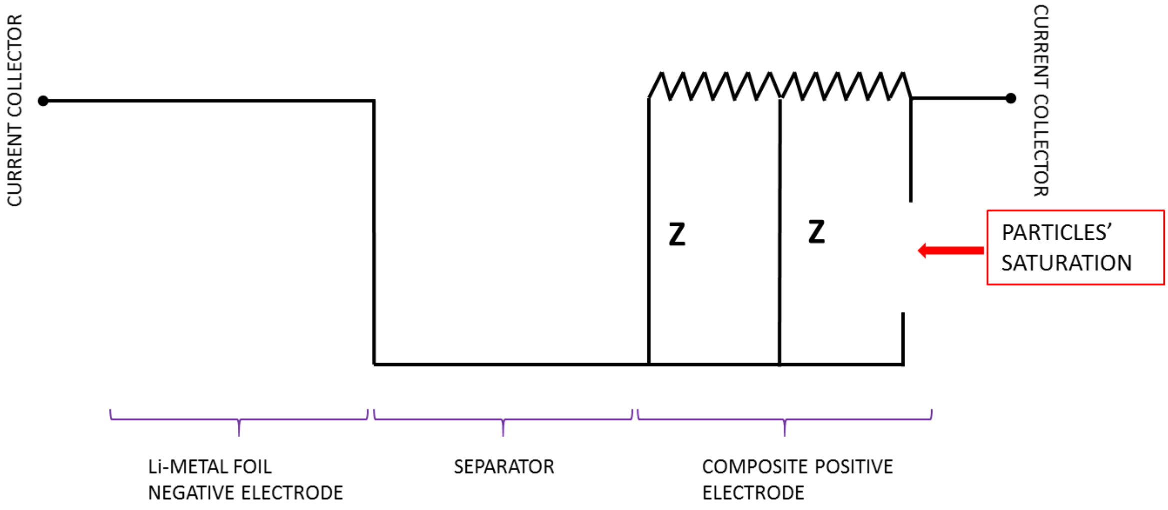

Figure 101 – The TLM is represented when the electronic transport limitation occurs.

6.1.4 Solid phase diffusivity

In this case, the solid phase mass transport limitation is discussed. Thus, a sufficient small current is applied $(\tilde{J} \ll 3)$ to avoid any mass transport limitation in the electrolyte, as studied in § 6.1.1.

The other limitations are avoided with the opportune choice of the parameters reported in Table 35.

CONSTANT PARAMETERS	
$A_{1+} = \frac{RT}{F} \frac{\sigma_+}{D_{e+}\, F\, C^*} \gg 1$	$A_{1+} = 1000$
$A_{4+} = \frac{a_+ d_+^2\, k_+^*}{D_{e+}} \frac{C_{s,max+}}{C^*} \gg 1$	$A_{4+} = 1000$
$A_{3+} = \frac{\varepsilon_{+s}}{\varepsilon_{+l}} \frac{C_{s,max+}}{C^*} = 100$	$\tilde{J} = 0.01$

Table 35 – The parameters reported in this table ensure that only the solid phase mass transport limitation can be observed.

The non-dimensional parameter expressing the solid phase diffusivity is A_{2+} and its expression is reported in Eq. 82.

$$A_{2+} = \varepsilon_{+s} \frac{D_{s+}}{D_{e+}} \frac{C_{s,max+}}{C^*} \left(\frac{d_+}{R_{p+}}\right)^2 \qquad \text{Eq. 82}$$

The galvanostatic discharge simulations show that the rated capacity decreases for low values of the parameter A_{2+}, Figure 102. The rated capacity is below 100% when $A_{2+} \approx 0.1$. The reason of such reduction of the rated capacity, are found from the analysis of the profiles of the concentration in either solid and liquid phases.

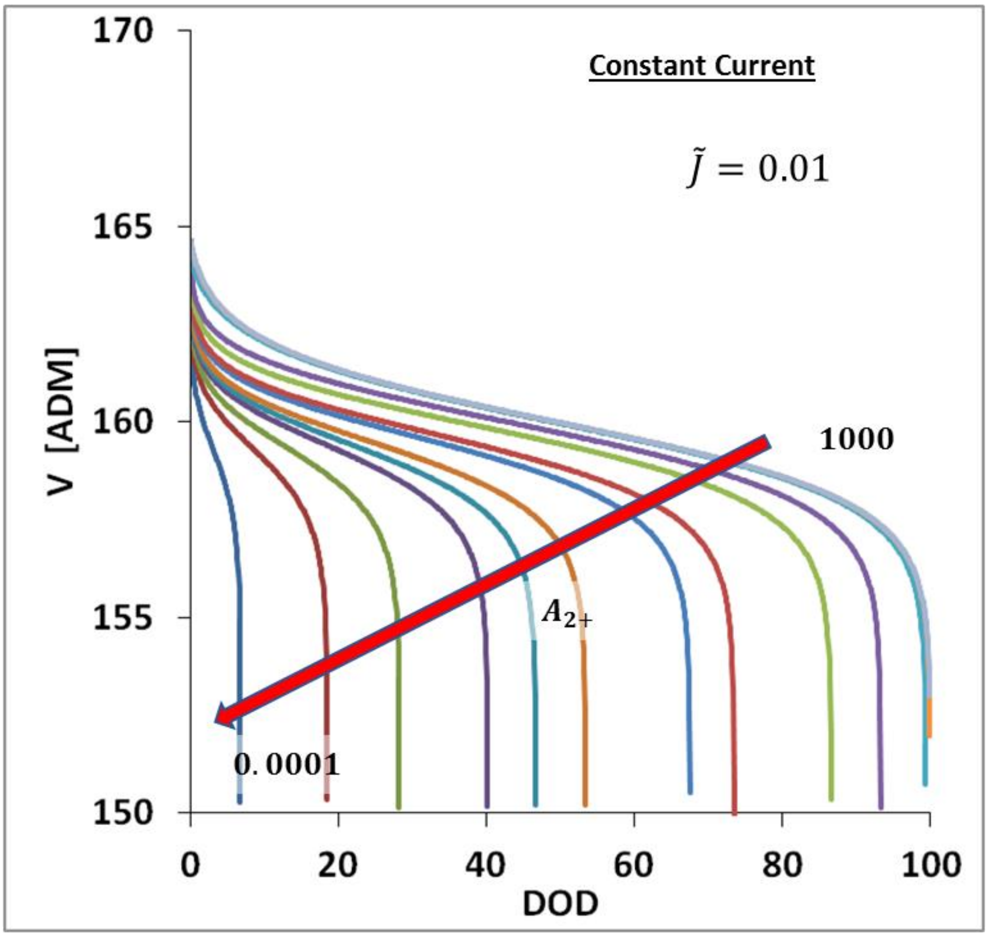

Figure 102 – The simulations of the cell voltage during the galvanostatic discharge in terms of DOD for the following non-dimensional parameters A_{2+}: $1000, 10, 1, 10^{-1}, 5 \cdot 10^{-1}, 10^{-2}, 2.5 \cdot 10^{-3}, 2 \cdot 10^{-3}, 1.25 \cdot 10^{-3}, 10^{-3}, 8 \cdot 10^{-4}, 5 \cdot 10^{-4}, 3 \cdot 10^{-4}, 10^{-4}$.

The concentration of intercalated lithium at the particle's surface is uniform in the electrode thickness, because there is no transport limitation in the solid phase nor in the liquid phase, as reported in Figure 103. However, the amount of concentration is not equidistant from two levels of DOD for a low value of the parameter A_{2+}. In fact, for $A_{2+} = 0.001$ the discharge is interrupted for a DOD between 40% and 50 %, while the concentration at the surface in all the particles are saturated. The active material is evidently underused.

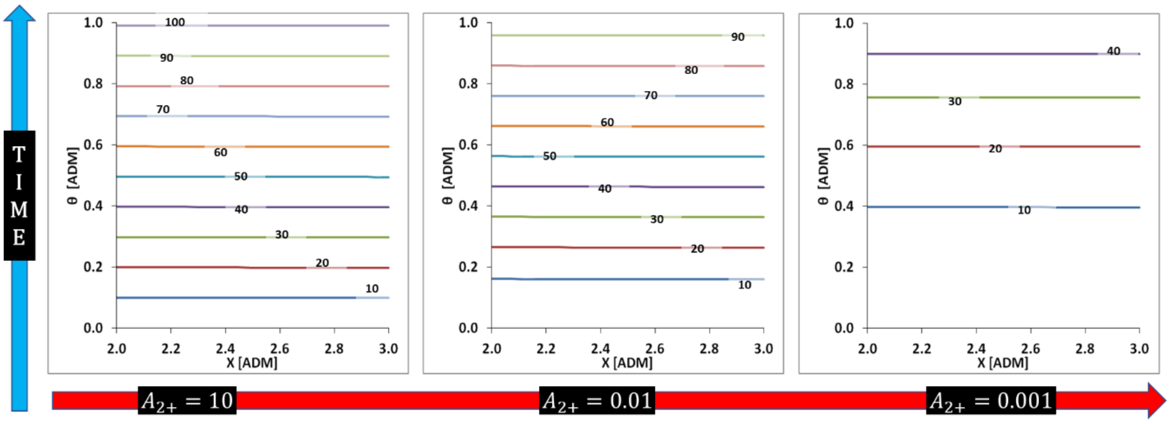

Figure 103 – The profiles of the concentration of intercalated lithium at the particle's surface in the positive electrode are reported every 10% of DOD. The blue arrow indicates the time direction during the discharge, while the red arrow indicates the direction of lower parameters A_{2+} .

Instead, the concentration of lithium ions in the electrolyte is constant, as expected, since the electrolyte transport limitation is avoided with a non-limiting value of $\tilde{J}$ (Figure 104).

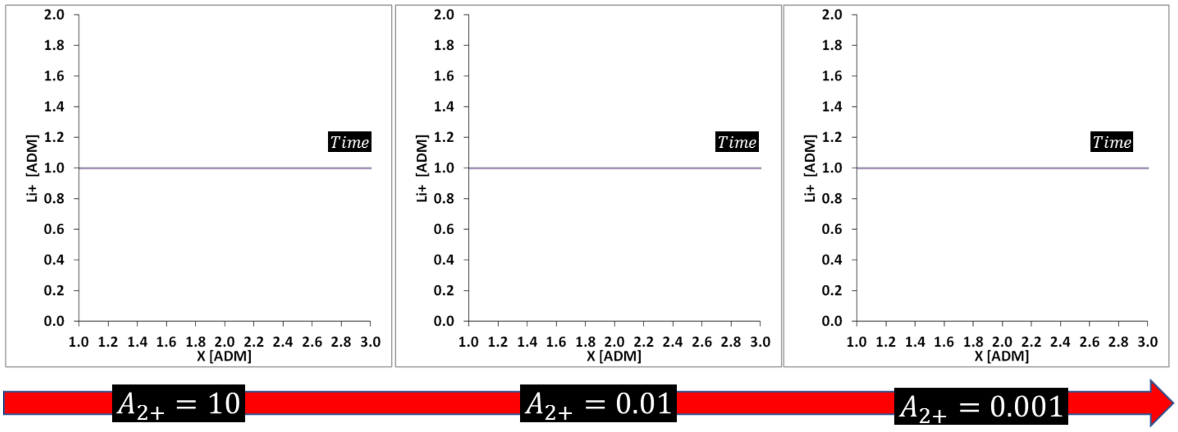

Figure 104 – The concentration of lithium ions in the electrolyte is constant during the whole discharge for any value of the parameter A_{2+}.

Figure 105 reports the concentration inside the particle near the separator (x=2). If the value of the parameter A_{2+} is sufficient the profile of concentration is uniform in the particle, and the level of concentration is constant for any DOD. Contrarily, when the parameter A_{2+} is small, a gradient of the lithium concentration in the solid phase is observed. Furthermore, the concentration of the intercalated lithium is predominant on the particle's surface (r=1), while its core stays empty (r=0) or at least with a lower concentration. In fact, once the lithium intercalates in the particles surface (r=1), because of the small parameter A_{2+}, the transport of lithium toward the core of the particle is very slow compared to the insertion on the particles surface.

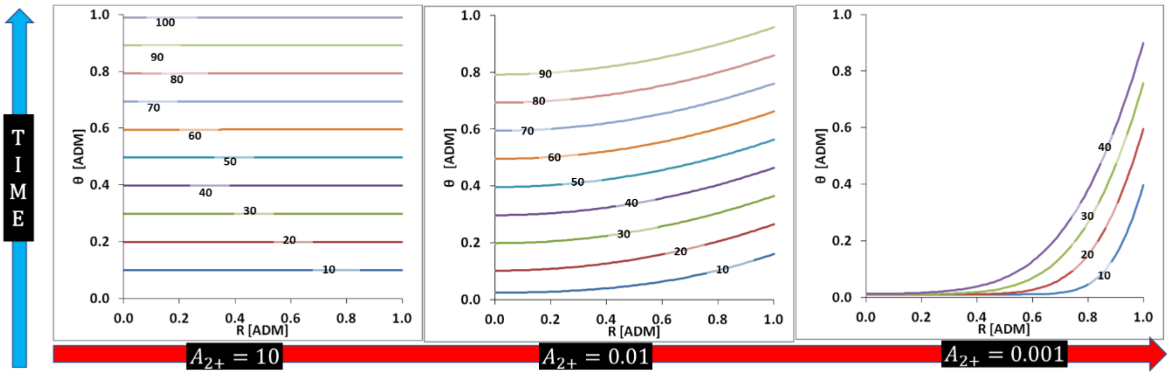

Figure 105 – The concentration as function of the radius for the particle near the separator is reported every 10 % of DOD. The blue arrow indicate the time direction while the red arrow indicate the direction of lower values of the parameter A_{2+}.

The concentration inside all the particles of the electrode at the end of the discharge is reported in Figure 106. This picture, like Figure 103, evidences that the concentration is uniform in all the particles. In the picture at the left side, where the parameter A_{2+} is higher, there is no gradient of concentration inside the particles. When the parameter A_{2+} decreases, the gradient inside the particles became more and more important, as shown in the picture at the right side. In this case, when the concentration at the particles' surface (r=1) reaches the maximum value the discharge is immediately interrupted, because no lithium can intercalate anymore. This underutilization of the active material explains why when the parameter A_{2+} is small (e.g. associated to the active materials particle size and diffusivity), the rated capacity decreases.

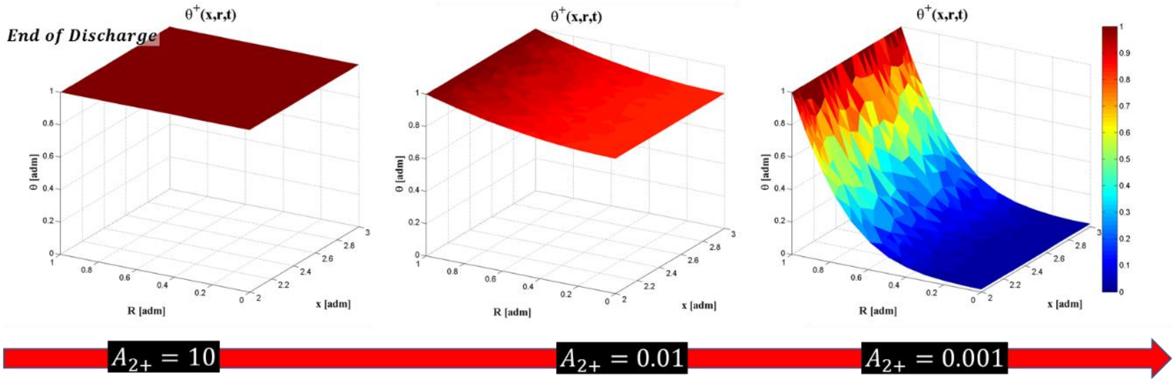

Figure 106 – The profile of the solid phase concentration in the positive electrode (the axis in the bottom of the figures are the electrode thickness and particle radii) is reported at the end of discharge. The red arrow indicate the direction of lower values of the parameter A_{2+}.

The draw in Figure 107, schematically represents the mass transport limitation in the solid phase when it limits the rated capacity. This picture illustrate a porous electrode with the separator and the current collector, at the left side and the right side, respectively. The vertical stripes represent the concentration of lithium in the electrolyte. The while the particles are darker in the outer surface and clearer in the core with a grey scale transition in between indicating the gradient of concentration. In fact, the particles are always surrounded with enough lithium ions in the electrolyte, that is necessary for the intercalation, but the poor diffusion in the particles creates a gradient of concentration in their core with a saturation of lithium on the surface. When the surface of the particles is saturated, the intercalation is interrupted and the rated capacity is smaller than the total capacity.

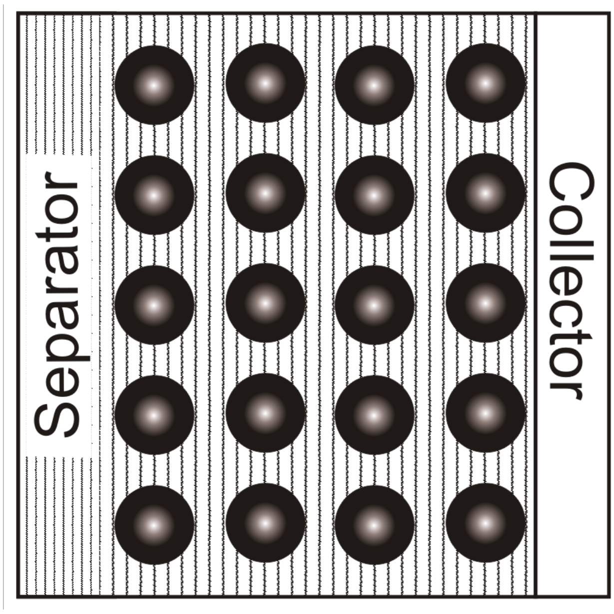

Figure 107 – The schematics of a porous electrode when the solid phase limitations interrupt the discharge.

In conclusion, a better utilization of the active material can be achieved when the particles are smaller and consequently the active surface is higher.

The transmission line model (TLM) reported in *Figure 94*, is used to schematically visualize, the mass transport limitation in the solid phase, as reported in Figure 108. For instances, there are no resistances associated to transport limitation, however once the particles are saturated the system acts like an open circuit (no charge transfer reactions allowed) and the discharge is interrupted.

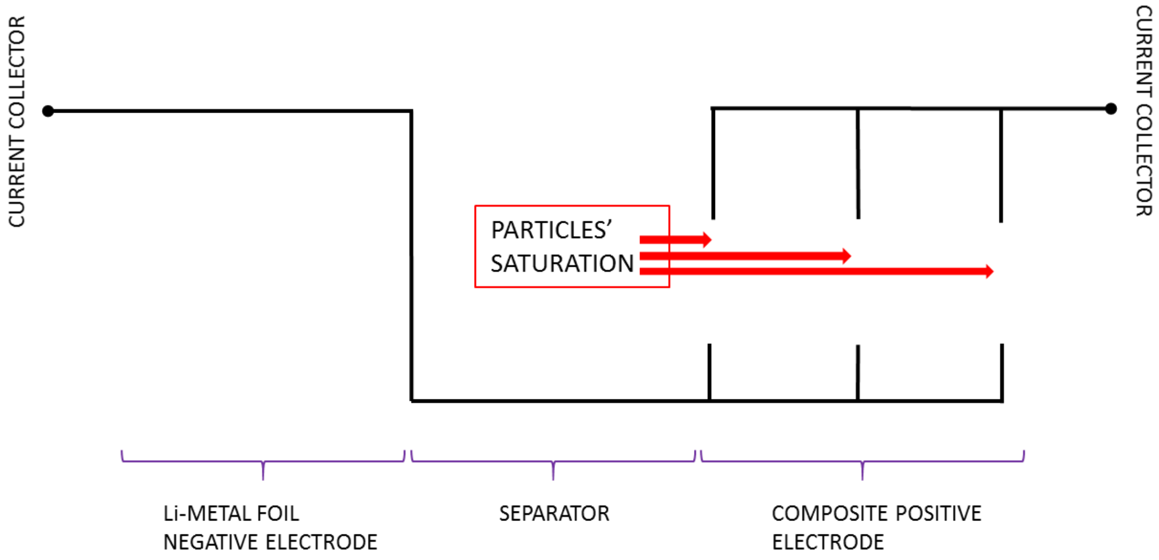

Figure 108 – The TLM is illustrates the situation when the solid phase mass transport limitation occurs.

6.1.5 Mixed case: solid phase diffusivity and electronic transport

In this case are studied the combination of both electronic transport (A_{1+}) and solid phase mass transport (A_{2+}) limitations. Like in the previous studies, a sufficient small current is applied $(\tilde{J} \ll 3)$ to avoid any electrolyte mass transport limitation.

The other kinetic limitations are avoided with the opportune choice of the parameters reported in Table 36.

CONSTANT PARAMETERS	
$A_{4+} = \dfrac{a_+ d_+^2\, k_+^*}{D_{e+}} \quad \dfrac{C_{s,max+}}{C^*} \gg 1$	$A_{4+} = 1000$
$A_{3+} = \quad \dfrac{\varepsilon_{+s}}{\varepsilon_{+l}} \dfrac{C_{s,max+}}{C^*} = 100$	$\tilde{J} = 0.01$

Table 36 – The parameters reported in this table ensure that the combination and solid phase diffusivity and electronic transport can be observed.

The cell voltage during the discharge simulation is reported in Figure 109 for different parameters A_{1+} and three values for the parameter A_{2+}: 0.001, 0.002 and 0.003.

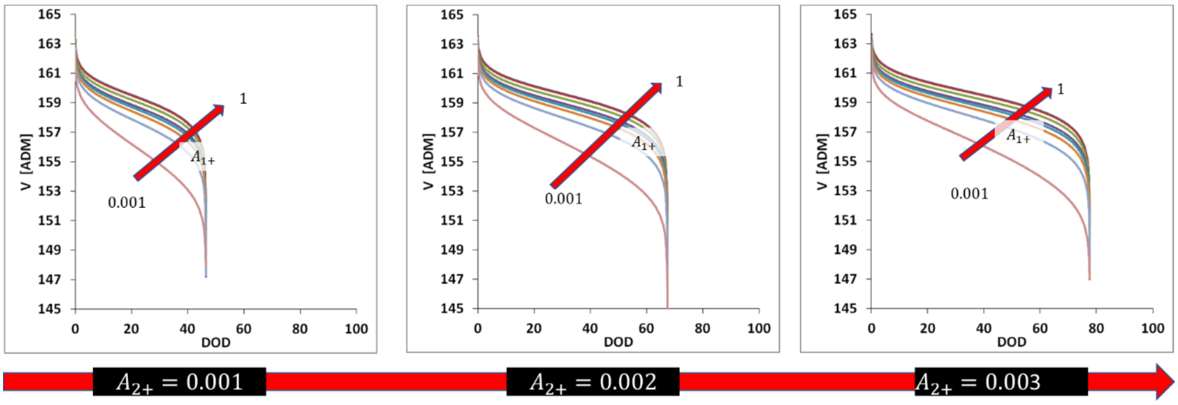

Figure 109 – The cell discharge voltages are traced as function of the DOD for different values of A_{2+}:0.001, 0.02 and 0.03 and different values for the A_{1+}. This latter ranges from 1 to 0.001.

The simulations clearly show that for a given solid phase parameter, the electronic transport parameter does not impact the rated capacity. Thus, there is no interaction betwheen the solid phase diffusion limitation with the electronic transport.

As the electronic conductivity decreases, the intercalation is predominant near the positive current collector because the voltage drop for their transport is minimized. At the same time, the diffusion in the solid phase creates a gradient inside the particles of the active material. Consequently, there is a gradient of lithium in the solid phase in either electrode thickness (x-axis) and particles radius (r-axis), Figure 110.

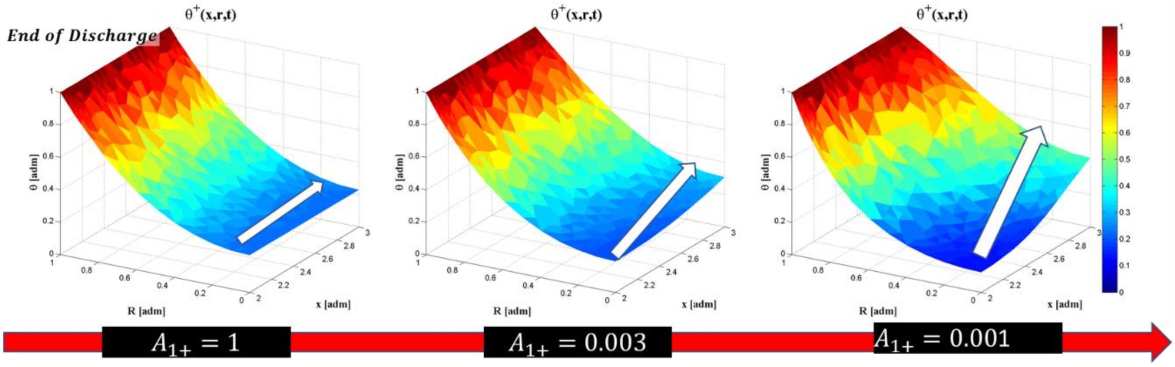

Figure 110 – The profile of the solid phase concentration in the positive electrode (the axis in the bottom of the figures are the electrode thickness and particle radii) is reported at the end of discharge. The red arrow indicates the direction of lower values of the parameter A_{1+} for the assigned value of $A_{2+} = 0.03$. The white arrows pointing toward the current collector, indicate the concentration gradient in the electrodes thickness, that increases for lower values of A_{1+}. The white arrows indicate the gradient of concentration toward x-direction.

6.1.6 Mixed case: solid phase diffusivity and electrolyte diffusivity

In this case are studied the interactions between the solid phase mass transport (A_{2+}) and the electrolyte mass transport ($\tilde{J}$). The other limitations are avoided with the opportune choice of the parameters reported in Table 37.

CONSTANT PARAMETERS	
$A_{1+} = \frac{RT}{F}\frac{\sigma_+}{D_{e+}\,F\,C^*} \gg 1$	$A_{1+} = 1000$
$A_{4+} = \frac{a_+ d_+^2\,k_+^*}{D_{e+}}\frac{C_{s,max+}}{C^*} \gg 1$	$A_{4+} = 1000$
$A_{3+} = \frac{\varepsilon_{+s}}{\varepsilon_{+l}}\frac{C_{s,max+}}{C^*} = 100$	

Table 37 – The parameters reported in this table ensure that the combination of the solid phase diffusivity and the electrolyte diffusivity can be observed.

The simulations of the discharge voltage are reported in Figure 111, for different combination of A_{2+} and $\tilde{J}$.

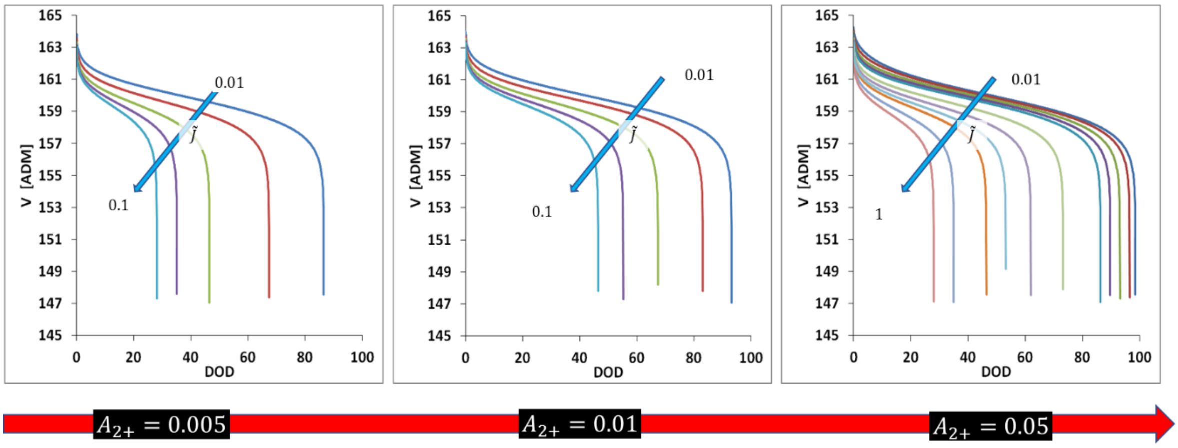

Figure 111 – The cell discharge voltage is reported as a function of the DOD, for different values of A_{2+}: 0.005, 0.01 and 0.05. The non-dimension current $\tilde{J}$ ranges from 0.01 to 0.1 when A_{2+} is 0.005 and 0.01, while $\tilde{J}$ ranges from 0.01 to 1 when A_{2+} is 0.05.

The rated capacity in these conditions is deeply influenced. Therefore, how the parameter A_{2+} influences the rated capacity as a function of the applied non-dimensional current $\tilde{J}$ is reported in Figure 112(A) and Figure 112(B) for the linear axis scale and logarithmic axis scale, respectively. In this figure, the rated capacity due to solid phase mass transport limitations decreases, as expected, but when electrolyte limitations occur, the rated capacity decreases much more. The limit condition is expressed for $A_{2+} = 1000$ when no mass transport in the solid phase occur and only the electrolyte limitations acts. Thus, for $\tilde{J} > 3$ both transport limitation occurs simultaneously, while for $\tilde{J} < 3$ the solid phase transport limitation is predominant. When $\tilde{J} > 3$ the reduction of the rated capacity is enhanced by low values of A_{2+}.

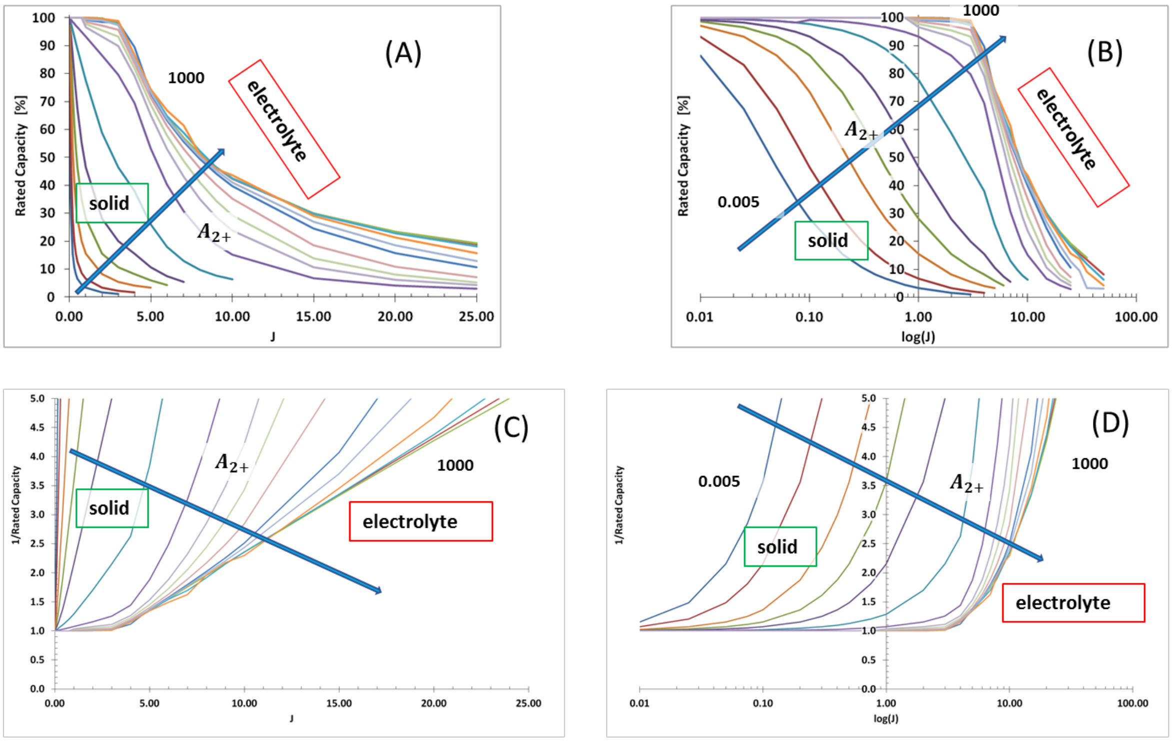

Figure 112 – The rated capacity and its inverse are reported as a function of the non-dimensional current in either linear and logarithmic scale. The arrow indicates the direction of lower values for the parameter A_{2+} .

The previous are reported in Figure 112(C) with the y-axis indicates the inverse of the rated capacity. The arrow indicates the direction of lower values for the parameter A_{2+}. The regions where the contribution of the respective limitations is predominant are evidenced, like in Figure 112(A), but with this representation, the effects of electrolyte limitation are more evident. In conclusion, the combination of both diffusion limitation in the solid phase and the transport in the electrolyte influences more the rate capacity than these limitations acting separately.

6.1.7 Mixed case: electronic transport and electrolyte mass transport diffusivity

In this case are studied the combined limitation of the electronic transport (A_{1+}) and the electrolyte mass transport ($\tilde{J}$). The other limitations are avoided with the opportune choice of the parameters reported in Table 38.

CONSTANT PARAMETERS	
$A_{2+} = \varepsilon_{+s} \dfrac{D_{s+}}{D_{e+}} \dfrac{C_{s,max+}}{C^*} \left(\dfrac{d_+}{R_{p+}}\right)^2 \gg 1$	$A_{2+} = 1000$
$A_{4+} = \dfrac{a_+ d_+^2\ k_+^*}{D_{e+}} \quad \dfrac{C_{s,max+}}{C^*} \gg 1$	$A_{4+} = 1000$
$A_{3+} = \quad \dfrac{\varepsilon_{+s}}{\varepsilon_{+l}} \dfrac{C_{s,max+}}{C^*} = 100$	

Table 38 – The parameters reported in this table ensure that the combination of electronic transport and electrolyte mass transport limitation can be observed.

The simulations of the discharge voltage are reported in Figure 113, each picture represents a simulation conducted with a different value of A_{1+} while the non-dimensional current density varies from 0.01 to 15 as indicated by blue arrows.

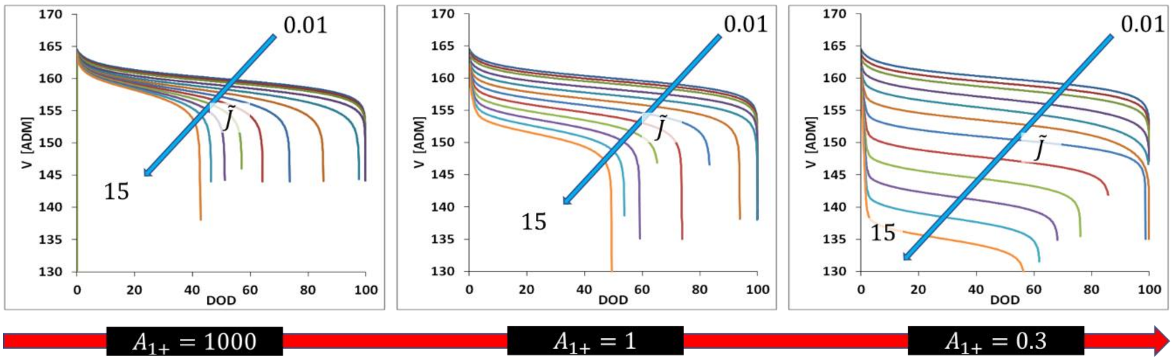

Figure 113 – The cell voltage during the discharge is reported as a function of the DOD. The values for the parameter A_{1+} *are 1000, 1 and 0.3, while the non-dimensional current density* from 0.01 to 15.

The mass transport in the electrolyte and the electronic conductivity are coupled and their interaction is more complex than in previous cases. In fact, while the voltage drop is expected for lower values of the parameter A_{1+}, how it contributes to increase the rated capacity for the same dimensionless current $\tilde{J}$ is more complex. In practice, for the same value of the non-dimensional current density, the rated capacity is slightly higher obtained when the electronic transport is more difficult.

This situation is investigated for $\tilde{J} = 15$ for different values of the parameter A_{1+}. For this value, when no electronic transport limitations occur, the rated capacity is the 35% of the available capacity. When the transport limitations increase, the rated capacity increases as reported in Figure 114.

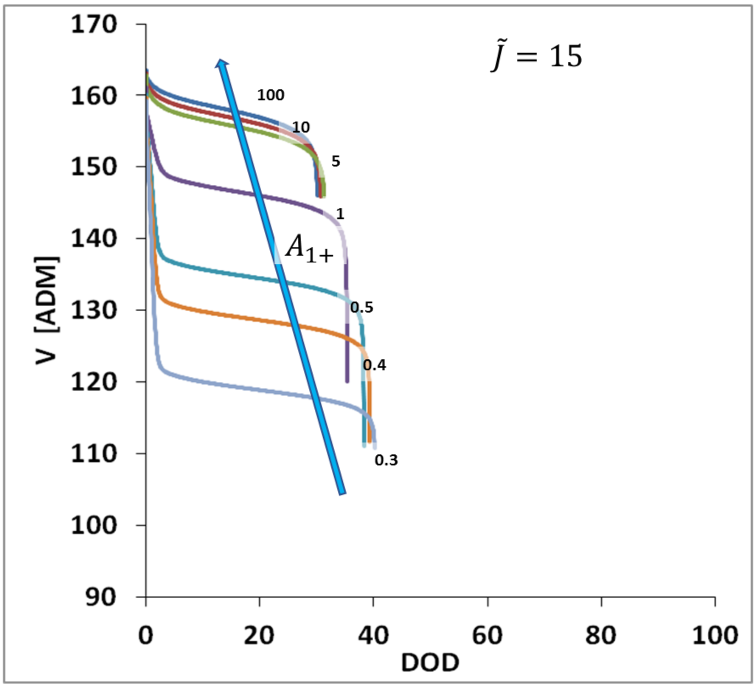

Figure 114 –The simulations of the discharge cell voltage are reported for a dimensionless current $\tilde{J} = 15$ while the parameters A_{1+} ranges from 1000 to 0.3.

The analysis of Figure 115 is helpful for understanding how the electronic conductivity is involved. The picture reports the concentration in the solid phase at the surface of the particles (R=1) across the electrode from the separator (x=2) to the current collector (x=3). The beneficial effects due to a low conductivity are still present but limited to 5 to 10 % in gains of the rated capacity. In fact, if the electrons are not easily transported in the solid matrix, a balance between the tendency to intercalate near the separator, where the lithium ions are abundant, and the tendency to intercalate near the current collector, where the electrons are abundant, is established. However, when the electrolyte transport limitations are stronger, the insertion is predominant near the separator and the conductivity is not able to uniform the insertion across the electrode, Figure 115.

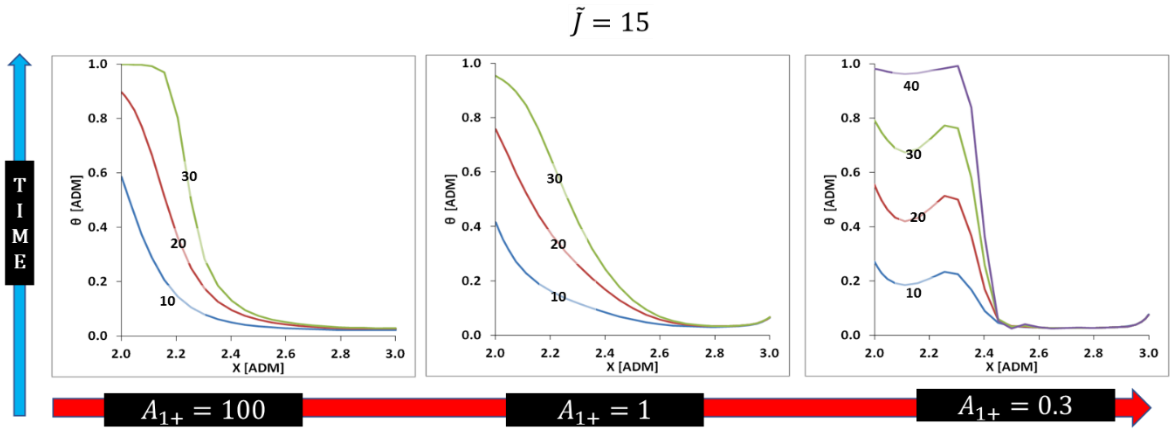

Figure 115 – The concentration of intercalated lithium across the electrode, at the particles' surface (R=1) is reported every 10 % of DOD. The red arrow indicates the direction of lower values of the parameter the parameter A_{1+} =100, 1, 0.3. The non-dimensional current is fixed to $\tilde{J} = 15$. The blue arrow indicates the direction of the discharge time.

The profiles of the concentration of lithium ions in the electrolyte are reported in Figure 116. The limited transport of lithium ion in the electrolyte creates a lithium poor area, near the current collector (x=3). When the concentration in the electrolyte drop to zero somewhere, the ohmic drop in the electrolyte rises in the reactions and the discharge is interrupted. In such a condition, the reduction of conductivity is positive because it forces the lithium to intercalate near the current collector and the lithium ions gains some time diffuse where their presence is required. Consequently, the cell discharge is immediately interrupted, and the active material is underutilized.

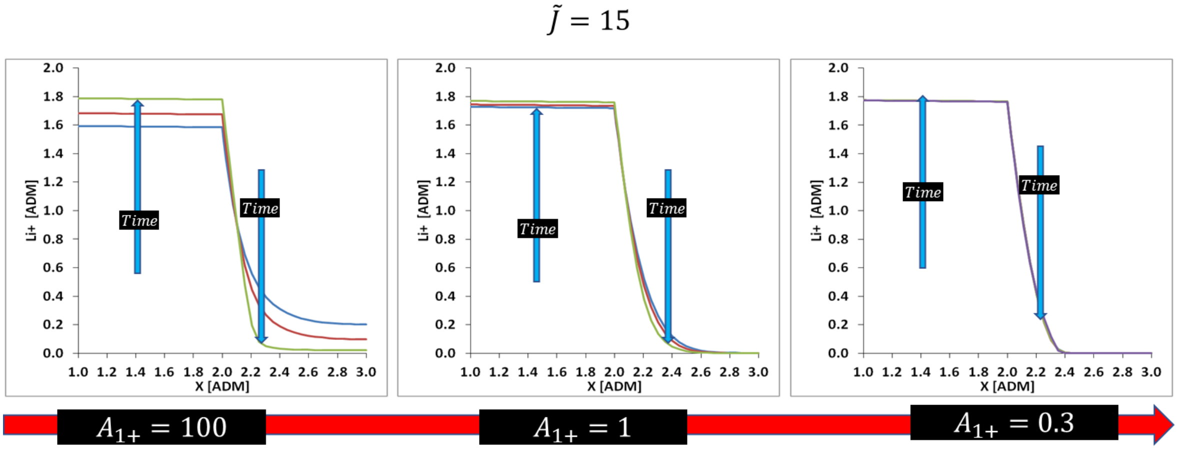

Figure 116 – The concentration of lithium ions in the electrolyte is reported for a fixed value of the non-dimensional current $\tilde{J} = 15$ and three different values of the parameter A_{1+} = 100, 1, 0.3. The profiles of concentration indicate a variation of 10% in the DOD. The blue arrow indicate the evolution of these profiles during time.

The rated capacity, as function of the applied current density for the values of the parameter A_{1+} indicated before is reported in Figure 117. In Figure 117(B) the inverse of the rated capacity as a function of the logarithm of the current density shows a linear slope, typical of the electrolyte mass transport limitation. The red dashed line, represent the condition where no electronic transport limitations occurs. When the electronic transport limitation increases, the curve translates and the gain in terms of rated capacity is evidencedin the yellow dashed box: the rated capacity decrease for $\tilde{J} \cong 3$ when $A_{1+} = 100$, while rated capacity shifts to $\tilde{J} \cong 6$ when $A_{1+} = 0.3$. In conclusion, when the parameter A_{1+} decreases, it is possible to slightly mitigate the reduction of the rated capacity induced by the electrolyte mass transport limitation.

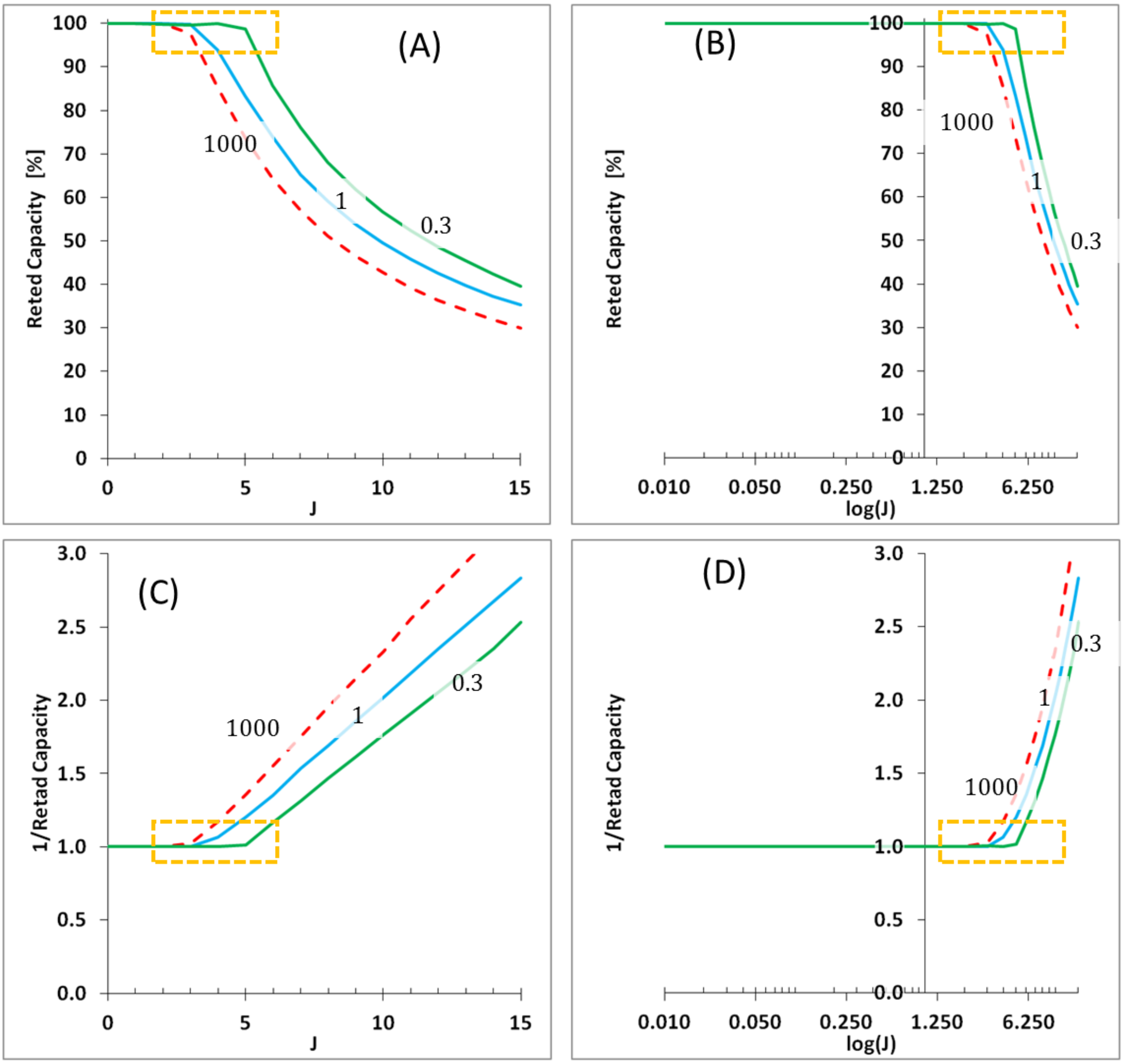

Figure 117 – In (A)The rated capacity is reported as a function of the current density for the values of the parameter A_{1+} = 1000, 1, 0.3. The inverse of the rated capacity is shown in (B) evidencing its linear behaviour.

6.1.8 Conclusions and perspectives

In this chapter some limiting factor have been studied and general results are obtained. It seems to be possible to identify or to exclude which one of the transport limitations is acting in a real cell by looking on the relation of the rated capacity vs C-rate. In fact, in Figure 76 (B) the cells [A] and [B] seems to be limited by the solid phase transport (linear behaviour), while the cell [C] is limited by electrolyte transport (constant and then linear reduction of the rated capacity).

Furthermore, the polarization at a given DOD can provide additional information on the nature of the transport limitation. As an example, in Figure 118 is reported the combination of solid and liquid phase mass transport limitations in Figure 118(A) and the combination of electronic transport and liquid phase mass transport limitations in Figure 118(B). Looking on the polarization at 20 % of DOD, the voltage drop is completely different. Thus, how the voltage drops is influenced by the transport limitation, should be investigated in further studies.

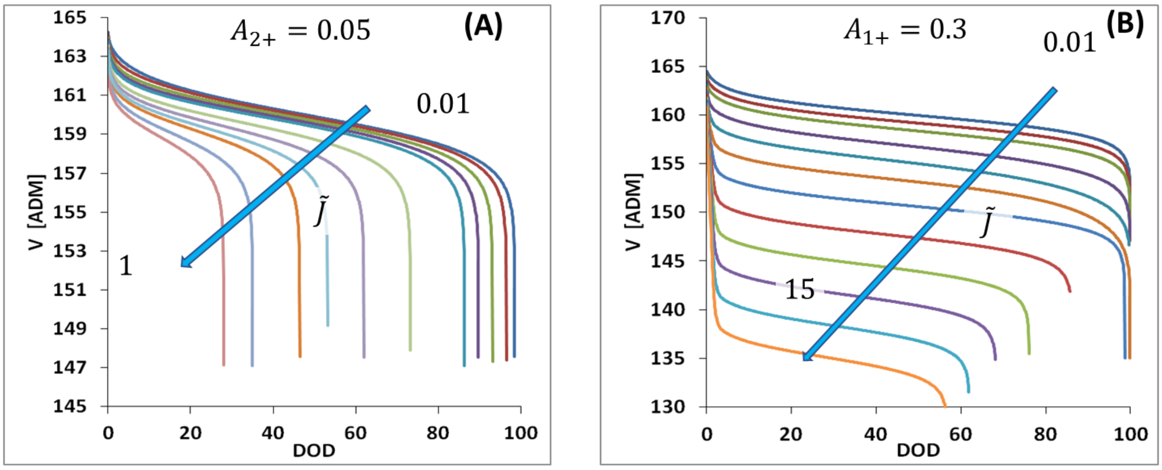

Figure 118 – The cell discharge voltage is reported as a function of the DOD, for different values of the non-dimension current $\tilde{J}$ in case of solid phase mass transport limitation A_{2+} in (A) or electronic limitation A_{1+} in (B).

6.2. Pulse-rest sequences

6.2.1 Introduction

The pulse-rest sequences are widely used for characterizing the internal resistance, the diffusion coefficient or the OCV. In this chapter, the measurement of voltage relaxation and of the solid phase diffusion coefficient, the time constants of this electrochemical model and the simulations of the pulse-rest sequences are discussed.

In the literature is reported the simplest equivalent electrical circuit able to simulate approximatively the dynamics of a lithium ion cell's, shown in Figure 119 [253]–[257]. In details, the internal resistance R_O represents the ohmic drop associated to charge transfer and conductivity in the components (e.g. harness, electrolyte, solid phase matrix). The resistance R_D – capacitance C_D parallel branch is attributed to a physic and chemical phenomena such as the charge transfer and representing the cell dynamics. These linear electrical components require several tests to be identified as functions of the SOC, temperature and SOH

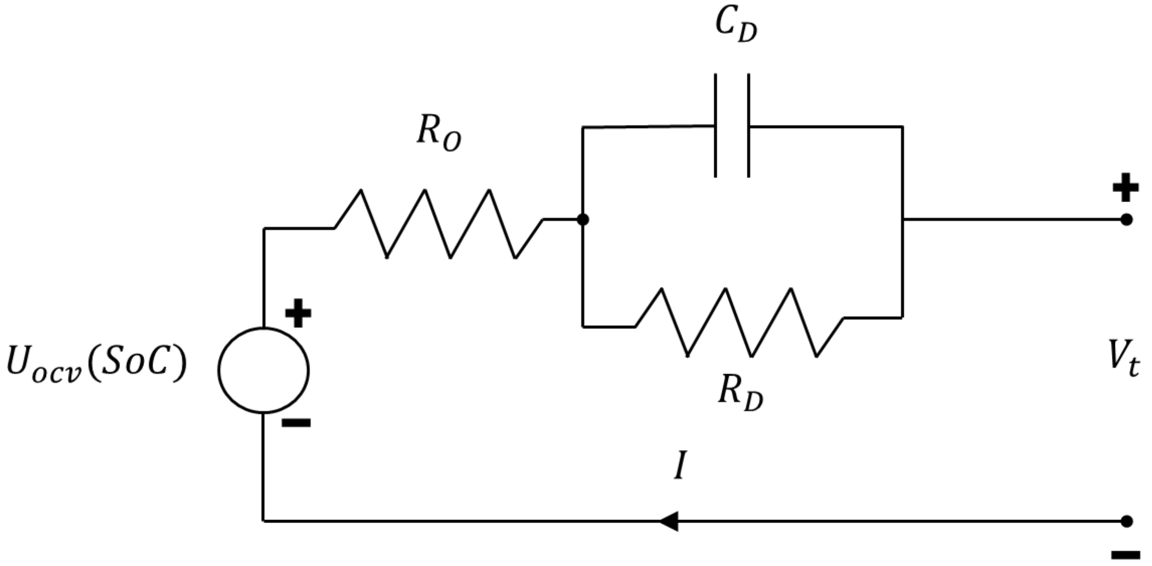

Figure 119 – A simple electrical circuit is illustrated able to reproduce the dynamics of lithium ion cells. In the drawing, the U_{OCV} represent the open circuit voltage as a function of the state of charge (SOC), the R_O the parallel branch between R_D and C_D represents the steady state and the dynamics of the ohmic drop.

Consequently, large libraries of resistances and capacitance are created and implemented in the model with a look-up table. As an example, the impulsion reported in Figure 120 for the LGC INR18650MH1 cells at 1C, 90 % SOC & 25°C, illustrates the part of the voltage used to identify these electrical components.

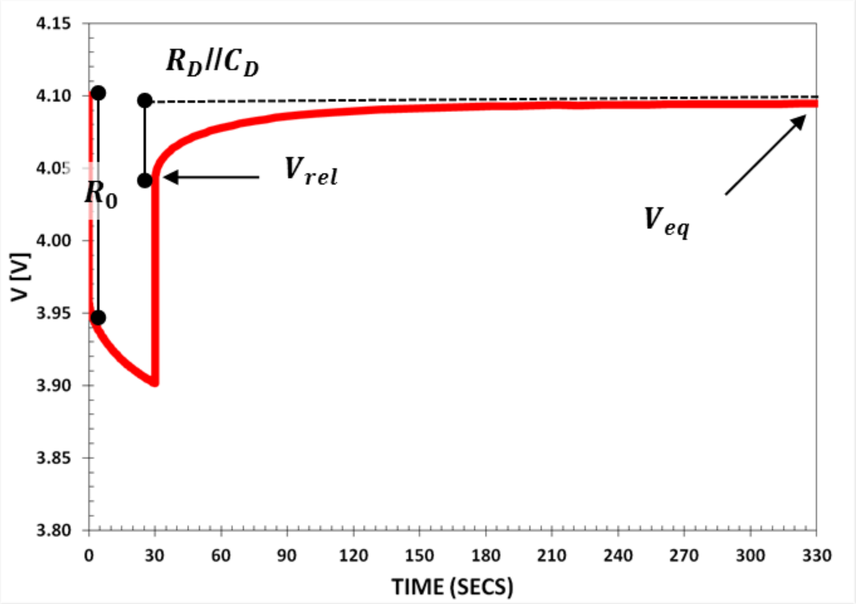

Figure 120 – The impulsion-rest sequence is illustrated in (A) for 30 secs at 1C & SOC = 90 % & 25°C for a LCG INR18650MH1 cell. The parts of the signal associated to ohmic internal resistance R_0 and the diffusion impedance, i.e. the RC parallel branch of the electrical circuit illustrated in Figure 119, are identified. The voltage at the beginning of the relaxation V_{rel} and at the equilibrium V_{eq} are also reported.

A dynamic system regulated by only one-time constant (i.e. only one parallel RC branch) is described with Eq. 83.

$$V = V_{eq} + (V_{rel} - V_{eq})e^{-\frac{t}{\tau}} \qquad \text{Eq. 83}$$

In this case, the voltage in the logarithmic scale of the time axis, shows a linear behavior. However in Figure 121 (A) is reported in the ordinates the logarithm of the voltage relaxation (described by Eq. 84, based on the initial and final voltages with V_{in} and V_{eq} identified in Figure 120) is observed, a non-linear behavior, as indicated by the inequality of Eq. 85. :

$$y = \ln\left(\frac{V - V_{eq}}{V_{rel}}\right) \qquad \text{Eq. 84}$$

$$\ln\left(\frac{V - V_{eq}}{V_{rel}}\right) \neq -\frac{t}{\tau} \qquad \text{Eq. 85}$$

In conclusion, the relaxation involves several time constants and the simple electrical circuit illustrated in Figure 119 does not reproduce the behavior. Thus, a pseudo-time constant $\tau_{pseudo}(t)$ can be defined using the slope (Eq. 86) of the relaxation defined in Eq. 83 as:

$$\frac{dV}{dt} = -\frac{1}{\tau}(V - V_{eq}) \qquad \text{Eq. 86}$$

Finally the pseudo-time constant is obtained in Eq. 87 and reported in Figure 121 (B).

$$\tau_{pseudo}(t) = -\left(\frac{dV}{dt}\cdot\frac{1}{V - V_{eq}}\right)^{-1} \qquad \text{Eq. 87}$$

This picture illustrates the value of the time constants and the evolution with time. As an example, at 50 seconds is $\tau_{psuedo}(50) = 50\,s$ while at 300 secs: $\tau_{psuedo}(300) = 220\,s$ (~ 4.4 times higher). Thus, Eq. 87 can be used to identify many time constants at different instants of time and the electric circuit reported in Figure 119 can be improved by adding RC branches based on the values of the pseudo-time constant.

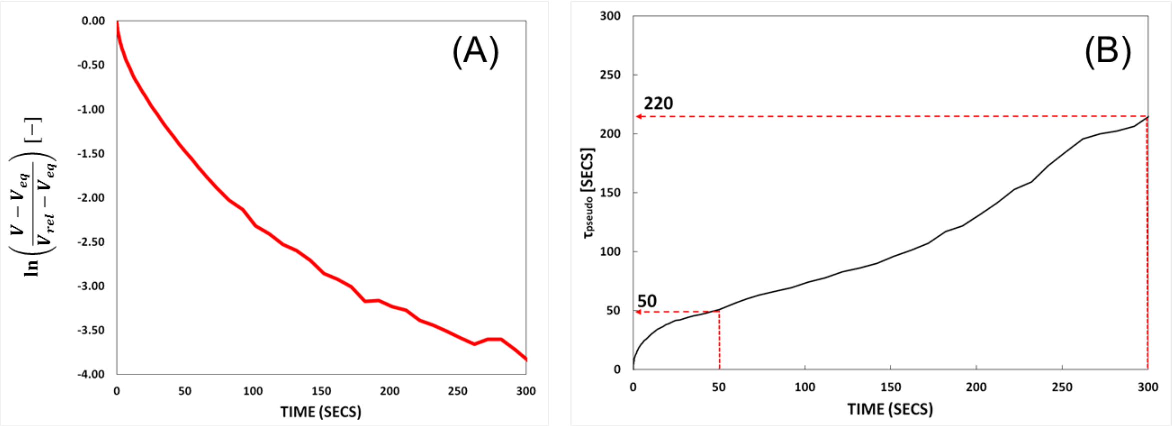

Figure 121 – In (A) the logarithm of the relaxation voltage described with Eq. 84 is reported as a function of time, while in (B) is reported the dynamic time constant derived in Eq. 87.

In conclusion, the dynamics of the cell relaxation is regulated via several time constants and many RC circuits estimated at different instant of times using the Eq. 87 are required to reproduce the behavior. Alternatively, is the electrochemical model can be used because it possesses naturally several time constants generated by the PDE that are complexly coupled. These time constants are identified and discussed in the next section.

6.2.2 Time constants

The time constants in the proposed model (§ 2.3.3), are reported in Table 39.

TIME CONSTANTS [S]	
$\frac{d_e^2}{D_e}$	Diffusion of lithium ions in the separator
$\varepsilon_{+l}\frac{d_+^2}{D_{e+}}$	Diffusion of lithium ions in the electrolyte confined in the positive electrode
$\frac{F}{RT}\;\frac{\varepsilon_{+l} d_+^2 F\, C^*}{\sigma_+}$	Transport of electrons in the positive electrode
$\frac{R_{p+}^2}{D_{s+}}$	Diffusion of intercalated lithium in the particles of the positive electrode

Table 39 – The time constants are identified for the half-cell configuration for the dimensionless model proposed in § 2.3.3 and their physical interpretation is reported.

For the “half-cell” configuration with no kinetic limitation there are 4-time constants, each one associated to characteristic phenomena. The pulse-rest simulation in Figure 122 illustrates in (A) the first 60 seconds of simulations and in (B) the logarithm of the voltage in the ordinates expressed by relation Eq. 84. The profile reported in Figure 122 (B), is nonlinear like in the experiment shown in Figure 120(B), proving the presence of several time constants in the model.

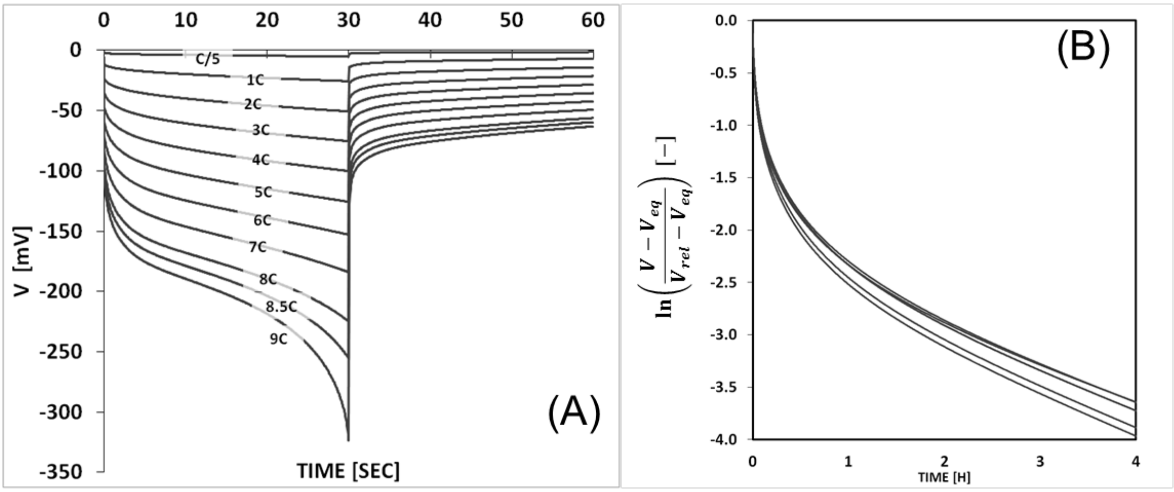

Figure 122 – The pulses are applied at SOC = 90% from C/5 to 9C, as indicated in picture (A), for 30 seconds, while the rest period is shown for only 30 seconds. In (B) is reported the complete rest period of the relaxation (4 hours) and in the ordinates, is reported the logarithm of the rest voltage.

The parameters used for these simulations are reported in Table 40:

CONSTANT PARAMETERS		
$S[m^2] = 0.08$	$R_+[m] = 10^{-6}$	$\theta_{+,in} = 0.9$
$d_+[m] = 150 \cdot 10^{-6}$	$d_e[m] = 50 \cdot 10^{-6}$	$\mathrm{d}_-[m] = 50 \cdot 10^{-6}$
$\varepsilon_{+,L} = 0.1$	$\varepsilon_{+,S} = 0.8$	$C_{S+,max}\left[\frac{mol}{m^3}\right] = 6 \cdot 10^{-4}$
$D_e\left[\frac{m^2}{s}\right] = 10^{-9}$	$D_{e,+}\left[\frac{m^2}{s}\right] = 10^{-12}$	$D_S\left[\frac{m^2}{s}\right] = 10^{-15}$
$\sigma_+\left[\frac{S}{m}\right] = 10$	$Q_+[A\mathrm{h}] = 15.44$	$Q_e[A\mathrm{h}] = 0.03$

Table 40 – The parameters used for the simulations reported in Figure 122 and Figure 125.

The concavity of the voltage is changing from 8C as shown in Figure 122 (A), this behavior was observed in a previous experiment conducted in Renault for a SOC<10%.

In the next studies, it should be demonstrated if the entire dynamics can be simulated.

The improvements obtained with the proposed PDE system solved in COMSOL are evident when compared with the previous results with Dualfoil® in a study conducted internally in Renault by D. Sicsic.

In the next section, a classical method used to measure the diffusivity in the solid phase is discussed and some weak points are detected with the simulations.

6.2.3 GITT

After a general introduction of the methods used to assess the solid phase diffusivity, the attention is focused on the GITT techniques.

The diffusivity of the active material is estimated in literature with three different electro- chemical techniques: the potentiostatic intermittent titration technique (PITT), the galvanostatic intermittent titration technique (GITT), and the electrochemical impedance spectroscopy (EIS) [111].

The impedance, during the EIS, is obtained by analyzing the voltage or the current signals obtained from the other variable applied with a sinusoidal shape to a system previously in equilibrium [185].

During the GITT or PITT the electrode at the equilibrium is forced to change the state of using a potential or current step the other variable [178], [179].

Each technique presents some limitations and the value of the diffusivity measured is significantly influenced.

The GITT was introduced by Weppner in 1977[179] by applying steps of current as illustrated in Figure 123 (A). The voltage between the working electrode and the reference electrode, E, is measured as a function of time during the pulse as shown in Figure 123 (B). It is assumed that: the diffusion can be approximated with the Fick's second law, the migration is neglect, the electrode is bulky and planar. The general solutions of the Fick’s law require the instantaneous value of the concentration at the electrolyte-electrode interface that is usually not directly measurable. An approximate solution is available using some mathematical manipulation. Recently, Delacourt proposes an improved mathematical equation to obtain the value of the diffusion [180]. However, even in this case the porous-electrode effects (i.e., transport limitations in the liquid phase and the voltage drop across the solid conductive matrix of the electrode) and the volume changes of the active material are neglected (around 10 % volume contraction). In Figure 123 (C) is reported the potential profile on LFSO$_4$ during a GITT test protocol.

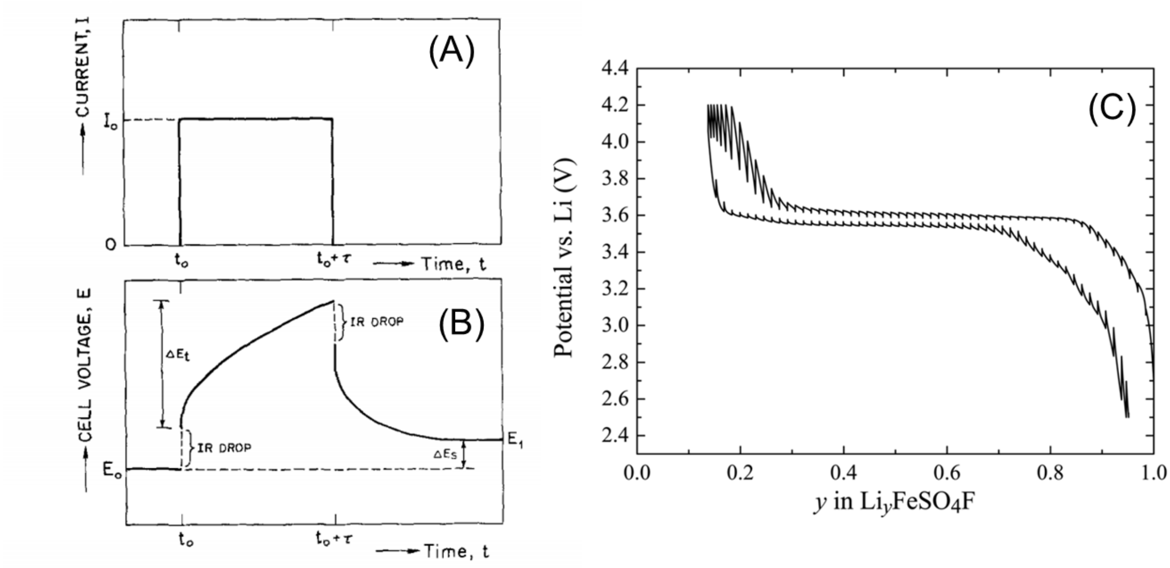

Figure 123 – In (A) is reported the current step applied during the GITT, while in (B) illustrates the voltage step whit the ohmic drop (RI) and the variation of the potential ΔE_S from the equilibrium states before and after the pulse[179]. In (C) Potential profile during GITT on LiyFeSO$_4$ at 25C. Conditions: 30 min charging/discharging segments at C/25 & 10 h rest. [180]

In conclusion, the GITT is basically a pulse-rest sequence where small currents (e.g. less than C/25) are applied for long time (e.g. 30 minutes).

The assumptions in the GITT are listed:

- bulk planar electrodes;
- chemical compounds with no phase changes;
- the kinetics (i.e. the migration of charged species) is neglected;
- the Fick's law is usually solved if $\tau \ll \frac{L^2}{D}$;
- small variation from one steady state to another.

In conclusion, the model, to estimate the solid phase diffusion as a function of the state of charge is much simpler than in the phenomena really involved. However, it is not discussed in literature the validity of these hypotheses.

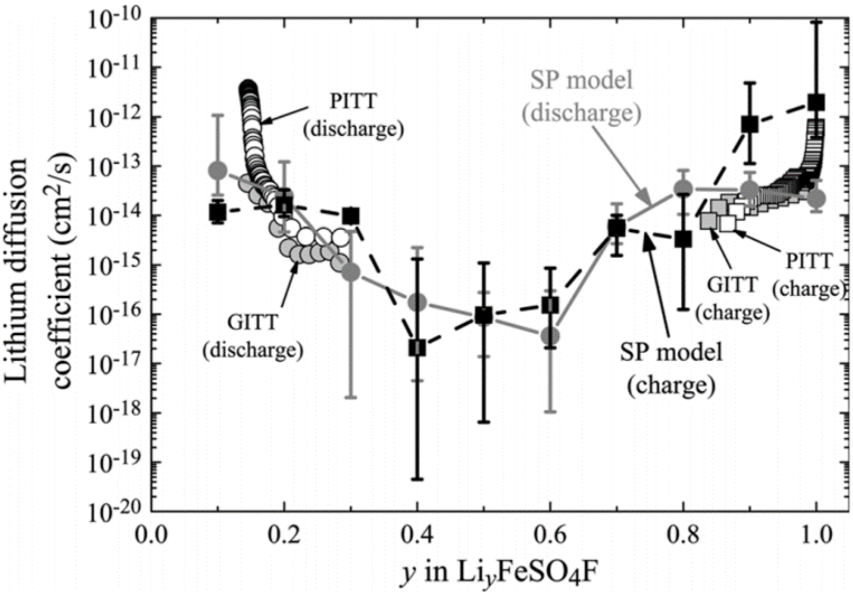

Figure 124 – The diffusion coefficient for the LFSO4 is measured with the PITT and the GITT. The values of the diffusivity effectively used in the single particle model for the simulation of the galvanostatic charges and discharges by Delacourt are also reported [180].

Finally, in Figure 124 the diffusion coefficients are reported as a function of the state of lithiation measured with the GITT, the PITT techniques are fitted with a simple particle model [180]. Very large uncertainty on measurements and a non-precise agreement between these techniques, is shown. This is in contrast with the good agreement that was found for a bulk electrode[178]. Furthermore, the PITT for some chemistries like the LFSO4 or LFP, cannot be used for voltage plateau because, the small voltage drops imposed by PITT cannot be applied.

For these reasons these studies and the following simulations are focused on the GITT only.

During a presentation illustrated by Gallagher 2012 the simulated GITT shows a good fit during the pulse but not during the relaxation[258]. We suggest that the time constants identified were not correct, however how to identify these values is still ongoing. In the last section, the GITT is simulated and some important phenomena are discussed.

6.2.4 First steps to an appropriate interpretative framework of GITT

The simulated impulsions are reported in Figure 125 for two set of parameters: in the first one the time constant associated to the diffusion in the solid phase higher than the one in the liquid phase while in the second set the situation is reversed.

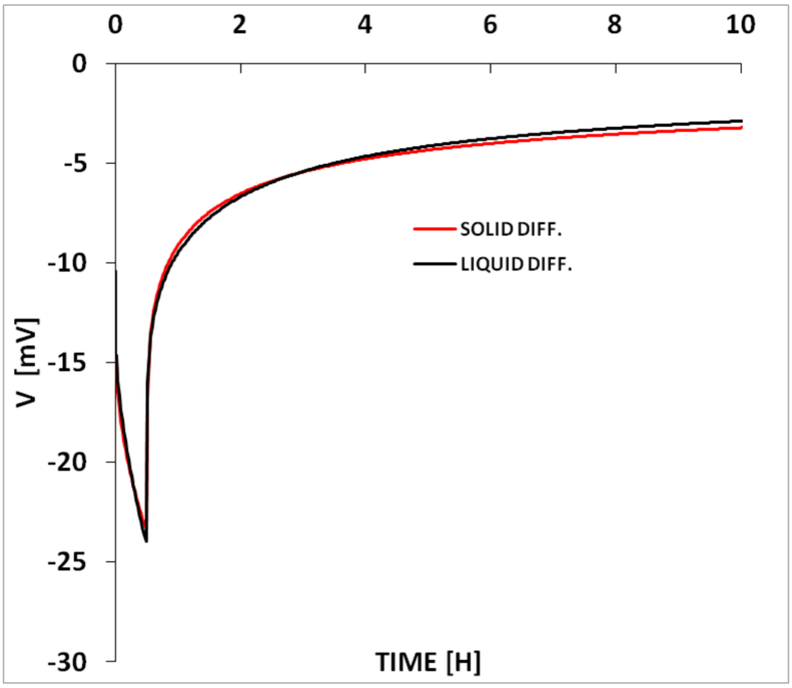

Figure 125 – The impulsions are simulated at C/25 for 30 minutes and 10 hours of rest period as reported by Delacourt [180]. The time constant for two set of parameters used for the simulations illustrated in Figure 125 are reported. Indeed, one show a higher time constant for the diffusion in the solid phase while the other has higher diffusion in the solid phase. The parameters not shown here can be found in Table 40.

As illustrated in Figure 125, the two set of parameters lead to different time constant but a similar voltage behavior is obtained. The values of these time constants are reported in Table 41, while the other parameters that are common in both simulations are reported in Table 40.

	TIME CONSTANTS [S]	
	SOLID DIFF.	**LIQUID DIFF.**
$\varepsilon_{+l}\frac{d_+^2}{D_{e+}}$	22.5	1731
$\frac{F}{RT}\frac{\varepsilon_{+l}d_+^2 F\,C*}{\sigma_+}$	0.169	16.906
$\frac{R_{p+}^2}{D_{s+}}$	10^6	10

Table 41 – The time constants used for the simulations reported in Figure 125.

Consequently, the GITT should be carefully used, as demonstrated in this simulation to identify accurately the solid phase diffusion coefficient. However, the ambiguity can be removed by using pulses with different amplitude and/or duration, as illustrated in Figure 126. The simulations are performed with the same time constants for 30 seconds but the C-rate is now 1C.

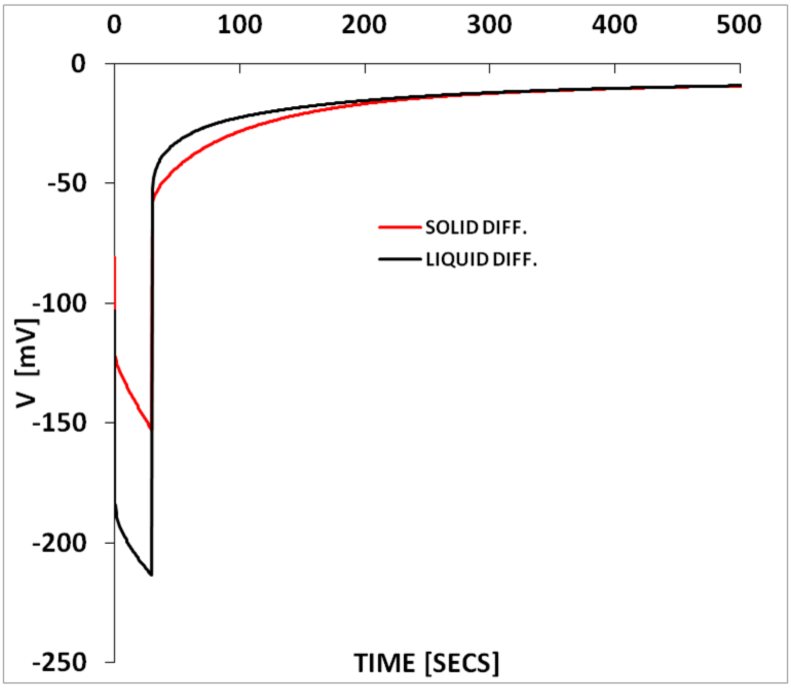

Figure 126 – The simulations are performed with the parameters used in the previous simulation reported in Figure 125, but the current rate is 1C and the pulse duration are 30 seconds.

In conclusion, the GITT can still be used to evaluate the diffusion time constants in a porous electrode but the diffusivity cannot be measured without improving this method. Yet $a\ priori$ it is not possible to say which one of the time constant is higher and so if the diffusion in the electrolyte is predominant or not. However, we demonstrate that a combination of pulse-rest having different C-rates and time lengths, can be used to discriminate this situation. A systematic study should be conducted to create a proper GITT protocol able to discriminate in which case the diffusion in the electrolyte is predominant and in which one the solid phase time constant can be measured. For this purpose, prior simulations are useful to drive the research through a good GITT protocol.

7 Conclusions and perspectives

The present work debates about the Newman's model, widely used in recent years and proposed with many variants without appropriate discussions and the connections between the model, the parameters and the experiments. The state of the art in electrochemical modelling and its critical review are presented.

A new dimensionless model based on the dilute solutions of the classical Newman's model is proposed for porous insertion and Li-metal electrodes. The dilute solution is used after the controversial uses of the concentrated solution in the literature as explained in the three chapters. Furthermore, the proposed dimensionless model reduces the number of parameters from 25 in dimensional to 16 in the dimensionless system of equations.

Then, the parameters from the literature are analysed and a large review of their values, never done previously at our knowledge, has been performed before. Thus, using these tables of parameters, the dimensionless parameters are calculated. Some parameters for the model such as porosity, particles size, electrode thickness, isotherms are identified with a physicochemical characterization in commercial LGC INR18650MH1 cells. Then, these cells are electrically characterized for different operating conditions: C-rates, SOC, temperature, SOH and cut-off voltage. It is observed, in the present study, that load history affects the precision of the electrical measurements, and a new protocol is developed to mitigate this behaviour.

The states of lithiation in the electrodes when the cell is completely charged are fundamentals for any simulations or the understanding of the battery degradation. These parameters are not known because when initially the SEI formation occurs, the state of lithiation in the pristine cell change. The first step was to understand how the shape of the isotherms influences the accuracy associated with the evaluation of the initial and final states of charge. This method was then applied at the LG-Chemical cells. Moreover, some aging scenarios are studied to discuss how the states of lithiation could change, and how it impacts the shape of the OCV.

In another section, the rated capacity for "half-cell" configuration is studied in limit cases using the support of numerical simulations. A limit case is a special configuration where the kinetic and transport limitations could be attributed, with no ambiguity, to a specific set of parameters. Among the seven proposed limit cases, one of them can explain the limitations observed in the tested LGC cells.

Finally, the simulations of pulse-rest sequences are used to discuss about a technique for the measurement of the solid-state diffusivity: the galvanostatic intermittent titration techniques (GITT). In fact, it is observed that the large number of time constants in both battery and its electrochemical model may lead to a miss-identification of the diffusion coefficient.

In further works, the simulations should be focused on the ohmic drop in the limit cases and extend the numerical prospection of limit cases for the complete cell. This work opens new avenues in several directions such as: the development of a proper method to identify the diffusion time constants, the understanding of the “voltage-dip”, the detection of lithium metal plating, and finally obtaining an electrochemical model able to predict the behaviour of a non-existing cells in different working temperatures.

8 Appendix

8.1. Mesoscopic 1D porous electrode model

A mesoscopic 1D porous electrode model having inter-particle diffusion is proposed in this section. The main difference with the P2D model, discussed in the present work, concerns the definition of the diffusion in the solid phase. In this case, the diffusion of the intercalated lithium occurs in the whole active material of the electrode with defining geometrically the particles. Consequently, the particles radii are not defined, reducing the number of parameters required in this model. The other hypothesis, detailed in § 2, are unchanged but they are shortly resumed in the followings: binary electrolyte (i.e. Li^+ et X^-) and ideal solution (i.e. the activity of the solution equals the concentration). The relation between mobility and diffusion is described by the Nernst-Einstein law and the values are independent from the concentration, the transport number and the effective electrolyte diffusivity are the same in both the electrodes and separator. The chemical reactions are described by the Butler-Volmer law and no side reactions occurs. The porous electrodes are modeled in a macroscopic scale. Consequently, there are two homogeneous interleaved media: one solid and the other liquid. The diffusion and the migration of cations and anions act in the liquid phase, while the diffusion of intercalated lithium and the electronic conductivity act in the solid phase. Thus, the current I circulating in the cell is, locally, the sum between the ionic current I_l in the liquid phase and the electronic current in the solid phase I_s. It is also assumed that a positive current is associated for the discharge current. The current collector of the negative electrode is set in $x = 0$. The Eq. 18 defines the transport number in the electrolyte, the Eq. 20 defines diffusion coefficient in the bulk electrolyte, and Eq. 21 defines the conductivity in the electrolyte.

The volume mass balance equations (or continuity equations) in the electrolyte are written in plane 1D geometry. These equations are reported for the separator in Eq. 23 to Eq. 29 and they are still valid for both electrodes by changing opportunely the parameters' subscripts:

$$\begin{cases} \dfrac{\partial \mathrm{C}}{\partial \mathrm{t}} = \mathrm{D_e} \dfrac{\partial^2 \mathrm{C}}{\partial \mathrm{x}^2} \\ (\mathrm{t}_- - \mathrm{t}_+) \dfrac{\partial \mathrm{C}}{\partial \mathrm{t}} = \mathrm{D_e} \dfrac{\mathrm{F}}{\mathrm{RT}} \dfrac{\partial}{\partial \mathrm{x}} \left(\mathrm{C} \dfrac{\partial \mathrm{V}}{\partial \mathrm{x}} \right) \end{cases} \qquad \text{Eq. 29}$$

In the electrodes, where chemical reaction occurs, a source term appears in the mass balance equations as reported in Eq. 30, for the positive electrode by changing the subscript + to – it is obtained the equations system for the negative electrode.

$$\begin{cases} \varepsilon_{+,l}\dfrac{\partial C_+}{\partial t} = -\dfrac{\partial N_+}{\partial x} + \dfrac{1}{F}a_+ j_+ \\ \varepsilon_{+,l}\dfrac{\partial C_-}{\partial t} = -\dfrac{\partial N_-}{\partial x} \end{cases} \qquad \text{Eq. 30}$$

The same production term in the volume appears in the solid phase for the balance of the concentration of intercalated lithium:

$$\varepsilon_{+s}\frac{\partial C_s}{\partial t} = -\frac{\partial N_s}{\partial t} - \frac{1}{F}a_+ j_+ \qquad \text{Eq. 88}$$

The flux is generated only by diffusion (i.e. no migration of charges in the solid phase) in the x-direction, as shown in Figure 5:

$$N_s = -D_s\frac{\partial C_s}{\partial x} \qquad \text{Eq. 89}$$

The local current density j_+ is described by the general Butler-Volmer equation reported in Eq. 90:

$$j_+ = Fk_+^{*\prime}\left(\theta e^{\alpha\frac{F}{RT}(W-V-\ddot{U}_+)} - \frac{C}{C^*}(1-\theta)e^{-(1-\alpha)\frac{F}{RT}(W-V-\ddot{U}_+)}\right) \qquad \text{Eq. 90}$$

The current conservation has been reported in equations Eq. 31 to Eq. 33.

The complete system of equations can be written in Eq. 91:

$$\begin{gathered} \varepsilon_{+l}\frac{\partial C}{\partial t} = D_{e+}\frac{\partial C^2}{\partial x^2} + \frac{t_+}{F}\sigma_+\frac{\partial^2 W}{\partial x^2} \qquad \text{Eq. 91} \\ \varepsilon_{+s}\frac{\partial C_s}{\partial t} = D_{s+}\frac{\partial C^2}{\partial x^2} + \frac{1}{F}\sigma_+\frac{\partial^2 W}{\partial x^2} \\ \sigma_+\frac{\partial^2 W}{\partial x^2} = a_+Fk_+^{*\prime}\left(\theta e^{\alpha\frac{F}{RT}(W-V-\ddot{U}_+)} - \frac{C}{C^*}(1-\theta)e^{-(1-\alpha)\frac{F}{RT}(W-V-\ddot{U}_+)}\right) \\ D_{e+}\frac{F}{RT}\frac{\partial}{\partial x}\left(C\frac{\partial V}{\partial x}\right) = (t_- - t_+)D_{e+}\frac{\partial C^2}{\partial x^2} - \frac{2t_+t_-}{F}\sigma_+\frac{\partial^2 W}{\partial x^2} \end{gathered}$$

There are 4 equations for 4 variables C,C_S, V and W, where C is the concentration in the electrolyte, C_S the concentration in the solid phase, the V is the potential in the liquid phase and W is the potential in the solid phase.

The boundary conditions for the solid phase at the current collector are expressed in Eq. 92:

$$-D_{s+}\left(\frac{\partial C_s}{\partial x}\right)_{x=L_+} = -\left(\frac{I}{FA} + \frac{\sigma_+}{F}\left(\frac{\partial W}{\partial x}\right)_{x=L_+}\right) \qquad \text{Eq. 92}$$

while at the separator are reported in Eq. 93:

$$-D_{s+}\left(\frac{\partial C_s}{\partial x}\right)_{x^+=L_e} = -\frac{\sigma_+}{F}\left(\frac{\partial W}{\partial x}\right)_{x^+=L_e} \qquad \text{Eq. 93}$$

For the liquid phase, the boundary conditions are reported in Eq. 37 to Eq. 40. The initial conditions are reported in Eq. 42. It should be noted that in the P2D model the concentration in the solid phase C_s (or θ if normalized with the maximum concentration in the electrode) is the concentration at the surface of the particle, while in the present model the concentration is only a function of the distance x across the electrode.

8.2. Estimation of the state of charge at 4.3 V

The state of lithiation at the charged state for the NMC electrode in the half cell (i.e. at 4.3V) can be estimate with Eq. 94 [88], [142], [237]:

$$Q_{M,+} = (1 - y_{max})Q_{Mth,+}$$

Eq. 94

Where $Q_{M,+}[mAh/g]$ is the effective mass capacity for the active material in the range from 4.3 V to 3.0 V, while $Q_{Mth,+}[mAh/g]$ is the theoretical loading of the electrode. The effective mass capacity is $Q_{M,+} = 190{,}96\ \mathrm{mAh/gr}$ obtained with:

$$Q_{M,+} = \frac{Q_{hc,+}}{\rho_+ \cdot \mu_+ \cdot S_{hc,+}}$$

Eq. 95

Where $Q_{hc,+} = 5.52\ mAh$ is the measured quantity of charge in the range from 4.3 V to 3.0 V, $\rho_+ = 23.7\ mg/cm^2$ is the electrode specific weight, $\mu_+ = 0.96$ is the effective amount of active material in the solid phase and the $S_{hc,+} = 1.27\ cm^2$ is the surface of the coin shaped half-cell. Finally, the $Q_{Mth,+} = 275{,}56\ \mathrm{mAh/g}$ is obtained with the expressions:

$$Q_{Mth,+} = \frac{F}{3.6 \cdot M_+}$$

Eq. 96

where $M_+ = 97.26\ \mathrm{gr/mol}$ is the molecular weight of the NMC811[2] and $F = 96485\ C/mol$ the Faraday’s constant.

The use of Eq. 94, provides in this case the result of $y_{max} \approx 0.3$.

8.3. Differential voltage

In this section is discussed the differential voltage technique introduced previously in § 5 and its filtering techniques to obtain a smooth signal.

---

[2] From the formulation $Li(Ni_{0.8}Mn_{0.1}Co_{0.1})O_2$ the molecular weight is the sum of the molecular weight of the species: $6.941 + 58.69 \cdot 0.8 + 54.93 \cdot 0.1 + 58.93 \cdot 0.1 + 15.99 \cdot 2$

The current rate during the measurement is small enough to consider a zero ohmic drop. Thus, the measured electrode voltage is the electrode isotherms. However, additional considerations are required on the signal sampling. In fact, the sampling frequency and the potentiometer accuracy may affect the results and an appropriate analysis on the DV signals requires a noise filter. The voltage measurement and its derivate are reported, in this study, as functions of the DOD (i.e. the normalized capacity) and conclusions are hold even if the DOD is replaced with the quantity of charge. In Figure 127(A) the OCV of the LGCMH02 and the number of samples of the voltage are reported. The OCV is measured with a galvanostatic discharge at 25°C for a C/25 current rate. The number of samples increases linearly with the DOD apart at the end of the discharge, identified in the dashed circle. In fact, the number of samples increases because of major voltage variation for the same amount of charge measured. Thus, excepted the end of the discharge, the sample frequency is almost constant. During the entire discharge are measured 1605 points corresponding approximately to 14-15 samples every 1% of DOD.

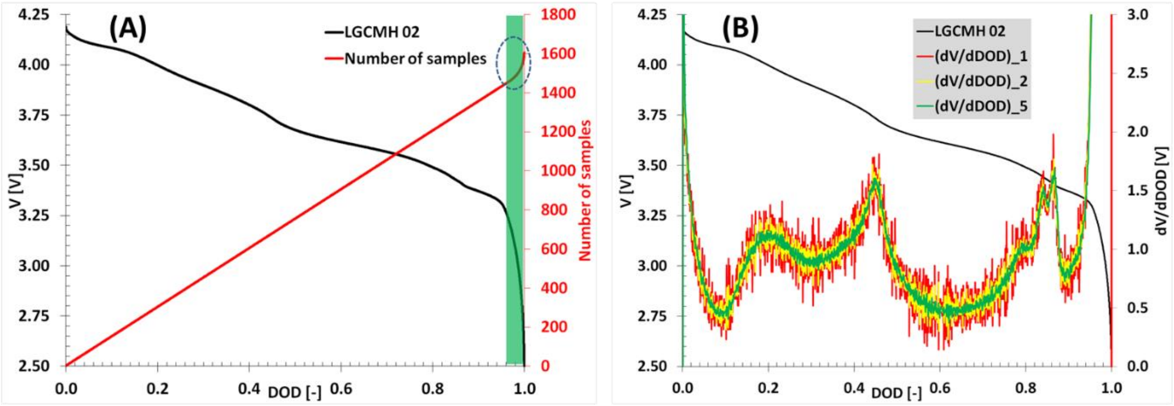

Figure 127 – The OCV of the LGCMH02 and the number of samples in (A). In (B) are reported the same OCV and the differential voltage calculated with Eq. 97.

In Figure 127(B) is reported in the second axis the voltage differential calculated with the Eq. 97:

$$\begin{aligned}(dV/dDOD)\_1 &= -\frac{V_k - V_{k-1}}{DOD_k - DOD_{k-1}} \text{ for } k = 2, \dots, N \\ (dV/dDOD)\_2 &= -\frac{V_k - V_{k-2}}{DOD_k - DOD_{k-2}} \text{ for } k = 3, \dots, N \\ (dV/dDOD)\_5 &= -\frac{V_k - V_{k-5}}{DOD_k - DOD_{k-5}} \text{ for } k = 6, \dots, N\end{aligned} \qquad \text{Eq. 97}$$

where k indicate the sample index and $N \in \mathbb{N}$ is the total number of samples.

The noise of the differential voltage depends on how it is defined. For example, the definition $(dV/dDOD)\_1$ has a higher noise than $(dV/dDOD)\_5$ because of the sampling path width.

Another approach available to reduce the signal noise is either filtering the curve $(dV/dDOD)$ or filtering the measured voltage before the differentiation as shown in Figure 128. In the picture, the moving average filter is used over 11 samples but to obtain clear signal only 7 samples are sufficient.

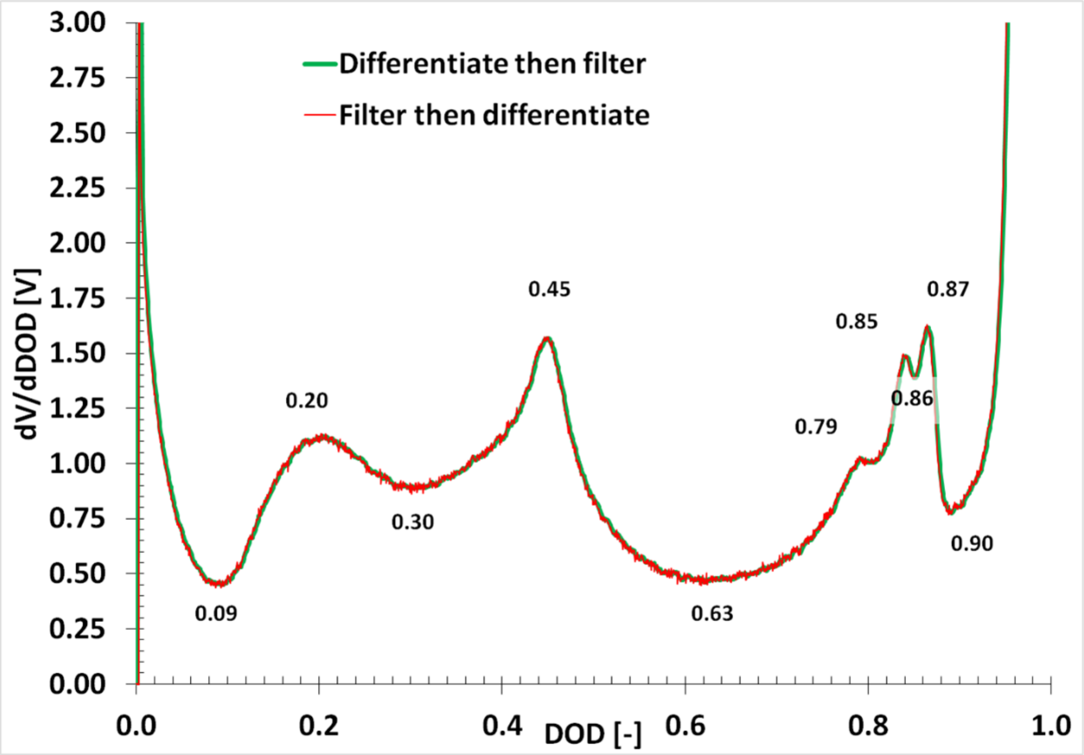

Figure 128 – The signals are obtained filtering the differential voltage (green) and filtering the voltage and the differentiate (red). The numbers indicate the DODs where either the peaks and valleys are detected.

8.4. PDE equations system in COMSOL® (half-cell)

In this section is explained how the PDE equations systems was implemented in COMSOL®.

The first step is to define the geometries and their mesh for the finite element solver. The model is obtained with a combination of two geometries: one is 1D geometry composed of three segments (negative electrode, separator and positive electrode) and the other is a 2D geometry (representing the particles in the positive electrode). The 1D geometry is represented in Figure 129 and the 2D geometry in Figure 130.

The red dashed boxes, in the "Model Builder" identifies the geometries information, while the boxes in the "Settings" provides the details on the geometry.

The dimensionless parameters are inserted by the user in the "Global Parameter" menu as reported in Figure 131. The details concerning these parameters such as the initial conditions and the definitions of time steps are reported in Table 42..

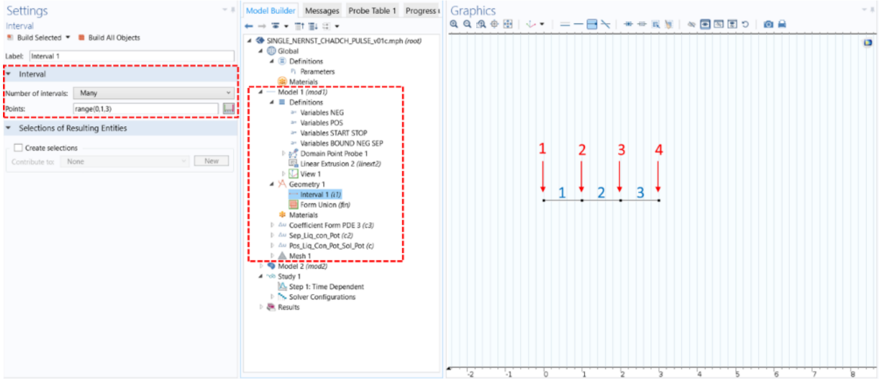

Label: Interval 1

Number of intervals: Many

Points: range(0,1,3)

☐ Create selections

Figure 129 – The 1D geometry is reported. The blue numbers identify the elements: negative electrode (1), separator (2) and the positive electrode (3). The red numbers identify the boundaries: current collector – negative electrode (1), negative electrode – separator (2) separator – positive electrode (3), positive electrode – current collector (4).

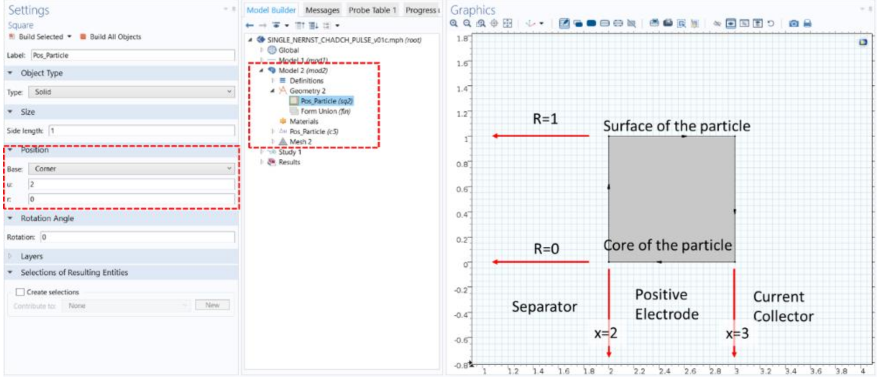

Label: Pos_Particle

Type: Solid

Side length: 1

Base: Corner

u: 2

r: 0

Rotation: 0

☐ Create selections

Figure 130 – The 2D geometry is reported. The red boxes indicate the position starting position of the electrode and the set of information in the Model Builder" such as: variable, equations, mesh and geometry.

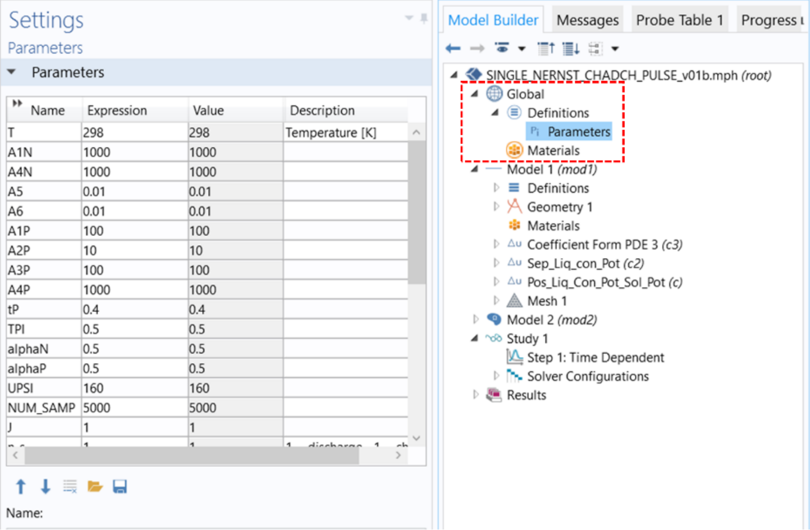

Name	Expression	Value	Description
T	298	298	Temperature [K]
A1N	1000	1000	
A4N	1000	1000	
A5	0.01	0.01	
A6	0.01	0.01	
A1P	100	100	
A2P	10	10	
A3P	100	100	
A4P	1000	1000	
tP	0.4	0.4	
TPI	0.5	0.5	
alphaN	0.5	0.5	
alphaP	0.5	0.5	
UPSI	160	160	
NUM_SAMP	5000	5000	
J	1	1	

Figure 131 – The user inputs and the global parameters that are applied to the entire model are reported. The details of the parameters are reported in Table 42.

INPUT PARAMETERS		
A1N	USER	adim. param. neg. electrode.
A4N	USER	adim. param.
A5	USER	adim. param.
A6	USER	adim. param.
A1P	USER	adim. param.
A2P	USER	adim. param.
A3P	USER	adim. param.
A4P	USER	adim. param.
tP	USER	Transference number
TPI	USER	Initial state lithiation positive electrode
alphaN	USER	Kinetic constant negative electrode
alphaP	USER	Kinetic constant positive electrode
UPSI 160	USER	dimensionless potential at the equilibrium for positive electrode
NUM_SAMP	USER	Number of time samples
J	USER	Dimensionless current
n_s	USER	Set 1 for discharge or -1 for charge
Qmax	TPSI*A3P	Definition of remaining capacity
Nsim_stop	USER	If N=1 galvanostatic discharge, if N > 1 pulse
TSTOP_DCH	TFIN_TH/ Nsim_stop	Duration of the applied current: pulse (if Nsim_stop >1)
Nsim_rest	USER	Duration of the rest period
TSIM	Nsim_rest *TSTOP_DCH	Total simulation time
TPSI	1-TPI	Initial state of lithiation (reversed: during the discharge, it goes from TPSI to 0)
CI	1	Initial concentration electrolyte
CHII	0	Initial potential in the liquid phase
TFIN_TH	abs(Qmax/J)	Definition of theorical remaining simulation time
tN	1-tP	Anionic transference number
C_min	10^-7	Minimum concentration in the electrolyte for improving the stability of the BV equation
RIT	1E-11	Initial delay before applying the current
DRIT	path_time/50	It guarantees the smoothness of the transition when the current is applied (sharp transition the solver could break)
path_time	TSIM/NUM_SAMP	Width of each time step
path_time_init	path_time/300	Width of each time steps at the beginning of the discharge

Table 42 – The input parameters form the User, the initial conditions and the simulations time steps are reported in the table. These parameters are in Global -> Definitions -> Parameters.

In Figure 132 are reported the variables attributed at the negative electrode, interface negative electrode - separator, positive electrode and the switch of the current. The details and the description of such variables are reported in Table 43.

The linear extrusion is then used to connect the two geometries by sharing the concentration at the surface of the particles and the exchange current density as reported in Figure 133.

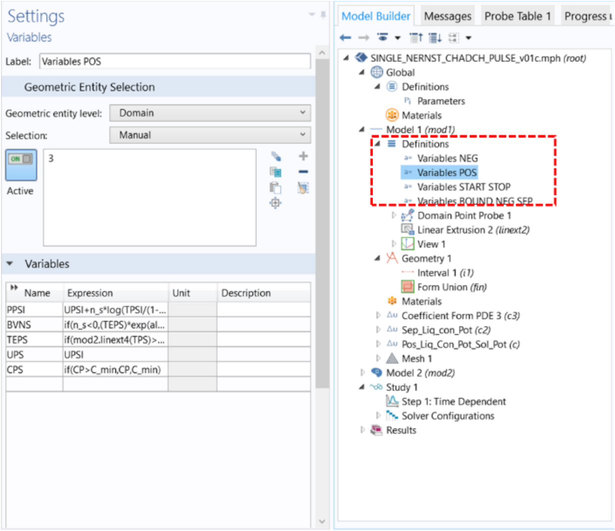

Settings

Variables

Label: Variables POS

Geometric Entity Selection

Geometric entity level: Domain

Selection: Manual

3

Active

Variables

Name	Expression	Unit	Description
PPSI	UPSI+n_s*log(TPSI/(1-...		
BVNS	if(n_s<0,(TEPS)*exp(al...		
TEPS	if(mod2.linext4(TPS)>...		
UPS	UPSI		
CPS	if(CP>C_min,CP,C_min)		

Figure 132 – The variable defined in the 1D geometry are evidenced in the red dashed boxes contains the variables for the: negative electrode, the positive electrode, the boundary at the negative electrode - separator and the variables associated to the current start and stop. The details are reported in Table 43.

	VARIABLES NEG	
	NEGATIVE ELECTRODE	DOMAIN: 1
PNI	log(CI)	Initial potential
	VARIABLES POS	
	POSITIVE ELECTRODE	DOMAIN: 3
PPSI	UPSI+n_s*log(TPSI/(1-TPSI))	Initial potential
BVNS	if(n_s<0,(TEPS)*exp(alphaP*(PP-CHIP-UPS))-(1-TEPS)*CPS*exp(-(1-alphaP)*(PP-CHIP-UPS)),(1-TEPS)*exp(alphaP*(PP-CHIP-UPS))-(TEPS)*CPS*exp(-(1-alphaP)*(PP-CHIP-UPS)))	Butler-Volmer equation.
TEPS	if(mod2.linext4(TPS)>Theta_min, mod2.linext4(TPS),Theta_min)	Concentration at the surface of the particles
UPS	UPSI	Equilibrium potential
CPS	if(CP>C_min,CP,C_min)	Minimum concentration in the electrolyte to ensures the stability of the solver (because of the exponential of B-V)
	VARIABLES START STOP	
	VARIABLE ASSOCIATED TO THE CURRENT SWITCH	ENTIRE MODEL
start	flc2hs(t-RIT,DRIT)*flc2hs(TSTOP_DCH-t,DRIT)	The flc2hs functions ensures the smooth switch of the current.
	VARIABLES BOUNDARY NEG SEP	
	NEGATIVE ELECTRODE	BOUNDARY: 2
BVNN	n_s*(exp(alphaN*(PN-CHIS-UN))-CS*exp(-(1-alphaN)*(PN-CHIS-UN)))	Butler-Volmer equation.
UN	log(CS)	Equilibrium potential

Table 43 – The variables associated to the model geometry 1D

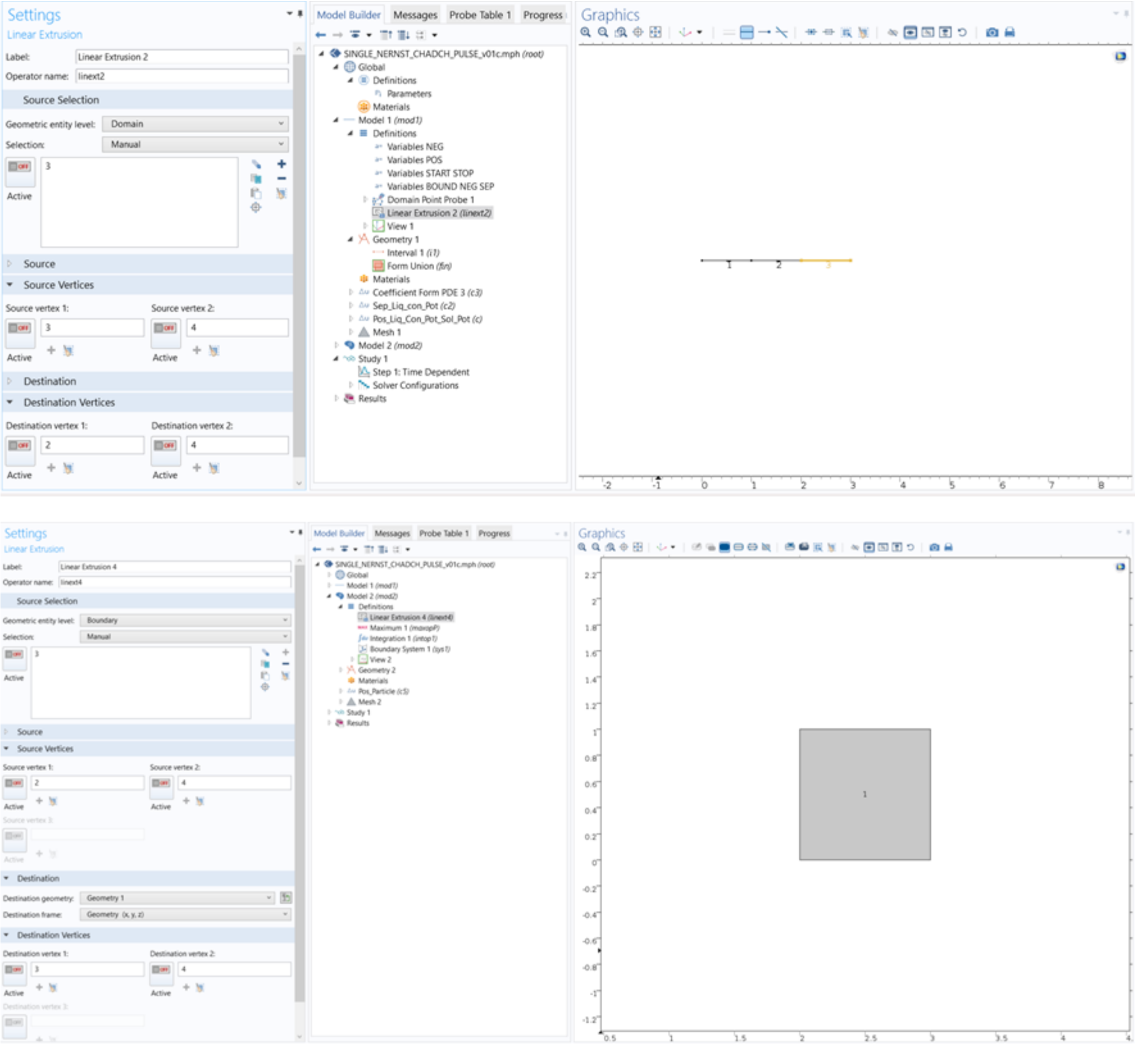

Label: Linear Extrusion 2
Operator name: linext2

Source Selection
Geometric entity level: Domain
Selection: Manual
3
Active

Source
Source Vertices
Source vertex 1: 3 Active
Source vertex 2: 4 Active

Destination
Destination Vertices
Destination vertex 1: 2 Active
Destination vertex 2: 4 Active

Label: Linear Extrusion 4
Operator name: linext4

Source Selection
Geometric entity level: Boundary
Selection: Manual
3
Active

Source
Source Vertices
Source vertex 1: 2 Active
Source vertex 2: 4 Active
Source vertex 3:

Destination
Destination geometry: Geometry 1
Destination frame: Geometry (x, y, z)

Destination Vertices
Destination vertex 1: 3 Active
Destination vertex 2: 4 Active
Destination vertex 3:

Figure 133 – The uses of the linear extrusion is reported for the 1D model (upper figure) and the 2D model (lower figure). The linear extrusion is used to connect the two geometries with the concentration in the solid phase at the particles surfaces and the local exchange current density.

The three 1D sub-domains have a system of equations implemented with a coefficient form PDE reported in Table 44, Table 45 and Table 46 , for the negative, separator and positive electrode, respectively.

The 2D sub-domain for the particles in the positive electrode have a 2x2 equations for the anisotropic solid phase diffusivity, as it is reported in Table 47.

COEFFICIENT FORM PDE - NEGATIVE ELECTRODE

DOMAIN SELECTION: 1
NUMBER OF DEPENDENT VARIABLES: 1 (PN)
$c = 0\ ; a = 0\ \ ; \ e_a = 0\ \ ; d_a = 0\ ; \alpha = 0\ ;\ \gamma = 0$
$f = \mathrm{n\_s} * \mathrm{J} * \mathrm{start/A1N}$
$\beta = 1$

INITIAL VALUES FOR PN: PNI

DIRICHLET BOUNARY CONDITIONS, BOUNDARY SELECTION: 1;
Prescribed value of PN: PNI

FLUX/SOURCE, BOUNDARY SELECTION: 2; $g = 0\ ; q = 0$

Table 44 – The PDE equations system for the Model 1D in the negative electrode.

COEFFICIENT FORM PDE - SEPARATOR

DOMAIN SELECTION:2
NUMBER OF DEPENDENT VARIABLES: 2 (CS, CHIS)
$[a\ ;\ e_a\ ; \alpha\ ;\ \beta] = \begin{bmatrix} 0 & 0 \\ 0 & 0 \end{bmatrix}$
$[f ; \gamma] = \begin{bmatrix} 0 \\ 0 \end{bmatrix}$
$c = \begin{bmatrix} 1/A5 & 0 \\ 1 - 2 * tP & -CS \end{bmatrix}$
$d_a = \begin{bmatrix} 1 & 0 \\ 0 & 0 \end{bmatrix}$

INITIAL VALUES FOR:
DOMAIN SELECTION:2
$\mathrm{CS} = \mathrm{CSI}, \mathrm{CHIS} = \mathrm{CHISI}, \dfrac{\partial CS}{\partial t} = 0, \dfrac{\partial CHIS}{\partial t} = 0$

FLUX/SOURCE
BOUNDARY SELECTION:2
$g = \begin{matrix} -1 * \mathrm{n\_s} * (-\mathrm{A6} * (1 - \mathrm{tP}) * \mathrm{A4N} * \mathrm{BVNN})/\mathrm{A5} \\ -1 * (-\mathrm{A6} * (1 - \mathrm{tP}) * \mathrm{A4N} * \mathrm{BVNN}) - (1 - 2 * \mathrm{tP}) * \mathrm{CSx} \end{matrix}$
$q = \begin{bmatrix} 0 & 0 \\ 0 & 0 \end{bmatrix}$

DIRICHLET BOUNDARY CONDITION: 2
Prescribed values of CHIS
$\mathrm{r}_2 = -(1/\mathrm{alphaN}) * \log(\mathrm{n\_s} * \mathrm{J} * \mathrm{start/A4N} + \mathrm{CS} * \exp((\mathrm{alphaN} - 1) * (\mathrm{PN} - \mathrm{CHIS} - \mathrm{UN})\ )) + \mathrm{PN} - \mathrm{UN}$

DIRICHLET BOUNDARY CONDITION: 3
Prescribed values of CS:
$\mathrm{r}_1 = \mathrm{CP}$
Prescribed values of CHIS:
$\mathrm{r}_2 = \mathrm{CHIP}$

Table 45 – The PDE equations system for the Model 1D in the separator.

COEFFICIENT FORM PDE - POSITIVE

DOMAIN SELECTION:3

NUMBER OF DEPENDENT VARIABLES: 3 (CP, CHIP, PP)

$$a = \begin{bmatrix} 0 & 0 & 0 \\ 0 & 0 & 0 \\ 0 & 0 & 0 \end{bmatrix} ; e_a = \begin{bmatrix} 0 & 0 & 0 \\ 0 & 0 & 0 \\ 0 & 0 & 0 \end{bmatrix} ; \alpha = \begin{bmatrix} 0 & 0 & 0 \\ 0 & 0 & 0 \\ 0 & 0 & 0 \end{bmatrix} ; \beta = \begin{bmatrix} 0 & 0 & 0 \\ 0 & 0 & 0 \\ 0 & 0 & 0 \end{bmatrix}$$

$$f = \begin{bmatrix} 0 \\ 0 \\ \mathrm{A4P} * \mathrm{BVNS}/\mathrm{A1P} \end{bmatrix} \quad ; \quad [\gamma] = \begin{bmatrix} 0 \\ 0 \\ 0 \end{bmatrix}$$

$$c = \begin{bmatrix} 1 & 0 & (1 - \mathrm{tP}) * \mathrm{A1P} \\ \mathrm{tN} - \mathrm{tP} & -\mathrm{CP} & -2 * \mathrm{tP} * \mathrm{tN} * \mathrm{A1P} \\ 0 & 0 & -1 \end{bmatrix}$$

$$d_a = \begin{bmatrix} 1 & 0 & 0 \\ 0 & 0 & 0 \\ 0 & 0 & 0 \end{bmatrix}$$

INITIAL VALUES FOR:

DOMAIN SELECTION:3

$$\mathrm{CP} = \mathrm{CPI}, \mathrm{CHIP} = \mathrm{CHIPI}, \mathrm{PP} = \mathrm{PSI}, \frac{\partial CP}{\partial t} = 0, \frac{\partial CHIP}{\partial t} = 0, \frac{\partial PP}{\partial t} = 0$$

FLUX/SOURCE

BOUNDARY SELECTION: 3

$$\mathrm{g} = \begin{cases} -1 * ((1 - tP) * A1P * PPx + CSx/A6) \\ -1 * ((tN - tP) * CPx + 2 * tP * tN * A1P * PPx - CP * CHISx/A6) \\ 0 \end{cases}$$

$$q = \begin{bmatrix} 0 & 0 & 0 \\ 0 & 0 & 0 \\ 0 & 0 & 0 \end{bmatrix}$$

FLUX/SOURCE

BOUNDARY SELECTION: 4

$$\mathrm{g} = \begin{cases} (1 - \mathrm{tP}) * \mathrm{A1P} * \mathrm{PPx} \\ (\mathrm{tN} - \mathrm{tP}) * \mathrm{CPx} - 2 * \mathrm{tP} * \mathrm{tN} * \mathrm{A1P} * \mathrm{PPx} + (1 - \mathrm{CP}) * \mathrm{CHIPx} \\ \mathrm{n\_s} * (\mathrm{J}/\mathrm{A1P}) * \mathrm{start} \end{cases}$$

$$q = \begin{bmatrix} 0 & 0 & 0 \\ 0 & 0 & 0 \\ 0 & 0 & 0 \end{bmatrix}$$

Table 46 – The PDE equations system for the Model 1D in the positive electrode.

COEFFICIENT FORM PDE – POSITIVE PARTICLES

DOMAIN SELECTION:1
NUMBER OF DEPENDENT VARIABLES: 1 (TPS)
$c = \begin{bmatrix} 0 & 0 \\ 0 & \mathrm{A2P} * \mathrm{r}\char`^2 \end{bmatrix}$
$a = 0\ ;\ f = 0; e_a = 0\ ;$
$d_a = A3P * r\char`^2$
$\alpha = \begin{bmatrix} 0 \\ 0 \end{bmatrix}; \beta = \begin{bmatrix} 0 \\ 0 \end{bmatrix};\ \gamma = \begin{bmatrix} 0 \\ 0 \end{bmatrix}$

ZERO FLUX

BOUNDARY SELECTION: 1, 2, 4

INITIAL VALUES

DOMAIN SELECTION:1
$\mathrm{TPS} = \mathrm{TPSI}\ , \frac{\partial \mathrm{TPS}}{\partial t} = 0$

FLUX/SOURCE

BOUNDARY SELECTION: 3
$\mathrm{g} = \mathrm{n\_s} * \mathrm{A4P} * \mathrm{mod1.linext2(BVNS)} * \mathrm{r}\char`^2/3$
$q = 0$

Table 47 – The PDE equations system for the Model 2D in the positive electrode active material.

Finally the time path for the simulations is defined as:

range(0, path_time_init,RIT+10*DRIT) …
range(RIT+10*DRIT, path_time,TSTOP_DCH-10*path_time) …
range(TSTOP_DCH-10*path_time, path_time_init,TSTOP_DCH+10*path_time) …
range(TSTOP_DCH+10*path_time, path_time,TSIM-10*path_time)…
range(TSIM-10*path_time, path_time_init, TSIM)…

The points "…" indicates that the expression is written in the same line. The number of steps is higher during the current switch on/off and less during the rest period when the variation of the voltage slope is smaller. It is not reported how to create the mesh but there is no complexity and it is chosen to guarantee the accuracy of the solution and the computational time.

8.5. PDE equations system in COMSOL® (full-cell)

In this section are reported the variables and the PDE equation system implemented in COMSOL for a cell having two insertion electrodes. Some features described in the previous section Appendix 8.4 such as the input parameter, the geometry and how the 1D and 2D geometries are connected, are still valid in this case and they will not be repeated. It should be mentioned that the present code is validated at the moment, only for galvanostatic discharges. Another difference with the previous case is that the real isotherms of LGCMH cells are used for the simulations.

The initial potential in Eq. 98 in the liquid phase is calculated using an interpolating function set in “Global->Definition->interpolation” as:

$$CHII = -\mathrm{Udd\_ref\_neg2(TNI)} - \log((1 - \mathrm{TNI})/\mathrm{TNI}) \qquad \text{Eq. 98}$$

The variables for the 1D geometry are described in Table 48:

	VARIABLES NEG	
	NEGATIVE ELECTRODE	DOMAIN: 1
PNI	UNI-log((TNI)/((1-TNI)*CI))	Initial potential
UN	((F/(R*T))*Udd_ref_neg(TEN))+log(TEN/(1-TEN))	Equilibrium potential of the experimental isotherm
UNI	(F/(R*T))*Udd_ref_neg(TNI)+log(TNI/(1-TNI))	Initial equilibrium potential for the isotherm
TEN	if(mod2.linext3(TPN)>Theta_min,mod2.linext3(TPN),Theta_min)	Concentration at the surface of the particles
BVNN	TEN*exp(alphaN*(PN-CHIN-UN))-(1-TEN)*CN*exp(-(1-alphaN)*(PN-CHIN-UN))	Butler-Volmer equation
	VARIABLES POS	
	POSITIVE ELECTRODE	DOMAIN: 3
PPSI	UPSI-log(TPSI/((1-TPSI)*CI))	Initial potential
BVNS	(1-TEPS)*exp(alphaP*(PP-CHIP-UPS))-TEPS*CPS*exp(-(1-alphaP)*(PP-CHIP-UPS))	Butler-Volmer equation.
TEPS	if(mod2.linext2(TPS)>Theta_min,mod2.linext2(TPS),Theta_min)	Concentration at the surface of the particles
UPS	(F/(R*T))*Udd_ref_pos(1-TEPS)-log(TEPS/(1-TEPS))	Equilibrium potential of the experimental isotherm
UPSI	(F/(R*T))*Udd_ref_pos(1-TPSI)-log(TPSI/(1-TPSI))	Inital equilibrium potential of the experimental isotherm
CPS	if(CP>C_min,CP,C_min)	Minimum concentration in the electrolyte to ensures the stability of the solver (because of the exponential of B-V)
	VARIABLES START	
	VARIABLE ASSOCIATED TO THE CURRENT SWITCH	ENTIRE MODEL
start	flc2hs(t-RIT,DRIT)*flc2hs(TSIM-t,DRIT)	The flc2hs functions ensures the smooth switch of the current.

Table 48 – The variables associated to the model geometry 1D for the complete cell

The variable Udd_ref_neg and Udd_ref_pos represents the isotherm in dimensionless unit of the electrodes. This variable is introduced using the interpolation function implemented in COMSOL.

The PDE equations system for the Model 1D in the negative electrode, separator and positive electrode are reported in Table 49, Table 50 and Table 51, respectively. The PDE equations system for the Model 2D in the particle of the negative electrode and positive electrode are reported in Table 52 and Table 53, respectively.

COEFFICIENT FORM PDE - NEGATIVE

DOMAIN SELECTION:1

NUMBER OF DEPENDENT VARIABLES: 3 (CN, CHIN, PN)

$$a = \begin{bmatrix} 0 & 0 & 0 \\ 0 & 0 & 0 \\ 0 & 0 & 0 \end{bmatrix}; e_a = \begin{bmatrix} 0 & 0 & 0 \\ 0 & 0 & 0 \\ 0 & 0 & 0 \end{bmatrix}; \alpha = \begin{bmatrix} 0 & 0 & 0 \\ 0 & 0 & 0 \\ 0 & 0 & 0 \end{bmatrix}; \beta = \begin{bmatrix} 0 & 0 & 0 \\ 0 & 0 & 0 \\ 0 & 0 & 0 \end{bmatrix}$$

$$f = \begin{bmatrix} 0 \\ 0 \\ \mathrm{A4N} * \mathrm{BVNN}/\mathrm{A1N} \end{bmatrix} \quad ; \quad [\gamma] = \begin{bmatrix} 0 \\ 0 \\ 0 \end{bmatrix}$$

$$c = \begin{bmatrix} 1 & 0 & (1-\mathrm{tP}) * \mathrm{A1N} \\ \mathrm{tN}-\mathrm{tP} & -\mathrm{CN} & -2 * \mathrm{tP} * \mathrm{tN} * \mathrm{A1N} \\ 0 & 0 & -1 \end{bmatrix}$$

$$d_a = \begin{bmatrix} A7 & 0 & 0 \\ 0 & 0 & 0 \\ 0 & 0 & 0 \end{bmatrix}$$

INITIAL VALUES FOR:

DOMAIN SELECTION:1

$$\mathrm{CN} = \mathrm{CI}, \mathrm{CHIN} = \mathrm{CHII}, \mathrm{PN} = \mathrm{PNI}, \frac{\partial CN}{\partial t} = 0, \frac{\partial CHIN}{\partial t} = 0, \frac{\partial PN}{\partial t} = 0$$

FLUX/SOURCE

BOUNDARY SELECTION: 1 (Negative Current Collector)

$$\mathrm{g} = \begin{matrix} -1 * (1-\mathrm{tP}) * \mathrm{A1N} * \mathrm{PNx} \\ -1 * ((\mathrm{tN}-\mathrm{tP}) * \mathrm{CNx} - 2 * \mathrm{tP} * \mathrm{tN} * \mathrm{A1N} * \mathrm{PNx} + (1-\mathrm{CN}) * \mathrm{CHINx}) \\ -1 * (\mathrm{A8} * \mathrm{J}/\mathrm{A1N}) * \mathrm{start} \end{matrix}$$

$$q = \begin{bmatrix} 0 & 0 & 0 \\ 0 & 0 & 0 \\ 0 & 0 & 0 \end{bmatrix}$$

FLUX/SOURCE

BOUNDARY SELECTION: 2 (Interface Negative Electrode / Separator)

$$\mathrm{g} = \begin{matrix} 1 * ((1-\mathrm{tP}) * \mathrm{A1N} * \mathrm{PNx} + \mathrm{A8} * \mathrm{CSx}/\mathrm{A6}) \\ 1 * ((\mathrm{tN}-\mathrm{tP}) * \mathrm{CNx} - 2 * \mathrm{tP} * \mathrm{tN} * \mathrm{A1N} * \mathrm{PNx} - \mathrm{A8} * \mathrm{CN} * \mathrm{CHISx}/\mathrm{A6}) \\ 0 \end{matrix}$$

$$q = \begin{bmatrix} 0 & 0 & 0 \\ 0 & 0 & 0 \\ 0 & 0 & 0 \end{bmatrix}$$

DIRICHLET BOUNDARY CONDITION

BOUNDARY SELECTION: 1 (Negative Current Collector)

Prescribed value of PN $r_3 = 0$, this represent the voltage refence for the cell (the other cases for r_1 and r_2 must stay unselected)

Table 49 – The PDE equations system for the Model 1D in the negative electrode.

COEFFICIENT FORM PDE - SEPARATOR

DOMAIN SELECTION:2

NUMBER OF DEPENDENT VARIABLES: 2 (CS, CHIS)

$a = \begin{bmatrix} 0 & 0 \\ 0 & 0 \end{bmatrix}$; $e_a = \begin{bmatrix} 0 & 0 \\ 0 & 0 \end{bmatrix}$; $\alpha = \begin{bmatrix} 0 & 0 \\ 0 & 0 \end{bmatrix}$; $\beta = \begin{bmatrix} 0 & 0 \\ 0 & 0 \end{bmatrix}$

$f = \begin{bmatrix} 0 \\ 0 \end{bmatrix} \quad ; \quad [\gamma] = \begin{bmatrix} 0 \\ 0 \end{bmatrix}$

$c = \begin{bmatrix} 1/A5 & 0 \\ 1 - 2 * tP & -CS \end{bmatrix}$

$d_a = \begin{bmatrix} 1 & 0 \\ 0 & 0 \end{bmatrix}$

INITIAL VALUES FOR:

DOMAIN SELECTION:2

$$\mathrm{CS} = \mathrm{CI}, \mathrm{CHIS} = \mathrm{CHII}, \frac{\partial CS}{\partial t} = 0, \frac{\partial CHIS}{\partial t} = 0$$

DIRICHLET BOUNDARY CONDITION

BOUNDARY SELECTION: 2 (Interface Negative Electrode / Separator)

Prescribed value of CS $r_1 = CN$

Prescribed value of CHIS $r_2 = CHIN$

DIRICHLET BOUNDARY CONDITION

BOUNDARY SELECTION: 3 (Interface Separator / Positive Electrode)

Prescribed value of CS $r_1 = CP$

Prescribed value of CHIS $r_2 = CHIP$

Table 50 – The PDE equations system for the Model 1D in the separator.

COEFFICIENT FORM PDE - POSITIVE

DOMAIN SELECTION:3

NUMBER OF DEPENDENT VARIABLES: 3 (CP, CHIP, PP)

$a = \begin{bmatrix} 0 & 0 & 0 \\ 0 & 0 & 0 \\ 0 & 0 & 0 \end{bmatrix}$; $e_a = \begin{bmatrix} 0 & 0 & 0 \\ 0 & 0 & 0 \\ 0 & 0 & 0 \end{bmatrix}$; $\alpha = \begin{bmatrix} 0 & 0 & 0 \\ 0 & 0 & 0 \\ 0 & 0 & 0 \end{bmatrix}$; $\beta = \begin{bmatrix} 0 & 0 & 0 \\ 0 & 0 & 0 \\ 0 & 0 & 0 \end{bmatrix}$

$f = \begin{bmatrix} 0 \\ 0 \\ \mathrm{A4P} * \mathrm{BVNS}/\mathrm{A1P} \end{bmatrix} \quad ; \quad [\gamma] = \begin{bmatrix} 0 \\ 0 \\ 0 \end{bmatrix}$

$c = \begin{bmatrix} 1 & 0 & (1 - \mathrm{tP}) * \mathrm{A1P} \\ \mathrm{tN} - \mathrm{tP} & -\mathrm{CP} & -2 * \mathrm{tP} * \mathrm{tN} * \mathrm{A1P} \\ 0 & 0 & -1 \end{bmatrix}$

$d_a = \begin{bmatrix} 1 & 0 & 0 \\ 0 & 0 & 0 \\ 0 & 0 & 0 \end{bmatrix}$

INITIAL VALUES FOR:

DOMAIN SELECTION:3

$$\mathrm{CP} = \mathrm{CI}, \mathrm{CHII} = \mathrm{CHII}, \mathrm{PP} = \mathrm{PPSI}, \frac{\partial CP}{\partial t} = 0, \frac{\partial CHIP}{\partial t} = 0, \frac{\partial PP}{\partial t} = 0$$

FLUX/SOURCE

BOUNDARY SELECTION: 3

$$\mathrm{g} = \begin{matrix} -1 * ((1 - \mathrm{tP}) * \mathrm{A1P} * \mathrm{PPx} + \mathrm{CSx}/\mathrm{A6}) \\ -1 * ((\mathrm{tN} - \mathrm{tP}) * \mathrm{CPx} - 2 * \mathrm{tP} * \mathrm{tN} * \mathrm{A1P} * \mathrm{PPx} - \mathrm{CP} * \mathrm{CHISx}/\mathrm{A6}) \\ 0 \end{matrix}$$

$q = \begin{bmatrix} 0 & 0 & 0 \\ 0 & 0 & 0 \\ 0 & 0 & 0 \end{bmatrix}$

FLUX/SOURCE

BOUNDARY SELECTION: 4

$$\mathrm{g} = \begin{matrix} 1 * (1 - \mathrm{tP}) * \mathrm{A1P} * \mathrm{PPx} \\ 1 * ((\mathrm{tN} - \mathrm{tP}) * \mathrm{CPx} - 2 * \mathrm{tP} * \mathrm{tN} * \mathrm{A1P} * \mathrm{PPx} + (1 - \mathrm{CP}) * \mathrm{CHIPx}) \\ 1 * (\mathrm{J}/\mathrm{A1P}) * \mathrm{start} \end{matrix}$$

$q = \begin{bmatrix} 0 & 0 & 0 \\ 0 & 0 & 0 \\ 0 & 0 & 0 \end{bmatrix}$

Table 51 – The PDE equations system for the Model 1D in the positive electrode.

COEFFICIENT FORM PDE – NEGATIVE PARTICLES

DOMAIN SELECTION:1
NUMBER OF DEPENDENT VARIABLES: 1 (TPN)
$c = \begin{bmatrix} 0 & 0 \\ 0 & \mathrm{A2N} * \mathrm{r}^\wedge 2 \end{bmatrix}$
$a = 0\ ;\ f = 0; e_a = 0\ ;$
$d_a = A3N * A7 * r^\wedge 2$
$\alpha = \begin{bmatrix} 0 \\ 0 \end{bmatrix}; \beta = \begin{bmatrix} 0 \\ 0 \end{bmatrix};\ \gamma = \begin{bmatrix} 0 \\ 0 \end{bmatrix}$

ZERO FLUX

BOUNDARY SELECTION: 1, 2, 4

INITIAL VALUES

DOMAIN SELECTION:1
$\mathrm{TPN} = \mathrm{TNI}\,, \frac{\partial \mathrm{TPN}}{\partial t} = 0$

FLUX/SOURCE

BOUNDARY SELECTION: 3
$\mathrm{g} = 1 * ((-\mathrm{A4N} * \mathrm{mod1.linext4(BVNN)} * \mathrm{r}^\wedge 2)/3)$
$q = 0$

Table 52 – The PDE equations system for the Model 2D in the negative electrode active material

COEFFICIENT FORM PDE – POSITIVE PARTICLES

DOMAIN SELECTION:1
NUMBER OF DEPENDENT VARIABLES: 1 (TPS)
$c = \begin{bmatrix} 0 & 0 \\ 0 & \mathrm{A2P} * \mathrm{r}^\wedge 2 \end{bmatrix}$
$a = 0\ ;\ f = 0; e_a = 0\ ;$
$d_a = A3P * r^\wedge 2$
$\alpha = \begin{bmatrix} 0 \\ 0 \end{bmatrix}; \beta = \begin{bmatrix} 0 \\ 0 \end{bmatrix};\ \gamma = \begin{bmatrix} 0 \\ 0 \end{bmatrix}$

ZERO FLUX

BOUNDARY SELECTION: 1, 2, 4

INITIAL VALUES

DOMAIN SELECTION:1
$\mathrm{TPS} = \mathrm{TPSI}\,, \frac{\partial \mathrm{TPS}}{\partial t} = 0$

FLUX/SOURCE

BOUNDARY SELECTION: 3
$\mathrm{g} = 1 * (\mathrm{A4P} * \mathrm{mod1.linext1(BVNS)} * \mathrm{r}^\wedge 2)/3$
$q = 0$

Table 53 – The PDE equations system for the Model 2D in the positive electrode active material

8.6. Simulation of the LGC INR18650MH1 with COMSOL®

In this section are reported the galvanostatic simulations of the LGC cells in Figure 134 with the parameters measured in Table 26. In addition, the parameters assumed from the literature or fitted are reported in Figure 134 (A-B).

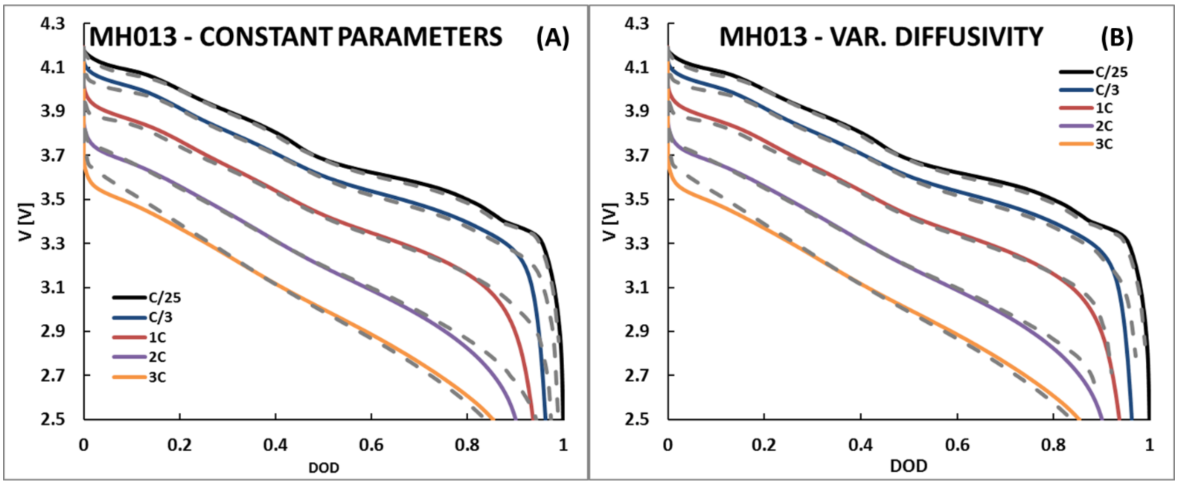

Figure 134 – The galvanostatic discharges at 25°C for a fresh LGCMH cell (i.e. the number 13) are reported as a function of the DOD for various C-rates: C/25, C/3, 1C, 2C and 3C. In (A) the discharges simulated are indicated with the grey dashed curves, and the parameters are reported in table Table 54. Instead, in (B) a diffusion coefficient is used as a function of the SOC and the values are reported in Figure 135.

In Figure 134 (A) are reported with different colours the voltage during the galvanostatic discharge a fresh LGCMH cell (the n°13) at 25°C for the following C-rates: C/25, C/3, 1C, 2C and 3C. It should be noted that these cells are highly resistive because of the high energy thus a very large polarization is observed (~ 0.5-0.8V) at only 3C. The difference between the measured and the simulated rated capacity is less than 5%. In Figure 134 (B) is used a solid phase diffusion coefficient as a fitting function of the SOC as reported in Figure 135, following the examples reported in literature and described in § 1.4, §2.2 and § 6.1.4. In this case the error is less than 1% but there is no improvement in the physics of the model. In further studies, it should be discussed that fitted parameters approximate the physically measured parameters.

Summary of the parameters	
$\sigma_- = 0.008\ [S/m]$	$C_0 = 1.1 \cdot 10^{-10}\ [mol/m^3]$
$\sigma_+ = 0.01\ [S/m]$	$D_{s,+} = 1.5 \cdot 10^{-14}\ [m^2/s]$
$D_{e,+} = 8 \cdot 10^{-11}\ [m^2/s]$	$D_{s,-} = 1 \cdot 10^{-13}\ [m^2/s]$
$D_{e,-} = 1 \cdot 10^{-10}\ [m^2/s]$	$k_+ = 1 \cdot 10^{-10}\ [mol/(m^2 s)]$
$D_{e,s} = 1.1 \cdot 10^{-10}\ [m^2/s]$	$k_- = 5 \cdot 10^{-10}\ [mol/(m^2 s)]$

Table 54 – The parameters used for the simulations illustrated in Figure 134 are reported.

The value of the electronic conductivity is low than the values reported in § 3.5. The fact can be attributed to the high value of the kinetic rate constant and because of the absence of a contact resistance between the particle. However, in other works the difficult to find an agreement between the measurement and the simulation, some authors use a conductivity as a function of the current rate as stated in § 1.4.

The dimensionless parameters are reported here below in Table 55:

Summary of the dimensionless parameters		
$A_{1-} = 0.021$	$A_{1+} = 0.033$	$A_5 = 0.086$
$A_{2-} = 0.932$	$A_{2+} = 0.485$	$A_6 = 0.111$
$A_{3-} = 86.3$	$A_{3+} = 148$	$A_7 = 2.30$
$A_{4-} = 0.210$	$A_{4+} = 0.087$	$A_8 = 1.10$

Table 55 – The dimensionless parameters used for the simulations illustrated in Figure 134 are reported.

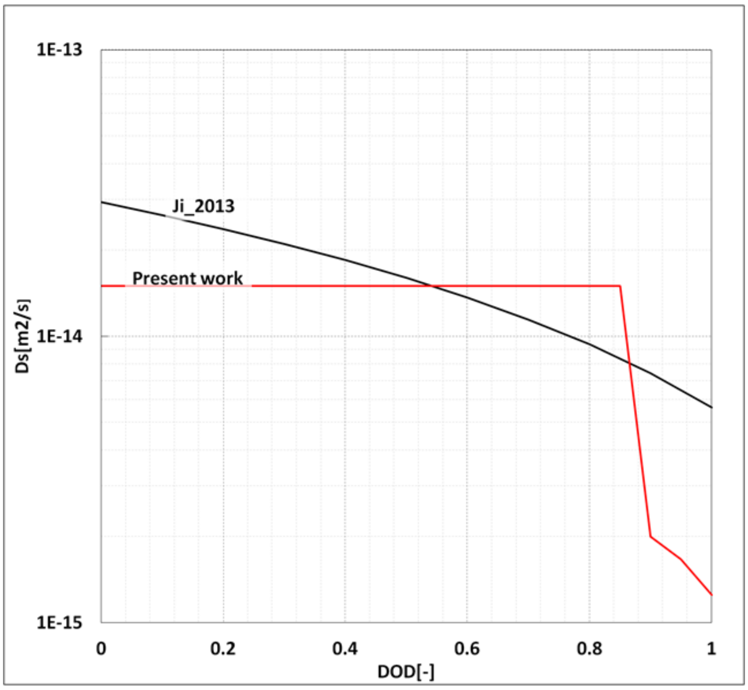

Figure 135 – The variable diffusion coefficient as a function of the SOC used for the simulations illustrated in Figure 134(B)

Despites this combination of parameters allows good simulations, it should be demonstrated that this is unique. Thus, there is no pretention to identify the real values of the parameters also because some effects are not accounted such as:

- temperature dependency of the parameters at high C-rates;
- inter-particle diffusion;
- lithium swelling in the active material;

In conclusion, these simulations indicate that the proposed model is able to reproduce the behaviour of lithium-ion battery like most of the "state-of-the-art" commercial tools does. However further studies are required to understand how to predict the behaviour of a new cell without fitting the experiences.

8.7. C-rate profile used in galvanostatic discharges in § 4.1.2

In Figure 136 the yellow boxes with green and blue contours indicate the first and the second part of the protocol, respectively. In the first part of the protocol, the discharge rate is set to C/3 for the different charge rates, in the second part, the charge rate is set to C/3 for the several discharge rates.

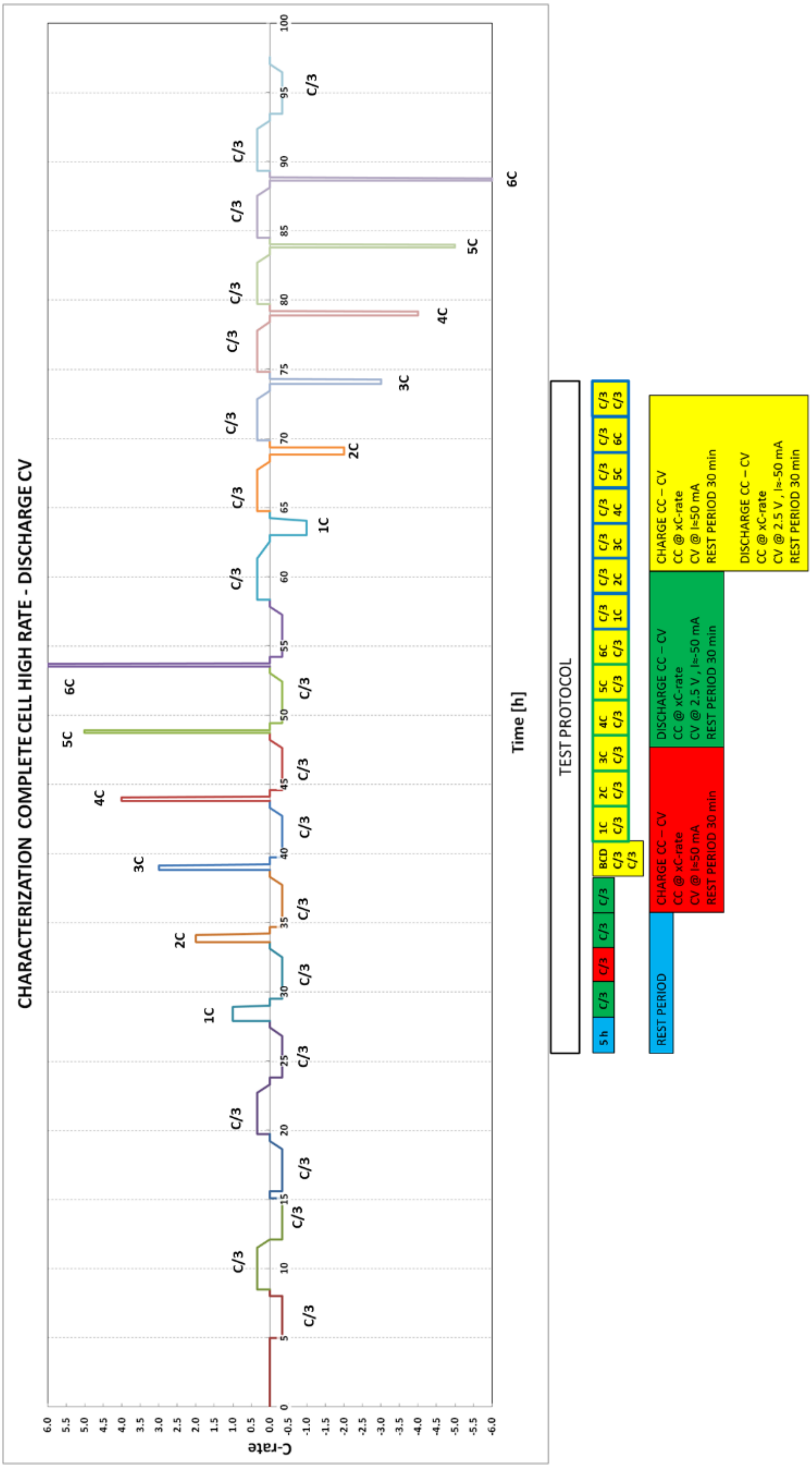

Figure 136 – The picture illustrates the current profile expressed in term of C-rate as a function of the expected test duration. A synthetic form of this test aiming to characterize the cell performances from 1C to 6C is reported above.

The discharge with a constant voltage of 2.5V guarantee the discharge of the residual capacity when the cell is discharged at high rates but it increases the degradation around 2% after the test sequence. In fact, the current can flow not because of intercalation reaction but because of side reactions such as the oxidation of the electrolyte [165], [259] . For these reasons, the constant voltage discharge will be avoided in further protocols.

8.8. C-rate profile used in galvanostatic discharges in § 4.1.3

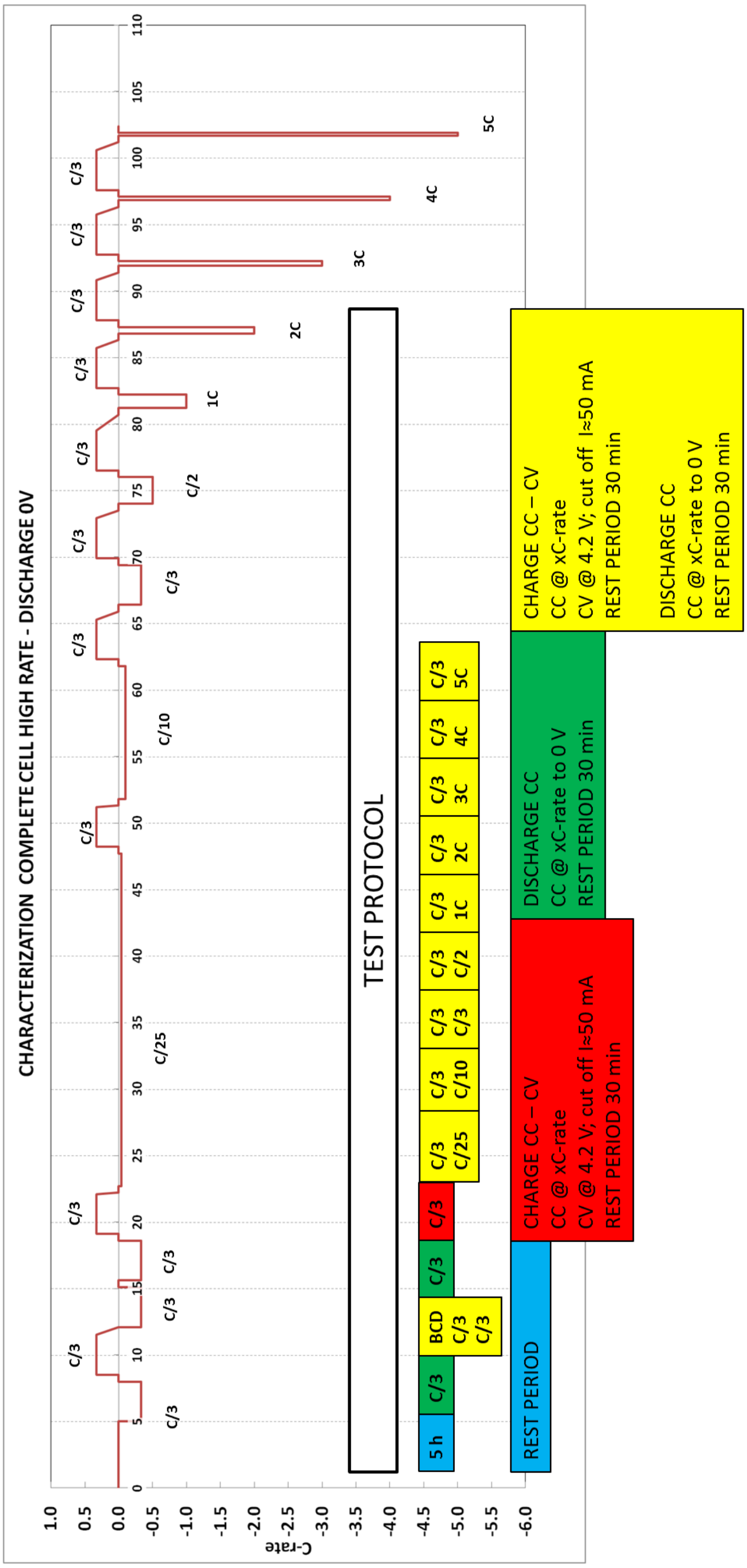

Figure 137 – The picture reports the current profile as C-rate and the expected test duration in the abscises. The test protocols with the associated C-rates are also reported in a compact format. Purpose of the test is to characterize the cell behavior at low voltage: between 2.5V and 0.05 V.

References

[1] M. T. Lawder, P. W. C. Northrop, and V. R. Subramanian, “Model-Based SEI Layer Growth and Capacity Fade Analysis for EV and PHEV Batteries and Drive Cycles,” *J. Electrochem. Soc.*, vol. 161, no. 14, pp. A2099–A2108, 2014.

[2] D. Larcher and J.-M. Tarascon, “Towards greener and more sustainable batteries for electrical energy storage,” *Nat. Chem.*, vol. 7, pp. 19–29, 2015.

[3] M. Lesemann, J. Wismans, E.-M. Malmek, C. Karlsson, N. Depner, M. Funcke, L. Ickert, B. Bayer, W. Schindler, G. Monfrino, M. Petiot, and Ntchouzou, “Advanced Electric Vehicle Architectures - Societal scenarios and available technologies for electric vehicle architectures in 2020,” no. 265898, 2011.

[4] O. Gröger, H. A. Gasteiger, and J.-P. Suchsland, “Review—Electromobility: Batteries or Fuel Cells?,” *J. Electrochem. Soc.*, vol. 162, no. 14, pp. A2605–A2622, 2015.

[5] R. E. Lyon and R. N. Walters, “Energy Release by Rechargeable Lithium-Ion Batteries in Thermal Runaway,” 2016.

[6] Richard N. Walters & Richard E. Lyon, “Measuring Energy Release of Lithium-ion Battery Failure Using a Bomb Calorimeter,” 2016.

[7] E. Karden, S. Ploumen, B. Fricke, T. Miller, and K. Snyder, “Energy storage devices for future hybrid electric vehicles,” *J. Power Sources*, vol. 168, no. 1 SPEC. ISS., pp. 2–11, 2007.

[8] S. Manzetti and F. Mariasiu, “Electric vehicle battery technologies: From present state to future systems,” *Renew. Sustain. Energy Rev.*, vol. 51, pp. 1004–1012, 2015.

[9] C. Fink and B. Kaltenegger, “Electrothermal and Electrochemical Modeling of Lithium-ion Batteries: 3D Simulation with Experimental Validation,” vol. 61, no. 27, pp. 105–124, 2014.

[10] A. Nyman and H. Ekström, “Modeling the Lithium-Ion Battery,” *Intertek - Comsol*.

[11] Comsol, “1D Isothermal Lithium-Ion Battery,” *Comsol Website*, pp. 1–30, 2013.

[12] M. Safari, “Aging of Li-Ion Batteries: Experiments and Modeling,” *Phd Thesis - Univ. Picardie Jules Verne*, p. 150, 2011.

[13] M. Safari and C. Delacourt, “Mathematical Modeling of Lithium Iron Phosphate Electrode: Galvanostatic Charge/Discharge and Path Dependence,” *J.*

Electrochem. Soc., vol. 158, no. 2, p. A63, 2011.

[14] D. W. Dees, V. S. Battaglia, and A. Bélanger, “Electrochemical modeling of lithium polymer batteries,” *J. Power Sources*, vol. 110, no. 2, pp. 310–320, 2002.

[15] S. Santhanagopalan, Q. Guo, P. Ramadass, and R. E. White, “Review of models for predicting the cycling performance of lithium ion batteries,” *J. Power Sources*, vol. 156, no. 2, pp. 620–628, Jun. 2006.

[16] W. A. van Schalkwijk and B. Scrosati, *Advances in Lithium-Ion Batteries*. 2002.

[17] H. Takahara, Y. Kobayashi, K. Shono, H. Kobayashi, M. Shikano, and T. Nakamura, “Analysis of Solid Electrolyte Interphase in Mn-Based Cathode/Graphite Li-Ion Battery with Glow Discharge Optical Emission Spectroscopy,” *J. Electrochem. Soc.*, vol. 161, no. 10, pp. A1716–A1722, 2014.

[18] B. V. Ratnakumar, M. C. Smart, and S. Surampudi, “Effects of SEI on the kinetics of lithium intercalation,” *J. Power Sources*, vol. 97–98, pp. 137–139, 2001.

[19] M. Tang, S. Lu, and J. Newman, “Experimental and Theoretical Investigation of Solid-Electrolyte-Interphase Formation Mechanisms on Glassy Carbon,” *J. Electrochem. Soc.*, vol. 159, no. 11, pp. A1775–A1785, 2012.

[20] M. B. Pinson and M. Z. Bazant, “Theory of SEI Formation in Rechargeable Batteries: Capacity Fade, Accelerated Aging and Lifetime Prediction,” *J. Electrochem. Soc.*, vol. 160, no. 2, pp. A243–A250, 2012.

[21] K. Edström, M. Herstedt, and D. P. Abraham, “A new look at the solid electrolyte interphase on graphite anodes in Li-ion batteries,” *J. Power Sources*, vol. 153, no. 2, pp. 380–384, 2006.

[22] S. Wenzel, T. Leichtweiss, D. Krüger, J. Sann, and J. Janek, “Interphase formation on lithium solid electrolytes - An in situ approach to study interfacial reactions by photoelectron spectroscopy,” *Solid State Ionics*, vol. 278, pp. 98–105, 2015.

[23] F. Kong, R. Kostecki, G. Nadeau, X. Song, K. Zaghib, K. Kinoshita, and F. McLarnon, “In situ studies of SEI formation,” *J. Power Sources*, vol. 97–98, pp. 58–66, 2001.

[24] K. Ui, D. Fujii, Y. Niwata, T. Karouji, Y. Shibata, Y. Kadoma, K. Shimada, and N. Kumagai, “Analysis of solid electrolyte interface formation reaction and surface deposit of natural graphite negative electrode employing polyacrylic acid as a binder,” *J. Power Sources*, vol. 247, pp. 981–990, 2014.

[25] L. Martin, H. Martinez, M. Ulldemolins, B. Pecquenard, and F. Le Cras, "Evolution of the Si electrode/electrolyte interface in lithium batteries characterized by XPS and AFM techniques: The influence of vinylene carbonate additive," *Solid State Ionics*, vol. 215, pp. 36–44, 2012.

[26] H. Buqa, A. Würsig, J. Vetter, M. E. Spahr, F. Krumeich, and P. Novák, "SEI film formation on highly crystalline graphitic materials in lithium-ion batteries," *J. Power Sources*, vol. 153, no. 2, pp. 385–390, 2006.

[27] G. C. Chung, "Reconsideration of SEI stability: Reversible lithium intercalation into graphite electrodes in trans-2,3-butylene carbonate," *J. Power Sources*, vol. 104, no. 1, pp. 7–12, 2002.

[28] V. A. Agubra and J. W. Fergus, "The formation and stability of the solid electrolyte interface on the graphite anode," *J. Power Sources*, vol. 268, pp. 153–162, 2014.

[29] C. Lin, A. Tang, H. Mu, W. Wang, and C. Wang, "Aging Mechanisms of Electrode Materials in Lithium-Ion Batteries for Electric Vehicles," vol. 2015, pp. 1–18, 2015.

[30] J. Vetter, P. Novák, M. R. Wagner, C. Veit, K. C. Möller, J. O. Besenhard, M. Winter, M. Wohlfahrt-Mehrens, C. Vogler, and A. Hammouche, "Ageing mechanisms in lithium-ion batteries," *J. Power Sources*, vol. 147, no. 1–2, pp. 269–281, 2005.

[31] V. Ramadesigan, P. W. C. Northrop, S. De, S. Santhanagopalan, R. D. Braatz, and V. R. Subramanian, "Modeling and Simulation of Lithium-Ion Batteries from a Systems Engineering Perspective," *J. Electrochem. Soc.*, vol. 159, no. 3, p. R31, 2012.

[32] J. Turner, S. Allu, M. Berrill, W. Elwasif, S. Kalnaus, A. Kumar, D. Lebrun-Grandie, S. Pannala, and S. Simunovic, "Safer Batteries through Coupled Multiscale Modeling," *Procedia Comput. Sci.*, vol. 51, no. 2, pp. 1168–1177, 2015.

[33] C. F. Chiasserini and R. R. Rao, "A Model for Battery Pulsed Discharge with Recovery Effect N-1," *Wirel. Commun. Netw. Conf.*, pp. 636–639, 1999.

[34] J. D. Kozlowski, "Electrochemical cell prognostics using online impedance measurements and model-based data fusion techniques," *IEEE Aerosp. Conf.*, vol. 7, pp. 3257–3270, 2003.

[35] A. J. Salkind, C. Fennie, P. Singh, T. Atwater, and D. E. Reisner, "Determination of state-of-charge and state-of-health of batteries by fuzzy logic

methodology," *J. Power Sources*, vol. 80, pp. 293–300, 1999.

[36] M. Jongerden and B. Haverkort, "Battery modeling," *Thecnical Rep. Fac. Electr. Eng. Math. Comput. Sci.*, p. 18, 2008.

[37] C. M. Shepherd, "Design of Primary and Secondary Cells," *J. Electrochem. Soc.*, vol. 112, no. 7, p. 657, 1965.

[38] D. N. Rakhmatov and S. B. K. Vrudhula, "An analytical high-level battery model for use in energy management of portable electronic systems," *2001 IEEE/ACM Int. Conf. Comput. Des.*, pp. 488–493, 2001.

[39] J. Euler and W. Nonnenmacher, "Stromverteilung in porösen elektroden," *Electrochim. Acta*, vol. 2, no. 4, pp. 268–286, 1960.

[40] R. de Levie, "On porous electrodes in electrolyte solutions," *Electrochim. Acta*, vol. 8, pp. 751–780, 1963.

[41] M. A. Xavier and M. S. Trimboli, "Lithium-ion battery cell-level control using constrained model predictive control and equivalent circuit models," *J. Power Sources*, vol. 285, pp. 374–384, 2015.

[42] A. Jossen, "Fundamentals of battery dynamics," *J. Power Sources*, vol. 154, no. 2, pp. 530–538, 2006.

[43] D. Pati, D. Gandolfo, and A. Brand, "Dynamic model of lithium polymer battery e Load resistor method for electric parameters identi fi cation," vol. 88, pp. 470–479, 2015.

[44] V. Muenzel, A. F. Hollenkamp, A. I. Bhatt, J. De Hoog, M. Brazil, D. A. Thomas, and I. Mareels, "A Comparative Testing Study of Commercial 18650-Format Lithium-Ion Battery Cells," *J. Electrochem. Soc.*, vol. 162, no. 8, pp. 1592–1600, 2015.

[45] S. M. Mousavi G. and M. Nikdel, "Various battery models for various simulation studies and applications," *Renew. Sustain. Energy Rev.*, vol. 32, pp. 477–485, 2014.

[46] S. Castano, L. Gauchia, E. Voncila, and J. Sanz, "Dynamical modeling procedure of a Li-ion battery pack suitable for real-time applications," *Energy Convers. Manag.*, vol. 92, pp. 396–405, 2015.

[47] L. G. L. Gao, S. L. S. Liu, and R. a. Dougal, "Dynamic lithium-ion battery model for system simulation," *IEEE Trans. Components Packag. Technol.*, vol. 25, no. 3, pp. 495–505, 2002.

[48] E. Barsoukov, J. H. Kim, C. O. Yoon, and H. Lee, "Universal battery parameterization to yield a non-linear equivalent circuit valid for battery

simulation at arbitrary load," *J. Power Sources*, vol. 83, no. 1–2, pp. 61–70, 1999.

[49] K. D. Stetzel, L. L. Aldrich, M. S. Trimboli, and G. L. Plett, "Electrochemical state and internal variables estimation using a reduced-order physics-based model of a lithium-ion cell and an extended Kalman filter," *J. Power Sources*, vol. 278, pp. 490–505, 2015.

[50] G. L. Plett, "Extended Kalman filtering for battery management systems of LiPB-based HEV battery packs Part 1 . Background," vol. 134, pp. 252–261, 2004.

[51] G. L. Plett, "Extended Kalman filtering for battery management systems of LiPB-based HEV battery packs Part 2 . Modeling and identification," vol. 134, pp. 262–276, 2004.

[52] G. L. Plett, "Extended Kalman filtering for battery management systems of LiPB-based HEV battery packs - Part 3. State and parameter estimation," *J. Power Sources*, vol. 134, no. 2, pp. 277–292, 2004.

[53] W. Lai and F. Ciucci, "Mathematical modeling of porous battery electrodes-Revisit of Newman's model," *Electrochim. Acta*, vol. 56, no. 11, pp. 4369–4377, 2011.

[54] E. Barsoukov, "Comparison of kinetic properties of LiCoO2 and LiTi0.05Mg0.05Ni0.7Co0.2O2 by impedance spectroscopy," *Solid State Ionics*, vol. 161, no. 1–2, pp. 19–29, 2003.

[55] R. de Levie, "On porous electrodes in electrolyte solutions—IV," *Electrochim. Acta*, vol. 9, no. 9, pp. 1231–1245, 1964.

[56] H. Nara, D. Mukoyama, T. Yokoshima, and T. Momma, "Impedance Analysis with Transmission Line Model for Reaction Distribution in a Pouch Type Lithium-Ion Battery by Using Micro," *J. Electrochem. Soc.*, vol. 163, no. 3, pp. 31–34, 2016.

[57] M. W. Verbrugge and R. S. Conell, "Electrochemical and Thermal Characterization of Battery Modules Commensurate with Electric Vehicle Integration," *J. Electrochem. Soc.*, vol. 149, no. 1, p. A45, 2002.

[58] J. Bisquert and S. Vikhrenko, "Analysis of the kinetics of ion intercalation . Two state model describing the coupling of solid state ion diffusion and ion binding processes," *Electrochim. Acta*, vol. 47, pp. 3977–3988, 2002.

[59] I. J. Ong and J. Newman, "Double-Layer Capacitance in a Dual Lithium Ion Insertion Cell," *J. Electrochem. Soc.*, vol. 146, no. 12, pp. 4360–4365, 1999.

[60] M. Doyle and Y. Fuentes, “Computer Simulations of a Lithium-Ion Polymer Battery and Implications for Higher Capacity Next-Generation Battery Designs,” *J. Electrochem. Soc.*, vol. 150, no. 6, pp. 706–713, 2003.

[61] D. Miranda, C. M. Costa, and S. Lanceros-Mendez, “Lithium ion rechargeable batteries: State of the art and future needs of microscopic theoretical models and simulations,” *J. Electroanal. Chem.*, vol. 739, pp. 97–110, 2015.

[62] T. F. Fuller, “Simulation and Optimization of the Dual Lithium Ion Insertion Cell,” *J. Electrochem. Soc.*, vol. 141, no. 1, p. 1, 1994.

[63] C. M. Doyle, “Design and Simulation of Lithium Rechargeable Batteries,” UNIVERSITY OF CALIFORNIA, 1995.

[64] Y. Lai, S. Du, L. Ai, L. Ai, and Y. Cheng, “Insight into heat generation of lithium ion batteries based on the electrochemical-thermal model at high discharge rates,” *Int. J. Hydrogen Energy*, vol. 40, no. 38, pp. 13039–13049, 2015.

[65] a. Salvadori, D. Grazioli, M. G. D. Geers, D. Danilov, and P. H. L. Notten, “A multiscale-compatible approach in modeling ionic transport in the electrolyte of (Lithium ion) batteries,” *J. Power Sources*, vol. 293, pp. 892–911, 2015.

[66] X. Zhang, “Multiscale Modeling of Li-ion Cells: Mechanics, Heat Generation and Electrochemical Kinetics,” pp. 1–178, 2009.

[67] A. Romero-Becerril and L. Alvarez-Icaza, “Comparison of discretization methods applied to the single-particle model of lithium-ion batteries,” *J. Power Sources*, vol. 196, no. 23, pp. 10267–10279, 2011.

[68] V. R. Subramanian, V. Boovaragavan, V. Ramadesigan, and M. Arabandi, “Mathematical Model Reformulation for Lithium-Ion Battery Simulations: Galvanostatic Boundary Conditions,” *J. Electrochem. Soc.*, vol. 156, no. 4, p. A260, 2009.

[69] P. M. Gomadam, J. W. Weidner, R. a. Dougal, and R. E. White, “Mathematical modeling of lithium-ion and nickel battery systems,” *J. Power Sources*, vol. 110, no. 2, pp. 267–284, 2002.

[70] S. Renganathan, G. Sikha, S. Santhanagopalan, and R. E. White, “Theoretical Analysis of Stresses in a Lithium Ion Cell,” *J. e*, vol. 157, no. 2, pp. 155–163, 2010.

[71] T. S. Dao, C. P. Vyasarayani, and J. McPhee, “Simplification and order reduction of lithium-ion battery model based on porous-electrode theory,” *J. Power Sources*, vol. 198, pp. 329–337, 2012.

[72] E. Martínez-Rosas, R. Vasquez-Medrano, and A. Flores-Tlacuahuac,

"Modeling and simulation of lithium-ion batteries," *Comput. Chem. Eng.*, vol. 35, no. 9, pp. 1937–1948, 2011.

[73] A. Nyman, T. G. Zavalis, R. Elger, M. Behm, and G. Lindbergh, "Analysis of the Polarization in a Li-Ion Battery Cell by Numerical Simulations," *J. Electrochem. Soc.*, vol. 157, no. 11, p. A1236, 2010.

[74] T. G. Zavalis, *Mathematical Models for Investigation of Performance , Safety , and Aging in Lithium- Ion Batteries*. 2013.

[75] J. M. Marcicki, "Modeling, Parametrization, and Diagnostics for Lithium-Ion Batteries with Automotive Applications," p. 272, 2012.

[76] G. Sikha, R. E. White, and B. N. Popov, "A Mathematical Model for a Lithium-Ion Battery/Electrochemical Capacitor Hybrid System," *J. Electrochem. Soc.*, vol. 152, no. 8, pp. A1682–A1693, 2005.

[77] J. Lee, Y. K. Anguchamy, and B. N. Popov, "Simulation of charge – discharge cycling of lithium-ion batteries under low-earth-orbit conditions," *J. Power Sources*, vol. 162, pp. 1395–1400, 2006.

[78] D. Bernardi, E. Pawlikowski, and J. Newman, "A General Energy Balance for Battery Systems," *J. Electrochem. Soc.*, vol. 132, no. 1, p. 5, 1985.

[79] T. M. Bandhauer, S. Garimella, and T. F. Fuller, "A Critical Review of Thermal Issues in Lithium-Ion Batteries," *J. Electrochem. Soc.*, vol. 158, no. 3, p. R1, 2011.

[80] R. Darling and J. Newman, "Modeling Side Reactions in Composite LiMn2O4 Electrodes," *J. Electrochem. Soc.*, vol. 145, no. 3, pp. 990–998, 1998.

[81] A. Awarke, S. Pischinger, and J. Ogrzewalla, "Pseudo 3D Modeling and Analysis of the SEI Growth Distribution in Large Format Li-Ion Polymer Pouch Cells," *J. Electrochem. Soc.*, vol. 160, no. 1, pp. 172–181, 2013.

[82] J. Christensen and J. Newman, "A Mathematical Model of Stress Generation and Fracture in Lithium Manganese Oxide," *J. Electrochem. Soc.*, vol. 153, no. 6, p. A1019, 2006.

[83] J. Christensen and J. Newman, "Stress generation and fracture in lithium insertion materials," *J. Solid State Chem.*, pp. 293–319, 2006.

[84] P. Barai, K. Smith, C.-F. Chen, G.-H. Kim, and P. P. Mukherjee, "Reduced Order Modeling of Mechanical Degradation Induced Performance Decay in Lithium-Ion Battery Porous Electrodes," *J. Electrochem. Soc.*, vol. 162, no. 9, pp. A1751–A1771, 2015.

[85] D. Miranda, C. M. Costa, a. M. Almeida, and S. Lanceros-Méndez, "Modeling

separator membranes physical characteristics for optimized lithium ion battery performance," *Solid State Ionics*, vol. 278, pp. 78–84, 2015.

[86] B. Suthar, P. W. C. Northrop, D. Rife, and V. R. Subramanian, "Effect of Porosity, Thickness and Tortuosity on Capacity Fade of Anode," *J. Electrochem. Soc.*, vol. 162, no. 9, pp. 1708–1717, 2015.

[87] R. Zhao, J. Liu, and J. Gu, "The effects of electrode thickness on the electrochemical and thermal characteristics of lithium ion battery," *Appl. Energy*, vol. 139, pp. 220–229, 2015.

[88] M. Ecker, K. Stefan, I. Laresgoiti, and D. Uwe, "Parameterization of a Physico-Chemical Model of a Lithium-Ion II . Model Validation," *J. Electrochem. Soc.*, vol. 162, no. 9, pp. 1849–1857, 2015.

[89] C.L. Cobb and C.-J. Bae, "Tortuosity of Binder-free and Carbon-free High Energy Density LiCoO2 Electrodes," *Trans. E C S Soc. Electrochem.*, vol. 58, no. 13, pp. 13–24, 2014.

[90] R. Chandrasekaran, "Quanti fi cation of bottlenecks to fast charging of lithium-ion-insertion cells for electric vehicles," *J. Power Sources*, vol. 271, pp. 622–632, 2014.

[91] R. Chandrasekaran, "Quantification of bottlenecks to fast charging of lithium-ion-insertion cells for electric vehicles," *J. Power Sources*, vol. 271, pp. 622–632, 2014.

[92] S. U. Kim, P. Albertus, D. Cook, C. W. Monroe, and J. Christensen, "Thermoelectrochemical simulations of performance and abuse in 50-Ah automotive cells," *J. Power Sources*, vol. 268, pp. 625–633, 2014.

[93] L. Zhang, L. Wang, C. Lyu, J. Li, and J. Zheng, "Non-Destructive Analysis of Degradation Mechanisms in Cycle-Aged Graphite/LiCoO2 Batteries," *Energies*, vol. 7, pp. 6282–6305, 2014.

[94] N. Legrand, B. Knosp, P. Desprez, F. Lapicque, and S. Raël, "Physical characterization of the charging process of a Li-ion battery and prediction of Li plating by electrochemical modelling," *J. Power Sources*, vol. 245, pp. 208–216, 2014.

[95] N. Legrand, S. Raël, B. Knosp, M. Hinaje, P. Desprez, and F. Lapicque, "Including double-layer capacitance in lithium-ion battery mathematical models," *J. Power Sources*, vol. 251, pp. 370–378, 2014.

[96] G. Sikha, S. De, and J. Gordon, "Mathematical model for silicon electrode - Part I. 2-d model," *J. Power Sources*, vol. 262, pp. 514–523, 2014.

[97] C. L. Cobb and M. Blanco, “Modeling mass and density distribution effects on the performance of co-extruded electrodes for high energy density lithium-ion batteries,” *J. Power Sources*, vol. 249, pp. 357–366, 2014.

[98] J. Mao, W. Tiedemann, and J. Newman, “Simulation of temperature rise in Li-ion cells at very high currents,” *J. Power Sources*, vol. 271, pp. 444–454, 2014.

[99] A. Ferrese and J. S. Newman, “Modeling Lithium Movement over Multiple Cycles in a Lithium-Metal Battery,” *J. Electrochem. Soc.*, vol. 161, no. 6, pp. A948–A954, 2014.

[100] A. Ferrese and J. S. Newman, “Mechanical Deformation of a Lithium-Metal Anode Due to a Very Stiff Separator,” *J. Electrochem. Soc.*, vol. 161, no. 9, pp. A1350–A1359, 2014.

[101] P. W. C. Northrop, B. Suthar, V. Ramadesigan, S. Santhanagopalan, R. D. Braatz, and V. R. Subramanian, “Efficient Simulation and Reformulation of Lithium-Ion Battery Models for Enabling Electric Transportation,” *J. Electrochem. Soc.*, vol. 161, no. 8, pp. E3149–E3157, 2014.

[102] R. Fu, M. Xiao, and S. Y. Choe, “Modeling, validation and analysis of mechanical stress generation and dimension changes of a pouch type high power Li-ion battery,” *J. Power Sources*, vol. 224, pp. 211–224, 2013.

[103] M. Guo and R. E. White, “A distributed thermal model for a Li-ion electrode plate pair,” *J. Power Sources*, vol. 221, pp. 334–344, 2013.

[104] M. Guo, G. H. Kim, and R. E. White, “A three-dimensional multi-physics model for a Li-ion battery,” *J. Power Sources*, vol. 240, pp. 80–94, 2013.

[105] Y. Ji and C. Y. Wang, “Heating strategies for Li-ion batteries operated from subzero temperatures,” *Electrochim. Acta*, vol. 107, pp. 664–674, 2013.

[106] Y. Ji, Y. Zhang, and C.-Y. Wang, “Li-Ion Cell Operation at Low Temperatures,” *J. Electrochem. Soc.*, vol. 160, no. 4, pp. A636–A649, 2013.

[107] J. Christensen, D. Cook, and P. Albertus, “An Efficient Parallelizable 3D Thermoelectrochemical Model of a Li-Ion Cell,” *J. Electrochem. Soc.*, vol. 160, no. 11, pp. A2258–A2267, 2013.

[108] X. Lin, J. Park, L. Liu, Y. Lee, a M. Sastry, and W. Lu, “A Comprehensive Capacity Fade Model and Analysis for Li-Ion Batteries,” *J. Electrochem. Soc.*, vol. 160, no. 10, pp. 1701–1710, 2013.

[109] J. N. Reimers, M. Shoesmith, Y. S. Lin, and L. O. Valoen, “Simulating High Current Discharges of Power Optimized Li-Ion Cells,” *J. Electrochem. Soc.*, vol. 160, no. 10, pp. A1870–A1884, 2013.

[110] T. G. Zavalis, M. Behm, and G. Lindbergh, “Investigation of Short-Circuit Scenarios in a Lithium-Ion Battery Cell,” *J. Electrochem. Soc.*, vol. 159, no. 6, p. A848, 2012.

[111] G. B. Less, J. H. Seo, S. Han, A. M. Sastry, J. Zausch, A. Latz, S. Schmidt, C. Wieser, D. Kehrwald, and S. Fell, “Micro-Scale Modeling of Li-Ion Batteries: Parameterization and Validation,” *J. Electrochem. Soc.*, vol. 159, no. 6, p. A697, 2012.

[112] a. Ferrese, P. Albertus, J. Christensen, and J. Newman, “Lithium Redistribution in Lithium-Metal Batteries,” *J. Electrochem. Soc.*, vol. 159, no. 10, pp. A1615–A1623, 2012.

[113] R. Chandrasekaran and T. F. Fuller, “Analysis of the Lithium-Ion Insertion Silicon Composite Electrode/Separator/Lithium Foil Cell,” *J. Electrochem. Soc.*, vol. 158, no. 8, p. A859, 2011.

[114] H. Jannesari, M. D. Emami, and C. Ziegler, “Effect of electrolyte transport properties and variations in the morphological parameters on the variation of side reaction rate across the anode electrode and the aging of lithium ion batteries,” *J. Power Sources*, vol. 196, pp. 9654–9664, 2011.

[115] J. Christensen, “Modeling Diffusion-Induced Stress in Li-Ion Cells with Porous Electrodes,” *J. Electrochem. Soc.*, vol. 157, no. 3, p. A366, 2010.

[116] D. E. Stephenson, E. M. Hartman, J. N. Harb, and D. R. Wheeler, “Modeling of Particle-Particle Interactions in Porous Cathodes for Lithium-Ion Batteries,” *J. Electrochem. Soc.*, vol. 154, no. 12, p. A1146, 2007.

[117] S. Stewart and J. Newman, “Measuring the Salt Activity Coefficient in Lithium-Battery Electrolytes,” *J. Electrochem. Soc.*, vol. 155, no. 6, p. A458, 2008.

[118] C.-V. Hemery, “Etude des phenomenes thermiques dans les batteries Li-ion,” *Univ. GRENOBLE*, pp. 1–269, 2014.

[119] R. Masoudi, T. Uchida, and J. McPhee, “Parameter estimation of an electrochemistry-based lithium-ion battery model,” *J. Power Sources*, vol. 291, pp. 215–224, 2015.

[120] D. Andre, M. Meiler, K. Steiner, H. Walz, T. Soczka-guth, and D. U. Sauer, “Characterization of high-power lithium-ion batteries by electrochemical impedance spectroscopy . II : Modelling,” *J. Power Sources*, vol. 196, no. 12, pp. 5349–5356, 2011.

[121] Y. Ye, Y. Shi, N. Cai, J. Lee, and X. He, “Electro-thermal modeling and experimental validation for lithium ion battery,” *J. Power Sources*, vol. 199, pp.

227–238, 2012.

[122] W. Luo, C. Lyu, L. Wang, and L. Zhang, “An approximate solution for electrolyte concentration distribution in physics-based lithium-ion cell models,” *Microelectron. Reliab.*, vol. 53, no. 6, pp. 797–804, 2013.

[123] A. Hess, Q. Roode-gutzmer, C. Heubner, M. Schneider, and A. Michaelis, “Determination of state of charge-dependent asymmetric Butler e Volmer kinetics for Li x CoO 2 electrode using GITT measurements,” *J. Power Sources*, vol. 299, pp. 156–161, 2015.

[124] T. F. Fuller, M. Doyle, and J. Newman, “Relaxation Phenomena in Lithium-Ion-Insertion Cells,” *J. Electrochem. Soc.*, vol. 141, no. 4, p. 982, 1994.

[125] J. Christensen and J. Newman, “Stress generation and fracture in lithium insertion materials,” *J. Solid State Electrochem.*, vol. 10, no. 5, pp. 293–319, 2006.

[126] M. Doyle, J. Newman, A. S. Gozdz, C. N. Schmutz, and J.-M. Tarascon, “Comparison of Modeling Predictions with Experimental Data from Plastic Lithium Ion Cells,” *J. Electrochem. Soc.*, vol. 143, no. 6, p. 1890, 1996.

[127] S. Basu, R. S. Patil, S. Ramachandran, K. S. Hariharan, S. M. Kolake, T. Song, D. Oh, T. Yeo, and S. Doo, “Non-isothermal electrochemical model for lithium-ion cells with composite cathodes,” *J. Power Sources*, vol. 283, pp. 132–150, 2015.

[128] J. Newman and W. Tiedemann, “Porous-electrode theory with battery applications,” *AIChE J.*, vol. 21, no. 1, pp. 25–41, 1975.

[129] E. a. Grens and C. W. Tobias, “The influence of electrode reaction kinetics on the polarization of flooded porous electrodes,” vol. 10, no. October 1964, pp. 761–772, 1965.

[130] K. H. Xue and G. L. Plett, “A convective transport theory for high rate discharge in lithium ion cells,” *Electrochim. Acta*, vol. 87, pp. 575–590, 2013.

[131] L. O. Valo/en and J. N. Reimers, “Transport Properties of LiPF6-Based Li-Ion Battery Electrolytes,” *J. Electrochem. Soc.*, vol. 152, no. 5, p. A882, 2005.

[132] M. Doyle, T. F. Fuller, and J. Newman, “The importance of the lithium ion transference number in lithium/polymer cells,” *Electrochim. Acta*, vol. 39, no. 13, pp. 2073–2081, 1994.

[133] M. Doyle, T. F. Fuller, and J. Newman, “Modeling of Galvanostatic Charge and Discharge of the Lithium/Polymer/Insertion Cell,” *J. Electrochem. Soc.*, vol. 140, no. 6, p. 1526, 1993.

[134] J. Newman, D. Bennion, and C. W. Tobias, “Mass Transfer in Concentrated Binary Electrolytes,” *Berichte der Bunsengesellschaft*, vol. 69, no. 7, pp. 608–612, 1965.

[135] K. Smith and C. Y. Wang, “Solid-state diffusion limitations on pulse operation of a lithium ion cell for hybrid electric vehicles,” *J. Power Sources*, vol. 161, no. 1, pp. 628–639, 2006.

[136] H. Lundgren, M. Behm, and G. Lindbergh, “Electrochemical Characterization and Temperature Dependency of Mass-Transport Properties of LiPF6 in EC:DEC,” *J. Electrochem. Soc.*, vol. 162, no. 3, pp. 413–420, 2015.

[137] R. Chandrasekaran, “Quantification of contributions to the cell overpotential during galvanostatic discharge of a lithium-ion cell,” *J. Power Sources*, vol. 262, pp. 501–513, 2014.

[138] S. With and C. Multiphysics, “Rechargeable Lithium-Ion Battery Rechargeable Lithium-Ion Battery,” *Engineering*, 2008.

[139] A. M. Ramos, “On the well-posedness of a mathematical model for lithium-ion batteries,” *Appl. Math. Model.*, 2015.

[140] T. F. Fuller, M. Doyle, and J. Newman, “Simulation and Optimization of the Dual Lithium Ion Insertion Cell,” *J. Electrochem. Soc.*, vol. 141, no. 1, p. 1, 1994.

[141] K. Smith and C.-Y. Wang, “Power and thermal characterization of a lithium-ion battery pack for hybrid-electric vehicles,” *J. Power Sources*, vol. 160, no. 1, pp. 662–673, 2006.

[142] M. Ecker, K. Dung, P. Dechent, K. Stefan, A. Warnecke, and D. U. Sauer, “Parameterization of a Physico-Chemical Model of a Lithium-Ion Battery I . Determination of Parameters,” *J. Electrochem. Soc.*, vol. 162, no. 9, pp. 1836–1848, 2015.

[143] A. M. Ramos and C. P. Please, “Some comments on the Butler-Volmer equation for modeling Lithium-ion batteries,” pp. 1–14, 2015.

[144] P. Kemper, S. E. Li, and D. Kum, “Simplification of pseudo two dimensional battery model using dynamic profile of lithium concentration,” *J. Power Sources*, vol. 286, pp. 510–525, 2015.

[145] G. Sikha, B. N. Popov, and R. E. White, “Effect of Porosity on the Capacity Fade of a Lithium-Ion Battery,” *J. Electrochem. Soc.*, vol. 151, no. 7, p. A1104, 2004.

[146] G. Kim, K. Smith, J. Ireland, and A. Pesaran, “Fail-safe design for large capacity lithium-ion battery systems,” *J. Power Sources*, vol. 210, pp. 243–253, 2012.

[147] K. E. Thomas, S. E. Sloop, J. B. Kerr, and J. Newman, “Comparison of lithium-polymer cell performance with unity and nonunity transference numbers,” *J. Power Sources*, vol. 89, no. 2, pp. 132–138, 2000.

[148] P. Arora, M. Doyle, A. S. Gozdz, R. E. White, and J. Newman, “Comparison between computer simulations and experimental data for high-rate discharges of plastic lithium-ion batteries,” *J. Power Sources*, vol. 88, no. 2, pp. 219–231, 2000.

[149] P. Amiribavandpour, W. Shen, D. Mu, and A. Kapoor, “An improved theoretical electrochemical-thermal modelling of lithium-ion battery packs in electric vehicles,” *J. Power Sources*, vol. 284, pp. 328–338, 2015.

[150] R. Chandrasekaran, A. Magasinski, G. Yushin, and T. F. Fuller, “Analysis of Lithium Insertion/Deinsertion in a Silicon Electrode Particle at Room Temperature,” *J. Electrochem. Soc.*, vol. 157, no. 10, p. A1139, 2010.

[151] D. Di Domenico, A. Stefanopoulou, and G. Fiengo, “Lithium-Ion Battery State of Charge and Critical Surface Charge Estimation Using an Electrochemical Model-Based Extended Kalman Filter,” *J. Dyn. Syst. Meas. Control*, vol. 132, no. 6, p. 61302, 2010.

[152] B. Vijayaraghavan, D. R. Ely, Y.-M. Chiang, R. García-García, and R. E. García, “An Analytical Method to Determine Tortuosity in Rechargeable Battery Electrodes,” *J. Electrochem. Soc.*, vol. 159, no. 5, p. A548, 2012.

[153] I. V Thorat, D. E. Stephenson, N. A. Zacharias, K. Zaghib, J. N. Harb, and D. R. Wheeler, “Quantifying tortuosity in porous Li-ion battery materials,” *J. Power Sources*, vol. 188, pp. 592–600, 2009.

[154] R. Darling and J. Newman, “Modeling a Porous Intercalation Electrode with Two Characteristic Particle Sizes,” *J. Electrochem. Soc.*, vol. 144, no. 12, pp. 4201–4208, 1997.

[155] C. H. Lee, S. J. Bae, and M. Jang, “A study on effect of lithium ion battery design variables upon features of thermal-runaway using mathematical model and simulation,” *J. Power Sources*, vol. 293, pp. 498–510, 2015.

[156] C.L. Cobb and C.-J. Bae, “Tortuosity of Binder-free and Carbon-free High Energy Density LiCoO2 Electrodes,” *ECS Trans.*, vol. 58, no. 13, pp. 13–24, 2014.

[157] K. Kumaresan, Q. Guo, P. Ramadass, and R. E. White, “Cycle life performance of lithium-ion pouch cells,” *J. Power Sources*, vol. 158, no. 1, pp. 679–688, 2006.

[158] B. Suthar, D. Sonawane, R. D. Braatz, and V. R. Subramanian, “Optimal Low Temperature Charging of Lithium-ion Batteries,” *IFAC-PapersOnLine*, vol. 48, no. 8, pp. 1216–1221, 2015.

[159] H. Arunachalam, S. Onori, and I. Battiato, “On Veracity of Macroscopic Lithium-Ion Battery Models,” *J. Electrochem. Soc.*, vol. 162, no. 10, pp. A1940–A1951, 2015.

[160] S. Santhanagopalan, Q. Guo, and R. E. White, “Parameter Estimation and Model Discrimination for a Lithium-Ion Cell,” *J. Electrochem. Soc.*, vol. 154, no. 3, p. A198, 2007.

[161] P. Albertus, J. Couts, V. Srinivasan, and J. Newman, “II. A combined model for determining capacity usage and battery size for hybrid and plug-in hybrid electric vehicles,” *J. Power Sources*, vol. 183, no. 2, pp. 771–782, 2008.

[162] P. Albertus, J. Christensen, and J. Newman, “Experiments on and Modeling of Positive Electrodes with Multiple Active Materials for Lithium-Ion Batteries,” *J. Electrochem. Soc.*, vol. 156, no. 7, p. A606, 2009.

[163] R. Fu, S. Y. Choe, V. Agubra, and J. Fergus, “Modeling of degradation effects considering side reactions for a pouch type Li-ion polymer battery with carbon anode,” *J. Power Sources*, vol. 261, pp. 120–135, 2014.

[164] K. Kumaresan, G. Sikha, and R. E. White, “Thermal Model for a Li-Ion Cell,” *J. Electrochem. Soc.*, vol. 155, no. 2, p. A164, 2008.

[165] G. Ning and B. N. Popov, “Cycle Life Modeling of Lithium-Ion Batteries,” 2004.

[166] E. Prada, D. Di Domenico, Y. Creff, J. Bernard, V. Sauvant-Moynot, and F. Huet, “A Simplified Electrochemical and Thermal Aging Model of LiFePO4-Graphite Li-ion Batteries: Power and Capacity Fade Simulations,” *J. Electrochem. Soc.*, vol. 160, no. 4, pp. A616–A628, Feb. 2013.

[167] J. M. Sullivan, D. C. Hanson, and R. Keller, “Diffusion Coefficients in Propylene Carbonate, Dimethyl Formamide, Acetonitrile, and Methyl Formate,” *J. Electrochem. Soc.*, vol. 117, no. 6, pp. 779–780, 1970.

[168] H. J. Gores and J. Barthel, “Conductance of salts at moderate and high concentrations in propylene carbonate-dimethoxyethane mixtures at temperatures from -45°C to 25°C,” *J. Solution Chem.*, vol. 9, no. 12, pp. 939–954, 1980.

[169] E. Prada, D. Di Domenico, Y. Creff, J. Bernard, V. Sauvant-Moynot, and F. Huet, “Physics-based modelling of LiFePO4-graphite Li-ion batteries for power and capacity fade predictions: Application to calendar aging of PHEV and EV,”

2012 IEEE Veh. Power Propuls. Conf. VPPC 2012, pp. 301–308, 2012.

[170] E. Prada, D. Di Domenico, Y. Creff, J. Bernard, V. Sauvant-Moynot, and F. Huet, “Simplified Electrochemical and Thermal Model of LiFePO4-Graphite Li-Ion Batteries for Fast Charge Applications,” *J. Electrochem. Soc.*, vol. 159, no. 9, pp. A1508–A1519, 2012.

[171] P. Ramadass, B. Haran, R. White, and B. N. Popov, “Mathematical modeling of the capacity fade of Li-ion cells,” *J. Power Sources*, vol. 123, no. 2, pp. 230–240, 2003.

[172] P. Ramadass, B. Haran, P. M. Gomadam, R. White, and B. N. Popov, “Development of First Principles Capacity Fade Model for Li-Ion Cells,” *J. Electrochem. Soc.*, vol. 151, no. 2, p. A196, 2004.

[173] E. J. Plichta and W. K. Behl, “A low-temperature electrolyte for lithium and lithium-ion batteries,” *J. Power Sources*, vol. 88, no. 2, pp. 192–196, 2000.

[174] A. Nyman, M. Behm, and G. Lindbergh, “Electrochemical characterisation and modelling of the mass transport phenomena in LiPF6-EC-EMC electrolyte,” *Electrochim. Acta*, vol. 53, no. 22, pp. 6356–6365, 2008.

[175] G.-A. Nazri and G. Pistoia, *Lithium Batteries Science and Technology*. 2009.

[176] M. Doyle, “Comparison of Modeling Predictions with Experimental Data from Plastic Lithium Ion Cells,” *J. Electrochem. Soc.*, vol. 143, no. 6, p. 1890, 1996.

[177] C. Capiglia, Y. Saito, H. Kageyama, P. Mustarelli, T. Iwamoto, T. Tabuchi, and H. Tukamoto, “7Li and 19F diffusion coefficients and thermal properties of non-aqueous electrolyte solutions for rechargeable lithium batteries,” *J. Power Sources*, vol. 81–82, pp. 859–862, 1999.

[178] C. J. Wen, B. A. Boukamp, R. A. Huggins, and W. Weppner, “Thermodynamic and Mass Transport Properties of ‘LiAl,’” *J. Electrochem. Soc.*, vol. 126, no. 12, p. 2258, 1979.

[179] W. Weppner and R. A. Huggins, “Determination of the Kinetic Parameters of Mixed-Conducting Electrodes and Application to the System LLSb,” *J. Electrochem. Soc.*, vol. 124, no. 10, pp. 1569–1578, 1977.

[180] C. Delacourt, M. Ati, and J. M. Tarascon, “Measurement of Lithium Diffusion Coefficient in LiyFeSO4F,” *J. Electrochem. Soc.*, vol. 158, no. 6, pp. 741–749, 2011.

[181] P. Yu, “Determination of the Lithium Ion Diffusion Coefficient in Graphite,” *J. Electrochem. Soc.*, vol. 146, no. 1, p. 8, 1999.

[182] J. Barker, R. Pynenburg, R. Koksbang, and M. Y. Saidi, “LITHIUM INSERTION

INVESTIGATION INTO THE LITHIUM INSERTION PROPERTIES OF LixCoO2," *Electrochim. Acta*, vol. 41, no. 15, pp. 2481–2488, 1996.

[183] Y.-M. Choi, S.-I. Pyun, and J. M. Paulsen, "Lithium transport through porous Li1−δCoO2 electrode: analysis of current transient," *Electrochim. Acta*, vol. 44, no. 4, pp. 623–632, 1998.

[184] A. Funabiki, M. Inaba, Z. Ogumi, S. Yuasa, J. Otsuji, and A. Tasaka, "Impedance Study on the Electrochemical Lithium Intercalation into Natural Graphite Powder," *J. Electrochem. Soc.*, vol. 145, no. 1, pp. 172–178, 1998.

[185] K. M. Shaju, G. V. Subba Rao, and B. V. R. Chowdari, "Influence of Li-Ion Kinetics in the Cathodic Performance of Layered Li(Ni[sub 1/3]Co[sub 1/3]Mn[sub 1/3])O[sub 2]," *J. Electrochem. Soc.*, vol. 151, no. 9, p. A1324, 2004.

[186] Y.-M. Choi and S.-I. Pyun, "Determination of electrochemical active area of porous Li1−δCoO2 electrode using the GITT technique," *Solid State Ionics*, vol. 109, no. 1–2, pp. 159–163, 1998.

[187] M. D. Levi and D. Aurbach, "Diffusion Coefficients of Lithium Ions during Intercalation into Graphite Derived from the Simultaneous Measurements and Modeling of Electrochemical Impedance and Potentiostatic Intermittent Titration Characteristics of Thin Graphite Electrodes," *J. Phys. Chem. B*, vol. 101, no. 23, pp. 4641–4647, 1997.

[188] N. Zhao, X. Zhi, L. Wang, Y. Liu, and G. Liang, "Effect of microstructure on low temperature electrochemical properties of LiFePO4/C cathode material," *J. Alloys Compd.*, vol. 645, pp. 301–308, 2015.

[189] V. R. Subramanian, V. Boovaragavan, and V. D. Diwakar, "Toward Real-Time Simulation of Physics Based Lithium-Ion Battery Models," *Electrochem. Solid-State Lett.*, vol. 10, no. 11, p. A255, 2007.

[190] M. Park, X. Zhang, M. Chung, G. B. Less, and A. M. Sastry, "A review of conduction phenomena in Li-ion batteries," *J. Power Sources*, vol. 195, no. 24, pp. 7904–7929, 2010.

[191] S. Watanabe, M. Kinoshita, T. Hosokawa, K. Morigaki, and K. Nakura, "Capacity fade of LiAlyNi1-x-yCoxO 2 cathode for lithium-ion batteries during accelerated calendar and cycle life tests (surface analysis of LiAlyNi1-x-yCo xO2 cathode after cycle tests in restricted depth of discharge ranges)," *J. Power Sources*, vol. 258, pp. 210–217, 2014.

[192] S. Watanabe, M. Kinoshita, and K. Nakura, "Capacity fade of LiNi(1-x-

y)CoxAlyO 2 cathode for lithium-ion batteries during accelerated calendar and cycle life test. I. Comparison analysis between LiNi(1-x-y)Co xAlyO2 and LiCoO2 cathodes in cylindrical lithium-ion cells during long term storage test," *J. Power Sources*, vol. 247, pp. 412–422, 2014.

[193] J. Xu, R. D. Deshpande, J. Pan, Y.-T. Cheng, and V. S. Battaglia, "Electrode Side Reactions, Capacity Loss and Mechanical Degradation in Lithium-Ion Batteries," *J. Electrochem. Soc.*, vol. 162, no. 10, pp. A2026–A2035, 2015.

[194] C. Hendricks, N. Williard, S. Mathew, and M. Pecht, "Review article A failure modes , mechanisms , and effects analysis (FMMEA) of lithium-ion batteries," *J. Power Sources*, vol. 297, pp. 113–120, 2015.

[195] J. Groot, "State-of-health estimation of Li-ion batteries: cycle life test methods," *PhD, CHALMERS Univ. Technol.*, p. 138, 2012.

[196] X. Han, M. Ouyang, L. Lu, J. Li, Y. Zheng, and Z. Li, "A comparative study of commercial lithium ion battery cycle life in electrical vehicle: Aging mechanism identification," *J. Power Sources*, vol. 251, pp. 38–54, 2014.

[197] R. Fu, S. Choe, V. Agubra, and J. Fergus, "Development of a physics-based degradation model for lithium ion polymer batteries considering side reactions," *J. Power Sources*, vol. 278, pp. 506–521, 2015.

[198] A. Barré, B. Deguilhem, S. Grolleau, M. Gérard, F. Suard, and D. Riu, "A review on lithium-ion battery ageing mechanisms and estimations for automotive applications," *J. Power Sources*, vol. 241, pp. 680–689, 2013.

[199] L. L. Lam and R. B. Darling, "Determining the optimal discharge strategy for a lithium-ion battery using a physics-based model," *J. Power Sources*, vol. 276, pp. 195–202, 2015.

[200] R. Darling and J. Newman, "Modeling Side Reactions in Composite Li[sub y]Mn[sub 2]O[sub 4] Electrodes," *J. Electrochem. Soc.*, vol. 145, no. 3, p. 990, 1998.

[201] Q. Zhang and R. E. White, "Calendar life study of Li-ion pouch cells," *J. Power Sources*, vol. 179, no. 2, pp. 785–792, May 2008.

[202] K. E. Aifantis and J. P. Dempsey, "Stable crack growth in nanostructured Li-batteries," vol. 143, pp. 203–211, 2005.

[203] M. Safari and C. Delacourt, "Aging of a Commercial Graphite/LiFePO4 Cell," *J. Electrochem. Soc.*, vol. 158, no. 10, p. A1123, 2011.

[204] Y. Cui, C. Du, G. Yin, Y. Gao, L. Zhang, T. Guan, L. Yang, and F. Wang, "Multi-stress factor model for cycle lifetime prediction of lithium ion batteries with

shallow-depth discharge," *J. Power Sources*, vol. 279, pp. 123–132, 2015.

[205] T. Wang, L. Pei, T. Wang, R. Lu, and C. Zhu, "Capacity-loss diagnostic and life-time prediction in lithium-ion batteries: Part 1. Development of a capacity-loss diagnostic method based on open-circuit voltage analysis," *J. Power Sources*, vol. 301, pp. 187–193, 2016.

[206] C. Delacourt and M. Safari, "Life Simulation of a Graphite/LiFePO4 Cell under Cycling and Storage," *J. Electrochem. Soc.*, vol. 159, no. 8, pp. A1283–A1291, Jul. 2012.

[207] P. Arora, R. E. White, and M. Doyle, "Capacity Fade Mechanisms and Side Reactions in Lithium-Ion Batteries," *J. Electrochem. Soc.*, vol. 145, no. 10, pp. 3647–3667, 1998.

[208] S. Brown, N. Mellgren, M. Vynnycky, and G. Lindbergh, "Impedance as a Tool for Investigating Aging in Lithium-Ion Porous Electrodes," *J. Electrochem. Soc.*, vol. 155, no. 4, p. A304, 2008.

[209] I. Laresgoiti, S. Käbitz, M. Ecker, and D. U. Sauer, "Modeling mechanical degradation in lithium ion batteries during cycling: Solid electrolyte interphase fracture," *J. Power Sources*, vol. 300, pp. 112–122, 2015.

[210] H. J. Ploehn, P. Ramadass, and R. E. White, "Solvent Diffusion Model for Aging of Lithium-Ion Battery Cells," *J. Electrochem. Soc.*, vol. 151, no. 3, p. A456, 2004.

[211] R. Narayanrao, M. M. Joglekar, and S. Inguva, "A Phenomenological Degradation Model for Cyclic Aging of Lithium Ion Cell Materials," *J. Electrochem. Soc.*, vol. 160, no. 1, pp. A125–A137, 2012.

[212] L. Zhang, Y. Ma, X. Cheng, C. Du, T. Guan, Y. Cui, S. Sun, P. Zuo, Y. Gao, and G. Yin, "Capacity fading mechanism during long-term cycling of over-discharged LiCoO2/mesocarbon microbeads battery," *J. Power Sources*, vol. 293, pp. 1006–1015, 2015.

[213] C. Delacourt, C. Ades, and Q. Badey, *Vieillissement des accumulateurs lithium-ion dans l'automobile*. TECHNIQUES DE L'INGÉNIEUR, 2014.

[214] T. Waldmann, G. Bisle, B.-I. Hogg, S. Stumpp, M. A. Danzer, M. Kasper, P. Axmann, and M. Wohlfahrt-Mehrens, "Influence of Cell Design on Temperatures and Temperature Gradients in Lithium-Ion Cells: An In Operando Study," *J. Electrochem. Soc.*, vol. 162, no. 6, pp. A921–A927, 2015.

[215] R. Hamlen, G. Au, M. Brundage, M. Hendrickson, E. Plichta, S. Slane, and J. Barbarello, "US Army portable power programs," vol. 98, pp. 97–99, 2001.

[216] S. C. Chen, C. C. Wan, and Y. Y. Wang, “Thermal analysis of lithium-ion batteries,” vol. 140, no. May 2004, pp. 111–124, 2005.

[217] P. E. Pascoe and A. H. Anbuky, “A unified discharge voltage characteristic for VRLA battery capacity and reserve time estimation,” vol. 45, pp. 277–302, 2004.

[218] C. P. De Oliveira and M. C. Lopes, “Early stages of the lead-acid battery discharge,” vol. 138, pp. 294–300, 2004.

[219] P. E. Pascoe and A. H. Anbuky, “The behaviour of the coup de fouet of valve-regulated lead – acid batteries,” vol. 111, pp. 304–319, 2002.

[220] P. E. Pascoe and A. H. Anbuky, “A VRLA battery simulation model,” vol. 45, pp. 1015–1041, 2004.

[221] A. Delaille, M. Perrin, F. Huet, and L. Hernout, “Study of the ‘ coup de fouet ’ of lead-acid cells as a function of their state-of-charge and state-of-health,” vol. 158, pp. 1019–1028, 2006.

[222] K. Chao and J. Chen, “Expert Systems with Applications State-of-health estimator based-on extension theory with a learning mechanism for lead-acid batteries,” *Expert Syst. Appl.*, vol. 38, no. 12, pp. 15183–15193, 2011.

[223] M. Nandanwar and S. Kumar, “Charge coup de fouet phenomenon in soluble lead redox fl ow battery,” *Chem. Eng. Sci.*, vol. 154, pp. 61–71, 2016.

[224] P. Arora, R. E. White, and M. Doyle, “Capacity Fade Mechanisms and Side Reactions in Lithium-Ion Batteries,” *J. Electrochem. Soc.*, vol. 145, no. 10, p. 3647, 1998.

[225] M. Broussely, P. Biensan, F. Bonhomme, P. Blanchard, S. Herreyre, K. Nechev, and R. J. Staniewicz, “Main aging mechanisms in Li ion batteries,” *J. Power Sources*, vol. 146, no. 1–2, pp. 90–96, 2005.

[226] C. R. Birkl, M. R. Roberts, E. McTurk, P. G. Bruce, and D. A. Howey, “Degradation diagnostics for lithium ion cells,” *J. Power Sources*, vol. 341, pp. 373–386, 2017.

[227] J.-K. Park, *Principles and Applications of Lithium Secondary Batteries*. John Wiley & Sons, Inc., 2012.

[228] A. J. Smith, J. C. Burns, and J. R. Dahn, “A High Precision Study of the Coulombic Efficiency of Li-Ion Batteries,” *Electrochem. Solid-State Lett.*, vol. 13, no. 12, p. A177, 2010.

[229] A. J. Smith, J. C. Burns, S. Trussler, and J. R. Dahn, “Precision Measurements of the Coulombic Efficiency of Lithium-Ion Batteries and of Electrode Materials

for Lithium-Ion Batteries," *J. Electrochem. Soc.*, vol. 157, no. 2, p. A196, 2010.

[230] I. Bloom, L. K. Walker, J. K. Basco, D. P. Abraham, J. P. Christophersen, and C. D. Ho, "Differential voltage analyses of high-power lithium-ion cells. 4. Cells containing NMC," *J. Power Sources*, vol. 195, no. 3, pp. 877–882, 2010.

[231] C. Weng, J. Sun, and H. Peng, "An open-circuit-voltage model of lithium-ion batteries for effective incremental capacity analysis," *Proc. ASME 2013 Dyn. Syst. Control Conf.*, pp. 1–8, 2013.

[232] M. Dubarry, C. Truchot, and B. Y. Liaw, "Synthesize battery degradation modes via a diagnostic and prognostic model," *J. Power Sources*, vol. 219, pp. 204–216, 2012.

[233] M. Dubarry, B. Y. Liaw, M. S. Chen, S. S. Chyan, K. C. Han, W. T. Sie, and S. H. Wu, "Identifying battery aging mechanisms in large format Li ion cells," *J. Power Sources*, vol. 196, no. 7, pp. 3420–3425, 2011.

[234] M. Dubarry and B. Y. Liaw, "Identify capacity fading mechanism in a commercial LiFePO4 cell," *J. Power Sources*, vol. 194, no. 1, pp. 541–549, 2009.

[235] M. Kassem, J. Bernard, R. Revel, S. Pélissier, F. Duclaud, and C. Delacourt, "Calendar aging of a graphite/LiFePO 4 cell," *J. Power Sources*, vol. 208, pp. 296–305, 2012.

[236] M. Kassem and C. Delacourt, "Postmortem analysis of calendar-aged graphite/LiFePO4 cells," *J. Power Sources*, vol. 235, pp. 159–171, 2013.

[237] M. Ouyang, D. Ren, L. Lu, J. Li, X. Feng, X. Han, and G. Liu, "Overcharge-induced capacity fading analysis for large format lithium-ion batteries with LiyNi1/3Co1/3Mn1/3O2 + LiyMn2O4 composite cathode," *J. Power Sources*, vol. 279, pp. 626–635, 2015.

[238] A. Marongiu, F. Gerd, W. Nußbaum, W. Waag, M. Garmendia, and D. Uwe, "Comprehensive study of the influence of aging on the hysteresis behavior of a lithium iron phosphate cathode-based lithium ion battery – An experimental investigation of the hysteresis," *Appl. Energy*, vol. 171, pp. 629–645, 2016.

[239] P. Keil, S. F. Schuster, J. Wilhelm, J. Travi, A. Hauser, R. C. Karl, and A. Jossen, "Calendar Aging of Lithium-Ion Batteries," *J. Electrochem. Soc.*, vol. 163, no. 9, pp. A1872–A1880, 2016.

[240] S. Krueger, R. Kloepsch, J. Li, S. Nowak, S. Passerini, and M. Winter, "How Do Reactions at the Anode/Electrolyte Interface Determine the Cathode Performance in Lithium-Ion Batteries?," *J. Electrochem. Soc.*, vol. 160, no. 4,

pp. A542–A548, 2013.

[241] W. Dreyer, J. Jamnik, C. Guhlke, R. Huth, J. Moskon, and M. Gaberscek, “The thermodynamic origin of hysteresis in insertion batteries,” *Nat. Mater.*, vol. 9, no. 5, pp. 448–453, 2010.

[242] A. Barai, W. D. Widanage, J. Marco, A. Mcgordon, and P. Jennings, “A study of the open circuit voltage characterization technique and hysteresis assessment of lithium-ion cells,” *J. Power Sources*, vol. 295, pp. 99–107, 2015.

[243] F. Baronti, N. Femia, R. Saletti, C. Visone, and W. Zamboni, “Preisach modelling of lithium-iron-phosphate battery hysteresis,” *J. Energy Storage*, vol. 4, pp. 51–61, 2015.

[244] H. Konishi, T. Hirano, D. Takamatsu, A. Gunji, and X. Feng, “Origin of hysteresis between charge and discharge processes in lithium-rich layer-structured cathode material for lithium-ion battery,” *J. Power Sources*, vol. 298, pp. 144–149, 2015.

[245] H. Konishi, T. Hirano, D. Takamatsu, A. Gunji, X. Feng, S. Furutsuki, S. Takahashi, and S. Terada, “Potential hysteresis between charge and discharge reactions in Li1.2Ni0.13Mn0.54Co0.13O2 for lithium ion batteries,” *Solid State Ionics*, vol. 300, pp. 120–127, 2017.

[246] M. Kasai, S. Nishimura, A. Gunji, and H. Konishi, “Electrochimica Acta layered complex cathode showing voltage hysteresis,” vol. 146, pp. 79–88, 2014.

[247] K. G. Gallagher, J. R. Croy, M. Balasubramanian, M. Bettge, D. P. Abraham, A. K. Burrell, and M. M. Thackeray, “Electrochemistry Communications Correlating hysteresis and voltage fade in lithium- and manganese-rich layered transition-metal oxide electrodes,” *Electrochem. commun.*, vol. 33, pp. 96–98, 2013.

[248] J. Moskon, J. Jamnik, and M. Gaberscek, “In depth discussion of selected phenomena associated with intrinsic battery hysteresis : Battery electrode versus rubber balloons,” *Solid State Ionics*, vol. 238, pp. 24–29, 2013.

[249] C. Edouard, M. Petit, C. Forgez, J. Bernard, and R. Revel, “Parameter sensitivity analysis of a simplified electrochemical and thermal model for Li-ion batteries aging,” *J. Power Sources*, vol. 325, pp. 482–494, 2016.

[250] J. Smekens, J. Paulsen, W. Yang, N. Omar, J. Deconinck, A. Hubin, and J. Van Mierlo, “Electrochimica Acta A Modified Multiphysics model for Lithium-Ion batteries with a Li x Ni 1 / 3 Mn 1 / 3 Co 1 / 3 O 2 electrode,” *Electrochim. Acta*, vol. 174, pp. 615–624, 2015.

[251] P. A. Johns, M. R. Roberts, Y. Wakizaka, J. H. Sanders, and J. R. Owen, “How the electrolyte limits fast discharge in nanostructured batteries and supercapacitors,” *Electrochem. commun.*, vol. 11, no. 11, pp. 2089–2092, 2009.

[252] R. Cornut, D. Lepage, and S. B. Schougaard, “Interpreting lithium batteries discharge curves for easy identification of the origin of performance limitations,” *Electrochim. Acta*, vol. 162, pp. 271–274, 2015.

[253] L. Lam, P. Bauer, and E. Kelder, “A Practical Circuit-based Model for Li-ion Battery Cells in Electric Vehicle Applications,” 2011.

[254] B. Schweighofer, K. M. Raab, G. Brasseur, and S. Member, “Modeling of High Power Automotive Batteries by the Use of an Automated Test System,” vol. 52, no. 4, pp. 1087–1091, 2003.

[255] M. Bahramipanah, D. Torregrossa, and M. Paolone, “Enhanced Electrical Model of Lithium-Based Batteries Accounting the Charge Redistribution Effect,” 2014.

[256] Y. Hu, S. Yurkovich, Y. Guezennec, and B. J. Yurkovich, “Electro-thermal battery model identification for automotive applications,” vol. 196, pp. 449–457, 2011.

[257] Y. Zou, X. Hu, H. Ma, and S. Eben, “Combined State of Charge and State of Health estimation over lithium-ion battery cell cycle lifespan for electric vehicles,” *J. Power Sources*, vol. 273, pp. 793–803, 2015.

[258] D. W. Dees and K. Gallagher, “Electrochemistry Cell Model,” *DOE Veh. Technol. Annu. Merit Rev.*, 2011.

[259] S. S. Zhang, “The effect of the charging protocol on the cycle life of a Li-ion battery,” vol. 161, no. April, pp. 1385–1391, 2006.

Résumé (long)

Régulièrement, les véhicules électrique (VE) sont proposés comme une alternative aux véhicules à combustion interne, représentant une solution viable à la pollution métropolitaine et à l'instabilité géopolitique des pays producteurs de combustible fossile. Le développement massif de cette technologie est pour le moment bloqué par la faible autonomie des véhicules et par leur cout élevé.

Néanmoins, le prix des batteries est en constante baisse et la volonté politique de réduire les émission polluantes (e.g. NO_x, pm10, CO_2) devrait accélérer la diffusion de cette technologie. Il est ainsi anticipé que des centaines de milliers de véhicules électriques circuleront dans le monde d'ici 2020.

Aujourd'hui le contexte industriel est en pleine mutation numérique et environnementale. Les acteurs du domaine de l'automobile, eux aussi, évoluent rapidement et la voiture s'électrifie, se connecte, s'automatise. Le programme « zéro émissions » est la réponse de Renault à la problématique des émissions polluantes, qui a rendu Renault leader de vente des véhicules électriques. L'objectif est d'assurer à tout le monde l'accès à des véhicules silencieux et sans émissions polluantes, le tout sans compromis sur les performances et la sécurité. Ce succès est envisageable grâce à la technologie des batteries lithium-ion, qui à ce jour représente la meilleure solution en termes de densité énergétique, puissance et durabilité ainsi que de coût pour le stockage d'énergie électrique.

Néanmoins, des améliorations sont désirables pour allonger la durée de vie à plus de 10 ans et réduire les temps de caractérisation sur les bancs d'essai. La modélisation pourrait être une solution pour mieux comprendre les phénomènes physico-chimiques complexes et donc améliorer la conception de nouvelles cellules, qui vont permettre de répondre à ces besoins de durabilité et de performances, grâce à un système de gestion des batteries amélioré. La procédure standard d'évaluation des performances d'une batterie consiste à effectuer des cycles de charge-décharge à courant constant. Généralement, plus le courant est élevé et plus la capacité obtenue diminue à cause de limitations cinétiques, due à la migration de ions, à la diffusion des espèces chimiques ou au transfert de charges. Idéalement un modèle électrochimique doit simuler les cellules lithium-ion à partir des paramètres psycho-chimique de ses matériaux constitutifs. Ainsi, si une caractérisation de chaque matériau permet de prévoir le comportement de la cellule avant sa fabrication, le modèle aura beaucoup d'intérêt pour la conception des nouvelles cellules.

Le modèle électrochimique le plus utilisé a été développé par le prof. J. Newman et son équipe de recherche à l'université de Berkeley aux Etats Unis. La cellule, constituée de deux électrodes et d'un séparateur, est représenté dans le modèle par sa section transversale, ce qui implique que les effets de bord dans la longueur et la hauteur de la batterie sont négligés. La diffusion décrit le transport dans les particules sphériques. L'équation de diffusion est exprimée en coordonnées sphériques pour le bilan matière du lithium dans les particules. Pour ces raisons le modèle est dit « pseudo bi-dimensionnel » avec une dimension orthogonale aux électrodes et une dimension pour le transport dans les particules de matière active. Les pores du séparateur et des électrodes sont remplis par un électrolyte, supposé binaire (i.e. ions lithium et ses anions), qui est décrit par la théorie des solutions concentrées. La réaction principale d'insertion du lithium est supposée suivre une loi de type Butler-Volmer. Les électrodes volumiques sont traitées comme des électrodes poreuses à l'échelle macroscopique avec deux milieux homogènes imbriqués : une phase liquide où agit le transport des ions et une phase solide où on simule la diffusion de lithium inséré et le transport d'électrons.

Au cours du temps, la communauté scientifique a complexifié ce modèle et plusieurs logiciels de simulations sont maintenant commerciaux. Après la commercialisation de la première batterie rechargeable au lithium ion par SONY en 1991 le nombre de publications sur la batterie lithium ions est passé de moins de 5 par année à plus de 3000 en 2016. Dans ce domaine, plus de 150 articles par année portent sur la modélisation, en sens large, de batteries lithium ion.

Dans une précédente thèse un modèle électrochimique simplifié (i.e. modèle dit de "la particule seule") a été développé chez Renault en 2011 par Safari. Ce modèle a permis de simuler les décharges jusqu'à 1C pour des cellules graphite / LFP. Aujourd'hui Renault souhaite intégrer ce travail à celui initié par le groupe de Newman, dont il souhaite identifier les points forts et les points faibles. Pour ces raisons la thèse a été structurée en cinq parties: une description critique de la littérature incluant le référencement des paramètres du modèle développé par le groupe de Newman et les techniques utilisées pour le mesurer, l'écriture du modèle dans un format adimensionnel pour réduire le nombre de paramètres, une partie expérimentale pour améliorer le reproductibilité des essais, l'identification des états de lithiation dans la cellule avec un attention particulière sur la précision obtenue, et enfin une prospection numérique pour examiner l'influence de chaque paramètre sur les performances de la batterie.

Les nouveaux modèles de « modèle de Newman » sont de plus en plus complexes, avec par exemple l'ambition de modéliser la température dans la batterie, les réactions parasites et les déformations mécaniques. Cette augmentation de complexité ne se limite pas seulement à la physique mais aussi à la géométrie qui passe d'un pseudo-2D au pseudo-4D (3D pour la géométrie de la cellule plus une dimension pour le transport dans les particules de matière active) ou 3D complet avec une structure poreuse mesurée par la tomographie. En conséquence, ces modèles ont de plus en plus de paramètres d'entrée, dont plusieurs sont difficilement mesurables, si bien que leur valeur est ajustée pour obtenir des simulations qui reproduisent les résultats expérimentaux. Malgré la sophistication physique et mathématique de ces modèles récents, ils ne s'avèrent pas plus prédictifs que les modèles plus simples. L'objectif d'une partie du travail présenté dans ce manuscrit est de simplifier le modèle électrochimique de Newman pour mieux comprendre l'effet de chaque paramètre sur les simulations.

Dans une première partie, le système d'équations et ses paramètres sont réécrits sous une forme adimensionnelle, pour permettre la généralisation des résultats. Cette technique est très exploitée dans plusieurs domaines dont la mécanique des fluides avec l'identification des nombres de Reynolds ou de Prandtl par exemple. Grâce à cette méthode, on réduit le nombre des paramètres du modèle et on identifie plus facilement les influences semblables de certains de ces paramètres.

Le modèle est écrit à partir des équations de la thermodynamique en supposant que l'électrolyte est idéal. Il ressort de cette hypothèse que l'activité est égale à la concentration des ions et que les paramètres de transport de la matière suivent la loi de Nernst-Einstein (avec des coefficients indépendants de la concentration). On suppose aussi que les nombres de transport des ions sont identiques dans les phases liquides des électrodes poreuses que dans le séparateur. Les coefficients de diffusion, dans le modèle proposé ne dépendent pas de la concentration et leurs valeurs effectives dans les électrodes poreuses et dans le séparateur sont décrites comme des paramètres différents en évitant de rajouter des relations entre eux avec des coefficients de correction (par exemple l'approximation de Bruggeman).

Dans cette étude on se focalise sur la capacité obtenue en fin de décharge. Pour simplifier l'étude, on travaille sur une seule électrode, l'électrode positive, avec une électrode négative et un séparateur dont les propriétés sont telles qu'aucune limitation n'y survient. Cela permet de réduire le nombre de paramètres de 25 (en grandeur dimensionnelle) à 4 paramètres adimensionnels. Dans ces conditions, bien que le nombre de combinaisons de paramètres à analyser reste important, une analyse prospective devient envisageable.

Dans une deuxième partie, nous avons discuté comment les paramètres de ce modèle sont mesurés dans la littérature, et, dans une troisième partie un protocole de cyclage a été mis en place pour garantir la reproductibilité des mesures (courbes de décharge à différents régimes et succession de pulse et repos) et réduire les effets de l'histoire du cyclage.

La détermination des états de lithiation dans une cellule complète a été investiguée dans une quatrième partie. Les états de lithiation représentent des paramètres indispensables pour simuler des systèmes complets. Ils sont aussi des éléments clés dans les études du vieillissement par l'impact de leurs variations sur les performances globales de la batterie. Ces paramètres ne sont pas connus sans étude : en effet après que les électrodes sont assemblées, lors de la première charge la réaction associée à la formation d'une couche interface solide (SEI) sur l'électrode négative change ces paramètres. *De facto*, l'état de charge des batteries en début et en fin de charge devient alors inconnu, tout en étant de plus sujet à se modifier au cours du temps par des processus de vieillissement. Notre première tâche a été de comprendre comment la forme des isothermes influence la précision associée à l'évaluation des états de charge initiaux et finaux. Cette méthode a ensuite été appliquée à des cellules commerciales LG-Chemical. Plusieurs scenarios de vieillissement ont été proposés pour observer comment l'OCV évolue avec les états de charge. Ces résultats ont finalement été discutés avec les OCV mesurés sur des cellules commerciales LGC après un vieillissement modéré.

Dans une cinquième partie, le système d'équations est implémenté et simulé avec le logiciel COMSOL Multiphysics, ce qui a permis d'étudier l'effet individuel des paramètres identifiés dans la première partie. L'étude a permis de comprendre les observations effectuées pendant les décharges à courant constant sur les cellules commerciales examinées. Puis, les simulations ont été conduites sur des séquences d'impulsions-relaxations. Ce type de protocole de caractérisation est généralement utilisé pour établir comment varie la résistance interne dans différentes conditions (e.g. température de stockage, état de charges, etc.). Expérimentalement, on observe que la relaxation de la tension contient plusieurs constantes de temps. Des constantes de temps se retrouvent dans le modèle étudié dans la première partie, chacune étant attribuable à des phénomènes physiques précisément identifiables. Les simulations ont permis de trouver 2 combinaisons différentes de constante de temps qui reproduisent la tension mesurée pendant et après l’impulsion de courant. Ce résultat met notamment en perspective une méthode largement utilisée pour mesurer le coefficient de diffusion du lithium dans la phase solide, appelé GITT (i.e. Galvanostatic Intermittent Titration Technique), dont la fiabilité est ainsi remise en cause.

L'étude a mis en évidence : (i) comment les combinaisons de paramètres, dans le nouveau système d’équations adimensionnel influencent les performances a diffèrent régimes, (ii) que l’évaluation des constantes des temps associée à différents phénomènes nécessite des méthodes plus appropriées que ce qui est proposée actuellement dans la littérature, (iii) que la forme des isothermes des électrodes influence de manière significative la précision avec laquelle on évalue les états de charge dans une cellule complète. La prospection numérique devrait être étendue à une cellule complète pour comprendre l’interaction du transport de matière dans un système de deux électrodes à insertion couplées. Sur un plan expérimental, le vieillissement des cellules devrait être fait dans des conditions plus agressives pour permettre d’établir une relation entre les conditions de vieillissement et l’évolution des états de charge des deux électrodes.

Abstract (grand public)

The future development of electric vehicles is mostly dependent of improvements in battery performances. In support of the actual research of new materials having higher performances it is useful to develop modeling tools. Furthermore, the battery models could be used to understand the physicochemical phenomena and to improve the design and reduce the testing time. One of the most common electrochemical model for lithium ion batteries is revisited and set in a dimensionless form. The influence of its parameters is analyzed with galvanostatic and pulse-rest sequence simulations performed with the software COMSOL Multiphysics. The electrode balancing and the accuracy during the estimation of the parameters associated to the electrode states of charge is discussed. Finally, a characterization protocol aiming to increases the precision of measurement is proposed.

Résumé (grand public)

Le développement des véhicules électriques dépend principalement des améliorations apportées aux performances de la batterie. En support à la recherche de nouveaux matériaux plus performantes, il est utile de développer des outils de modélisation, pour comprendre les phénomènes physico-chimiques et pour améliorer la conception. Cette étude contient une description critique de la littérature incluant le référencement des paramètres du modèle développé par le groupe de Newman et les techniques utilisées pour le mesurer, l’écriture du modèle dans un format adimensionnel pour réduire le nombre de paramètres, une partie expérimentale pour améliorer le reproductibilité des essais, l’identification des états de lithiation dans la cellule avec un attention particulière sur la précision obtenue, et enfin une prospection numérique pour examiner l’influence de chaque paramètre sur les performances de la batterie.

Acknowledgments

I would like to thank my supervisors Christine Lefrou, Renaud Cornut and David Sicsic for their supports and the funding from the ANRT (Association Nationale de la Recherche et de la Technologie) and the Renault Group.

I am deeply grateful to all members of the jury for agreeing to read the manuscript and to participate in the defense of this thesis.

The LICSEN (Laboratory of Innovation in Surface Chemistry and Nanosciences) from the French Atomic Commission (CEA), the Battery Innovation Group in Renault, directed by Derycke Vincent and Tran-Van Pierre, respectively, and the LEPMI (Laboratory of Electrochemistry and Physicochemistry of Materials and Interfaces) are gratefully acknowledged.

Nathalie Cornet, Bruno Delobel, Masato Origuchi, Lucas Sannier, Philippe Gyan, Mohammed Chakir, David Leray, Aurelien Gohier, Frabrice Bidault, Magali Maccario, François Orsini, Nicolas Besnard and Issam Baghdadi from Renault, Fabio Bocchi and Tommy Zavalis from Comsol, Mikhail Cugnet from INES, Charles Delacourt and Alejandro A. Franco from the LRCS and Marcello Canova from the Ohio State University are acknowledged for valuable discussions.

Claire Barreau and Tuan-Tu Nguyen from Serma Technologie are very acknowledged for valuable support.